Universität Rostock Traditio et Innovatio

LEIBNIZ-INSTITUTE OF ATMOSPHERIC PHYSICS IAP

On Kilometer-Scale Varicose-Mode Flows in the Polar Summer Mesosphere

Dissertation
zur Erlangung des akademischen Grades
doctor rerum naturalium (Dr. rer. nat.)
der Mathematisch-Naturwissenschaftlichen Fakultät
der Universität Rostock

vorgelegt von
Jennifer Hartisch,
geboren am 8. September 1995 in Strausberg

Rostock, den 03.09.2025

https://doi.org/10.18453/rosdok_id00005756



Dieses Werk ist lizenziert unter einer
Creative Commons Namensnennung 4.0 International Lizenz.

1. Gutachter und Betreuer: Prof. Dr. J. L. Chau, IAP, Germany
2. Gutachter: Prof. Dr. Cora Randall, University of Colorado, USA

eingereicht am: 03.09.2025
verteidigt am: 30.01.2026

Adresse: Universität Rostock
Institut für Physik
18051 Rostock
Tel: +49 381 498-6926
Internet: http://www.physik.uni-rostock.de
E-Mail: jennifer.hartisch@uni-rostock.de

Abstract

The mesosphere and lower thermosphere (MLT) region remains one of the least understood layers of the atmosphere, largely due to the observational challenges associated with its altitude and the complexity of its dynamics. Radar-based remote sensing, particularly through observations of Polar Mesospheric Summer Echoes (PMSE), has proven invaluable for investigating processes in this region. The Middle Atmosphere ALOMAR Radar System (MAARSY), located in northern Norway (69°N, 16°E), provides high-resolution measurements that use PMSE as tracers of MLT dynamics. Following the discovery of a highly localized varicose-mode event by Chau et al. (2021), characterized by simultaneous up- and downdrafts and vertical velocities exceeding 50 m/s, this thesis set out to examine whether such events are isolated or part of a more frequent pattern. A manual search through MAARSY PMSE data from 2015 to 2021 revealed over 700 varicose-mode events, corresponding to occurrence rates of up to 2.5% per month during peak season. These structures exhibit durations of roughly 20 minutes, PMSE layer expansions by factors up to 1.5, and maximum vertical extensions of 8 km. Remarkably, 17% of these events showed vertical velocities beyond three standard deviations from the mean, indicating their non-Gaussian, extreme nature. Their seasonal and diurnal patterns reflect typical PMSE behavior, peaking in June and July. To further investigate the dynamics behind these events, a detailed case study analysis was conducted for four representative cases featuring high vertical velocities and layered structures. Using MAARSY's multibeam and imaging capabilities, combined with horizontal wind data from Multistatic Multi-frequency Agile Radar for Investigations of the Atmosphere (MMARIA) Norway, temperature profiles from the SABER (Sounding of the Atmosphere using Broadband Emission Radiometry) satellite instrument, and directional scattering information from the Saura Partial Reflection Radar (PRR), the events were analyzed in terms of their horizontal propagation, spatial evolution, and ambient conditions. The results reveal consistent propagation across the radar field of view with speeds between 15 and 75 m/s, often at oblique angles or even against the background wind. In several cases, directional information from Saura PRR supported the inferred motion and structure orientation from MAARSY imaging. Additional observations of rotating or undulating fronts, enhanced wind shear, and mesospheric temperature inversions suggest the presence of ducted gravity waves and bore-like behavior.
Altogether, this thesis demonstrates that varicose-mode events are not rare anomalies but a recurring dynamical feature of the polar summer MLT. Their frequent occurrence, coherence, and strong vertical motions highlight the importance of small-scale processes

in shaping mesospheric dynamics – processes that must ultimately be better understood and represented in atmospheric models.

Kurzzusammenfassung

Die Region der Mesosphäre und unteren Thermosphäre (MLT) zählt weiterhin zu den am wenigsten verstandenen Schichten der Atmosphäre, vor allem wegen der beobachtungstechnischen Herausforderungen in dieser Höhe und der Komplexität ihrer Dynamik. Radarbasierten Fernerkundungsverfahren, insbesondere Beobachtungen polarer mesospherischer Sommerechos (PMSE), kommt für die Untersuchung der Prozesse in dieser Region ein hoher Stellenwert zu. Das Middle Atmosphere ALOMAR Radar System (MAARSY) in Nordnorwegen (69° N, 16° E) liefert hochauflösende Messungen, die PMSE als Tracer der MLT-Dynamik nutzen. Ausgelöst durch die von Chau et al. (2021) beobachtete außergewöhnliche variköse Struktur mit extremen vertikalen Geschwindigkeiten von mehr als 50 m/s wurde in dieser Arbeit systematisch nach ähnlichen Erscheinungen gesucht. Dazu wurde eine umfassende manuelle Datenanalyse der MAARSY-PMSE-Beobachtungen zwischen 2015 und 2021 durchgeführt. Die Analyse zeigte: Solche Ereignisse treten keineswegs selten auf — mehr als 700 wurden identifiziert, mit einer typischen monatlichen Auftretenswahrscheinlichkeit von bis zu 2,5% während der Hauptsaison. Sie dauern meist rund 20 Minuten, dehnen die PMSE-Schicht deutlich aus und erreichen vertikale Geschwindigkeiten von bis zu 45 m/s. Bemerkenswert ist, dass 17% dieser Ereignisse vertikale Geschwindigkeiten jenseits von drei Standardabweichungen vom Mittel zeigten, was auf ihren nicht-gaußschen, extremen Charakter hinweist. Ihre saisonalen und tageszeitlichen Muster entsprechen dem typischen PMSE-Verhalten mit Maxima im Juni und Juli. Zur weiteren Untersuchung der zugrunde liegenden Dynamik wurde eine detaillierte Fallstudienanalyse für vier repräsentative Fälle mit hohen Vertikalgeschwindigkeiten und dercharacteristischen varikösen Strukturen durchgeführt. Unter Nutzung der Multibeam- und Imaging-Fähigkeiten von MAARSY, kombiniert mit horizontalen Winddaten des Multistatic Multi-frequency Agile Radar for Investigations of the Atmosphere (MMARIA) in Norwegen, Temperaturprofilen des Satelliteninstruments SABER (Sounding of the Atmosphere using Broadband Emission Radiometry) sowie richtungsabhängigen Streuinformationen des Saura Partial Reflection Radar (PRR), wurden diese Strukturen hinsichtlich ihrer horizontalen Ausbreitung, räumlichen Entwicklung und Umgebungsbedingungen analysiert. Die Ergebnisse zeigen eine konsistente Ausbreitung über das Radarsichtfeld mit Geschwindigkeiten zwischen 15 und 75 m/s, häufig in einem Winkeln zum oder sogar gegen den Hintergrundwind. In mehreren Fällen stützten Richtungsinformationen des Saura PRR die aus den MAARSY-Imagingdaten abgeleitete Bewegung und Eventausrichtung. Weitere Beobachtungen rotierender oder wellenförmiger Fronten, erhöhter Windscherung und mesospherischer Temperaturinversionen deuten auf das Vorliegen von in einem Kanal

gefangenen Schwerewellen und Bore-ähnlichen Verhaltens hin.
Insgesamt zeigt diese Arbeit, dass Ereignisse im varikösen Modus keine seltenen Anomalien sind, sondern ein wiederkehrendes dynamisches Merkmal der polaren Sommer-MLT. Ihr häufiges Auftreten, Kohärenz und zum teil hohen vertikalen WIndgeschwindigkeiten unterstreichen die Bedeutung kleinskaliger Prozesse für die mesospherische Dynamik – Prozesse, die letztlich besser verstanden und in Atmosphärenmodellen adäquat abgebildet werden müssen.

Acknowledgements

First of all, I would like to thank my supervisor, Prof. Dr. Jorge L. Chau, for giving me the chance to work on this topic and for the formative and demanding environment at the Leibniz Institute of Atmospheric Physics that shaped me over these years. His expertise and scientific knowledge have provided steady guidance in the research process. Altogether, this time brought valuable experiences on many levels and created a setting in which I could learn, grow, and further develop my own ideas. The lessons I gained will stay with me well beyond this thesis.

I also want to thank Dr. Ralph Latteck and Prof. Dr. Toralf Renkwitz for the close collaboration, the honest feedback, and the many discussions that helped shape this work. They were there not only to celebrate achievements but also to listen in times of doubt and struggle. Their support reached beyond scientific questions and touched many personal challenges, and I am deeply grateful for the motivation and reassurance they offered.

I am also thankful to all members of the RRS working group, where I could always come with questions and where the doors were always open for help and feedback. This supportive atmosphere was invaluable and made daily work much easier and rewarding. I also want to thank colleagues from other groups for bringing in fresh ideas, new perspectives, and many inspiring discussions. Their input and encouragement provided important motivation and helped me to look beyond the narrow scope of my own work.

Beyond the institute, I would like to acknowledge the members of the Leibniz PhD Network working groups and of the Mental Health Initiative at the physics institute at Uni Rostock for broadening my perspective and providing inspiration outside the academic context. Their involvement offered balance and important impulses during these years.

I especially want to thank my fellow doctoral researchers Eframir, Juli, Kesava, Thorben, and Philipp, with whom I started this journey almost side by side as well as Robin and Laura. Over the years, we developed a close bond, supporting each other, sharing ideas, and motivating one another through both challenges and successes. What began as a collaboration grew into true friendship, and together, they made this time one of the most memorable periods of my life.

Finally, I owe my heartfelt thanks to my family and friends. Their patience, understanding, and unwavering encouragement have been a constant source of strength. In a time that is naturally accompanied by pressure and uncertainty, they managed to take much of that weight off my shoulders and reminded me of what truly matters. I am deeply grateful for their presence and support throughout this journey.

Table of Contents

List of Figures xiii

List of Tables xxii

List of Symbols xxiii

List of Abbreviations xxvi

1 Introduction into the Earth's Atmosphere 1
- 1.1 The Structure of the Atmosphere . . . 1
- 1.2 The (polar) Mesosphere and Lower Thermosphere . . . 3
- 1.3 Current Understanding of Mesospheric Small-Scale Instabilities . . . 12

2 Motivation and Objectives of this Work 18

3 Instrumentation, Data Collection, and Dataset 21
- 3.1 Basic Radar Concepts . . . 21
- 3.2 MAARSY . . . 25
- 3.3 SIMONe Meteor Radar - MMARIA Norway . . . 31
- 3.4 Partial Reflection Radar in Saura, Norway . . . 33

4 Data Analyses 35
- 4.1 Varicose-Mode Event Identification Methodology . . . 35
- 4.2 Cross-Correlation Analysis of Multibeam Radar Observations for Event Tracking . . . 37

5 Observation and Statistics of Varicose-Mode Events 41
- 5.1 Event Occurrence and Frequency . . . 41
- 5.2 Diurnal Variation and Event Patterns . . . 42
- 5.3 Duration and Vertical Extent of Events . . . 43
- 5.4 Vertical Velocity Characteristics . . . 44
- 5.5 Investigation of the Connection between Varicose-Mode Event Parameters 45
- 5.6 High-Velocity Varicose-Mode Events . . . 46
- 5.7 Consideration of Horizontal Background Winds . . . 46
- 5.8 Summary and Discussion: Varicose-Mode Event Statistics . . . 48

6 Multi-Instrument Studies of Selected Varicose-Mode Events **54**
6.1 Case I: 02.06.2015 54
6.2 Case II: 03.07.2018 66
6.3 Case III: 01.08.2018 73
6.4 Case IV: 01.07.2023 76
6.5 Summary and Discussion: Multi-Instrument Case Studies 81

7 Conclusions and Outlook **89**

Appendix **A-1**

List of Figures

1.1 The layers of the atmosphere from the ground up to 120 km altitude. In blue the temperature profiles for summer (solid) and winter (dashed) are shown. The orange profile represents the N_2 density profile of the atmosphere. Both quantities are 2-week averages using data from the empirical atmospheric model NRLMSIS2.0 1

1.2 Plasma density profile through the daytime (solid) and night time (dashed) ionosphere. 3

1.3 Photograph of noctilucent clouds over Kühlungsborn, Germany from 2021 with a sketch of the mechanism that makes them visible to the observer with the naked eye. 5

1.4 Schematic representation of the spectral energy distribution across different atmospheric scales, from large-scale motions to small-scale turbulence. The x-axis shows the logarithmic scale of the wavenumber, which corresponds to different spatial scales, moving from larger synoptic scales (left) to smaller dissipative scales (right). The y-axis displays the logarithmic scale of energy, illustrating how energy varies across these scales. 7

1.5 Photograph of wave patterns often associated with atmospheric gravity waves over Kühlungsborn, Germany. 9

1.6 Latitude-altitude cross section through the atmospheric temperature field for the month of July. Temperature values are given in K. The white dashed lines display the tropopause, stratopause and mesopause. The thermosphere is the layer above the mesopause (temperature data produced with the NRLMSISE-00 climatological model). 11

1.7 Sketch of the formation process of a KHI. 13

1.8 Sketch of a simplified density profile acting as the simplest guiding structure. 15

1.9 Schematic diagram of the oscillating duct. The dashed line indicates the center of the duct. The solid black and red colors indicate the airglow layer being pushed up and down leading to a dark and bright bore, respectively. b) Sketch of the inversion layer and the associated thermal duct (adapted from. 16

2.1 Summary of an observed extreme vertical velocity event with MAARSY. (a) Time evolution of the vertical velocities between 75 and 95 km altitude over a time period of 1.5 hours. The red and blue colors indicate the strong up- and downdrafts, respectively, green indicates vertical velocities around 0 m/s, and the brightness of the colors represents the strength of the signal (SNR). (b) One example of the vertical velocity spectra during the event with the 3σ presented as the red dashed lines. (c) Cut through the event at Y = 0 showing the horizontal extent along X at one specific time. (d) Temporal evolution of the event at X = 0 along Y. 18

2.2 PDFs of the Lagrangian vertical velocity (red solid line) and Lagrangian horizontal velocity (blue solid line) normalized by their standard deviation obtained from direct numerical simulations of a stratified flow. Both quantities are normalized by their dispersion. A Gaussian PDF is indicated as a reference (black solid line). 19

3.1 Schematic representation of specular reflection. 22

3.2 Schematic representation of partial reflection. 22

3.3 Comparison of the principle of coherent and incoherent scattering. Black arrows: transmitted radiation, red: re-emitted radiation in the direction of the antenna. 23

3.4 Doppler Effect. Black: emitted radiation, red and blue: received radiation, depending on the movement direction of the target. 23

3.5 Side lobes sketch for a vertically pointing antenna. The Signal strength is proportional to the angle θ. 24

3.6 Schematic representation of the different perspectives available from radar imaging. The strength of the signal is dependent on θ. 26

3.7 (a) Number of hours during which the radar was operational and included in the data analysis and (b) Number of 20-minute windows in which PMSE were detected and included in the data analysis, separately for each month of 2015 to 2021. 27

3.8 Sketch of the determination of the Doppler parameters from the complex auto-correlation function. 29

3.9 Visualization of the impact of six additional coherent integrations on received spectra and vertical velocities during an extreme event reported by Chau et al. (2021). Panel a) displays the velocity spectrum versus altitude with additional coherent integrations, while panel b) shows the same spectrum without them. Panels b) and c) compare two hours of the Range-Time-Intensity plot for the event, with and without additional coherent integration, respectively. 29
3.10 Schematic setup of a multistatic specular meteor radar (not scaled). . . 32
3.11 Array schematic of the partial reflection radar in Saura PRR. Red dots mark antennas with individual receiver channels used for interferometry. 34

4.1 Example of a varicose-mode event found on 13 June 2021. a) Shown is the vertical velocity evolution in time (color-coded) in an altitude range between 75 and 95 km, exhibiting the simultaneous up and downwards motions (varicose mode). b) depicts the schematic of the event with h_0 and h_1 as the thickness of the PMSE layer in its undisturbed and disturbed state, respectively. t_0 represents the starting time and d their duration. The red and blue colors emphasize the vertical wind direction, as in a). 35
4.2 Panel (a) shows the power-range plot for a single pulse, from which the velocity spectrum in panel (b) is derived. In the second half of panel (a), between 82 and 95 km, two meteor signatures are visible, marked by the arrows. Panel (b) illustrates the impact of these meteors on the normalized radial velocity spectrum, where the velocities are overestimated at the altitudes affected by meteor echoes. Here, the spectrum is normalized to the maximum value at each altitude. 36
4.3 (a) Unsmoothened velocity data from five radar beam directions (top to bottom: V, N, E, S, W) over one hour, PMSE-surrounding gates were filled with random values to ensure valid input for the correlation algorithm. (b) Smoothed data using a 5×5-point moving average, with red and blue lines marking the altitudes selected for analysis. (c) Lag times obtained by cross-correlating the corresponding line pairs from panels (a) and (b): blue with blue and red with red. 38
4.4 Sketch of beam positions and velocity vectors to aid in calculating angle and velocity. 39

5.1 Occurrence of varicose-mode events in the PMSE months (May, June, July, August) between 2015 and 2021. (a) The absolute number of events counted per year, broken down by individual months. (b) The number of events counted per month relative to the number of 20-minute PMSE windows counted during the same period, broken down by individual years. The more heavily colored and contoured bars represent the absolute (relative) number of those events in the respective period with |w| $\geq$ 15 m/s. 41

5.2 (a) The distribution of the occurrence of events in varicose mode relative to the number of 20-minute PMSE windows observed within the time frame of interest over the course of a day. The gray line illustrates the mean diurnal variation in the frequency of PMSE by Latteck et al. (2021). (b) The absolute number of varicose-mode events occurring as single events, as pairs, or in groups for each individual year. 43

5.3 Duration (a), maximum vertical extent (b) and h_1/h_0 (c) distribution of the varicose-mode events. The red solid (dashed) line represents the mean of all events (|w| $\geq$ 15 m/s events). 43

5.4 Distribution (a) of vertical velocities across all altitudes and throughout the observation period and (b) of the maximum vertical velocities of varicose-mode events in blue (down-drafts) and red (up-drafts). The black curve represents a Gaussian reference. 44

5.5 Correlation between the absolute maximum vertical velocities and the duration of the varicose-mode events (a), and their extent factor (b), along with the correlation between event duration and extent factor (c). Each dot represents an individual varicose-mode event, with green dots indicating events where |w| exceeded 15 m/s. The salmon-colored line denotes the linear regression for all varicose-mode events, while the green lines represent the linear regression specific to events with $|w| \geq 15$ m/s. 45

5.6 Distribution of wind directions in the altitude ranges 81 to 83 (orange) and 87 to 89 km (green) altitude during all varicose-mode cases between 2015 and 2023. 47

5.7 Normalized bore amplitudes of the varicose-mode events in general. The red solid (dashed) line represents the mean of all events (events with |w| $\geq$ 15 m/s). 51

6.1 Range-time-radial velocity representation of case I, observed on June 2, 2015, between 10:30 UT and 12:30 UT. The events are highlighted by the dashed ellipses. 55

6.2 Mean wind parameters around the first event on June 2, 2015, at 10:30 UT, from horizontal wind components u (green) and v (orange) in panel a. Panels b–e show wind magnitude, direction (0° = North), shear, and shear direction. Strongest colors in panel a and black in panels b–e indicate measurements closest to the event; different symbols and lighter shades of colors indicate ±1.5 hours. 56
6.3 The same as Fig. 6.2 but for the second event of this case at around 11:30 UT. 56
6.4 The same as Fig. 6.2 but for the third event of this case at around 12:30 UT. 57
6.5 Residuals of zonal (left) and meridional (right) wind components from MMARIA Norway, after removing a running mean over 3, 6, 8, and 10 hours, for 48 hours around the three events in this case study (green vertical lines). 59
6.6 Absolute magnitudes of the zonal (a) and meridional (b) wind components at 85 km altitude, measured by MMARIA Norway over the course of 48 hours around the events (green vertical lines). 60
6.7 Spectral width (top) and radial velocity (bottom) around the time of the event observation with MAARSY. Shown are the NE, SE, and SW beam measurements (left to right). Black arrows point at patterns that coincide with the timing of the three events of Case I. 61
6.8 Temporal evolution of the three events of this case (first to third row, respectively) from along x-axis and altitude at a fixed point y = 0 from their initial to their final stage. The colors represent the vertical velocity (blue: downward, red: upward, green: no vertical movement) and the strength of the color represents the strength of the received signal. . . . 62
6.9 Same as Fig. 6.8 but along y-axis and altitude at a fixed point x = 0. . 63
6.10 Temporal evolution of the three events of this case from along y-axis (a) and along the x-axis (b) at a fixed altitude z = 81 km over a time period of 2.5 h. The color representation is the same as in 6.8. 64
6.11 SABER temperature profiles near MAARSY (±250 km) for a period of ±5 days around the target date (D) 2 June 2015. Profiles obtained on D are shown in black, with individual profiles differentiated by line styles. Profiles from days after D are shown in grey, with profiles horizontally offset for better visibility. There were no available temperature measurements prior to D. As a comparison, the mean summer temperature profile is shown in green. 65

6.12 Range-time-radial velocity representation of Case II, observed on July 3, 2018, between 15:25 and 15:45 UT. The event is highlighted by the dashed ellipse. 66
6.13 Mean wind parameters around the first event on July 3, 2018, at 15:30 UT, from horizontal wind components u (green) and v (orange) in panel a. Panels b–e show wind magnitude, direction (0° = North), shear, and shear direction. Strongest colors in panel a and black in panels b–e indicate measurements closest to the event; different symbols and lighter shades of colors indicate ±1.5 hours. 67
6.14 Vertical velocity measurements for Case II for 5 beam pointing directions (top to bottom: Vertical, North, East, South and West) using MAARSY. 69
6.15 Event front slopes and velocities derived from beam positions and time differences in the Multibeam data obtained for Case II. Different colors represent each quadrant, with solid and dashed lines indicating results from two distinct beam triplet combinations per quadrant. Filled and empty arrows depict velocities, with thick lines and arrows representing mean values, while thin lines indicate results within the uncertainty range of lag times. To improve clarity, only the mean velocity arrows are shown for the thin-line solutions. 71
6.16 Spectral width (top) and radial velocity (bottom) around the time of the event observation with MAARSY. Shown are the vertical, SW, and NW beam measurements (left to right). Black arrows point at patterns that coincide with the timing of the event of Case II. 72
6.17 Range-time-radial velocity representation of Case III, observed on August 1, 2018, between 19:45 and 21:00 UT. The event is highlighted by the dashed ellipse. 73
6.18 Mean wind parameters around the first event on August 1, 2018, at 20:00 UT, from horizontal wind components u (green) and v (orange) in panel a. Panels b–e show wind magnitude, direction (0° = North), shear, and shear direction. Strongest colors in panel a and black in panels b–e indicate measurements closest to the event; different symbols and lighter shades of colors indicate ±1.5 hours. 74
6.19 Event front slopes and velocities derived from beam positions and time differences in the multibeam data obtained for Case III. Color coding and arrow conventions follow Fig. 6.15. 75
6.20 Range-time-radial velocity representation of Case IV, observed on July 1, 2023, between 10:50 and 11:50 UT. The event is highlighted by the dashed ellipse. 76

6.21 Mean wind parameters around the first event on July 1, 2023, at 11:00 UT, from horizontal wind components u (green) and v (orange) in panel a. Panels b–e show wind magnitude, direction (0° = North), shear, and shear direction. Strongest colors in panel a and black in panels b – e indicate measurements closest to the event; different symbols and lighter shades of colors indicate ±1.5 hours. 77
6.22 Event front slopes and velocities derived from beam positions and time differences in the multibeam data obtained for Case III. Color coding and arrow conventions follow Fig. 6.15. 78
6.23 Spectral width (top) and radial velocity (bottom) around the time of the event observation with MAARSY. Shown are the vertical, NW, and SE beam measurements (left to right). Black arrows point at patterns that coincide with the timing of the event of Case IV. 79
6.24 Directional analysis of strong reflections during the Case IV event using the MUSIC algorithm. Signal intensity is shown from weak (blue) to strong (red) across azimuth and elevation. Data were collected between 78–81 km. Top: cross-polarization; bottom: parallel polarization. 80
6.25 Summary of the selected varicose-mode events for case studies. Shown are the Range-Time-Intensity, Range-Time-Velocity, and Range-Time-spectral width plots for each case. The plots illustrate the temporal evolution and vertical structure of the observed events, enabling direct comparison across cases. 81
6.26 Summary of wind and event propagation directions for all four cases. The first column shows the three events of Case I; the second column shows Cases II–IV. Black arrows indicate mean front propagation: from radar imaging for Case I and time-delay estimates for Cases II–IV. Gray sectors represent angular uncertainty. Orange arrows show mean wind direction and relative strength at three PMSE altitudes (lower, middle, upper). 83
6.27 Schematic of selected scenarios illustrating how a varicose-mode event (black contours) may pass over the FOVs of MAARSY (red) and Saura PRR (blue). The event is assumed to propagate from southwest to northeast with a slight inclination, representative of typical observations. 85

A0.1 Two Examples of varicose-mode events found on 5 June 2020 and 26 June 2021. a) and c) Shown is the vertical velocity evolution in time (color-coded) in an altitude range between 75 and 95 km, exhibiting the simultaneous up and downwards motions (varicose modes). b) and d) depict the schematics of the events with h_0 and h_1 as the thickness of the PMSE layer in its undisturbed and disturbed state, respectively. t_0 represents the starting time and d their duration. The red and blue colors emphasize the vertical wind direction, similar to a) and c). A-1
A0.2 Range-Time-radial velocity plots. Top: before applying data cleaning via applying masks. Bottom: cleaned dataset for varicose-mode event identification. A-2
A0.3 Range-time-spectral width (top) and -signal-to-noise-ratio (bottom) representation of case I, observed on June 2, 2015, between 10:30 UT and 12:30 UT. The events are highlighted by the dashed ellipses. A-3
A0.4 Residuals of zonal (left) and meridional (right) wind components from MMARIA Norway, after removing a running mean over 3, 6, 8, and 10 hours (rows 1–4), for 5 days before and after the event (green vertical lines). A-4
A0.5 Absolute magnitudes of the zonal (a) and meridional (b) wind components at 85 km altitude, measured by MMARIA Norway over the course of 48 hours around the events (green vertical lines). A-5
A0.6 Temporal evolution of the first event of this case along xy-plane at a fixed altitude of z = 81 km from their initial to their final stage. The color representation is the same as in Fig. 6.8. . . . . A-6
A0.7 Same as Fig. A0.6 but for the second event. A-7
A0.8 Same as Fig. A0.6 but for the third event. A-7
A0.9 Signal strength (top), Doppler shift (middle), and spectral width (bottom) around the time of the Case I event observation with MAARSY. Shown are all five beam pointing directions: vertical, NE, SW, NW, and SE (left to right). A-8
A0.10 Same as Fig. A0.3 but for Case II. A-9
A0.11 Residuals of zonal (left) and meridional (right) wind components from MMARIA Norway, after removing a running mean over 3, 6, 8, and 10 hours, for 48 hours around the event (green vertical lines). A-10
A0.12 Same as Fig. A0.4 but fore Case II. A-11
A0.13 Absolute magnitudes of the zonal (a) and meridional (b) wind components at 85 km altitude, measured by MMARIA Norway over the course of 48 hours around the events (green vertical lines). A-12

A0.14 Same as Fig. A0.5 but for Case II. A-12
A0.15 Signal-to-Noise ratio for Case II for 5 beam pointing directions (top to bottom: Vertical, North, East, South and West) using MAARSY. The event is highlighted with yellow ellipses. A-13
A0.16 Same as Fig. A0.9 but for Case II. A-14
A0.17 Same as Fig. A0.3 but for Case III. A-15
A0.18 Same as Fig. A0.11 but for Case III. A-16
A0.19 Same as Fig. A0.4 but for Case III. A-17
A0.20 Absolute magnitudes of the zonal (a) and meridional (b) wind components at 85 km altitude, measured by MMARIA Norway over the course of 48 hours around the events (green vertical lines). A-18
A0.21 Same as Fig. A0.5 but for Case III. A-18
A0.22 Vertical velocity measurements for Case III for 5 beam pointing directions (top to bottom: Vertical, North, East, South and West) using MAARSY. A-19
A0.23 Signal-to-Noise ratio for Case III for 5 beam pointing directions (top to bottom: Vertical, North, East, South and West) using MAARSY. . . .A-20
A0.24 Vertical velocity measurements for Case III for 5 beam pointing directions (top to bottom: Vertical, North, East, South and West) using MAARSY. The event is highlighted with black ellipses. A-21
A0.25 Same as Fig. A0.15 but for Case III. A-22
A0.26 Same as Fig. A0.3 but for Case IV. A-24
A0.27 Same as Fig. A0.18 but for Case IV. A-25
A0.28 Same as Fig. A0.4 but for Case IV. A-26
A0.29 Same as Fig. A0.20 but for Case IV. A-27
A0.30 Same as Fig. A0.5 but for Case IV. A-27
A0.31 Same as Fig. A0.24 but for Case IV. A-28
A0.32 Same as Fig. A0.15 but for Case IV. A-29
A0.33 Same as Fig. A0.9 but for Case IV. A-31
A0.34 Temporal evolution of the three events of Case I along y-axis and altitude at a fixed point x = 0 from their initial to their final stage. The color representation is the same as in Fig. 6.8. . . . . .A-39

List of Tables

5.1 Summary of the absolute numbers of varicose-mode events per month and year. In parentheses, the number of 20-minute windows that contained PMSE for the same time period (only the days included in this study). In the last column and row, the total numbers are shown, respectively. . 42

6.1 Summary of the instrument data available for each case included in the case study. 54
6.2 Summary of geographic directions, beam positions at 85 km altitude, time differences determined by eye and by using cross-correlation, and mean velocities and angles of the event front for Case II determined by using the time differences observed by eye. Row colors correspond to the quadrant colors used in the Fig. 6.15. 70
6.3 Residual-wind summary for four cases: event presence, components, timescales, off-event enhancements, vertical structure 86
6.4 Summary of key findings for each case study. 87

A0.1 Summary of geographic directions, beam positions at 85 km altitude, time differences determined by eye and by using cross-correlation, and mean velocities and angles of the event front for Case III determined by using the time differences observed by eye. Row colors correspond to the quadrant colors used in the Fig. 6.19. . . . . .A-23
A0.2 Same as Tab. A0.1 but for Case IV. A-30
A0.3 Crossing altitudes for beam pairs in each case study. 41

List of Symbols

U	characteristic velocity
L	characteristic length scale
f	Coriolis frequency
Ω	angular frequency
Φ	geopotential
ϕ	latitude
ω	wave frequency
λ	wavelength
B	Rossby parameter
k_z	zonal wavenumber
k	wavenumber
l	meridional wavenumber
r	radius of the Earth
m	vertical wavenumber
k_h	horizontal wavenumber
Ro	Rossby Number
Ri	Richardson Number
N^2	Brunt-Väisälä frequency
θ	potential temperature
g	acceleration due to gravity
P_r	received power
P_t	transmitted power
G_r	gain of the reveiving antenna
G_t	gain of the transmitting antenna
σ	radar cross-section

R	range of the target
δ	angle of arrival
$\mathbf{k}$	wave vector of the transmitted wave
$\mathbf{u}$	total horizontal wind
u	zonal wind component
v	meridional wind component
w	vertical wind component
ξ	zonal wind component
f_D	Doppler shift
d	irregularity scale
Δf	frequency change
ν_{rad}	radial velocity
T	period
a	antenna distance
$B(s)$	brightness distribution
A_N	normalized antenna effective area
S'	Entropy
ψ	antenna pattern
$P(V\|B)$	propability function
σ_j	standard deviation of the noise
$\mathcal{L}(B)$	objective function for MaxEnt
γ	step size MaxEnt
$\mathbb{R}$	covariance matrix
$\mathbf{x}(i)$	signal vector received at point i
N	Number of points
$\mathbf{x}^H$	Hermitian transpose of $\mathbf{x}(i)$
f_N	Nyquist frequency

w_N	Nyquist velocity
n_{coh}	number of coherent integrations
w	vertical velocity
$\rho(\tau)$	complex autocorrelation function
τ	time delay
P_S	power of the received signal
$S(f)$	power density spectrum
$\Phi(\tau)$	phase
τ_σ	standard deviation of the autocorrelation function
f_σ	spectral width
h_0	undisturbed width
h_1	disturbed width
β	bore strength
Fr	Froude number
$g\prime$	reduced gravity term
ρ	density
OH	Hydroxide
Na	Sodium
OI	excited atomic oxygen
O	atomic oxygen
V_h	total horizontal wind speed
$V_{h,r}$	radial component of the horizontal wind
Θ	Zenith angle
H	scale height
k_s	scattering vector (receiver minus target)
k_i	incident vector (target minus transmitter)

List of Abbreviations

IAP	Leibniz Institute of Atmospheric Physics
GW	Gravity Waves
MLT	Mesosphere Lower Thermosphere
NLC	Noctilucent Clouds
PMSE	Polar Mesospheric Summer Echoes
RTDI	Range-Time-Doppler-Intensity
UV	Ultra Violet
HF	High Frequency
KHI	Kelvin-Helmholtz-Instability
VHF	very high frequency
UHF	ultra-high frequency
DNS	direct numerical simulation
PDF	probability density function
CGCAM-PMC	Complex Geometry Compressible Atmosphere Model for Polar Mesospheric Clouds function
MST	mesosphere/stratosphere/troposphere
PRF	pulse-repetition frequency
MAARSY	Middle Atmosphere Alomar Radar System
DBS	Doppler beam swing
SIMONe	Spread Spectrum Interferometric Multistatic Meteor Radar Observing Network
MMARIA	Multistatic Multi-frequency Agile Radar for Investigations of the Atmosphere
SMR	specular meteor radar
MaxEnt	maximum Entropy method

PRR	partial reflection radar
EISCAT	European Incoherent Scatter Scientific Association
KAIRA	Kilpisjärvi Atmospheric Imaging Reiceiver Array
MIMO	Multiple Input Multiple Output
ALWIN	Alomar Wind radar
EISCAT	European Incoherent SCATter Scientific Association
ESR	EISCAT Svalbard Radar
N	North
E	East
S	South
W	West
NE	North-East
SE	South-East
NW	North-West
SW	South-West
WSW	West-South-West
FOV	field of view
SABER	Sounding of the Atmosphere using Broadband Emission Radiometry
TIMED	Thermosphere Ionosphere Mesosphere Energetics Dynamics

1 Introduction into the Earth's Atmosphere

Our planet is surrounded by a dynamic, multi-layered atmosphere, each layer playing a distinct role, having unique decompositions and physical and dynamical characteristics.

1.1 The Structure of the Atmosphere

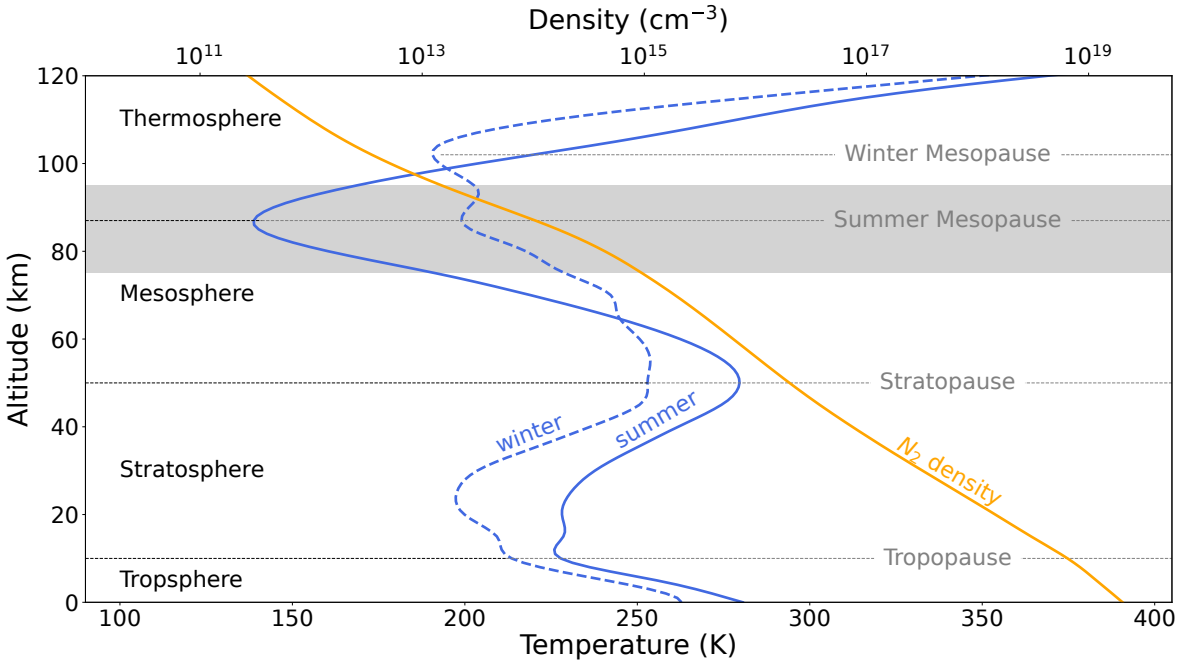


Figure 1.1: The layers of the atmosphere from the ground up to 120 km altitude. In blue the temperature profiles for summer (solid) and winter (dashed) are shown. The orange profile represents the N_2 density profile of the atmosphere. Both quantities are 2-week averages using data from the empirical atmospheric model NRLMSIS 2.0. The grey area represents the region of interest in the scope of this thesis.

The Earth's atmosphere is composed primarily of nitrogen (78.09%), oxygen (20.95%), and argon (0.93%) (Wallace and Hobbs, 2006). Additionally, there is a variable proportion of water vapor (Ahrens, 2012). Other gases such as carbon dioxide, sulfur dioxide, methane, and trace noble gases make up the remaining 0.03% (Wallace and Hobbs, 2006).
The atmosphere can be divided into five main layers based on temperature profiles: the Troposphere, Stratosphere, Mesosphere, Thermosphere, and Exosphere. The layering from the Troposphere to the Thermosphere is presented in Fig. 1.1, together with the temperature profile for one summer and one winter day in 2023 at high latitudes

at 69°N and 16°E (position of MAARSY), which can be seen as representative of this region.

Troposphere

The troposphere is the lowest layer, extending from the Earth's surface to the tropopause. It contains about 99% of the total water vapor and 90% of the atmospheric mass (Holton, 2004), earning it the designation "weather layer" due to the frequent formation of clouds. The temperature in the troposphere decreases with altitude, dropping approximately 6°C(K) per kilometer (environmental lapse rate) due to adiabatic cooling (Salby, 2012), from an average of 17°C (290.15 K) at the surface to around -52°C (221.15 K) at the tropopause (Ahrens, 2012).
The tropopause is the boundary between the troposphere and the stratosphere, characterized by an abrupt change in the lapse rate. It is defined as the lowest level where the lapse rate decreases to 2°C(K)/km or less, provided that the average lapse rate between this level and all higher levels within 2 km does not exceed 2°C(K)/km. The altitude of the tropopause varies with latitude and season, being around 8 km at the poles and about 18 km at the equator.

Stratosphere

Above the troposphere lies the stratosphere, extending up to an altitude of 50 km. The stratosphere is marked by a significant increase in temperature due to the presence of the ozone layer, which absorbs ultraviolet (UV) radiation with a typical lapse rate of approximately +1 to +3 K/km in the upper stratosphere. This absorption of UV radiation during the formation and decomposition of ozone increases the temperature, creating a stable stratification that limits vertical mixing. The stratosphere is also notable for being dry due to its lower presence of water vapor compared to the troposphere, which is attributed to the cold trap formed by the tropopause.

Mesosphere

The mesosphere extends from the stratopause to on average 100 km. It is characterized by a strong decrease in temperature, reaching lows around -100°C or colder, due to the absence of a significant heating mechanism such as ozone in the stratosphere (typical lapse rate: -2 to -3 K/km). The mesosphere is the region the interest of this thesis lies in. In Fig. 1.1 it is marked by the grey background. A detailed description of the part of this atmosphere will be given in 1.2.

Thermosphere

Above the mesopause lies the thermosphere, which extends up to about 600 km. In this layer, the density of molecules is extremely low, resulting in mean free paths of molecules in the order of meters to more. The low molecular density means there is minimal filtering of high-intensity radiation from space and the sun, leading to large temperature increases up to 1700°C. The thermosphere is also characterized by strong ionization of

molecules and atoms, which contributes to phenomena such as auroras.
Throughout the atmosphere, density decreases with altitude, as illustrated by the orange line in Fig. 1.1. This fundamental characteristic significantly influences the propagation of waves and the transport of energy and momentum, shaping the dynamics of atmospheric processes.

1.2 The (polar) Mesosphere and Lower Thermosphere

This thesis concentrates on the mesosphere and lower thermosphere (MLT), the intersection region between the third and fourth layer of the atmosphere. Before diving deeper into special characteristics and dynamics, it is necessary to understand its specifics and get some general information on its dynamics and energy budget.
The MLT region, serving as the boundary layer between Earth's atmosphere and space, presents a fascinating subject in terms of its dynamics and physical processes. However, the continuous observation of this atmospheric region poses significant challenges because of its altitude, which is too high for most in situ measurement methods, such as balloons, and too low for satellites, which gave this region another name: the "ignorosphere".

Remote sensing techniques, particularly radar systems, but also lidars and airglow cameras, have emerged as highly advantageous and valuable tools for scientific investigations of the MLT. The ability of radars to consistently and effectively probe the relevant altitudes, regardless of weather conditions and time of day, makes them indispensable in this field. A key outcome of the MLT dynamics is the unexpected thermal structure of the atmosphere, which diverges significantly from the state predicted by radiative processes alone. This phenomenon is prominently observed in the polar summer mesopause, situated between 78 and 88 km altitude, which is the coldest region in the Earth's system with temperatures falling to approximately 130 K. These extremely low temperatures are a result of dynamic processes, such as the breaking of atmospheric gravity waves (GW), which disturb the thermodynamic equilibrium of the atmosphere (Lübken et al., 1999a). A more detailed explanation of this is available in Section 1.2.2. Besides these dynamic influences, radiative and adiabatic cooling, along with a continuous upwelling associated with

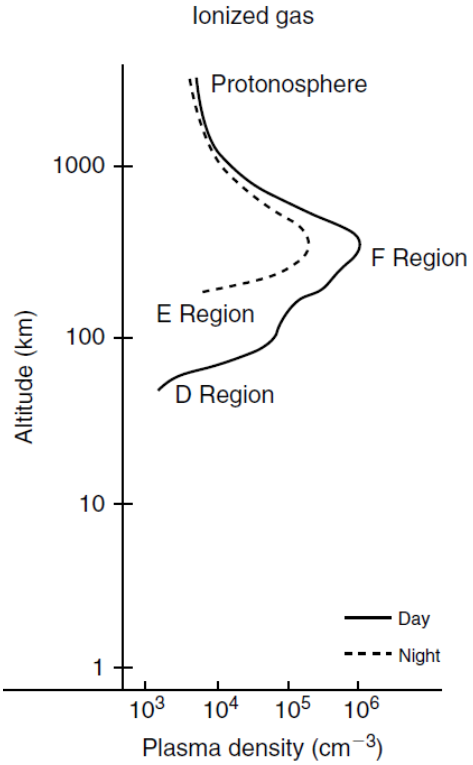


Figure 1.2: Plasma density profile through the daytime (solid) and night time (dashed) ionosphere (Hocking et al., 2016).

the summer-to-winter mesospheric circulation pattern, also play significant roles.
That the MLT overlaps with the lowest layers of the ionosphere as shown in Fig. 1.2 adds another significance to it: while the MLT itself is not directly involved in conventional telecommunication systems, it plays a crucial role in the propagation of radio waves, particularly in high-frequency (HF) communication. The ionospheric layers, located just above the MLT, are essential for reflecting HF radio waves back to Earth, enabling long-distance communication. Disturbances within the MLT can influence ionospheric conditions, thereby affecting the quality and reliability of these signals.
Additionally, as will be discussed in Section 1.2.1, the electron density and charged particles in general play a role in the formation of polar mesospheric summer echoes.
Moreover, the MLT is an important altitude region for the ablation of meteors. As these meteors streak through the Earth's atmosphere, they burn up and leave behind plasma trails that can be detected by radar. Observing these trails as they move with the wind allows for gaining valuable insights into atmospheric movements and behaviors (e.g. Lindzen and Chapman, 1969). This aspect of atmospheric science will be further explored in 3.3 dedicated to meteor radars.

1.2.1 Key Phenomena in the MLT

The MLT is the boundary layer between Earth's atmosphere and space, leading to a range of fascinating phenomena observable with the naked eye and with ground-based, airborne, and satellite instruments. The most prominent of these phenomena will be introduced next, both to aid in interpreting the results of this thesis and to provide future perspectives on the topic.

Noctilucent clouds and Polar Mesospheric Summer Echoes

The polar summer mesopause (78-88 km) is the coldest region in Earth's system, with temperatures dropping to around 130 K. These conditions facilitate the formation, growth, and sedimentation of ice crystals. Ice particles larger than approximately 20 nm can be observed as noctilucent clouds (NLC) at about 82 km, making them the highest clouds in our atmosphere (e.g. Vaste, 1993; Lübken et al., 1996; Savigny et al., 2020). These clouds are visible by eye at high and mid-latitudes, illuminated by the sun during twilight and nighttime (see Fig. 1.3). Their occurrence and properties, influenced by atmospheric constituents and physical parameters like temperature, provide valuable insights into the composition and dynamics of the MLT region. NLCs can be observed using various remote sensing techniques such as optical cameras, satellites, and lidars (e.g. Baumgarten et al., 2002; Savigny et al., 2020).
Smaller ice particles, light enough to exist up to an altitude of around 90 km, can become charged when immersed in the D-region plasma. In the 80 - 90 km altitude range, GWs frequently propagate from lower atmospheric layers, becoming unstable and generating turbulence in the mesosphere. This turbulent velocity field transports the charged ice particles, resulting in small-scale structures in their spatial distribution and the attached electron number density (Strelnikov et al., 2006).
The turbulence-induced transport of charged ice particles leads to irregularities in the radio refractive index, determined by the electron number density at these altitudes.

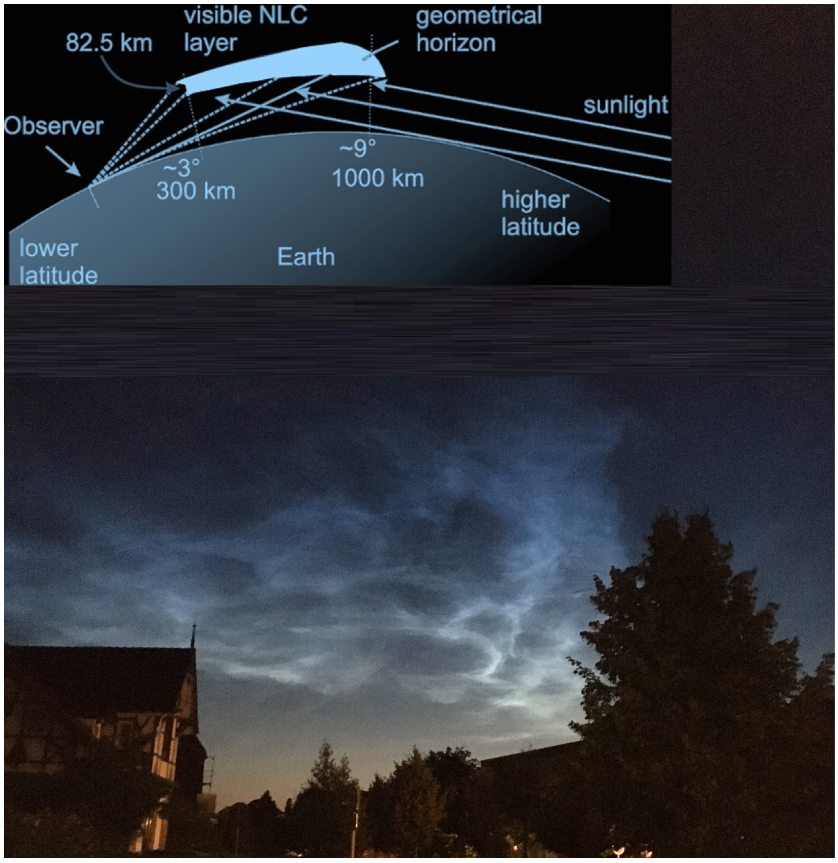


Figure 1.3: Photograph of noctilucent clouds over Kühlungsborn, Germany from 2021 with a sketch of the mechanism that makes them visible to the observer with the naked eye. Sketch adapted from Savigny et al. (2020).

These irregularities cause radar echoes, predominantly observed at very high frequencies, known as Polar Mesospheric Summer Echoes (PMSE). Those echoes are significantly influenced by background conditions and dynamic processes at different scales, making them valuable tracers for studying dynamical processes within the MLT (e.g. Rapp and Lübken, 2004). Whether they can be used as a tracer or not is dependent on the time of the year and day as they undergo seasonal variations as well as variations during the progress of a day. Long-term radar observations over the Norwegian island Andøya have shown that PMSE occurrence rates peak in June and July, with frequencies reaching over 90%. These rates also exhibit strong diurnal variation, with maximum occurrence typically around local noon and early afternoon hours (e.g. Latteck and Bremer, 2017). Further details on the techniques used to detect them will be elaborated in Section 3.2.

Meteors

Every day, a vast number of meteors enter the Earth's atmosphere. The middle atmosphere and ionosphere, especially the region between 80 and 120 km altitude is referred to as the meteoric region of our atmosphere, as the detection of them above and below is less likely (Reid, 2024). This is because most meteoroids ablate and release their material in this layer, where the atmospheric density is sufficient to cause intense heating

but not yet high enough to decelerate them completely. While only a small fraction of meteors are produced by meteoroids large enough to be seen with the naked eye, even those from much smaller meteoroids can still be detected by radar. This is because the radar does not observe the meteoroids themselves, but the ionized trails created as they ablate through collisions with atmospheric molecules. Depending on the number of links, several tens of thousands of meteors can be detected with one system per day. IAP's specular Meteor radar system in Germany and Norway, for example, detects approximately 40,000 meteors per day (Vierinen et al., 2019; Poblet et al., 2023; MMARIA/SIMONe, 2024).
Various radar systems can measure the radar echoes produced by mainly meteor trails but also meteor heads, allowing for the derivation of different atmospheric parameters (see, for example, Section 3.3). The meteoric smoke produced acts as nuclei for NLCs and stratospheric aerosols (e.g. Kalashnikova et al., 2000; Strelnikova, 2009). Additionally, these particles play a significant role in the chemistry of our atmosphere (e.g. Saunders et al., 2012).

1.2.2 Overview of MLT Dynamics

As indicated before, the dynamics within the MLT region are especially distinctive and of great importance as they are known to connect the lower atmosphere and the edge of space. Understanding the interhemispheric and vertical atmospheric coupling mechanisms is crucial to comprehending the whole system "atmosphere".

As summarized in Fig. 1.4, the dynamical processes in the atmosphere can have many appearances – they vary on both temporal and spatial scales.
The atmospheric sciences community mainly distinguishes three scale groups: microscales or small scales (wavelength $\lambda \leq 20\,\text{km}$, and period $\text{T} \leq 1$ h), mesoscales ($20\,\text{km} < \lambda < 500\,\text{km}$, and $1\text{ h} < \text{T} < 2$ d), and synoptic scales ($\lambda \geq 500\,\text{km}$, and $\text{T} \geq 2$ d) (e.g. Fiedler and Panofsky, 1970). From kilometer-scale fluctuations lasting only a few minutes to wavy motions of planetary scales with periods of several days, atmospheric dynamics cover an enormous range.
This section begins by focusing on small-scale instabilities, progresses to mesoscale gravity waves (GWs), discussing how they form and propagate, and their importance in transporting energy and momentum through the atmosphere, and ends with larger-scale atmospheric phenomena like planetary waves and tides. The latter are largely driven by the Earth's rotation and variations in solar heating, and they play a crucial role in transferring energy both horizontally and vertically, thus influencing weather patterns worldwide.

Small-Scale Atmospheric Instabilities

The smallest scales of atmospheric dynamics, though limited in spatial and temporal extent, are critical for driving dissipation and turbulence. These processes facilitate the transfer of energy from larger-scale motions to smaller scales, where it is ultimately dissipated.
A key concept in understanding small-scale motions is the balance between inertial and

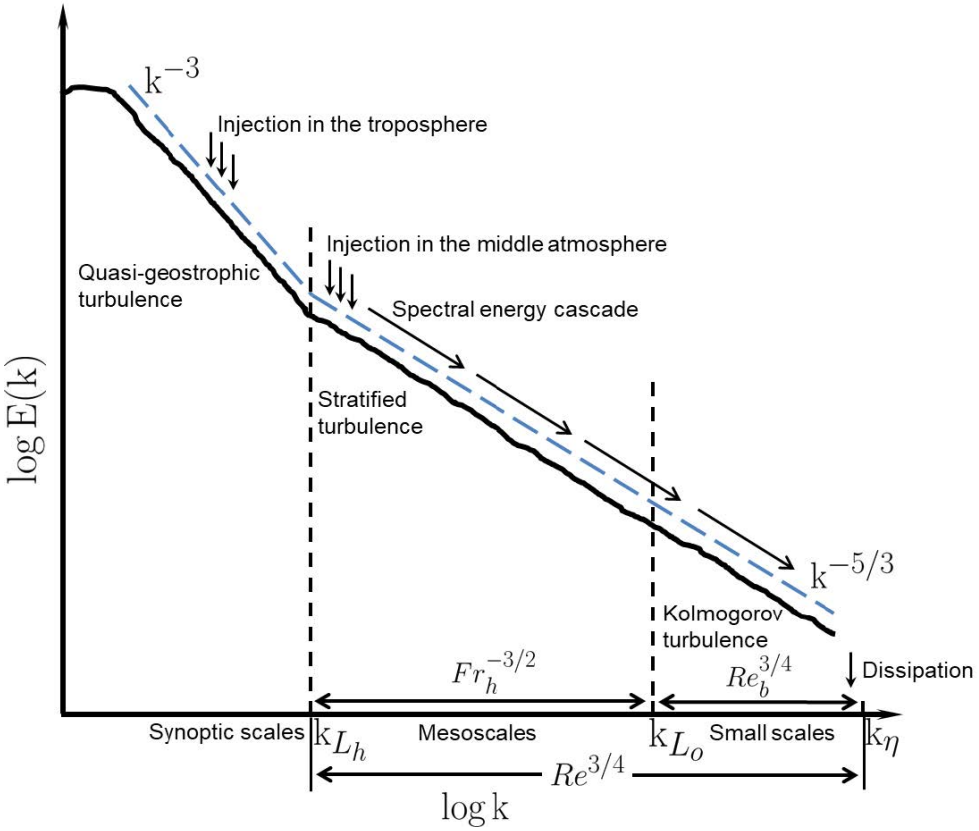


Figure 1.4: Schematic representation of the spectral energy distribution across different atmospheric scales, from large-scale motions to small-scale turbulence. The x-axis shows the logarithmic scale of the wavenumber, which corresponds to different spatial scales, moving from larger synoptic scales (left) to smaller dissipative scales (right). The y-axis displays the logarithmic scale of energy, illustrating how energy varies across these scales (courtesy of Dr. Victor Avsarkisov).

rotational forces, represented by the Rossby number (Ro):

$$Ro = \frac{U}{fL}, \tag{1.1}$$

where the Coriolis parameter f is given by:

$$f = 2\Omega \sin(\phi), \tag{1.2}$$

with Ω being the angular frequency of the Earth's rotation and ϕ the latitude. U and L are characteristic velocity and length scales of the phenomenon. When Ro is much smaller than one, the Coriolis force strongly influences the flow. However, at smaller scales, Ro increases, and the Coriolis effect becomes negligible. Thus, for small-scale motions such as Kelvin-Helmholtz instabilities or turbulent dissipation, the Earth's rotation (and hence the Coriolis force) does not play a role. At these scales, turbulent cascades dominate atmospheric dynamics, redistributing energy from larger-scale motions to smaller dissipative scales (e.g. Kolmogorov, 1941; Avsarkisov et al., 2022). Kolmogorov's theory of turbulence describes the energy spectrum of this cascade, where the

energy (E_k) varies with the wavenumber k as:

$$E(k) \sim k^{-5/3}, \tag{1.3}$$

as shown by Kolmogorov (1941) (see Fig. 1.4). This -5/3 power law is fundamental to understanding how kinetic energy is distributed across scales in turbulent flows.

Small-scale instabilities play a critical role in this cascade. The most commonly observed small-scale instabilities in the upper atmosphere include Kelvin-Helmholtz instabilities (KHI), bores, and solitary waves, each contributing to the generation of turbulence and the dissipation of energy (Fritts, 1984; Rapp and Lübken, 2004).
For example:

- **Kelvin-Helmholtz instabilities** form where velocity shear is present, generating wave-like patterns that break into turbulence.
- **Mesospheric bores** arise under specific ducting conditions, propagating as non-linear waves and redistributing energy in the upper atmosphere.
- **Solitary waves** represent stable, localized wave structures.

Gravity Waves

They may be described as oscillations of air parcels that have been displaced from their equilibrium level. A parcel lifted upward expands and cools adiabatically, while a parcel displaced downward is compressed and warms; buoyancy and gravity act as restoring forces, producing oscillatory motion analogous to a harmonic oscillator. In contrast to small-scale instabilities, the propagation and dynamics of gravity waves can be influenced by the Earth's rotation through the Coriolis force, which alters their phase speed and behaviour. This rotational effect is substantial only for the largest waves, while for shorter waves it is generally small. The relationship between wave frequency, background stability, and geometry in a rotating, exponentially stratified atmosphere is described by the gravity-wave dispersion relation:

$$\omega^2 = f^2 + N^2 \left(\frac{k_h^2}{k_h^2 + m^2 + \frac{1}{4H^2}} \right), \tag{1.4}$$

where ω is the wave frequency, N^2 is the Brunt-Väisälä frequency, k_h and m are the horizontal and vertical wavenumbers, respectively, and H the scale height (Nappo, 2002; Achatz et al., 2010).

Extensive research by various scientists already gives a broad overview of the variety of processes that lead to the formation of GWs. Following e.g. Fritts and Alexander (2003), the most dominant of them are:

- **Orographic Gravity Waves**: Generated when air flows over mountains or other large-scale terrain features. The forced upward and downward movement of air creates oscillations as it attempts to return to equilibrium.

- **Convective Gravity Waves**: Produced by deep convection and thunderstorms, where rapid vertical motion generates buoyant oscillations that propagate as waves.
- **Wind Shear**: Variations in wind speed and direction at different atmospheric levels induce instabilities that generate gravity waves.
- **Geostrophic Adjustments**: The reduction of flow imbalances, such as those caused by weather fronts or jet streams, producing oscillations that propagate as gravity waves.

Beyond intermittent effects in the lower atmosphere, where they can become visible to the eye by forming distinct patterns in the clouds as captured in the photograph in Fig. 1.5, the most significant influences of GWs are observed in the middle and upper atmosphere, spanning altitudes between 10 and 110 km. This prominence is due to the reduction in air density and the corresponding increase in wave amplitudes with altitude (Fritts and Alexander, 2003).
GWs can only propagate as long as the surrounding atmosphere does not trigger processes that lead to their dissipation or breaking. Such processes include a continuous increase in wave amplitude, the presence of strong shear (which can lead to Kelvin–Helmholtz instability, described in the following) (e.g. Nappo, 2002), convective instabilities (e.g. Holton, 2004), interactions with critical and turning levels in the background wind (e.g. Fritts and Alexander, 2003), as well as thermal and viscous damping. Once these conditions arise, GWs dissipate or break, releasing the energy and momentum they have transported from their source regions and thereby altering the surrounding atmospheric dynamics.

Planetary Waves and Tides

At the largest scales, planetary waves and atmospheric tides dominate. The behavior of these large-scale processes is, in contrast to smaller-scale atmospheric processes, governed strongly by the Coriolis force. Planetary waves, for example, are directly driven by variations in the Coriolis parameter with latitude. As air masses move between the equator and the poles, their angular momentum is conserved.
This necessitates adjustments in their velocity relative to their latitude to maintain rotational equilibrium. The Coriolis effect, resulting from Earth's rotation, causes these air masses to curve as they move.
These oscillations of the jet streams



Figure 1.5: Photograph of wave patterns often associated with atmospheric gravity waves over Kühlungsborn, Germany.

result in the formation of Rossby waves.

The Rossby wave dispersion relation mathematically describes this dependence:

$$\omega = B\frac{k}{k^2 + l^2 + \frac{1}{r^2}}, \tag{1.5}$$

where ω is the frequency of the wave, B is the Rossby parameter ($= \frac{df}{dy}$), k_z and l are the zonal and meridional wavenumbers, and r is the Earth's radius.
These waves propagate through the atmosphere and influence weather patterns by redistributing energy and momentum (e.g. Smith, 2012; Andrews et al., 1987) with periods of several days to weeks. As shown for example by Smith (2003), planetary waves can act as a filtering mechanism for GW propagating upwards from the troposphere and thus influence large-scale variations in the GW flux that propagates into the MLT. When GWs break or dissipate, they can generate a planetary wave pattern in the MLT winds and temperatures.
While Rossby waves are crucial in shaping weather patterns and the movement of jet streams, they are only one part of a bigger picture.
Atmospheric tides, much like oceanic tides, are global oscillations driven by solar and lunar forces. These tides interact with planetary waves and GWs, influencing the dynamics of the middle atmosphere.
To describe tidal oscillations in the atmosphere, the tidal oscillation equation is used:

$$\frac{\partial^2\Phi}{\partial t^2} + 2\Omega\cos\phi\frac{\partial\Phi}{\partial t} + \Omega^2\cos^2\phi\Phi = 0 \tag{1.6}$$

where Φ is the geopotential, Ω is the Earth's angular velocity, and ϕ is the latitude. Solar tides arise from the periodic heating of the atmosphere by the sun, leading to diurnal, semi-diurnal and higher-order oscillations. The community distinguishes between migrating and non-migrating tides: the former move westward, following the apparent motion of the Sun, while the latter do not follow the Sun's path and may propagate eastward or remain stationary (e.g. Hagan and Forbes, 2003). Non-migrating tides have emerged as important sources of tidal variability in the MLT and play a crucial role in vertically propagating energy and momentum, influencing the dynamics of the thermosphere and ionosphere (e.g. Hagan and Forbes, 2003; Vincent, 2015).
Lunar tides are caused by the moon's gravitational pull, resulting in oscillations with a main period of $\approx$ 12.42 hours corresponding to the moon's orbit (e.g. Lindzen and Chapman, 1969; Vincent, 2015).
Tides interact with planetary waves and gravity waves, modulating their amplitude and phase. Like planetary waves, they can filter gravity waves and thereby influence the distribution of energy and momentum in the middle atmosphere. In turn, gravity wave–tide interactions also contribute to short-term tidal variability (e.g. Fritts and Vincent, 1987). They can lead to large variations in winds, temperature, density, and atmospheric constituents like airglow emissions or trace species (Smith, 2012). Globally, variations over time scales longer than five days can result from shifts in the relative amplitudes and phases of different tidal modes, influenced by changes in the distribution of ozone or

water vapor, or by varying propagation conditions. Another suggested mechanism is the non-linear interaction between planetary waves and tides (e.g. Beard et al., 1999; He et al., 2024).
The interplay across these scales – from small-scale turbulence to planetary motions – highlights the complexity of MLT dynamics. Each scale influences and is influenced by the others, forming a dynamic system that shapes atmospheric behavior and coupling. This mutual influence of different kinds of waves and wavy patterns across various scales highlights the complex interactions within the atmosphere, as discussed by now, where each wave type can influence and be influenced by others, creating a dynamic and ever-changing atmospheric system and determining the energy budget of the atmosphere. This leads to one of the most curious characteristics of the MLT region: the polar summer mesopause is, at around 130 K, the coldest place on Earth.

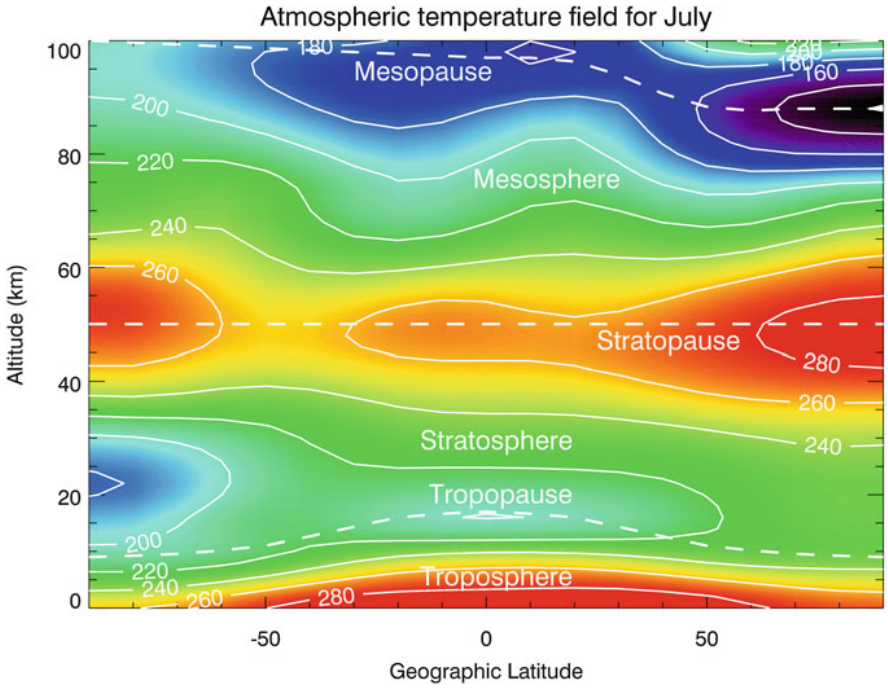


Figure 1.6: Latitude-altitude cross section through the atmospheric temperature field for the month of July. Temperature values are given in K. The white dashed lines display the tropopause, stratopause and mesopause. The thermosphere is the layer above the mesopause (temperature data produced with the NRLMSISE-00 climatological model (Savigny, 2017)).

Consequently, temperatures are typically higher in the tropics than at the summer pole, despite continuous sunlight at the summer pole. Under radiative equilibrium, one would expect atmospheric temperatures to closely follow the distribution of solar heating, with maximum temperatures over the summer pole and progressively cooler temperatures towards the winter pole. The fact that the opposite is true cannot be explained solely by cooling effects and the lack of heating mechanisms, but rather by a dynamical cooling mechanism.
Following, for example, Garcia (1989), Lübken et al. (1999b), and Rapp and Lübken (2004), the explanation lies in the deposition of angular momentum by GWs. In the summer hemisphere, where the zonal mean wind is predominantly westward, gravity waves propagating eastward are preferentially filtered out at lower altitudes, resulting in a wave spectrum biased toward westward-propagating waves reaching the mesosphere.

These waves dissipate and break, depositing westward momentum and exerting a westward drag on the mean flow, which drives a residual meridional circulation from the summer pole to the winter pole. This circulation induces strong upwelling over the summer polar mesopause region, leading to adiabatic cooling – a process where rising air expands and cools due to decreasing pressure with altitude. The cooled air at the summer pole then sinks over the winter pole, resulting in warming due to adiabatic compression (Brewer-Dobson Circulation). This dynamic cooling mechanism is so efficient that it overrides the expected radiative heating effects, leading to the extreme cold observed at the polar summer mesopause visualized in Fig. 1.6 (e.g. Shepherd, 2000).

1.3 Current Understanding of Mesospheric Small-Scale Instabilities

As previously mentioned, larger atmospheric motions, such as tides and gravity waves, are strongly influenced by Earth's rotation and the Coriolis force, which is measured by the Rossby number (Ro). When the Ro is low, the Coriolis force has a major influence; however, when Ro is high, inertial and shear forces become more significant. In regions where the Coriolis effect is weaker, small-scale instabilities can develop more readily, driven primarily by localized shear and buoyancy forces. Unlike waves, which tend to propagate energy away from their source while maintaining a regular, oscillating pattern, instabilities amplify disturbances. Thus, instabilities in the atmosphere describe situations where small disturbances in flows grow rather than dissipate, leading to complex and sometimes chaotic outcomes. Two of the most commonly discussed small-scale dynamics in the MLT region are Kelvin-Helmholtz-Instabilities (KHI) and bores. Next to those small-scale instabilities, the atmosphere is the host of mesoscale and large-scale instabilities as well, which however should not be of concern in the scope of this work. How stable the layering of a fluid is normally defined by the Richardson Number (Ri) that expresses the ratio of potential energy to kinetic energy in a stratified shear flow. It determines the relative importance of the stabilizing effect of stratification (buoyancy) compared to the destabilizing effect of shear:

$$Ri = \frac{N^2}{\frac{dU}{dz}^2}, \tag{1.7}$$

where the Brunt-Väisälä frequency N being a measure of the stability of the stratification within a fluid is defined as:

$$N = \sqrt{\frac{g}{\theta}\frac{d\theta}{dz}}, \tag{1.8}$$

where θ is the potential temperature and g the acceleration due to gravity.

1.3.1 Kelvin-Helmholtz-Instabilities

The study of Kelvin-Helmholtz instabilities was first theoretically grounded by Lord Kelvin and Hermann von Helmholtz in the mid-1800s, who described these phenomena as instabilities arising when two fluid layers with differing velocities interact, forming wave-like patterns at the interface. This theoretical foundation was later validated by observations of natural Kelvin-Helmholtz billow clouds in both atmospheric and oceanic contexts, as well as through controlled laboratory experiments (Drazin, 2015). Atmospheric KHI are a type of fluid instability that emerges in the presence of a velocity shear $\frac{dU}{dz}$ within a continuous fluid or between two fluid layers, creating the destabilizing conditions required for instability development. It is widely accepted that a Ri<0.25 is necessary for such instabilities to develop (e.g. Fritts and Rastogi, 1985; Drazin, 2015), indicating that shear forces exceed buoyancy. Under these conditions, small perturbations at the layer interface can grow into larger waves, which eventually overturn, break, and lead to turbulence (see Fig. 1.7).

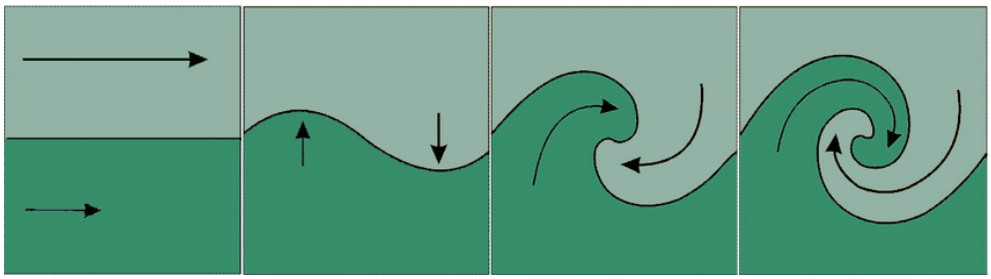


Figure 1.7: Sketch of the formation process of a KHI (Philippi et al., 2015).

KHI illustrate the interplay between atmospheric dynamics on different scales. GW, for instance, can alter wind velocity profiles within the atmosphere, introducing significant wind shear (e.g. Liu et al., 2020). These waves also cause vertical displacements of air parcels, which can impact the vertical structure of potential temperature (e.g. Ehard et al., 2014), thus modifying both stratification (through N) and stability (via Ri), as seen in Eqs. 1.7 and 1.8.

The distinctive rolling wave structures of KHI contribute to turbulence and promote mixing within the atmosphere, aiding in the transfer of momentum and energy between different atmospheric layers (e.g. Baumgarten and Fritts, 2014; Drazin, 2015). Observations indicate that they play a key role in the energy cascade within the MLT region, breaking down larger-scale wave structures into smaller turbulent eddies. This cascade is essential for understanding the distribution and dissipation of energy and momentum within the mesosphere (Kjellstrand et al., 2022).

KHI frequently interact with other mesospheric phenomena, such as atmospheric bores. For example, bore passages can generate localized wind shear that fosters KHI development (e.g. Smith et al., 2017; Fritts et al., 2020). This interaction can amplify initial perturbations, accelerating instability growth and enhancing turbulence. Notably, they often appear along the leading edges of atmospheric bores, further intensifying turbulence in these regions (Fritts et al., 2020).

In the lower and middle atmosphere, KHI are sometimes visible to the naked eye as Kelvin-Helmholtz billows when humidity levels allow rising air within a vortex to condense into clouds while descending air leads to evaporation (Drazin, 2015). In the upper

atmosphere, however, instruments such as radars, lidars, and airglow cameras are essential to detect and study these instabilities.

1.3.2 Mesospheric Bores

The term "bore" – believed to originate from the Icelandic word "bara," meaning billow or wave, and describing a potentially dangerous phenomenon such as a breaking tidal bore – was first applied to a phenomenon observed in riverbeds as a result of tidal forces (Chanson, 2010). In this context, a bore describes a sharp wavefront followed by a train of trailing waves propagating upstream within a duct or channel, generated by a hydraulic jump. A hydraulic jump occurs when a faster-moving fluid encounters a slower-moving region.
The study of such hydraulic-jump phenomena began with the work of Russell (1845), who first observed and documented solitary waves. These solitary waves were later linked to the study of tidal bores in riverbeds, where (e.g. Lamb, 1916) expanded on the mathematical descriptions and underlying physical conditions that make these special waveforms possible. These works showed that when tidal forces push a high volume of water upstream against the current, a sudden, turbulent rise occurs, creating the bore's characteristic steep front.
This hydraulic-jump phenomenon is characterized by the Froude number (Fr), a dimensionless parameter that compares flow inertia to gravitational force:

$$Fr = \frac{U}{\sqrt{gL}}, \tag{1.9}$$

where the upstream $Fr > 1$ indicates a transition from supercritical flow (flow faster than wave speed) to subcritical flow (flow slower than wave speed) (e.g. White, 1999).
The strength of a bore can be further characterized by the bore strength parameter β, defined as the normalized bore amplitude:

$$\beta = \frac{h_1 - h_0}{h_0} \leq 0.3, \tag{1.10}$$

where h_1 is the post-bore fluid height and h_0 is the pre-bore fluid height (Lighthill, 1979). When β exceeds the upper bound of 0.3, breaking occurs, leading to turbulent bores with no trailing waves (Lighthill, 1979; Dewan and Picard, 1998). For weak bores, where $\beta \ll 1.0$, the waves behind the discontinuity are predominantly sinusoidal.
The concept of tidal bores in river beds was later adapted to atmospheric sciences to describe a similar phenomenon in an open environment without fixed boundaries. Here, a rigid channel bottom cannot be assumed. Instead, in the atmosphere, the lower boundary is formed by a statically stable layer that can be vertically displaced and deformed by wave motion, similar to the upper boundary, resulting in what is referred to as an internal bore (e.g. Seyler, 2005a). A simplified sketch of a density profile

providing these conditions was proposed by Dewan and Picard (1998) as the simplest guiding structure to support an internal bore and can be seen in Fig. 1.8.

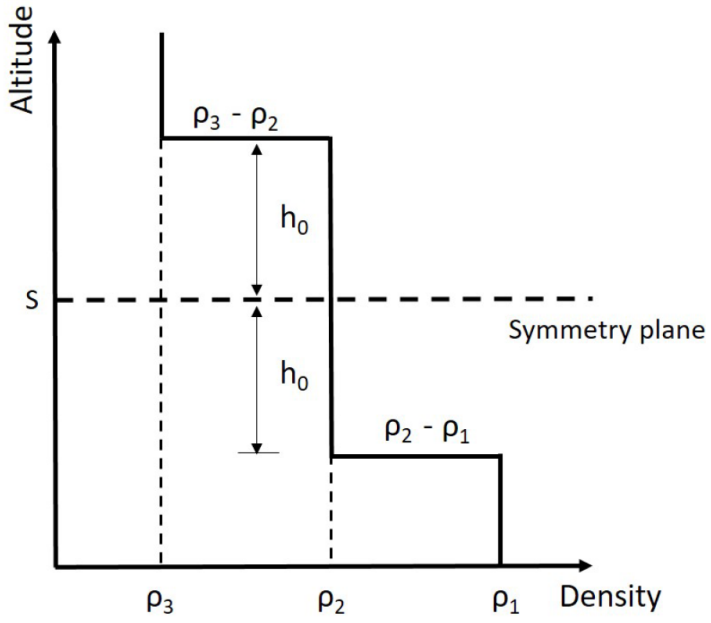


Figure 1.8: Sketch of a simplified density profile acting as the simplest guiding structure (Dewan and Picard, 1998).

What can be seen are three layers on top of each other, all characterized by a lower density than the one before. It is assumed, that the layers with densities ρ_1 and ρ_3 are semi-finite, while the layer with density ρ_2 is finite in thickness.
Assuming that there are no vertical motions involved, disturbances below and above the symmetric plane will thus have a mirrored effect. Here, bore propagation can be described mathematically by modifications to the hydraulic jump model to a stratified atmosphere, where the acceleration due to gravity is replaced by a reduced gravity term, $g\prime$, accounting for buoyant forces rather than gravitational forces alone (Dewan and Picard, 1998):

$$g' = g\frac{\Delta\rho}{\rho}. \tag{1.11}$$

Here, $\Delta\rho$ is the density difference across the interface, and ρ is the mean density. Concerning the formation of a guiding structure without a fixed lower boundary as in riverbeds, the concept of evanescence plays a significant role. Evanescence refers to the rapid attenuation or decay of wave amplitude when it cannot propagate freely. This occurs when a wave encounters environmental conditions that prevent sustained propagation. In atmospheric contexts, the discussion often centers on atmospheric GW trapped in a duct typically formed due to temperature inversion layers or wind shear in the MLT region (e.g. Ramachandran et al., 2023; Yue et al., 2010; Dewan and Picard, 1998). When GW encounter a layer where wind speed is significantly lower or static stability is higher, the wave's energy becomes insufficient for continued upward propagation, causing the amplitude to decay exponentially and effectively trapping the wave within the duct. For a wave to become evanescent, its vertical wavenumber m must

become imaginary, a condition given by:

$$m^2 = \frac{N^2}{U^2} - k_h^2 < 0, \tag{1.12}$$

where m being negative means the wave cannot propagate vertically and instead decays exponentially. Variations in N due to these factors create ducts that trap GW, leading to their amplification and steepening, observable as a steep wave crest followed by trailing waves.

In the lower atmosphere, bores can sometimes be observed as "Morning Glory" clouds. Over the past three decades, observations and simulations of bores in mesospheric altitudes have become more frequent (e.g., Taylor et al., 1995; Seyler, 2005b; Nielsen et al., 2006; Ramachandran et al., 2023). A notable example was reported by Taylor et al. (1995), later identified as a mesospheric bore by Dewan and Picard (1998). This event, observed on October 10, 1993, exhibited a bright, sharp wavefront followed by trailing waves in the OH and Na airglow layers at altitudes of 85 to 90 km. Uniquely, in the OI and O layers above 94 and 96 km, the opposite behavior was noted, with wave crests appearing darker than the troughs. The upwelling reduced the brightness as it moved the layer further away from the camera, while the downwelling had the opposite effect, as illustrated in Fig. 1.9a.

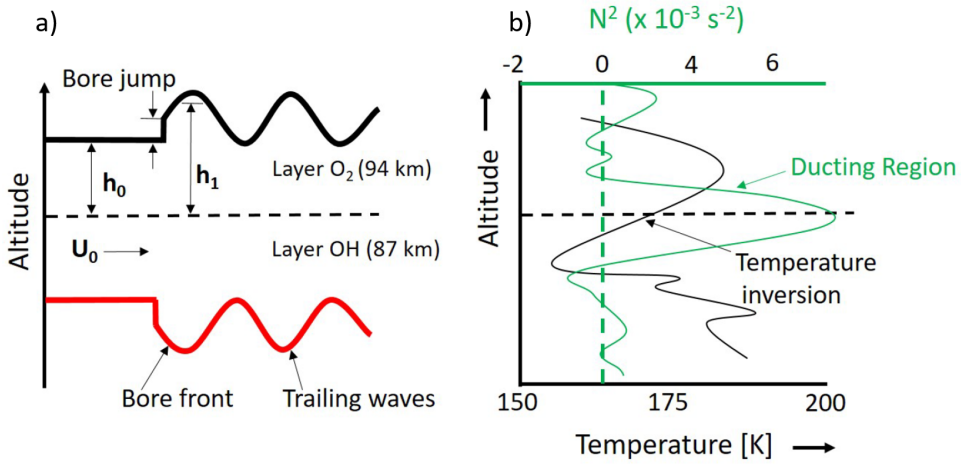


Figure 1.9: Schematic diagram of the oscillating duct. The dashed line indicates the center of the duct. The solid black and red colors indicate the airglow layer being pushed up and down leading to a dark and bright bore, respectively. b) Sketch of the inversion layer and the associated thermal duct (adapted from Ramachandran et al. (2023)).

The ducting mechanism behind this event was linked to a temperature inversion observed in lidar profiles (Fig. 1.9b). The potential contribution of wind shear was also considered, a question revisited in recent work by Ramachandran et al. (2023). Their study combined multi-instrumental observations of an undular (wave-like) mesospheric bore over Northern Germany in March 2021 with 2D direct numerical simulation (DNS) using the Boussinesq approximation[1]. Observations confirmed both a thermal duct created by temperature inversion and a Doppler duct formed by wind shear. Their DNS replicated key features of the observed bore and revealed that the Doppler duct enhanced

[1] A simplification assuming negligible density variation except where it affects buoyancy.

nonlinearity, affecting bore dissipation, trailing wave count, and formation time. The bore morphology depended on initial perturbation and duct width; narrow ducts and high-amplitude perturbations led to solitary wave formations. Importantly, a Doppler duct alone did not produce bores but instead led to turbulence.

2 Motivation and Objectives of this Work

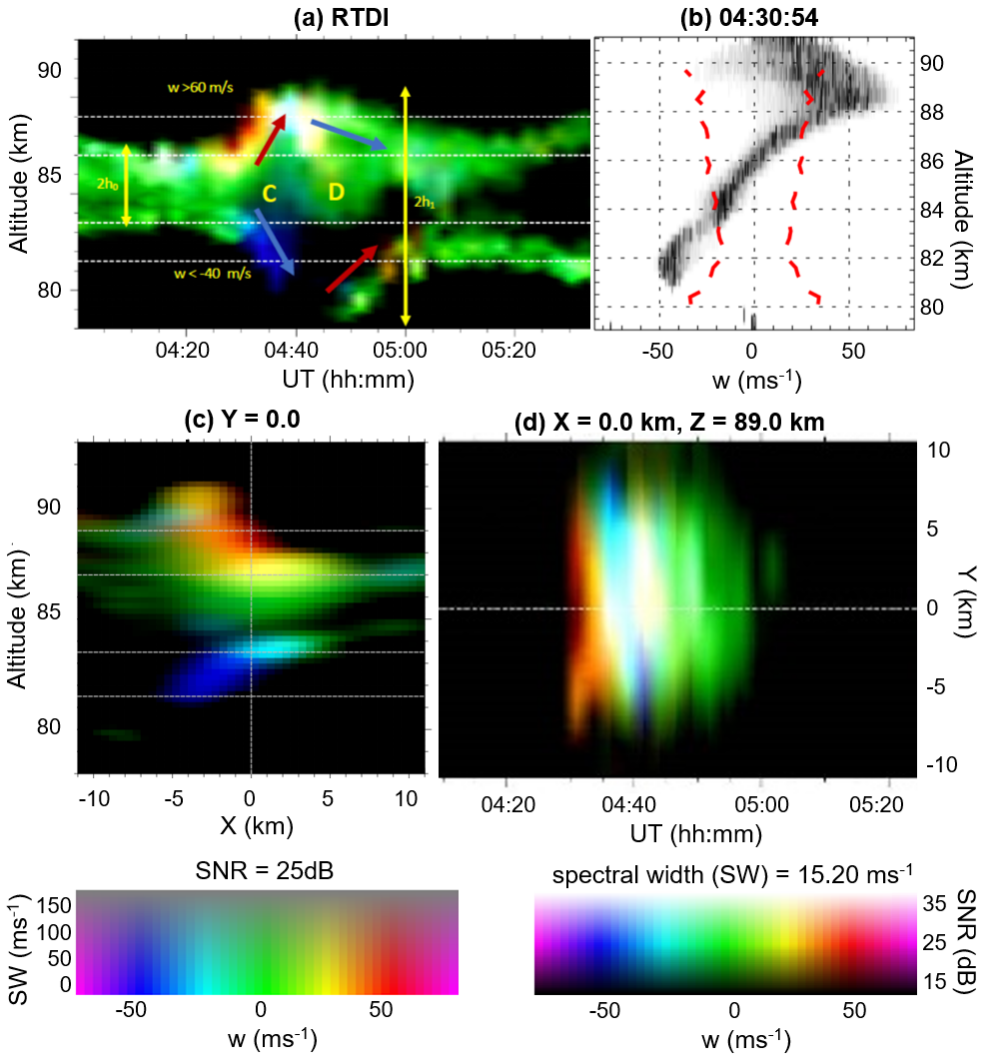


Figure 2.1: Summary of an observed extreme vertical velocity event with MAARSY. (a) Time evolution of the vertical velocities between 75 and 95 km altitude over a time period of 1.5 hours. The red and blue colors indicate the strong up- and downdrafts, respectively, green indicates vertical velocities around 0 m/s, and the brightness of the colors represents the strength of the signal (SNR). (b) One example of the vertical velocity spectra during the event with the 3σ presented as the red dashed lines. (c) Cut through the event at Y = 0 showing the horizontal extent along X at one specific time. (d) Temporal evolution of the event at X = 0 along Y (adapted from Chau et al. (2021)).

The spectrum of atmospheric dynamics in the MLT is characterized by a broad range of scales – from planetary-scale wave motions with periods of several days to kilometer-scale fluctuations that last only a few minutes. Understanding this variety of scales

and their interactions is essential for comprehensively modeling atmospheric behavior, crucial to improving our predictions of weather patterns and climate changes. Although there is research on extreme events like tornadoes and tsunamis in the lower atmosphere and ocean, unpredictable short-term and small-scale events with significant impacts can also occur in the upper atmosphere. However, in-situ observation and studies of extreme events and small-scale dynamics in the polar MLT region are limited, mainly due to the observational challenges posed by its altitude range.

In 2021, a very peculiar structure in PMSE measurements reported by Chau et al. (2021) caught the attention of several scientists in the radar remote sensing community. This event, visualized in Fig. 2.1, was observed in MAARSY data from July 2016 at altitudes between approximately 80 and 90 km. Fig. 2.1a is a Range-Time-Doppler-Intensity (RTDI) plot where vertical velocities are color-coded, with the brightness of the color representing the strength of the measured signal. Upward motion is indicated in red, downward motion in blue, and vertical velocities around 0 m/s in green. The event is characterized by simultaneous upward and downward motions, leading to a widening of the PMSE layer (later referred to as "varicose-mode events") that lasts only a few minutes. What makes this event particularly noteworthy is the presence of extreme vertical velocities in both updrafts and downdrafts. The term "extreme" becomes clear when examining Fig. 2.1b, which shows an example of the vertical velocity spectra measured during the event. The velocities exceed three times the standard deviation (3σ), marked by the red dashed lines. The σ-profile used here was determined from several months of vertical velocity data from PMSE measurements in 2016 (Chau et al., 2021). Radar imaging (Fig. 2.1c-d) revealed that the event was not only restricted in time but also localized in space along the X dimension – spanning approximately 3-4 km along X and at least 10 km along Y. The motivation kindled by that was even enhanced by DNS results presented in Feraco et al. (2018). Their research revealed that under certain flow conditions and specific stratification values with a Fr around 0.1 to 0.01, extreme vertical velocities can be expected. The probability density function (PDF) of the velocities is visualized in Fig. 2.2 and it can clearly be taken from this, that more values lie outside the Gaussian reference on the wings of the PDF. As demonstrated by Chau et al. (2021), comparing events directly is not straightforward because their study challenges common assumptions about vertical wind magnitudes and is constrained by the limited spatial and temporal coverage of radar observations. These factors may influence both the characterization and interpretation of extreme vertical-velocity events, which must be kept in mind when relating their findings to our own observations. Addition-

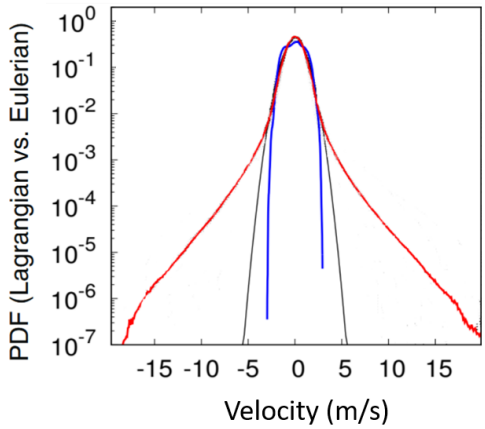


Figure 2.2: PDFs of the Lagrangian vertical velocity (red solid line) and Lagrangian horizontal velocity (blue solid line) normalized by their standard deviation obtained from direct numerical simulations of a stratified flow. Both quantities are normalized by their dispersion. A Gaussian PDF is indicated as a reference (black solid line). (adapted from Feraco et al. (2018)).

ally, Dong et al. (2021) reported simulated vertical velocities of around ±40 m/s in MLT altitude ranges using the Complex Geometry Compressible Atmosphere Model for Polar Mesospheric Clouds (CGCAM-PMC). These recent findings imply that such high vertical velocities may have been previously overlooked or misinterpreted in earlier analyses. Conventionally, outliers or anomalies in a data set have been recognized as values that exceed three times the standard deviation (e.g. Lehmann, 2013).
The primary goal of this study is to investigate the small-scale dynamics within the polar MLT region, focusing on varicose-mode structures and extreme vertical velocity events. Inspired by the unique observation of an event with high vertical velocities, this research aims to identify and analyze similar phenomena to enhance our understanding of the dynamic processes in this less-explored atmospheric layer.
This study will provide a detailed analysis of these events, examining their frequency, spatial and temporal characteristics, and associated vertical velocities. By integrating data from MAARSY, the SIMONe network, and other observational tools, the research will explore the ambient conditions and potential ducting mechanisms that facilitate these phenomena.
Ultimately, this work seeks to advance our understanding of small-scale dynamics in the MLT region. By studying these rare and extreme events, the research aims to improve knowledge of middle atmosphere dynamics, contributing to better atmospheric modeling and prediction of weather and climate patterns.

In the preceding sections, a general introduction to the area of interest and the basic concepts relevant to this study have been provided. Building on this foundation, the next chapters will focus on the methods, data, and results of the research. Chapter 3 introduces the instruments and datasets used in this study, while Chapter 4 describes the data analysis techniques.
Chapter 5 presents a statistical analysis of varicose-mode events observed between 2015 and 2021, including results published in Hartisch et al. (2024). Chapter 6 focuses on four case studies of varicose-mode events, including events from 2023 that were not part of the statistical dataset presented in Chapter 5. These case studies provide detailed insights into the events' appearance, background conditions, and movement, and include comparisons between the cases.
The results chapters will conclude with a summary of the findings from Chapters 5 and 6. This final Chapter 7 will also discuss the validity of the observed extreme vertical velocities and offer ideas for future research to improve our understanding of varicose-mode events.

3 Instrumentation, Data Collection, and Dataset

This chapter details the instrumentation and data collection methodologies used to study small-scale instabilities in the Mesosphere and Lower Thermosphere (MLT). It examines the operational principles of the **M**iddle **A**tmosphere **A**lomar **R**adar **Sy**stem (MAARSY) alongside complementary measurements from instruments like the SIMONe Meteor Radar and the Saura Partial Reflection Radar. The chapter also describes the data collection procedures, dataset characteristics, and analytical techniques that form the basis of the research, ensuring a comprehensive understanding of the study's technical framework.

3.1 Basic Radar Concepts

Continuous observation of the atmospheric region between 60 and 100 km poses significant challenges because of its altitude, which is too high for most in situ measurement methods, such as balloons, and too low for satellites. Remote sensing techniques, particularly radar systems, have emerged as highly advantageous and valuable tools for continuous scientific investigations of the MLT. Their ability to consistently and effectively probe the relevant altitudes, regardless of weather conditions and time of day, makes them indispensable in this field. This chapter will begin by presenting key concepts essential for understanding the necessity of specific setups, interpreting results, and recognizing the opportunities and limitations of using data from radars.
Radar stands for **Ra**dio **D**etection **a**nd **R**anging. It involves transmitting electromagnetic waves in the radio wavelength range towards a target at a certain distance. These waves interact with the target, get reflected, and some of the reflected waves are received back. The received signal strength in a radar system is determined by several factors described by the radar equation (Eq. 3.1), which is fundamental for understanding radar performance and is given by.

$$P_r = \frac{P_t G_t G_r \lambda^2 \sigma}{(4\pi)^3 R^4}, \tag{3.1}$$

where P_r is the received power, P_t is the transmitted power, G_t and G_r are the gains of the transmitting and receiving antennas, λ is the wavelength, σ is the radar cross-section of the target, and R is the range to the target. The strength of the transmitted signal determines the range and detectability of targets. Higher power allows for the detection of farther and weaker targets. Antenna gain, influenced by the antenna's size and design, focuses the emission in one direction, enhancing detection range. Wavelength affects resolution and target type: shorter wavelengths provide higher resolution for smaller targets, while longer wavelengths penetrate the atmosphere better due to less attenuation. The radar cross-section measures the signal scattered back from the target, depending on its size, shape, material, and orientation. The received power is inversely

proportional to the fourth power of the target's distance from the radar.
In atmospheric science, the reflection or scattering of radio waves almost always happens due to changes in the refractive index, and the targets are not solid but rather large soft structures, which makes the following concepts play an important role:

specular reflection Surfaces that are very smooth compared to the used radar wavelength reflect the radar signal mirror-like back (see Fig. 3.1). The angle of arrival (δ) is equal to the angle of reflection.

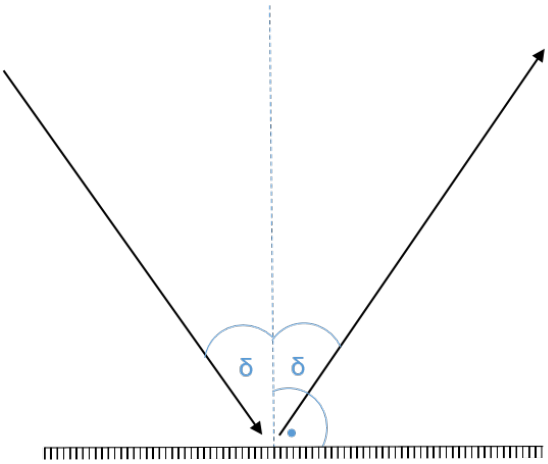


Figure 3.1: Schematic representation of specular reflection.

partial reflection When an electromagnetic wave encounters a boundary between two media with different refractive indices, part of the wave is reflected back into the original medium while the remaining part is transmitted and refracted into the second medium (see Fig. 3.2).

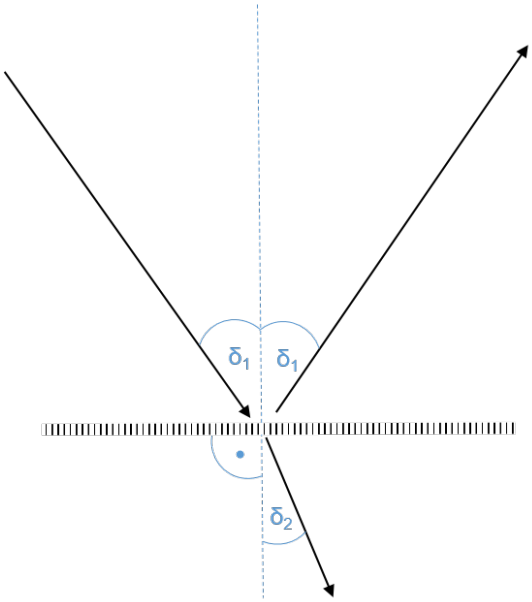


Figure 3.2: Schematic representation of partial reflection.

This phenomenon is known as partial reflection or Fresnel reflection (or Fresnel scattering). It occurs when the irregularity in the refractive index is transverse to the incident wave and also thin compared to the wavelength. The degree to which the wave is reflected or refracted depends on the properties of the media and the angle of incidence (Reid, 2015; Fukao and Hamazu, 2014).

Bragg Scattering Bragg scattering occurs when there is constructive interference between periodic irregularities in the atmosphere and the transmitted radio wave. When radar waves encounter a medium with periodic variations in refractive index or dielectric properties, the waves are scattered in a specific direction, determined by the Bragg condition. This condition is given by:

$$n\lambda = 2d\sin(\theta). \tag{3.2}$$

In other terms, the wavelength should be chosen such that it is twice the scale of the irregularities one wants to observe, considering the angle of incidence. For vertical incidence ($\theta = 90°$), this simplifies to $\lambda = 2d$, where d is the scale of the irregularities.

coherent and incoherent scatter Incident radio waves can interact with the atmosphere through either coherent or incoherent scattering (see Fig. 3.3). In coherent scattering, the radar signal is reflected in phase from larger-scale, organized structures in the atmosphere, for example, from refractive index irregularities or field-aligned plasma structures, producing a strong, well-defined return. In contrast, incoherent scattering arises from the interaction of the radio wave with free electrons whose velocities vary due to random thermal motion in the ionospheric

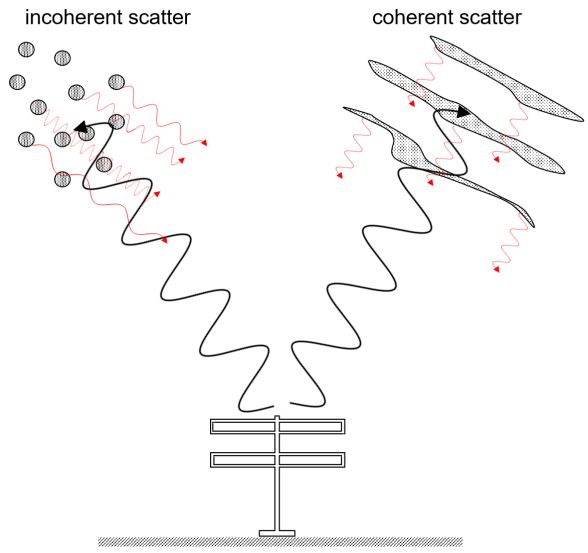


Figure 3.3: Comparison of the principle of coherent and incoherent scattering, adapted from Häggström (2017). Black arrows: transmitted radiation, red: re-emitted radiation in the direction of the antenna.

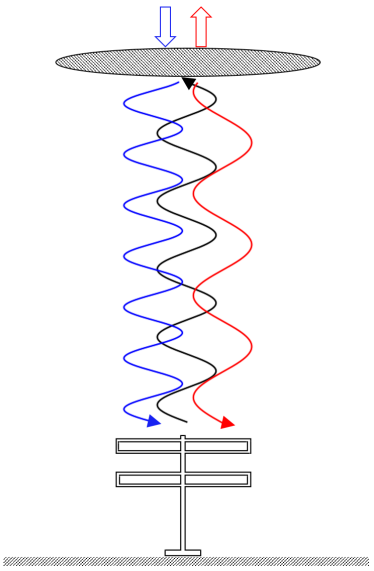


Figure 3.4: Doppler Effect. Black: emitted radiation, red and blue: received radiation, depending on the movement direction of the target.

part of the MLT. Each electron scatters the incoming wave slightly differently, like a tiny antenna, and the receiver detects the superposition of a vast number of such signals, each with small frequency shifts. These scattering processes occur at the Bragg scale, where the radar wavelength matches the scale of electron density fluctuations (e.g. Häggström, 2017; Hocking et al., 2016).

Doppler Effect As an electromagnetic wave interacts with a target that is moving along the line of sight of the radar beam, the signal wavelength undergoes a certain change. If the target is moving toward the radar, the wavelength becomes compressed and thus shorter, while it becomes stretched and therefore longer as the target is moving away from it (e.g. Hocking et al., 2016).
This is called the Doppler effect sketched in Fig. 3.4. From the change in frequency Δf, the radial (line-of-sight) velocity ν_{rad} of the target can be determined using the relation:

$$\Delta f = \frac{2}{\lambda}\nu_{rad}. \tag{3.3}$$

The application of this principle on actual radar data is detailed in 3.2.4.

Main and Side Lobes Depending on the architecture and design of the antenna or antenna array, emitted power is not transmitted solely in one direction. Due to the finite size of antennas and arrays, the electromagnetic waves – similar to how light behaves when passing through a small aperture – will diffract and disperse into a specific pattern. Consequently, although the majority of emitted power is directed toward a preferred direction, smaller amounts of the radar's power are also transmitted into adjacent directions. In this pattern, the emitted power varies as a function of angle; as the angle increases, the signal strength diminishes until it reaches a minimum. Beyond this initial minimum, the signal strength increases again to form a secondary maximum, known as a sidelobe (Hocking et al., 2016). A schematic representation of this phenomenon is

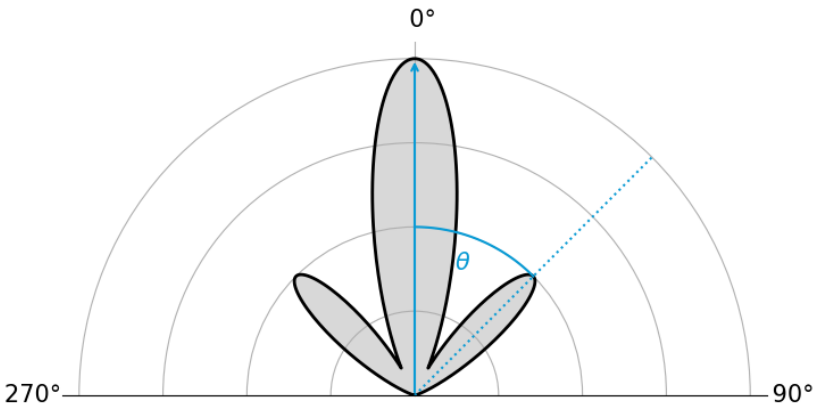


Figure 3.5: Side lobes sketch for a vertically pointing antenna. The Signal strength is proportional to the angle θ.

shown in Fig. 3.5. This pattern of emission is mirrored in the way signals are received, provided the strength of the echo is sufficiently high. For ground-based radar systems, side lobes can complicate data interpretation as they reduce the radar's ability to focus on a single direction, leading to interference, clutter, and reduced accuracy in target detection. Therefore, an effort is made to reduce side lobe levels, often referred to as side lobe suppression.

3.2 MAARSY

When talking about irregularities within the plasma that cause changes in the refractive index, one refers to spatial scales in the order of a few meters. To detect these small-scale structures, very high frequency (VHF) and ultra-high frequency (UHF) radars are typically used, considering the Bragg scattering principle (see Section 3.1).

MAARSY, operated by IAP, performs in the VHF range at 53.5 MHz. MAARSY is a monostatic mesosphere / stratosphere / troposphere (MST) phased array radar system located near the town of Andenes on the northern Norwegian island of Andøya (69.30°N, 16.04°E). Its location makes it ideal for probing middle atmosphere dynamics using PMSE as tracers. MAARSY's design consists of an array of 433 three-element Yagi antennas, each connected to its own transceiver with independent phase control, allowing for a minimum beam width of 3.6° and highly flexible beam forming and steering capabilities. The beam can be steered in arbitrary directions up to 30° off-zenith, and multiple beams can be formed and steered simultaneously. A peak power of around 800 kW ensures that the radar signal can travel long distances and penetrate deep into the atmosphere, reaching the MLT. This increases the likelihood of detecting weak gradients or structures such as those caused by wind.
MAARSY's most compelling capabilities include detailed observation of PMSE and tracking meteor head echoes. Using PMSE, MAARSY is capable of measuring vertical velocities in the MLT region. To maximize its observational capabilities and flexibility in studying various atmospheric phenomena, MAARSY is designed to operate in several different modes. A more detailed description of MAARSY and its different operation modes can be found in Latteck et al. (2010) and Latteck et al. (2012). For this thesis especially the multibeam and radar imaging capabilities play a significant role and will thus be introduced briefly in the following.

3.2.1 MAARSY Multibeam Capabilities

MAARSY's design includes each antenna with its own transceiver, allowing it to form and steer beams flexibly. This capability enables MAARSY to observe several directions almost simultaneously. However, to keep the beam narrow, the entire antenna array focuses on one direction at a time (see Section 3.1). In this thesis, the multi-beam experiment used the whole antenna array to focus the narrow beam into five directions: vertically ($\Phi = 0°$, $\Theta = 0°$), North(0°, 10.5°), East (90°, 10.5°), South (180°, 10.5°), and West (270°, 10.5°), changing direction with each pulse. With a pulse-repetition frequency (PRF) of 850 Hz, the direction changes every 1.176 ms. This technique, called

Doppler Beam Swinging (DBS), allows for high-resolution observation of small-scale atmospheric structures both spatially and temporally.

3.2.2 Radar Imaging with MAARSY

In radar imaging, inversion techniques play a vital role in reconstructing spatial images from received signals. A commonly used approach is the Maximum Entropy (MaxEnt) method, which selects the most unbiased image consistent with the data (e.g. Urco Cordero, 2020). While this method is not implemented directly in this thesis, the results presented here are based on data products generated with it.
The MAARSY array is divided into several receiving elements that are spatially separated by equal distances. The signals received by these elements are transformed into the frequency domain and cross-correlated to produce visibility data, which are then used to reconstruct the spatial distribution of radar scatterers. From these data, a spatial image is obtained through an inverse transformation and subsequently refined using MaxEnt. This method maximizes entropy while ensuring consistency with the visibility data, resulting in statistically robust and high-resolution images.
In this study, only the vertically directed beam was used, operated in a narrow-beam configuration with an estimated width of 6°. At PMSE altitudes (approx. 85 km), this corresponds to an illuminated area with a diameter of about 18 km. The temporal resolution of the imaging data is 2 minutes, the resolution in x and y is 500 m, and the range resolution is 250 m. Signals received outside the illuminated area are considered to result from sidelobes in the case of very strong PMSE (see Chapters 3.1 and 3.2).
The imaging of the radar observation volume enables a three-dimensional representation for each time step, which can be used to illuminate a structure from different perspectives, as shown in Fig. 3.6. In the scope of this study, this was done by slicing the volume containing the structure (the cube in the figure) along different axes.

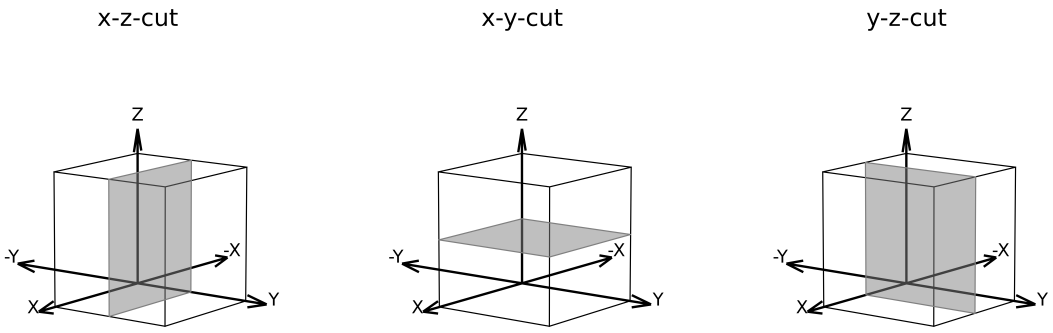


Figure 3.6: Schematic representation of the different perspectives available from radar imaging. The strength of the signal is dependent on θ.

3.2.3 MAARSY Dataset

This study primarily analyzes data obtained with MAARSY, focusing on its Signal-to-Noise Ratio (SNR), full spectral width (f_σ), and radial velocities (ν_{rad}). A detailed explanation of how these parameters were derived from the received signals is provided in Section 3.2.4.
The first part of the study comprises PMSE observations from the summer months of

May to August over a period of 7 years from 2015 to 2021, including a total of 766 observation days. Although MAARSY measures practically continuously, the number of observation hours was not constant during the mentioned period, as shown in Fig. 3.7a). The main reason for this is special campaigns that changed the experiment setup. It should be emphasized that the measurement hours shown here cover the total operation time of the radar, which includes periods when PMSE were not detected (see Fig. 3.7b). The sometimes limited number of observation hours must be taken into account when interpreting the results. In 2017, 2019, and 2021, almost every day was included in the analysis. However, in the first half of the 2016 PMSE season and in the second half of the 2018 and 2020 seasons, only about one-third of the days were available. During these periods, special experiments were carried out with MAARSY, which are characterized by a very low Nyquist frequency (f_N), which does not allow an analysis with regard to extreme events.

The data considered are derived from a range of experiments, all of which involve measurements using a vertically upward-directed beam. In the majority of cases, a pulse repetition frequency (PRF) of 1 kHz combined with only two coherent integrations[1] (n_{coh}) – due to the complementary code – was sufficient to achieve a f_N of 250 Hz, enabling the accurate determination of extremely high vertical velocities (250 Hz corresponding to 700 m/s) [2] .

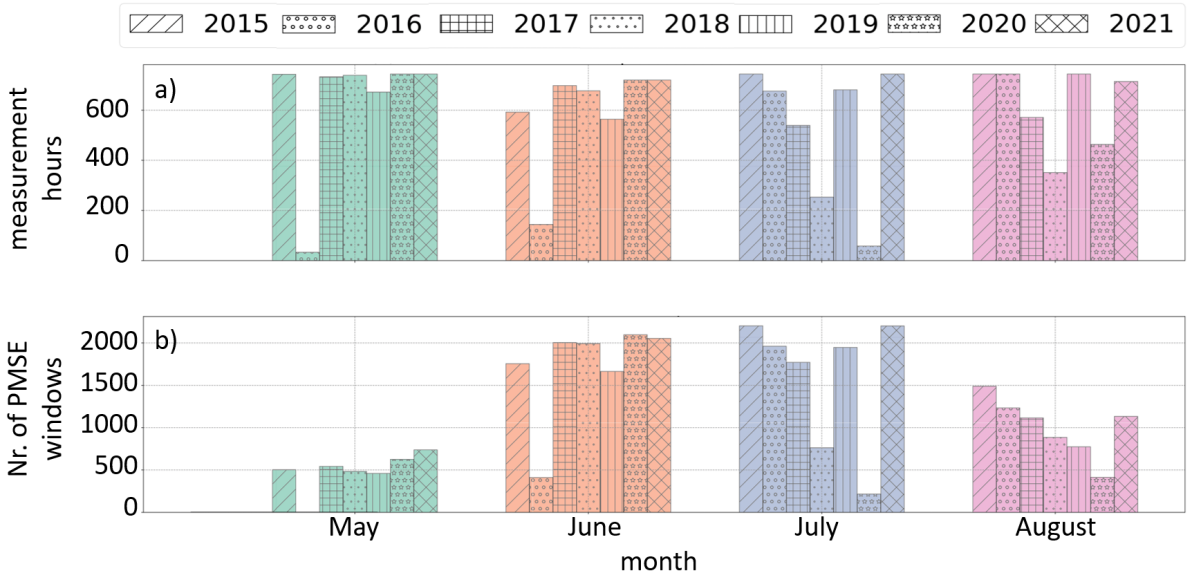


Figure 3.7: (a) Number of hours during which the radar was operational and included in the data analysis and (b) Number of 20-minute windows in which PMSE were detected and included in the data analysis, separately for each month of 2015 to 2021 (Hartisch et al., 2024).

Exceptions to the standard setup occurred during the years 2015 to 2017, and in the months of June, July, and August of 2018, as well as in July of 2019 and 2020. In 2015, the raw data featured a reduced f_N of 15.64 Hz, corresponding to v_{rad} = 43.8 m/s, due to 16 additional coherent integrations. In 2016, f_N was 62.5 Hz, corresponding to v_{rad} = 175 m/s, with 4 additional coherent integrations still allowing for the identification

[1] Summation of phase-coherent received radar signals over multiple pulses to enhance the signal-to-noise ratio and reduce the amount of data.

[2] In this context, $f_N = \frac{\mathrm{PRF}}{2\,n_{\mathrm{coh}}}$ and $w_N = \frac{\lambda_{\mathrm{MAARSY}}}{2}\,f_N$.

the extreme event described by Chau et al. (2021). After 2017, the PRF was varied, taking values of 828 Hz, 850 Hz, and 900 Hz, which influenced the temporal resolution and, consequently, f_N (Hartisch et al., 2024). Data from before 2015 were excluded from this study due to a significant reduction in f_N. Throughout the observed period and all experiments, the range resolution was 300 m, and the temporal resolution averaged around 100 s, depending primarily on the number and duration of the experiments.

The second part of this thesis focuses on the detailed study of selected varicose-mode events recorded in 2015, 2018, and 2023. The analysis includes four pivotal events, specifically on 2 June 2015, 3 July 2018, 1 August 2018, and 1 July 2023. Measurements from MAARSY for the first three cases used the previously mentioned f_N. For the event on 1 July 2023, the PRF was also set at 1 kHz, resulting in the same f_N and corresponding velocity as those established in the initial experimental setup of prior years.

3.2.4 Vertical Wind Velocity Estimation from MAARSY Data using Complex Autocorrelation

As mentioned in Section 3.2.3, this study of MAARSY measurements exclusively uses data from the radar beam directed vertically upwards. Given the beam's narrow width of 3.6°, it allows for a focused and precise measurement of scatterers directly above the radar. This narrow beam width minimizes contamination by off-vertical scatterers. The assumption is that the measured ν_{rad} primarily reflect vertical velocities (w). This assumption is important, as radial velocities derived from the Doppler shift f_D (see Section 3.1) are directly interpreted as vertical velocities in this context.
The presence of multiple scatterers within the radar's observation volume can lead to variations in f_D. Each scatterer, depending on its velocity relative to the radar, contributes a slightly different f_D. As a result, the received power spectrum of the signal does not present a single, uniform shift but rather displays a distribution of shifts centered around a mean value. This variability in the Doppler shift can provide insights into the range of velocities and turbulence within the observed air column represented by the full spectral width.
Assuming that the power density spectrum of the complex signal can be represented by a Gaussian:

$$S(f) = \frac{P_S}{\sqrt{2\pi} f_\sigma} \exp\left[-\frac{(f - f_D)^2}{2 f_\sigma^2}\right], \tag{3.4}$$

where $S(f)$ is the power density spectrum, P_S is the power of the received signal, and f_σ represents the spectral width, then the Doppler parameters can be determined in several ways. On the one hand, the spectral moments of the power density spectrum can be used to determine the f_σ and the f_D. On the other hand, these parameters can also be determined using the autocorrelation function.

In the scope of this study, the latter option demonstrated in Fig. 3.8 was used (e.g. Zecha, 1999).

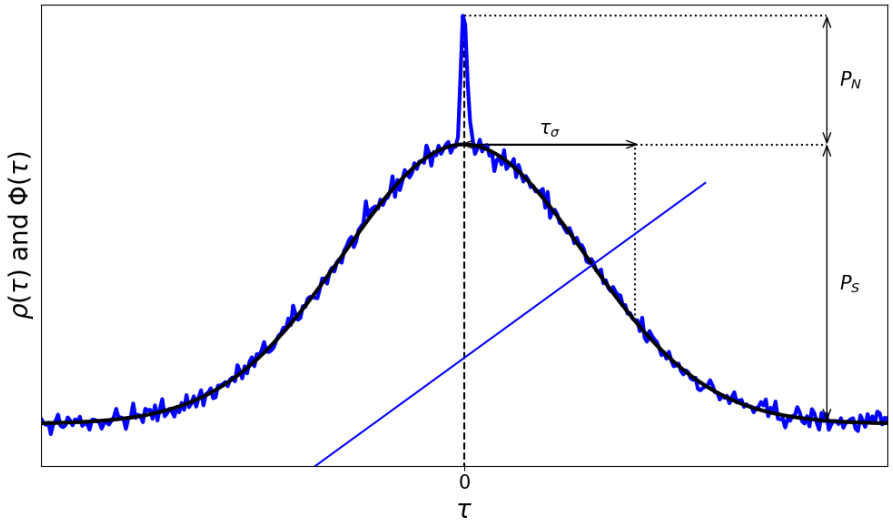


Figure 3.8: Sketch of the determination of the Doppler parameters from the complex autocorrelation function (adapted from Zecha (1999)).

The continuous operation of MAARSY generates a vast amount of data, making efficient management or significant reduction necessary. Additionally, atmospheric measurements often include noise, which should be minimized. In previous MAARSY experiments, both challenges were addressed by coherently integrating the radar signal (Farley, 1985), in addition to the two coherent integrations already incorporated through the complementary code (see Section 3.2). However, the side effect of this analysis technique on the determination of the velocity is clearly demonstrated in Fig. 3.9. The first two panels,

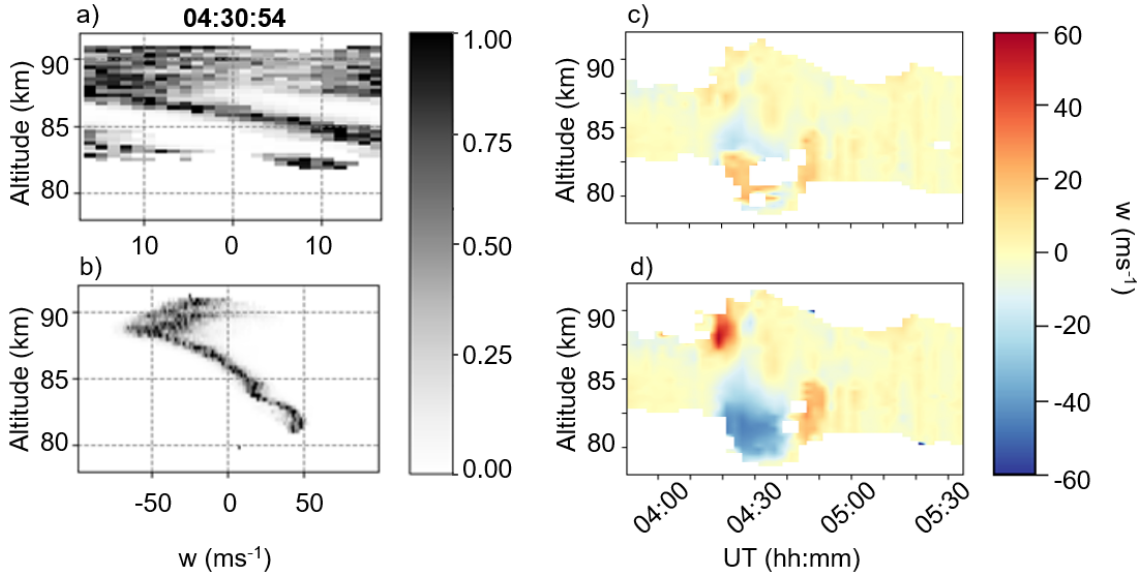


Figure 3.9: Visualization of the impact of six additional coherent integrations on received spectra and vertical velocities during an extreme event reported by Chau et al. (2021). Panel a) displays the velocity spectrum versus altitude with additional coherent integrations, while panel b) shows the same spectrum without them. Panels b) and c) compare two hours of the Range-Time-Intensity plot for the event, with and without additional coherent integration, respectively.

a) and b), display the normalized velocity spectra against altitude. Panel a) is derived from a signal with 6-fold coherent integration, while panel b) shows the spectra without additional coherent integration. It is evident that the spectra in panel a) appear "folded" or aliased, whereas in panel b) the spectra are fully visible. This phenomenon is known as the aliasing effect, which occurs when the sampling frequency – here determined by the PRF – is too low to capture the true Doppler shift without ambiguity. In coherent integration, for example, summing six pulses effectively reduces the PRF by a factor of six, lowering f_N. When spectra are affected by aliasing, it becomes impossible to reliably determine f_σ or f_D, leading to faulty values and even gaps in the Range-Time-Velocity plot, as clearly shown in the comparison between panels c) and d). In this plot, negative velocities mean a movement towards the radar (downward), and positive velocities are motions in the opposite direction (upward). A reduction of f_N increases the risk of aliasing, as f_D exceeding f_N – corresponding to w above the Nyquist velocity $w_N = \lambda 2\ f_N$ – fold into lower, misleading values. In this sense, aliasing can act as a misleading filtering mechanism, suppressing the apparent occurrence of strong vertical motion. The analysis in the scope of this thesis thus avoids coherent integrations additional to those due to the complementary code. In Section 3.2.3, it was already mentioned that data from experiments prior to 2015 are excluded from this study since the number of coherent integrations was nominally set too high to allow for the detection of high w. Starting in 2017, the MAARSY experiments did not include any additional coherent integrations anymore in order to prevent this limitation. The frequency distribution of the received signals from various experiments, each with different f_N, is described by Eq. 3.4. By applying the inverse Fourier transform, the complex autocorrelation function $\rho(\tau)$, where τ represents the time delay, is obtained:

$$\rho(\tau) = \int_{-\infty}^{\infty} S(f) e^{j2\pi f \tau}\, df. \tag{3.5}$$

In this case, it is assumed that $\rho(\tau)$ follows a Gaussian profile:

$$\rho(\tau) = P_S \exp\left[-\frac{\tau^2}{2\left(\frac{1}{2\pi f_\sigma}\right)^2}\right] \exp(j2\pi f_D \tau), \tag{3.6}$$

Here, the first exponential term describes the decrease in correlation with increasing time delay τ, while the second term represents the linear phase change over time. A key property of the signal power P_S is:

$$P_S = |\rho(\tau = 0)|. \tag{3.7}$$

This indicates that, in the absence of a time delay, the magnitude of the autocorrelation function equals the signal power. The Doppler shift f_D can be determined from the phase $\Phi(\tau) = 2\pi f_D \tau$ by differentiating with respect to τ:

$$\frac{d\Phi(\tau)}{d\tau} = 2\pi f_D, \tag{3.8}$$

This relation shows that the f_D is directly proportional to the rate of phase change over time, allowing it to be determined from the slope of the phase curve. The spectral width f_σ is directly related to the standard deviation τ_σ of $\rho(\tau)$ in the time domain:

$$\tau_\sigma = \frac{1}{2\pi f_\sigma} \tag{3.9}$$

This relationship highlights the connection between the temporal spread of the autocorrelation function and the spectral width of the signal.

3.3 SIMONe Meteor Radar - MMARIA Norway

The case studies in the second part of the thesis include considerations of the mean wind around and during their observation measured with a meteor radar (schematic of the operating principle in Fig. 3.10). The Spread Spectrum Interferometric Multistatic Meteor Radar Observing Network (SIMONe), part of the Multistatic Multi-frequency Agile Radar for Investigations of the Atmosphere (MMARIA) concept in Norway, is a multistatic specular meteor radar (SMR) system. This system enhances the traditional meteor radar setup by incorporating multiple spatially separated receivers (Rx) and a transmitter (Tx) site equipped with six transmitting antennas. In Norway, the system consists of one transmitting site with six antennas and four additional receiving antennas positioned at a distance between 12 and 200 km from the transmitter. It employs continuous wave signals at 32.55 MHz (VHF), which is ideal for detecting meteor trails. The continuous wave signals allow for very high temporal resolution, while the spaced antennas provide higher spatial resolution. According to the concept outlined in section 3.1 and sketched in Fig. 3.10, specular reflection in a multistatic configuration occurs when the directions of the transmitted and received radar waves form a right angle at the meteor trail. The ionized meteor trail drifts with the background wind and serves as a target for the radar, effectively acting as a tracer of the background wind.

3.3.1 Determination of Horizontal Winds from Meteor Radar Data

The radial velocity of meteor trails can be used to determine horizontal winds in the MLT region by analyzing the Doppler shift of the signal scattered from the ionized meteor trail (see Eq. 3.3). The measured radial velocity includes contributions from the zonal (u), meridional (v), and vertical (w) wind components. Because a single Doppler measurement provides only the line-of-sight component of the wind field, it does not yield the horizontal wind vector by itself. To determine the horizontal wind components,

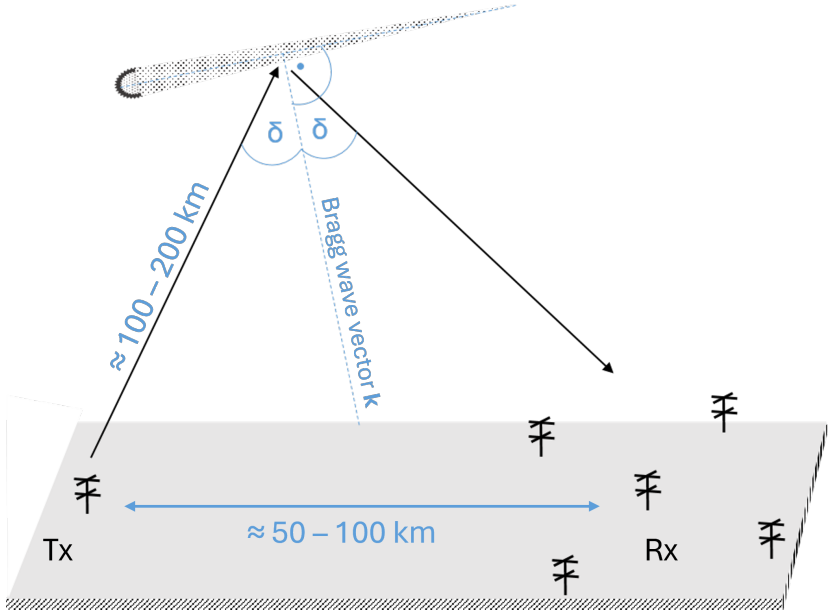


Figure 3.10: Schematic setup of a multistatic specular meteor radar (not scaled) (adapted from Jean (2024)).

Doppler measurements from several different viewing directions are required. In general, the Doppler shift for a given transmitter–meteor–receiver geometry can be expressed as

$$2\pi f_d = \mathbf{k} \cdot \mathbf{u}, \tag{3.10}$$

where f_d denotes the Doppler shift, $\mathbf{k}$ the effective wave vector of the radar system, and $\mathbf{u}$ the atmospheric wind vector.

The effective scattering wave vector $\mathbf{k}$ describes the direction of phase propagation relevant for the Doppler measurement and is defined as

$$\mathbf{k} = \mathbf{k}_\mathrm{s} - \mathbf{k}_\mathrm{i}, \tag{3.11}$$

where $\mathbf{k}_\mathrm{i}$ is the incident wave vector (transmitter $\rightarrow$ scatterer) and $\mathbf{k}_\mathrm{s}$ the scattered wave vector (scatterer $\rightarrow$ receiver). This formulation is general and applies to multistatic radar geometries.
In the monostatic case, the scattered and incident wave vectors are antiparallel, $\mathbf{k}_\mathrm{s} = -\mathbf{k}_\mathrm{i}$, such that $\mathbf{k} = -2\,\mathbf{k}_\mathrm{i}$ with magnitude $|\mathbf{k}| = 4\pi/\lambda$. The incident wave vector can be written as $\mathbf{k}_\mathrm{i} = (2\pi/\lambda)\,\hat{\mathbf{e}}_\mathrm{beam}$, where $\hat{\mathbf{e}}_\mathrm{beam}$ denotes the unit vector pointing along the radar beam direction.

For specular meteor scattering, the effective wave vector must be perpendicular to the meteor trail, which defines the geometric condition under which scattering is observed. By combining measurements from multiple $\mathbf{k}$-directions, the horizontal wind field can be reconstructed. It is typically assumed that vertical winds are small compared to the horizontal flow, such that $\mathbf{u} = (u, v, 0)$. $\mathbf{k}$-directions, the horizontal wind field can be reconstructed. It is typically assumed that vertical winds are small compared to the horizontal flow, so that $\mathbf{u} = (u, v, 0)$.

The SIMONe radar system provides additional capability to determine the horizontal wind components from each receiver at slightly different viewing geometries, thereby increasing the accuracy of the wind retrieval. Multiple receivers do not observe the same meteor trail; rather, they detect many individual trails within the sampling volume, each under its own transmitter–meteor–receiver configuration. The resulting diversity of viewing geometries leads to an overdetermined set of line-of-sight velocity measurements, from which the horizontal wind vector can be estimated with improved precision, typically using a least-squares fit (e.g. Poblet et al., 2023). The winds derived in this way and used in this study have an altitude resolution of 1 km and a temporal resolution of 30 minutes, and represent an average over an area spanning several hundreds of kilometers in diameter.

3.4 Partial Reflection Radar in Saura, Norway

Close to the MAARSY and SIMONe radar systems in Norway, near the town of Saura (69.14°N, 16.02°E), there is a partial reflection radar (PRR) system operated by the IAP, which transmits at 3.17 MHz with a phased array whose radar beam can be steered electronically in various directions. Fig. 3.11 shows a sketch of the antenna distribution with the connected antennas in black and positions marked for individually sampled antennas lately used for interferometry in red. This system falls into the category of high-frequency (HF) radars although it is historically referred to as an MF radar and covers an altitude range between 60 and approximately 95 km, encompassing the lower part of the ionosphere known as the D-region (Renkwitz et al., 2017). The transmitted radio waves travel upwards through the atmosphere, and their behavior changes based on the properties of the atmospheric layers they encounter. When the radio waves reach the ionospheric D-region, they interact with variations in electron density. At the boundaries where these changes occur, some of the radio wave energy is reflected towards the radar due to differences in refractive index between layers with varying electron densities (Reid, 2015). The reflected portion of the radio wave carries crucial information about the ionospheric layer it encountered.

The strength and timing of the reflected signal depend on the electron density and the altitude of the reflecting layer, with stronger reflections indicating higher electron densities. The power and Doppler spectra obtained from these reflections help researchers understand variations in electron density, ionospheric layering, temporal changes, and dynamic processes within the D-region. The width of the spectra also carries information on turbulence parameters (Renkwitz et al., 2018; Renkwitz and Latteck, 2019).

3.4.1 Saura PRR Imaging Using the MUSIC Algorithm

The phased array configuration of the Saura PRR enables beam steering in multiple directions, allowing for the quasi-simultaneous reception of partially reflected signals from various directions. This capability enhances the accuracy of determining the directions from which the signals are received. To find this direction, the covariance matrix of the

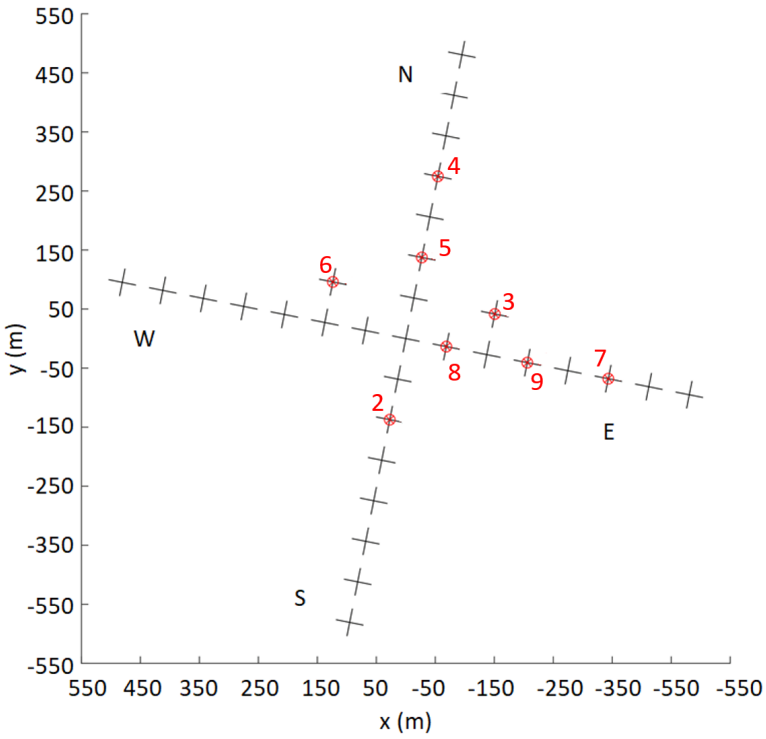


Figure 3.11: Array schematic of the partial reflection radar in Saura PRR. Red dots mark antennas with individual receiver channels used for interferometry (Renkwitz et al., 2018).

signal $\mathbb{R}$ is used:

$$\mathbb{R} = \frac{1}{N} \sum_{i=1}^{N} \mathbf{x}(i)\mathbf{x}^H(i), \tag{3.12}$$

where $\mathbf{x}(i)$ represents the signal vector received by the array at the i-th snapshot, N denotes the number of snapshots, and $\mathbf{x}^H$ indicates the Hermitian transpose of $\mathbf{x}(i)$. The eigenvalues and eigenvectors derived from $\mathbb{R}$ provide information on the signal strength and direction, respectively. By applying the Multiple Signal Classification (MUSIC, e.g. Schmidt, 1986) algorithm, the strongest signals and their respective directions can be identified. This data is then utilized to generate an image of the probed volume.

4 Data Analyses

4.1 Varicose-Mode Event Identification Methodology

The data set described in Section 3.2.3 was analyzed thoroughly to find more instances of the extreme event reported by Chau et al. (2021). This search has been challenging due to the stochastic nature of meteor occurrences, which are unpredictable and sudden, often displaying remarkably high radial velocities. In the context of this study, such meteor echoes act as outliers that can distort the analysis and therefore need to be identified and masked. These challenges are exacerbated by system-induced artifacts, such as strong echoes received through side lobes from off-vertical directions during instances of intense PMSE. Moreover, the absence of prior knowledge about the characteristics and occurrence patterns of such events meant that no reliable criteria existed to train an automated detection algorithm. Combined, these factors hinder automated detection, making manual inspection essential for reliably identifying notably high vertical wind velocities and varicose structures. A description of what was being sought is given in Fig. 4.1: Varicose-mode events were defined as phenomena characterized by simultaneous vertical ascending and descending winds, lasting only a few minutes, making them particularly confined in time.

Panel a) shows an example event on 6 June 2021 presented in an RTDI plot. Panel b) shows a sketch of the structure within the yellow frame. This structure, like the ex-

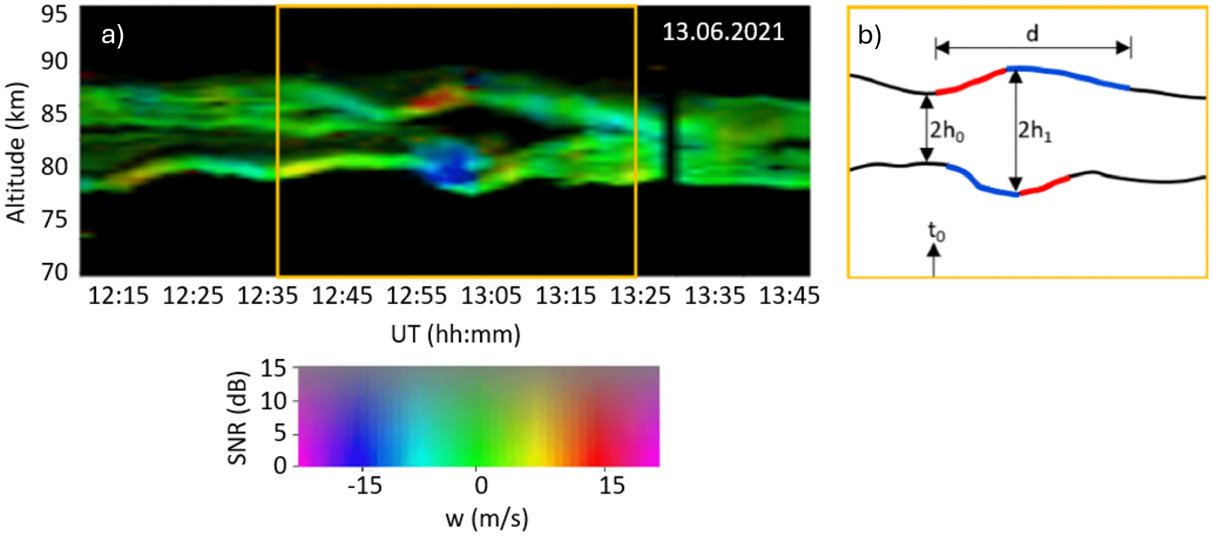


Figure 4.1: Example of a varicose-mode event found on 13 June 2021. a) Shown is the vertical velocity evolution in time (color-coded) in an altitude range between 75 and 95 km, exhibiting the simultaneous up and downwards motions (varicose mode). b) depicts the schematic of the event with h_0 and h_1 as the thickness of the PMSE layer in its undisturbed and disturbed state, respectively. t_0 represents the starting time and d their duration. The red and blue colors emphasize the vertical wind direction, as in a) (adapted from Hartisch et al. (2024)).

treme event, causes the PMSE layer to temporarily expand, often returning to nearly its original thickness afterward. The boundaries of the PMSE layer are outlined in black, with red indicating updrafts and blue indicating downdrafts. The vertical extent of the PMSE layer is shown as $2h_0$ before the events and $2h_1$ during the events, following the nomenclature also used in Chau et al. (2021) and introduced by Dewan and Picard (1998) to sketch varicose-structured bores. The beginning of each event is marked as t_0, and the duration is shown as d. The example in this figure can be seen as representative of all the observed events.
Due to the mentioned challenges, the identification of varicose-mode events was conducted manually, primarily utilizing daily vertical velocity plots, which were color-coded to highlight events exceeding the 3σ threshold within a range of -15 to 15 m/s. The data analysis begins with a masking process, where only data points that met specific criteria were retained for visualization. These criteria include maintaining a SNR above -5 dB and vertical velocities below 100 m/s, leading to the exclusion of data points outside these limits. This selective approach provides a clearer representation of PMSE and is visualized in Fig. A0.2 in Appendix A0.1.1.

By zooming into and closely examining the figures, the timing of events becomes clearer, allowing for the identification of event boundaries and the determination of the PMSE layer's upper and lower limits before, during, and after each event. As in the schematics in Fig. 4.1, the width of the PMSE layer just before an event starts (t_0) is labeled as $2h_0$, while $2h_1$ indicates the event's maximum width, measured from the first pixels at the upper and lower edges. The widest point generally aligns with the transition between

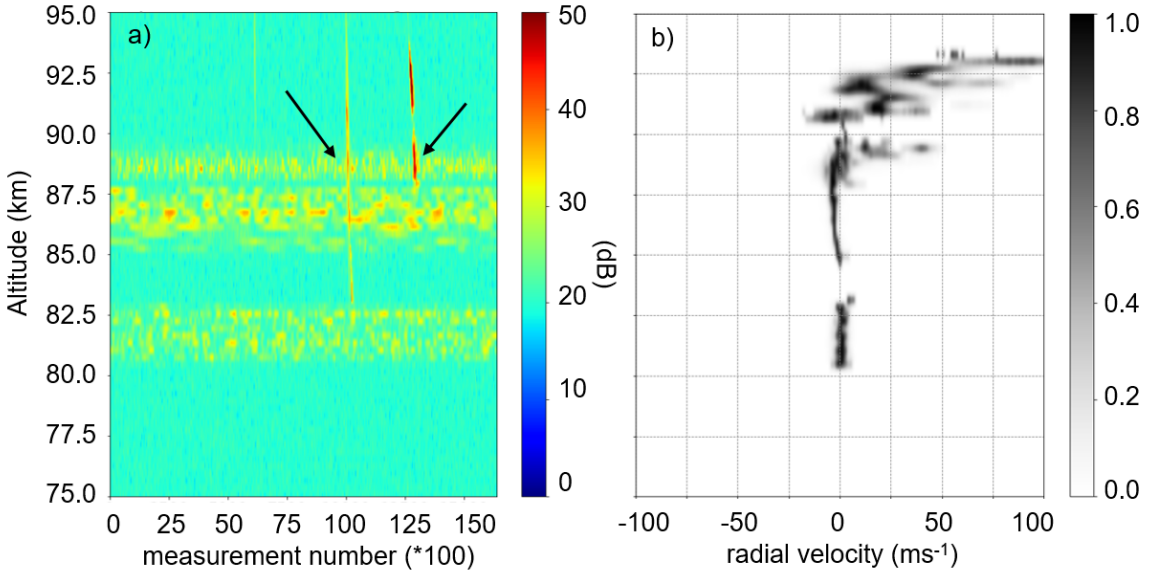


Figure 4.2: Panel (a) shows the power-range plot for a single pulse, from which the velocity spectrum in panel (b) is derived. In the second half of panel (a), between 82 and 95 km, two meteor signatures are visible, marked by the arrows. Panel (b) illustrates the impact of these meteors on the normalized radial velocity spectrum, where the velocities are overestimated at the altitudes affected by meteor echoes. Here, the spectrum is normalized to the maximum value at each altitude.

the initial updraft and downdraft phases within the event. In some cases, updrafts and downdrafts occur only nearly simultaneously, with a slight time difference between them, meaning the midpoint of the event does not always match the point of maximum width. The event duration was determined manually by visual inspection, with the start defined as the first clear and simultaneous appearance of an updraft and a downdraft, identified as the first visible red and blue structures, respectively, and the end as the last occurrence of either.
After identifying and defining an event's spatial and temporal characteristics, further analysis is conducted to determine the maximum vertical velocities.
Due to the sporadic nature of meteors, automated detection methods are challenging, as meteors can enhance the signal and falsely indicate exceptionally high vertical velocities (see Fig.4.2b). To prevent these meteor events from affecting the study of varicose-mode events, power-time plots used for the velocity analysis (see Fig. 4.2a) are carefully examined. If a suspected velocity peak coincides with a short-term, intense signal across multiple altitude channels, it is discarded as it indicates the presence of a meteor, and the next highest value is used instead.
To account for the impact of diurnal and annual PMSE variability mentioned in Section 3.2.3, as well as fluctuating observation hours, the event counts are normalized to the occurrence of PMSE within specific time frames. Within the MAARSY dataset, PMSE are classified based on specific criteria. The normalization process involves dividing the daily PMSE data into twenty-minute intervals, focusing on the altitude range of 82 to 88 km, where PMSE are most prevalent. These intervals are analyzed for PMSE, using a threshold of 50% PMSE-labeled pixels across all altitudes to confirm their presence.

4.2 Cross-Correlation Analysis of Multibeam Radar Observations for Event Tracking

The extreme event that motivated this study was investigated using radar imaging, revealing that it passed through MAARSY's field of view (FOV). In this study, an assessment was attempted to determine if similar behavior could be observed in four case studies. However, radar imaging was not feasible for all selected cases, necessitating an alternative approach.
The multibeam capabilities of MAARSY were employed to observe five beam directions (vertical (V), North (N), East (E), South (S), and West (W)) quasi-simultaneously, as described in Section 3.2.1. This capability enabled event tracking across beams without relying on full imaging. The method relied on determining whether an event could be detected across all beam directions with lagged timings, indicating its passage through the FOV. The following assumptions were made in this approach:

(1) elongated Shape: The event was assumed to be elongated in one dimension and highly localized in the perpendicular direction, forming an oval shape. This assumption aligns with radar imaging observations of the extreme event studied by Chau et al. (2021).

(2) rigid Front: The event was treated as a rigid front, maintaining a constant width in its localized dimension across the radar's FOV.

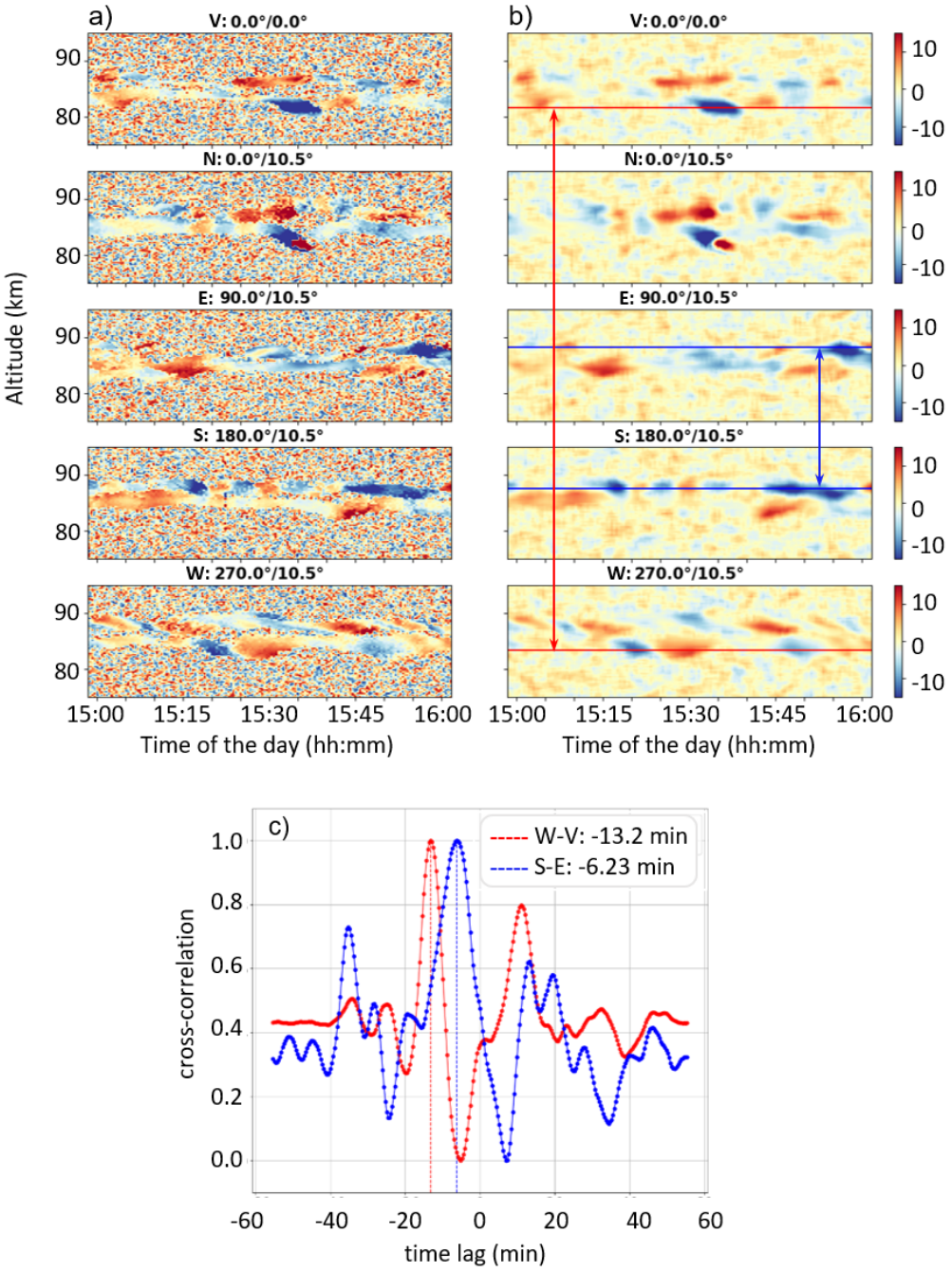


Figure 4.3: (a) Unsmoothened velocity data from five radar beam directions (top to bottom: V, N, E, S, W) over one hour, PMSE-surrounding gates were filled with random values to ensure valid input for the correlation algorithm. (b) Smoothed data using a 5×5-point moving average, with red and blue lines marking the altitudes selected for analysis. (c) Lag times obtained by cross-correlating the corresponding line pairs from panels (a) and (b): blue with blue and red with red.

(3) uniform Phase Speed: It was assumed that the event's phase speed remains constant within the area defined by three key points used for analysis, allowing for consistent time lag measurements.

(4) neglecting Earth Curvature: Given the radar's relatively small FOV, Earth's curvature was neglected in calculations.

Fig. 4.3a illustrates one example – examined in more detail in 6.25 – to demonstrate the visibility of the event across multiple beams, albeit with varying clarity. To determine time lags reliably, one range gate per beam was selected, and cross-correlation was applied between corresponding gates in different beams. Since the Python cross-correlation function used here does not handle missing data correctly, the remaining range gates surrounding the PMSE signature were filled with random noise to avoid processing errors. To enhance feature detection and ensure a clearer cross-correlation signal, the data were smoothed prior to analysis. Fig. 4.3b shows two specific examples: one focusing on the upper part of the event (indicated by blue horizontal lines), and one on the lower part (red horizontal lines). This distinction was necessary due to differences in the prominence of features across beams. Fig. 4.3c presents the resulting cross-correlation curves for the upper and lower segments, colored in blue and red, respectively. Negative lag times indicate that the event reaches the W-beam before V and the S-beam before E. Positive lag times would suggest the opposite. By analyzing these cross-correlation pairs, an estimation of the event's direction and angle relative to the N-S axis was obtained using the following logic:
Based on the known beam positions at PMSE altitudes (P_1, P_2, P_3), their known distances towards each other, and the knowledge that the velocity vector (L_v) stands per-

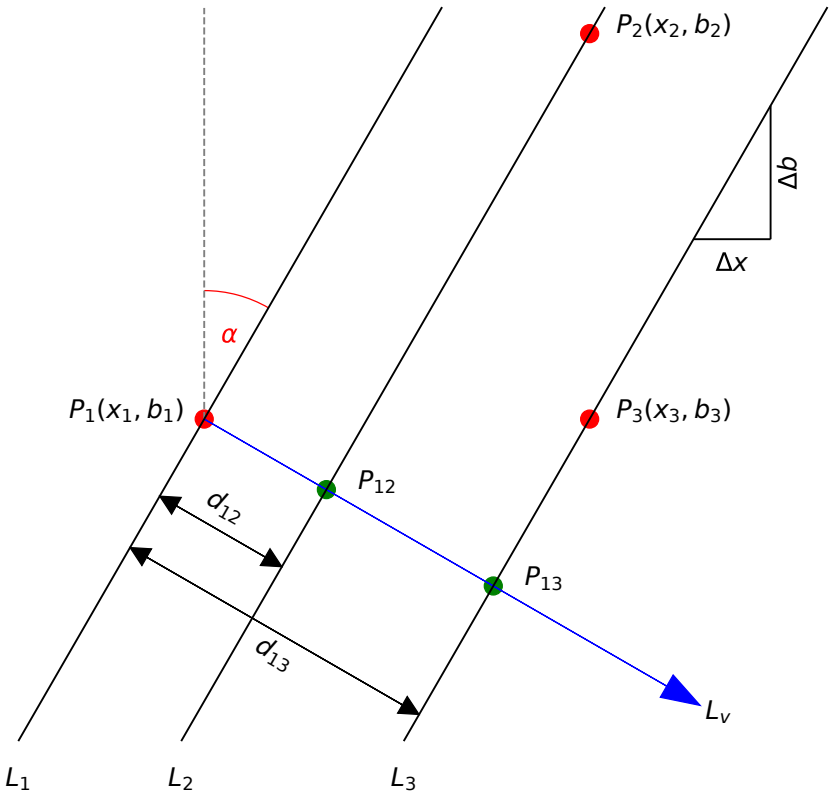


Figure 4.4: Sketch of beam positions and velocity vectors to aid in calculating angle and velocity.

pendicular to the wavefront (L_1, L_2, L_3), the angle α of the wavefront relative to the y-axis or in other words the slope of the wavefront and the event's velocity across the area the three points span were determined. Fig. 4.4 presents an example sketch of this setup for one radar array quadrant, aiding in understanding the following method. The lag times calculated from cross-correlation are time differences of when the event was observed at each point, e.g., between P_1 and P_2. Since the wavefront does not necessarily align with the x or y-axis, this time lag represents the distance between P_1 and the yet unknown point P_{12} where the wavefront (L_2) intersects the velocity line L_v, and not the known distance of the two beam positions P_1 and P_2. Detailed explanations, equations, and procedures for this method are provided in A0.3.2.

In general, this procedure compares lag times for four pairs of beams to ensure consistency. For instance, one comparison involves P_1-P_2 and P_1-P_3 giving one pair of lag times, while the other uses P_2-P_1 and P_2-P_3 giving another pair of lag times. If the structure is indeed a rigid front with a constant velocity between the involved points and maintains shape, slopes from both lag time pairs should align.

To account for measurement uncertainties, maximum estimated errors were included with the lag times due to factors such as the 1.5-minute temporal resolution of the measurements and variations in feature quality across beams. Overlapping results within error bars for both comparisons would support assumptions (2) and (3).

5 Observation and Statistics of Varicose-Mode Events

This chapter provides an in-depth analysis of varicose-mode events observed in the MAARSY dataset, with findings published in Hartisch et al. (2024). Spanning from 2015 to 2021, the dataset revealed frequent occurrences of over 700 varicose-mode events. The chapter explores these events' occurrence patterns, and temporal and spatial characteristics. While these events share structural similarities, their vertical extent and substructures, such as additional layers, can vary significantly. Detailed data on their occurrence, duration, vertical extent, and vertical wind speeds were systematically collected to provide comprehensive insights into these phenomena.

5.1 Event Occurrence and Frequency

Analysis of 766 observation days revealed that varicose structures were present on 249 days, equating to about 33% of the days. Across seven PMSE seasons, a total of 707 varicose-mode events were observed. Figs. 5.1a and 5.1b provide a detailed breakdown of these occurrences by month and year, with supplementary data available in Tab. 5.1.

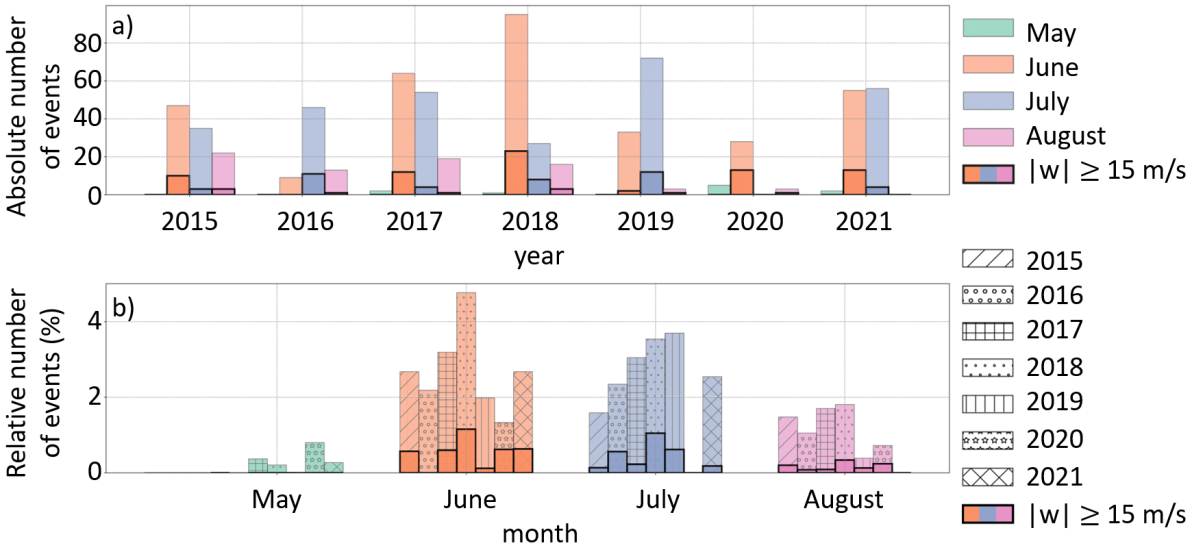


Figure 5.1: Occurrence of varicose-mode events in the PMSE months (May, June, July, August) between 2015 and 2021. (a) The absolute number of events counted per year, broken down by individual months. (b) The number of events counted per month relative to the number of 20-minute PMSE windows counted during the same period, broken down by individual years. The more heavily colored and contoured bars represent the absolute (relative) number of those events in the respective period with $|w| \geq 15\,\mathrm{m/s}$.

Fig. 5.1a shows the annual distribution of events per month during the PMSE season. Events with vertical velocities $|w| \geq 15\,\mathrm{m/s}$ are highlighted, as this threshold represents a conservative 3σ standard value. While varicose-mode events were observed in all years, the total number of events varied, with a notable peak in 2018 and a lower count in 2020. Monthly contributions to the total event count also varied across years.
Fig. 5.1b normalizes the occurrence of varicose-mode events relative to the number of 20-minute PMSE windows, providing a clearer perspective on event frequency. Most events were concentrated in June and July, with fewer in August, and May showing the lowest frequency. On average, the probability of observing a varicose-mode event during the PMSE season was about 2.5% in June and July, 0.3% in May, and 1.0% in August, given the presence of PMSE.

Table 5.1: Summary of the absolute numbers of varicose-mode events per month and year. In parentheses, the number of 20-minute windows that contained PMSE for the same time period (only the days included in this study). In the last column and row, the total numbers are shown, respectively.

Varicose-Mode Events by Month and Year								
Year / Month	**2015**	**2016**	**2017**	**2018**	**2019**	**2020**	**2021**	**Total per Month**
May	0 (504)	0 (0)	2 (543)	1 (484)	0 (460)	5 (626)	2 (738)	10 (3355)
June	47 (1755)	9 (412)	64 (2005)	95 (1992)	33 (1664)	28 (2097)	55 (2054)	331 (11979)
July	35 (2202)	46 (1961)	54 (1771)	27 (762)	72 (1947)	0 (216)	56 (2201)	290 (11060)
August	22 (1489)	13 (1233)	19 (1115)	16 (885)	3 (774)	3 (414)	0 (1133)	76 (7043)
Total per Year	104 (5950)	68 (3606)	139 (5434)	139 (4123)	108 (4845)	36 (3353)	113 (6126)	**707 (33437)**

5.2 Diurnal Variation and Event Patterns

Fig. 5.2a depicts the relative occurrence of varicose-mode events throughout the day, averaged over the 7-year period. These events can happen at any time, but there is a clear peak between 12:00 and 16:00 UT and a minimum between 18:00 and 20:00 UT. Varicose events can occur as single events, in pairs, or in groups (Fig. A0.1 in the Appendix). The absolute numbers for these categories are shown in Fig. 5.2b, where single occurrences (371 events, 52%) were most common, followed by pairs (92 pairs, 26%) and groups (46 instances, 22%). High-velocity events ($|w| \geq 15\,\mathrm{m/s}$) were more likely to occur in pairs or groups, with a higher proportion of such events observed as the number of events within a group increased.

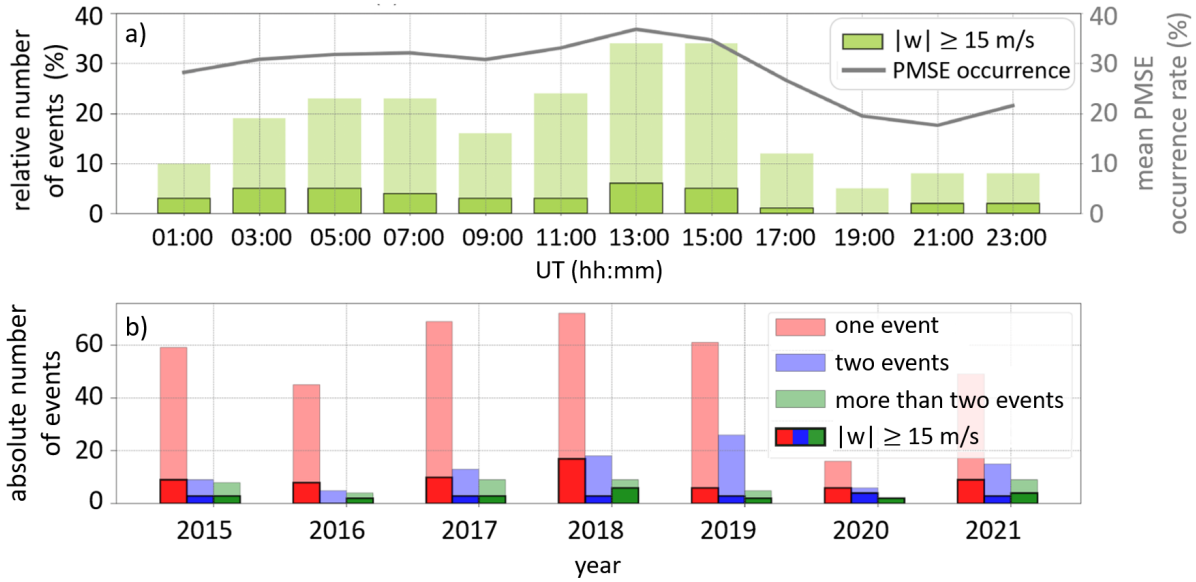


Figure 5.2: (a) The distribution of the occurrence of events in varicose mode relative to the number of 20-minute PMSE windows observed within the time frame of interest over the course of a day. The gray line illustrates the mean diurnal variation in the frequency of PMSE by Latteck et al. (2021). (b) The absolute number of varicose-mode events occurring as single events, as pairs, or in groups for each individual year.

5.3 Duration and Vertical Extent of Events

The duration of varicose-mode events, illustrated in Fig. 5.3a, typically averaged around 20 ± 9 minutes, with some lasting from 4 minutes to over 100 minutes. The vertical extent and expansion of the PMSE layer during these events are summarized in Figs. 5.3b and 5.3c. The average maximum vertical extent was approximately 8 ± 2 km, with the

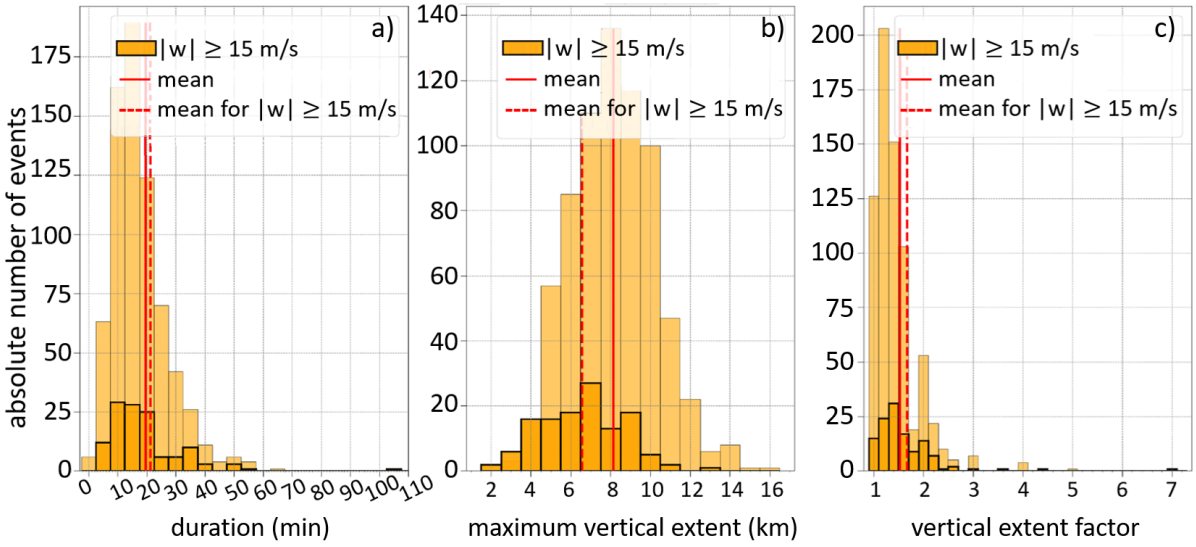


Figure 5.3: Duration (a), maximum vertical extent (b) and h_1/h_0 (c) distribution of the varicose-mode events. The red solid (dashed) line represents the mean of all events ($|w| \geq 15\,m/s$ events).

layer widening by a factor of about 1.5 ± 0.5 during the events. High-velocity events exhibited a similar average duration of around 22 ± 13 minutes but with greater variability, and their maximum vertical extent was slightly smaller, around 6.5 ± 2 km.

5.4 Vertical Velocity Characteristics

This study was initially motivated by the aim of understanding the variability of vertical wind velocities during varicose-mode events. To interpret event velocities, we first examined the overall distribution across 82-88 km over seven PMSE seasons (Fig. 5.4a, green). It is approximately Gaussian, centered at 0 m/s with a standard deviation of about 3 m/s, but shows a slight asymmetry with more frequent downward (negative) velocities. For each varicose-mode event, the highest upward and downward velocities (two values per event) were extracted and summarized in Fig. 5.4b (red = updraft, blue = downdraft), with a Gaussian reference (black) matching Fig. 5.4a. Most event velocities lie within ±15 m/s, and updrafts exhibit a somewhat broader distribution than downdrafts. Threshold exceedances of $|w| \geq 15$ m/s were observed in about 17% of all varicose-mode events. A detailed analysis of these high-velocity events – occurrence rates, durations, and associated properties – is presented in a dedicated section below.

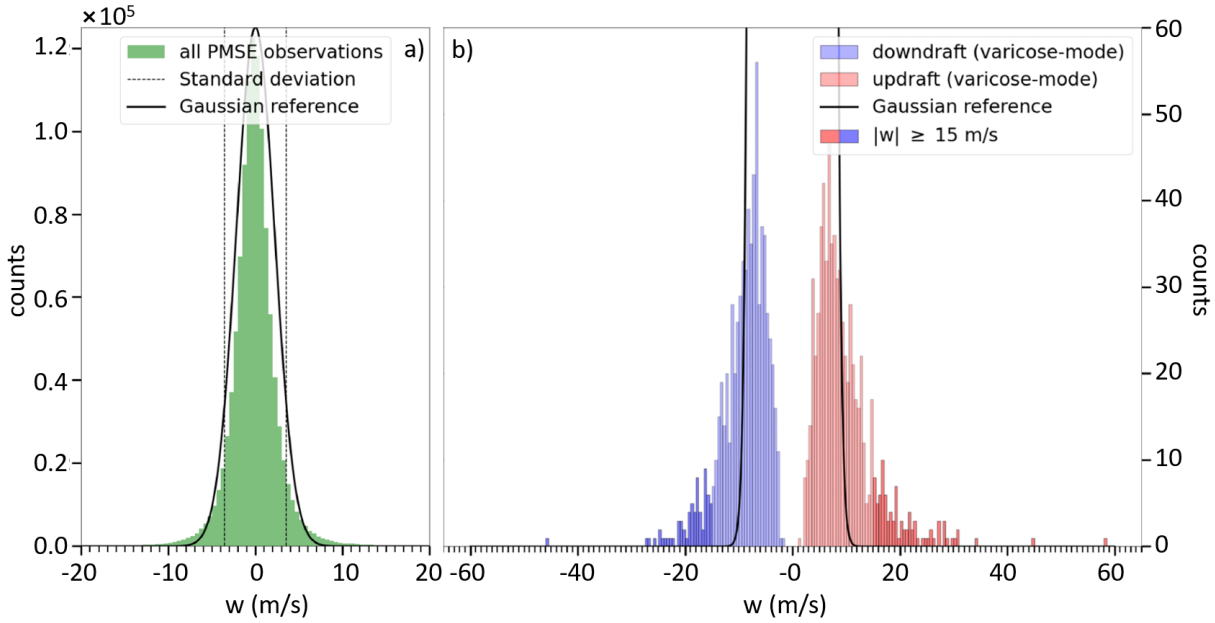


Figure 5.4: Distribution (a) of vertical velocities across all altitudes and throughout the observation period and (b) of the maximum vertical velocities of varicose-mode events in blue (down-drafts) and red (up-drafts). The black curve represents a Gaussian reference.

The accuracy of these vertical velocity measurements can be influenced by several factors, including radar system limitations and the presence of horizontal wind components. Despite these challenges, the velocities observed in this study are considered representative of the vertical component, particularly for velocities exceeding a few meters per second.

5.5 Investigation of the Connection between Varicose-Mode Event Parameters

The relationship between the absolute vertical velocity ($|w|$) of varicose-mode events and their duration and spatial extent (extent factor) was investigated to enhance the understanding of the dynamics driving these atmospheric phenomena. Higher velocities may intuitively correlate with longer durations or larger spatial extents, as greater energy might contribute to more sustained or expansive event development. Identifying such correlations could provide insights into the underlying mechanisms of these events, supporting predictive modeling under varying atmospheric conditions.

Fig. 5.5 presents these correlations by comparing $|w|$, duration, and extent factor for the observed varicose-mode events. Two linear regression analyses are shown: one for all data points and another specifically for events with $|w| \geq 15\,\mathrm{m/s}$. Panel a) shows the relationship between w and duration. The regression line for this full dataset yields an R^2 value of 0.01, indicating a minimal linear correlation between w and duration across all observed events. Panel b) presents the relationship between w and extent factor. The regression line for all data points in this case has an R^2 value of 0.04, suggesting a very weak linear relationship between w and extent factor. Panel c) depicts the relationship between duration and extent factor. The regression for the full dataset results in an R^2 value of 0.00, indicating no meaningful linear correlation between duration and extent factor in the observed events. Overall, the regression analyses for the full dataset show low R^2 values across all panels, suggesting minimal or no linear correlation between w, duration, and extent factor for all varicose-mode events.

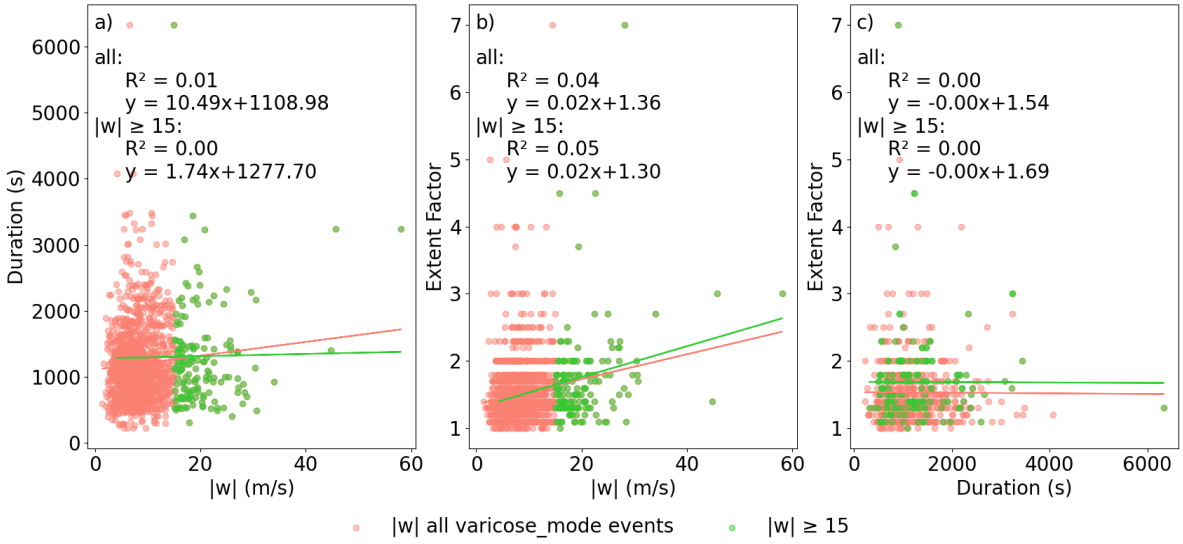


Figure 5.5: Correlation between the absolute maximum vertical velocities and the duration of the varicose-mode events (a), and their extent factor (b), along with the correlation between event duration and extent factor (c). Each dot represents an individual varicose-mode event, with green dots indicating events where |w| exceeded 15 m/s. The salmon-colored line denotes the linear regression for all varicose-mode events, while the green lines represent the linear regression specific to events with $|w| \geq 15$ m/s.

5.6 High-Velocity Varicose-Mode Events

The range of vertical velocities observed in varicose-mode events is quite broad, with high-velocity events ($|w| \geq 15\,\mathrm{m/s}$) making up about 17% of the total events recorded. Previous figures not only show the distribution of all varicose-mode events over different time scales (year, month, or day), as well as providing information on their duration, vertical extent, and vertical extent change, but they also show the high-velocity events. They are visually emphasized in the figures with more vibrant colors and thicker bar outlines.

High-velocity varicose-mode events were observed annually and could occur in any month of the PMSE season, except May, and at any time of day except 18:00 UT. These events were found as isolated occurrences, in pairs, or within groups of multiple events. Specifically, 65 events were single occurrences, representing about 9% of all single events. In pairs, high-velocity events accounted for roughly 20%, and in groups for about 47%. With increasing event grouping—from single occurrences to pairs and larger groups—the absolute number of events in each category decreases, whereas the relative proportion of high-velocity events within each category increases.

On average, these significant events last around 22 ± 13 minutes, reach a maximum vertical extent of approximately $6.5 \pm 2\,\mathrm{km}$, and exhibit a vertical extent change factor of about 1.7 ± 0.7.

The data also shows that updrafts tend to have more instances of velocities above $15\,\mathrm{m/s}$ than downdrafts (42 vs. 39). Although the numbers are close, the range of high-velocity events is broader for updrafts, particularly for velocities exceeding $20\,\mathrm{m/s}$. In this category, there are 7 downdrafts and 17 updrafts.

For high-velocity events ($|w| \geq 15\,\mathrm{m/s}$), linear regression analysis reveals no obvious correlation between absolute velocity and both duration and extent factor. Specifically, the R^2 values for $|w|$ versus duration and $|w|$ versus extent factor are 0.00 and 0.05, respectively, indicating that even these higher-energy events do not display a significant linear relationship with these parameters. Compared to the full dataset, where similarly low correlations were observed, the high-velocity subset shows that absolute velocity alone does not strongly influence the duration or spatial extent of varicose-mode events.

5.7 Consideration of Horizontal Background Winds

In the case studies following in chapter 6.25, the background mean wind conditions play an important role. To effectively interpret the relationship between mean wind and varicose-mode events in these specific cases, a statistical overview of the mean wind conditions is valuable – particularly the wind direction within the 80 to 90 km altitude range, where the events typically form. The wind data for this study is obtained from the PRR at Saura. As the 2023 cases are also included in these studies (extending beyond the 2015 to 2021 period), this analysis incorporates data from years after 2021, thus covering a broader set of events compared to previous considerations. Fig. 5.6 illustrates the distribution of wind directions at the upper (green) and lower (orange) boundaries of the PMSE layer, specifically at 82 km and 88 km, based on wind profiles recorded near the time of each event in the entire dataset (one profile per event). These two altitudes were chosen as key reference points because directional changes between

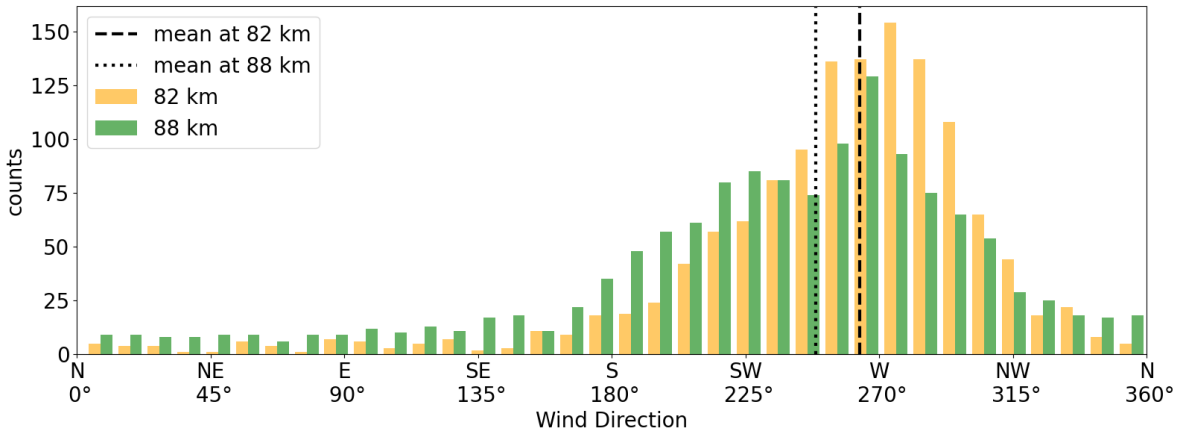


Figure 5.6: Distribution of wind directions at 82 (green) and 88 km (orange) altitude during all varicose-mode cases between 2018 and 2023.

the upper and lower regions of the PMSE layer can produce wind shear, potentially forming a guiding channel. This phenomenon is further discussed in 5.8.2 and 6.25. As shown in Fig. 5.6, there is a pronounced peak around 270° from N for the upper boundary. In most cases, the wind at approximately 82 km is directed toward the W, NW, or SW, while winds towards the opposite directions (E, NE, and SE) are seldomly observed. The general distribution is also observed at around 88 km altitude, although a pronounced peak as it is observed for the lower part is not observed. The circular means[1] are represented by the dashed and dotted black vertical lines for the lower and upper part, respectively, which are approximately 263° (W) and 249° (West-South-West, WSW). About 72% of the wind directions at around 82 km fall within the range from 225° to 315°. In the upper part this range contains approximately 54% of the measured directions.

[1]The circular mean accounts for the circular nature of directional data, treating 0° and 360° as equivalent:$\bar{\theta} = \tan^{-1}\left(\frac{\sum_{i=1}^{n}\sin(\theta_i)}{\sum_{i=1}^{n}\cos(\theta_i)}\right)$, with θ_i as the individual angles in radians and n is the total number of angles.

5.8 Summary and Discussion: Varicose-Mode Event Statistics

Driven by the occurrence of an extreme event marked by high vertical velocities within a varicose structure, this study embarked on a thorough manual search for similar events. These events are relatively rare, as confirmed by a manual search of PMSE data from 2015 to 2021. They exhibit strong similarities to mesospheric bores, with a leading wave crest often accompanied by trailing waves, though some events appear as solitary waves. Propagation is likely facilitated by channel-like structures formed through temperature inversions or wind shear (e.g. Dewan and Picard, 2001; Ramachandran et al., 2023). An average event rate of 33 per 100 days was observed, with notable variability across years, including a peak in 2018 and a decline in 2020. Seasonal and diurnal patterns were evident, with most events occurring in June and July, peaking between 12:00 and 16:00 UT, and showing a minimum between 18:00 and 20:00 UT. Both isolated and grouped events were identified, with grouped events often displaying trailing waves of similar amplitude to the leading crest. The events had an average duration of 20 minutes and a vertical extent of 8 ± 2 km. Notably, no correlation was found between vertical velocity and other parameters such as duration or vertical extent.

5.8.1 Observations and Implications

Driven by the occurrence of an extreme event marked by high vertical velocities within a varicose structure, this study embarked on a thorough manual search for similar events. The results confirm predictions made by DNS models, which suggested that such events are infrequent. This investigation spans the PMSE months from 2015 to 2021, highlighting the significance of identifying localized, temporally confined structures in the varicose mode.

5.8.2 Varicose-Mode Events and Atmospheric Instabilities

The varicose structures observed in this study bear a strong resemblance to mesospheric bores, a concept first introduced by Dewan and Picard (1998). These internal mesospheric undular bores are characterized by a sharp wave crest followed by smaller trailing waves, affecting different atmospheric layers in varying ways. For instance, such events were noted to increase the airglow brightness of the OH layer at 85 km and the Na layer at 90 km, while reducing brightness in the O and OI layers at 94 km and 96 km, respectively (Taylor et al., 1995). Dewan et al. likened these mesospheric phenomena to undular tidal bores in rivers and "morning-glory" clouds in the troposphere, proposing that such bores require a channel-like structure, possibly formed by a temperature inversion layer or wind shear.
This hypothesis of a ducted propagation was later supported by She et al. (2004), who observed temperature inversion layers coinciding with mesospheric undular bore events over Fort Collins, Colorado. Further research by Hozumi et al. (2019) revealed that most mesospheric bores between 55°N and 55°S occurred within such inversion layers. However, unlike Dewan and Picard (1998)'s original findings, not all observations in this study exhibited the trailing waves typically associated with bores. Instead, many events

appeared as solitary wave crests unattached to trailing waves, which sometimes emerge from bores (Koch et al., 2008).
The varicose-mode events documented here can be described as solitary waves with near-simultaneous upward and downward movements (Lighthill, 1979).

5.8.3 Statistical Analysis of Event Occurrence

The analysis of over 700 varicose structures in the MLT region revealed an occurrence rate of approximately 33 out of every 100 days. While no clear pattern emerged across the years, the total number of events fluctuated, with a noticeable increase in 2018 and a decrease in 2020. This variation may be partially explained by differences in the dataset's size across the years, but further investigation is required to understand the underlying reasons fully. Monthly contributions to the total number of events also varied, indicating the influence of temporal factors on varicose-mode event occurrence.
Events were most concentrated in the middle of the PMSE season, particularly in June and July, which aligns with previous studies that identified these months as peak periods for PMSE activity. The study normalized event occurrences by considering the number of 20-minute PMSE windows to account for diurnal and seasonal variations. This normalization ensures that event counts per PMSE season or month are comparable and accurate.
The diurnal variation of varicose-mode events, peaking between 12:00 and 16:00 UT and showing a minimum between 18:00 and 20:00 UT, mirrors the known diurnal variability of PMSE over Andøya (e.g. Hoffmann et al., 1999; Latteck et al., 2021). This significant variability suggests a strong link between varicose-mode events and the factors influencing PMSE patterns, possibly indicating that both phenomena share common underlying mechanisms.
If these events are indeed mesospheric bores, their occurrence rates can be compared to those observed by Hozumi et al. (2019), who examined mesospheric bores using airglow imagers on the International Space Station. While it is important to note the absence of direct evidence confirming varicose structures as bores, and the limitations of satellite observations outside MAARSY's range, this comparison suggests that similar structures might frequently occur in mid-latitudes and equatorial regions, particularly during equinox seasons. Diurnal variations, as noted by Hozumi et al. (2019), showed a stronger daytime dependence at mid-latitudes than near the equator.
The discovery of events occurring in pairs or groups, initially unexpected, highlights the potential conditioning and influence one event might have on another when occurring in close succession. The differences in behavior between isolated events and those in pairs or groups raise intriguing questions about memory effects and the origins of these events. Group events tend to follow a pattern of a leading wave crest with trailing waves, resembling bores, although the amplitudes of these trailing waves are nearly equivalent to the leading wave, contrary to earlier reports (e.g. Taylor et al., 1995; Dewan and Picard, 1998). The statistical significance of these observations remains to be fully determined.
Interestingly, the occurrence patterns of high-velocity varicose-mode events ($|w| \geq 15\,\mathrm{m/s}$) align with general varicose events, but there is no direct correlation between the total number of events and the number of high-velocity events. For instance, in 2021, more events were recorded in July than in June, yet June had significantly more high-velocity events. This lack of correlation is also evident when considering the relative number of

varicose-mode events per PMSE window, where higher event counts do not necessarily correspond to more high-velocity occurrences. The diurnal variation of high-velocity events is less pronounced, with a notable absence between 18:00 and 20:00 UT.

5.8.4 Event Duration and Vertical Characteristics

The relatively short-lived nature of varicose-mode events, with an average duration of 20 minutes, justifies the selection of a 20-minute window for counting PMSE occurrences. This duration is slightly shorter than the event described by Chau et al. (2021), which lasted 25-30 minutes. The narrow radar illumination area in the mesosphere limits the observed duration of these structures, as they only pass through the radar's FOV briefly, depending on their speed of phase propagation.

Mesospheric bores, on the other hand, can last several hours, as seen in simultaneous airglow and lidar observations (e.g. Smith et al., 2017; Fritts et al., 2020). The small observation volume in the mesosphere complicates determining exact lifetimes and understanding the production and dissipation mechanisms of varicose-mode events.

High-velocity events exhibit a similar average duration of around 22 ± 13 minutes compared to general varicose events, though with greater variability. This suggests that further investigation is needed to explore the potential relationship between maximum vertical velocity and event duration.

The maximum vertical extent of the PMSE layer in varicose-mode events, averaging 8 ± 2 km, is smaller than the 12 km observed in the extreme event reported by Chau et al. (2021). Similarly, the expansion factor of the PMSE layer due to the varicose structure, with a mean value of 1.5, is significantly smaller than the factor of 3 observed in the extreme event. Notably, high-velocity events have a slightly smaller expansion factor (1.7 ± 0.7) than general varicose-mode events, while the maximum vertical extent for high-velocity events is about 20% less than that for all events.

The factors influencing the expansion in varicose-mode events are not fully understood, but it is believed that vertical velocities, horizontal wind properties, and temperature profiles play a role in determining the propagation duct in which these events are likely to travel (e.g. Ramachandran et al., 2023).

Most bore observations are conducted using airglow, lidar, or satellites, which provide a two-dimensional view. In such cases, only the initial height h_0 is typically known, while the disturbed height h_1 remains unknown. Bore amplitude is often calculated using a normalized bore amplitude, or bore strength, β, which serves as a measure to differentiate between turbulent and undular bores. Radar-based bore observations, however, allow for the direct determination of $2h_1$, eliminating the need for assumptions. In this study, the average β for all observed varicose-mode events was 0.53, with high-velocity events showing a slightly higher average β of 0.68 (see Fig. 5.7). This suggests that if these structures are indeed bores, they may exhibit a turbulent nature with potential for wave breaking. However, an alternative theory by She et al. (2004) proposes that for internal bores, a $\beta > 0.3$ can still sustain an undular bore configuration, as energy might leak out of the duct region. Radar observations are limited to the radar's FOV, making it uncertain whether these observed structures dissipate outside the observed area. Comparisons with findings by Fritts et al. (2020), who observed a similar β (0.7) in their study of bore observations using an all-sky imager and lidar, suggest that while such a value indicates a turbulent solitary wave, undular bores were observed, possibly

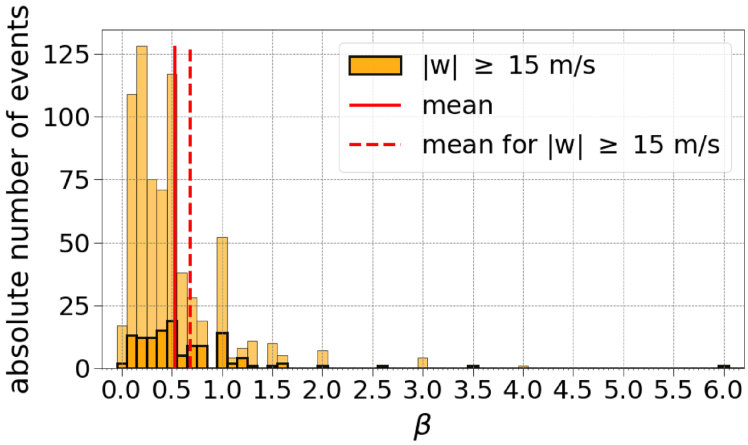


Figure 5.7: Normalized bore amplitudes of the varicose-mode events in general. The red solid (dashed) line represents the mean of all events (events with $|w| \geq 15\,m/s$).

due to the absence of a thermal duct supporting soliton development. This underscores the importance of investigating ducting conditions in future studies of varicose-mode events.

5.8.5 Vertical Velocities

Accurately measuring vertical velocities using radar is challenging due to factors that introduce uncertainty. Systematic errors, such as variations in beam width and beam orientation inaccuracies, contribute to this uncertainty. To minimize these effects, MAARSY has been carefully calibrated for transmission and reception, with pointing accuracy and nominal beam width verified by various experiments, as described by Renkwitz et al. (2017). While it is possible to determine vertical velocities by analyzing the Doppler shift of the received signal when the scatterer is directly above the vertically aligned radar beam, limitations must be considered. Scatterers in the atmosphere are randomly distributed, and even with MAARSY's narrow beam width, there is a chance that scatterers will be detected that are not perfectly over the center of the radar location. This means that the measured radial wind will also include a horizontal wind component, depending on the mean angle of arrival and the magnitude and direction of the horizontal wind. Assuming most scatterers are captured within the main beam, and zenith angles of arrival fall predominantly within the radar beam's width, typical horizontal wind speeds below 100 m/s suggest a maximum potential difference of approximately $\pm 5\,m/s$ between radial and vertical velocities. Therefore, it is reasonable to infer that the velocities observed in this study are primarily representative of the vertical component, especially for velocities exceeding a few meters per second.
The identification of events in this study relied on visual assessment, which has inherent limitations. The choice of the color bar used in visualizations determined the detectability of varicose-mode events. A color bar ranging from -15 to 15 m/s was chosen to focus on events exceeding the 3σ threshold, although this might have limited the identification of lower-velocity events, which was deemed unnecessary for this study's objectives.
The mean vertical velocity of varicose-mode events observed in this study, approximately 10 m/s, is already twice the expected maximum vertical velocity in the MLT, which was

anticipated to be around ±5 m/s. Considering the extreme event reported by Chau et al. (2021) and earlier model predictions, it is unsurprising to find instances where $|w| \geq 15$ m/s.
These high velocities exceed six times the standard deviation of roughly 2.5 m/s (see black dashed lines in Fig. 5.4). It is worth noting that in Chau et al. (2021)'s study, vertical velocities were classified as "extreme" when they exceeded five times the standard deviation, so the high-velocity events in this study can also be considered "extreme".
Furthermore, the occurrence of winds surpassing a threshold of ±15 m/s is similar between updrafts and downdrafts. However, downdrafts exhibit a narrower range of velocities compared to updrafts, likely due to the larger number of updrafts with velocities exceeding 20 m/s. The general asymmetry in vertical velocities observed in this study, with more downward-directed velocities than upward, is consistent with previous findings. The gravitational sedimentation of ice particles forming PMSE, as described by Gudadze et al. (2019), contributes to this asymmetry. The use of PMSE as tracers in the vertical radar beam may introduce a bias toward downward-directed vertical velocities, as discussed by Hoppe and Fritts (1995) using the EISCAT VHF radar. They suggested that gravity waves could cause a tendency to underestimate upward motion when using VHF radars because of a negative relationship between vertical motion caused by gravity waves and the radar's ability to detect them. Turbulence generated by upward-moving gravity waves can disrupt the radar's ability to measure them accurately. Additionally, downdrafts that reach regions with higher temperatures quickly lead to the melting of ice particles and the subsequent disappearance of PMSE, once again removing the tracer necessary to determine vertical velocities. Therefore, the observed asymmetries may not reflect true atmospheric conditions but rather result from these influencing factors (e.g. Hoppe and Fritts, 1995; Gudadze et al., 2019).

5.8.6 Connection between Event Parameters

The investigation of possible correlations between different parameters that characterize varicose-mode events showed minimal linear correlation between absolute velocity ($|w|$), duration, and extent factor, as indicated by consistently low R^2 values for both the full dataset and the subset of high-velocity events ($|w| \geq 15$ m/s). This analysis aimed to determine whether higher velocities in varicose-mode events would correlate with either longer durations or greater vertical extents. By performing linear regressions for all data and then for a subset of high-velocity events, the hypothesis that increased velocity might sustain or expand these events was tested. The results imply that the vertical velocity does not predict or determine the duration or the factor of the vertical extension of varicose-mode events. This lack of correlation holds for both the full dataset and the high-velocity subset, suggesting that even higher velocities do not necessarily translate to longer-lasting or larger-scale events. The findings indicate that simple linear relationships may not capture the complexities underlying the dynamics of varicose-mode events. Making again the connection to bores or solitary waves – GWs trapped in a duct –, this finding aligns with the findings by e.g. Fritts and Alexander (2003). Studies on GWs have shown that their properties are influenced by non-linear interactions and multi-dimensional processes that go beyond single-variable relationships (e.g. Vadas and Fritts, 2005). Studies on GWs have shown that their properties are shaped by nonlinear interactions and multi-dimensional processes that defy straightforward, single-variable

correlations (e.g. Vadas and Fritts, 2005). In analogy, it is plausible that varicose-mode events are influenced by a combination of factors such as atmospheric stability, wind shear, and thermodynamic conditions, which govern their structure and evolution.
The absence of clear relationships between key observables is thus not unexpected and has previously been reported for similar wave phenomena (Seyler, 2005a). While studies such as Dewan and Picard (2001) and Ramachandran et al. (2023) suggest potential links between bore speed and channel thickness, these remain conditional and context-dependent.

6 Multi-Instrument Studies of Selected Varicose-Mode Events

Building on the initial identification of over 700 varicose-mode events, the following sections focus on four representative cases to examine their distinct features. This chapter of the thesis aims to provide an initial analysis of the background conditions present during these four cases as a first step toward understanding their occurrence.
The varicose-mode events selected for this study occurred on 2 June 2015, 3 July 2018, 1 August 2018, and 1 July 2023.
To investigate these events and their associated background conditions, data from several instruments located around the MAARSY site were utilized where available and analyzed using different signal processing techniques and approaches. The instruments relevant to the selected cases are listed in Tab. 6.1.

Table 6.1: Summary of the instrument data available for each case included in the case study.

Instrument Data Availability						
Instrument / Case	**MAARSY Multi-beam**	**MAARSY Imaging**	**MMARIA Norway**	**Saura PRR**	**Saura MUSIC**	**SABER Temper-atures**
02.06.2015		x	x	x		x
03.07.2018	x		x	x		
01.08.2018	x		x			
01.07.2023	x		x	x	x	

In the following, results from each instrument available for the respective case study are presented, discussed, and compared across cases. Case I is used to describe the analysis methods and the interpretation of results in detail, serving as a reference for all subsequent cases where data from the same instrument are available. In later cases, only deviations from this approach are highlighted. Whenever data from an instrument are shown for the first time, the corresponding method is introduced.

6.1 Case I: 02.06.2015

The first case, observed on June 2, 2015, spans an altitude range from approximately 80 to 87 km. This case is notable for the sequential occurrence of three varicose-mode structures, each separated by around one hour (see Fig. 6.1). Although multiple consecutive events have been observed in other instances, they are not part of the present case studies. Here, the initial event begins at 10:30 UT and lasts for 24 minutes, followed by a second event at 11:30 UT lasting 14 minutes, and a third event at approximately 12:25 UT, which persists for around 18 minutes. These structures collectively expand the PMSE layer to 8-9 km, indicating a widening factor between 1.4 and 1.6. This case

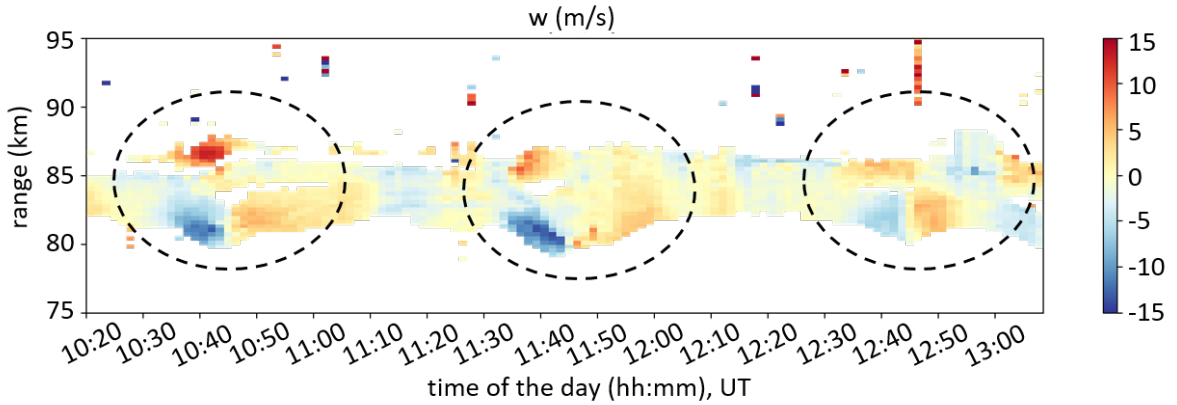


Figure 6.1: Range-time-radial velocity representation of case I, observed on June 2, 2015, between 10:30 UT and 12:30 UT. The events are highlighted by the dashed ellipses.

is distinguished by the successive varicose-mode structures, where velocities, though less intense than in subsequent cases, still reach more than twice the maximum values typically observed in the MLT. The peak updraft and downdraft velocities for these events are as follows: 12 and 13 m/s, 10 and 14 m/s, and 6 and 6 m/s. In the first two events, the initial phase of the varicose structure shows higher vertical velocities compared to the later phase. However, in the third event, the updraft during the later phase is equally distinct, showing velocity values similar to those of the initial phase. The spectral width remains minimal, with slight increases observed in the up- and downdrafts, each lasting only a few minutes (see Fig. A0.10). This is particularly notable in the lower portions of the drafts during the second event. The occurrence of multiple varicose-mode structures within a three-hour window implies sustained favorable conditions over this period. The low spectral width values indicate minimal turbulence during these events; however, the small increases, primarily following the downdraft in the second event, suggest the potential onset of a transient turbulent regime induced by the draft.
The following sections will analyze background horizontal wind conditions, mean temperatures, radial velocity spectra from the Saura PRR, and insights from radar imaging.

6.1.1 MMARIA Norway Mean Winds

The mean wind data used in this study were obtained from the MMARIA system operated by the IAP in Norway. These measurements have a temporal resolution of 30 min and, as they represent averages over an area of several hundred kilometers, provide less detailed temporal information than the higher-resolution vertical wind observations from MAARSY. To characterize the mean background wind conditions at the onset of each event, the profile closest to the event start time was selected. Figs. 6.2–6.4 show the corresponding zonal and meridional wind profiles as solid orange and green lines in panel (a), respectively. From these components, the wind magnitude (panel b), wind direction measured clockwise from N (panel c), wind shear magnitude (panel d; vertical rate of change of wind velocity, in $\mathrm{ms}^{-1}\,\mathrm{km}^{-1}$), and shear direction measured clockwise from N (panel e; direction of the vertical shear vector, i.e. the direction toward which

the horizontal wind vector changes with increasing altitude) were derived and are shown as solid black profiles in the respective panels; the detailed methodology is described in the Appendix Section A0.3.1. To provide context, profiles at 1.5 h intervals before and after each event are included for all parameters as dashed and dotted lines, respectively, allowing short-term variability immediately surrounding the event to be assessed relative to the profile closest to the event onset. This methodology is applied consistently across all case studies and is therefore not repeated in the following. Across all three events, the vertical structure is strongly height-dependent, but the character changes markedly from event 1 to events 2 and 3:

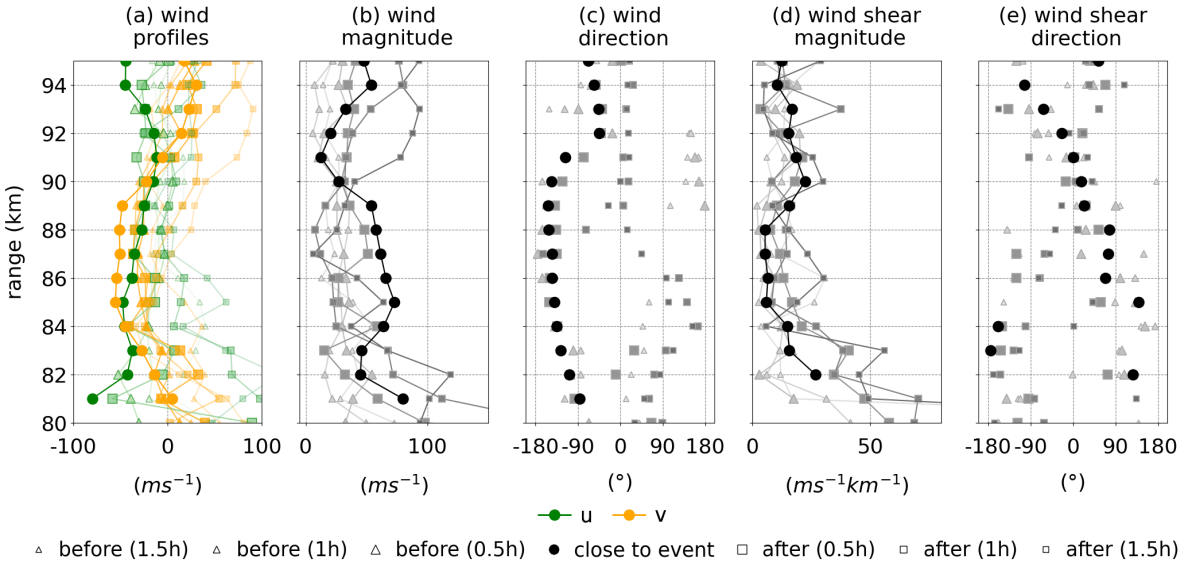


Figure 6.2: Mean wind parameters around the first event on June 2, 2015, at 10:30 UT, from horizontal wind components u (green) and v (orange) in panel a. Panels b–e show wind magnitude, direction (0° = North), shear, and shear direction. Strongest colors in panel a and black in panels b–e indicate measurements closest to the event; different symbols and lighter shades of colors indicate ±1.5 hours.

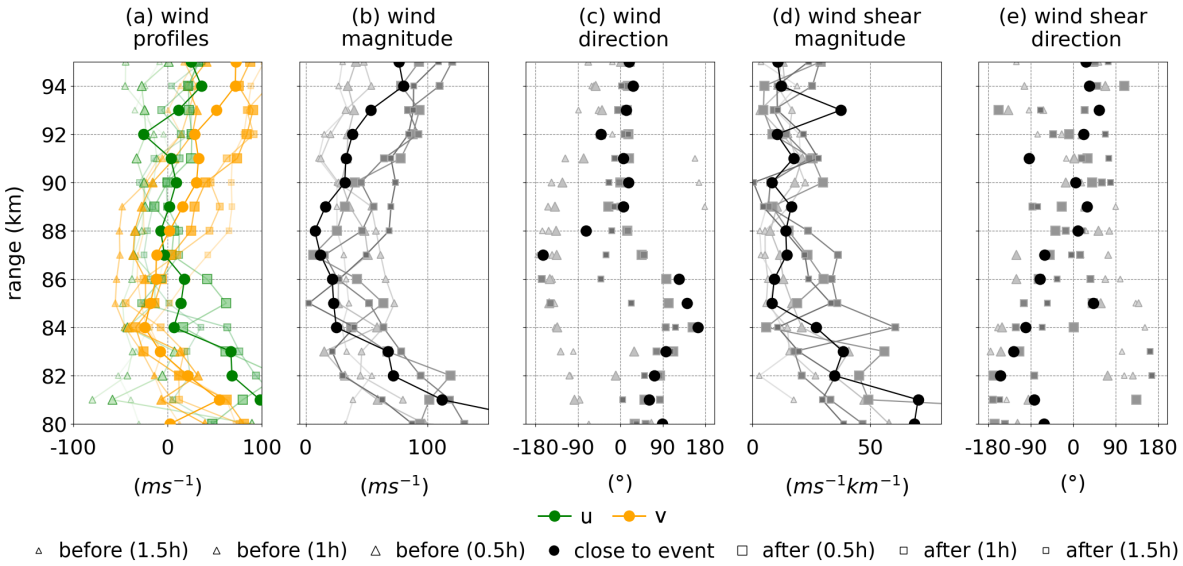


Figure 6.3: The same as Fig. 6.2 but for the second event of this case at around 11:30 UT.

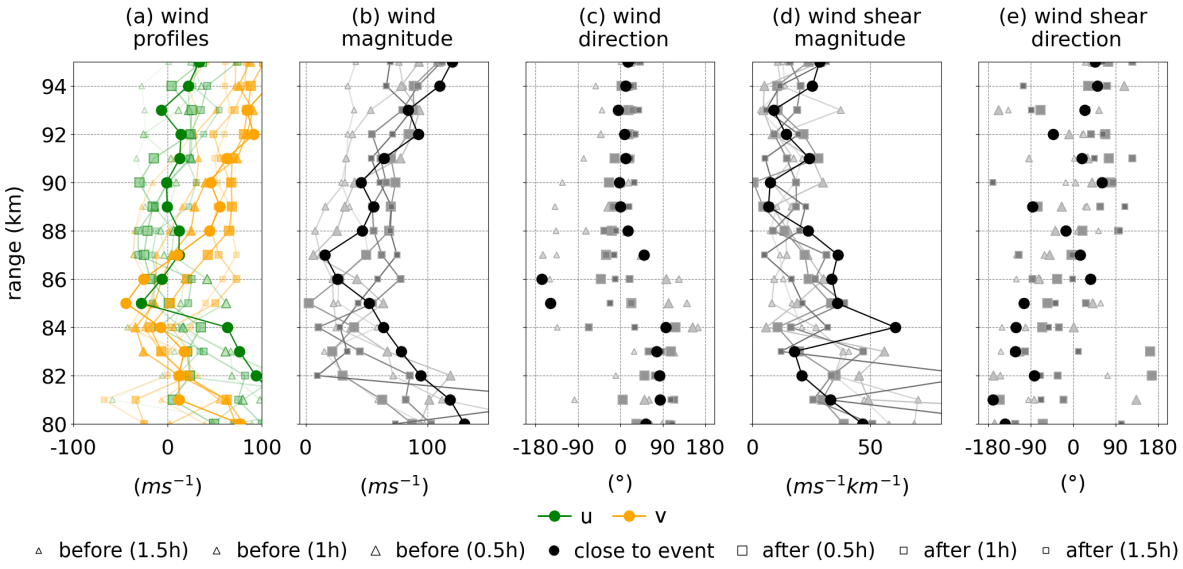


Figure 6.4: The same as Fig. 6.2 but for the third event of this case at around 12:30 UT.

During event 1 (Fig. 6.2), the PMSE layer extends from 82–87 km and the wind-speed magnitude (panel b) reaches a maximum of about 75 ms^{-1} within the PMSE interior, while speeds are lower at the PMSE boundaries and increase again outside the layer. The wind direction (panel c) turns gradually from West (W) at the PMSE base toward Southwest (SW) at the top, indicating a comparatively smooth vertical rotation. Consistent with this behaviour, the shear magnitude (panel d) peaks at about 25 $ms^{-1}\,km^{-1}$, with one maximum near the PMSE base (≈82 km) and a second maximum above the PMSE layer (≈90 km), while the shear direction (panel e) changes from Southeast (SE) to SW with relatively modest height-to-height variability.
Comparing the solid, dashed, and dotted profiles shows noticeable differences between consecutive 30-minute profiles. Following event 1, the wind direction varies more strongly with altitude than at the event time. For event 1, the shear magnitudes in the dashed and dotted profiles are higher than in the solid profile, and the shear direction shows stronger altitude-dependent variability in the dashed and dotted profiles than in the solid profile. event 2 occurs within about one hour of event 1, and one dotted profile shown for Event 1 corresponds to the conditions near the onset of event 2; in this profile, wind magnitudes are lower than at the event 1 time, wind direction varies more strongly with altitude, and shear is stronger and more altitude-dependent.

Event 2 (Fig. 6.3) occurs in a slightly thinner PMSE layer (82–86 km) and is characterized by markedly stronger winds and shear compared to event 1. In panel (b), wind magnitudes increase to about 100–110 ms^{-1}, but in contrast to event 1 these maxima occur predominantly outside the PMSE altitude range, whereas a relative minimum is found within the layer. At the same time, the wind direction (panel c) varies much more strongly with altitude than during the first event, with the most pronounced change confined to the PMSE region (E to SE, then to SW, W, and finally N with increasing altitude). This enhanced directional variability is accompanied by a substantial strengthening of the shear (panel d): the shear magnitude reaches slightly above 60 $ms^{-1}\,km^{-1}$ below the PMSE layer and shows an additional local maximum of around 54 $ms^{-1}\,km^{-1}$ near the PMSE base, i.e. at comparable reference altitudes where the first event exhib-

ited only moderate shear. Correspondingly, the shear direction (panel e) varies strongly within the PMSE region from W over N to E, mirroring the abrupt turning of the mean wind and contrasting with the smoother SE–SW change seen in event 1. In the 1.5 hours following event 2, wind magnitude and shear magnitudes increase in the dotted profile relative to the solid profile.

Event 3 (Fig. 6.4) takes place in an even narrower PMSE layer (83–85 km) and, relative to event 2, maintains similarly enhanced shear while exhibiting even higher wind-speed maxima outside the PMSE region. Wind speeds (panel b) reach up to roughly 120 ms^{-1} outside the layer, again accompanied by a minimum between the high-speed regions, reinforcing the pattern introduced in the second event that the largest wind-speed magnitudes are not centered within the PMSE altitude range. The wind direction (panel c) continues to show strong vertical variability (E over S to N), remaining considerably more variable than in the first and broadly comparable in strength to the second event. The shear magnitude (panel d) stays high, reaching about 55–60 $\mathrm{ms}^{-1}\,\mathrm{km}^{-1}$ near 84 km and remaining comparably elevated throughout the PMSE layer where the event is observed; compared to event 2, the shear in this event appears less localized to a single altitude and instead persists across the narrow PMSE interval. In panel (e), the shear direction is strongly variable throughout the altitude profile, consistent with the pronounced turning of the mean wind and reinforcing the similarity between the second and third event, while both differ markedly from the comparatively smooth, moderate-shear conditions during the first event.
Across events 1 to 3, the maximum wind speeds increase from about 75 m/s (event 1) to 100–110 m/s (event 2) and to about 120 m/s (event 3), and the maximum shear magnitudes increase from about 25 m/s/km (event 1) to slightly above 60 m/s/km (Event 2) and to about 55–60 m/s/km (event 3).

While the overall background wind conditions provide critical insights into the broader dynamics influencing the PMSE layer and the large-scale atmospheric state, they do not capture the shorter-period variations that may play a pivotal role in the formation and development of varicose-mode events. To investigate the role of background wind variability in the formation and evolution of such structures, the horizontal wind components were filtered using running means with window lengths of 3, 6, 8, and 10 hours. This residual analysis removes long-period variations and highlights transient deviations from the median background state, offering a more detailed view of the dynamic environment in which these small-scale events occur.
For each case study, two complementary visualizations are used. First, Fig. 6.5 shows altitude–time–velocity plots of the zonal and meridional residuals over a two-hour interval surrounding the event. These plots reveal the vertical structure and temporal evolution of wind fluctuations and enable a direct comparison of both wind components. Second, Fig. 6.6 presents the absolute magnitudes of the residuals at 85 km altitude for the zonal and meridional winds in two separate panels. For each component, residuals obtained using different background mean time windows are shown in varying shades of the respective color, illustrating how the residual amplitudes depend on the choice of filtering window. This format enables a clear assessment of the dominant variability near the height of the PMSE layer. In both plots, the event timing is indicated by green vertical lines.
To provide a broader view of the background variability, a full 10-day residual time series

is shown in the Appendix in Section A0.2.1 in Figs. A0.4 and A0.5. Naturally, in these plots, the duration of the events is shorter than the thickness of the lines used in these long-term plots; the lines are only meant to mark the approximate timing of the events during the 10-day period.

The first example, observed on 2 June 2015, serves as a representative case to illustrate this visualization approach, which is applied consistently across all case studies discussed in the following sections.

On this day, three distinct varicose-mode events occurred within a five-hour window, each exhibiting strong vertical motion and well-defined structural features. The corresponding residual wind analysis (see Fig. 6.5) reveals that the residuals of the meridional component appear slightly larger than those of the zonal component, especially for the 3 h and 8 h background time scales. In both components, enhanced magnitudes are visible near the event times marked by the green vertical lines, with pronounced features near the lower and upper altitude boundaries around 82 km and 97 km. Before the event period, the residuals remain comparatively low throughout the displayed 48-hour win-

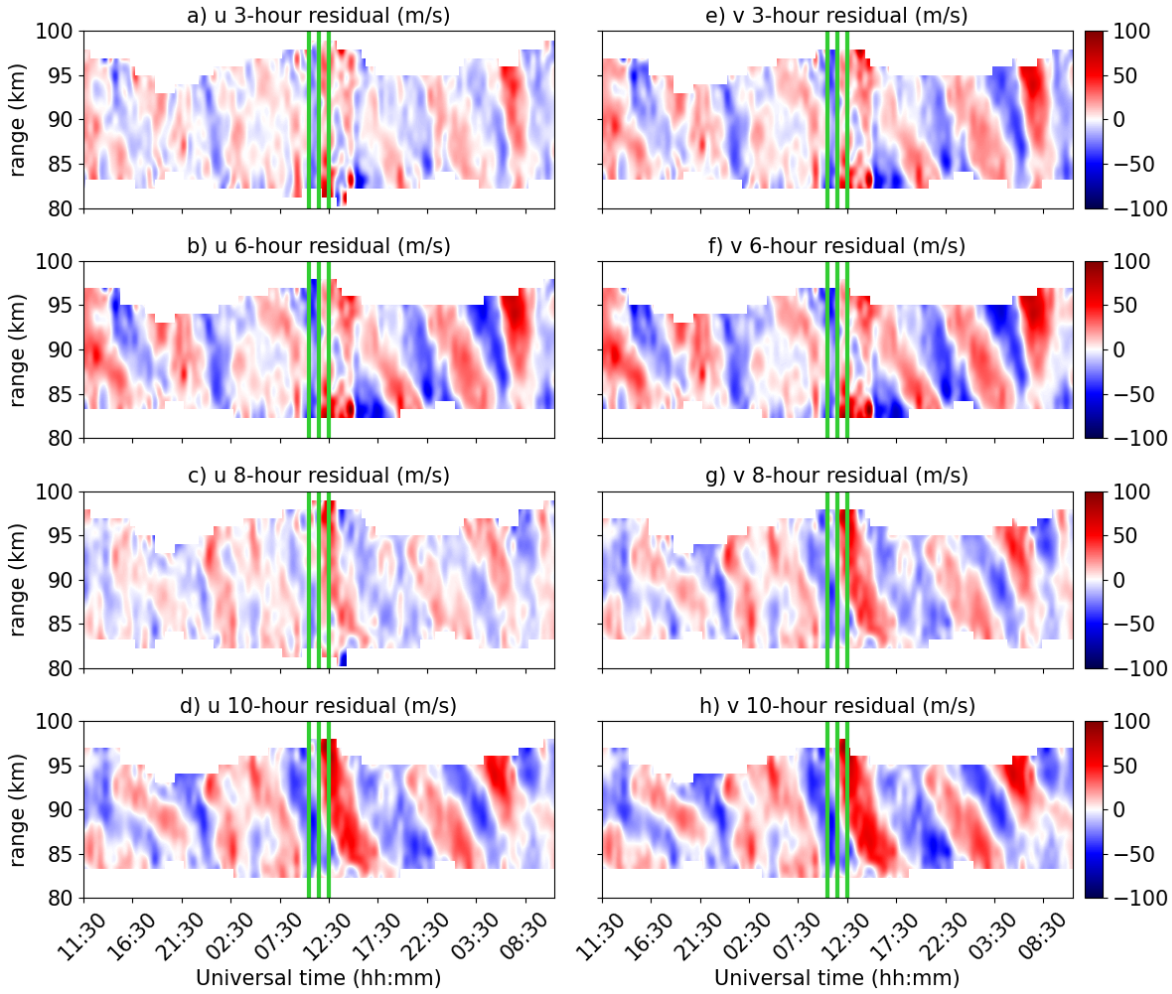


Figure 6.5: Residuals of zonal (left) and meridional (right) wind components from MMARIA Norway, after removing a running mean over 3, 6, 8, and 10 hours, for 48 hours around the three events of this case study (green vertical lines).

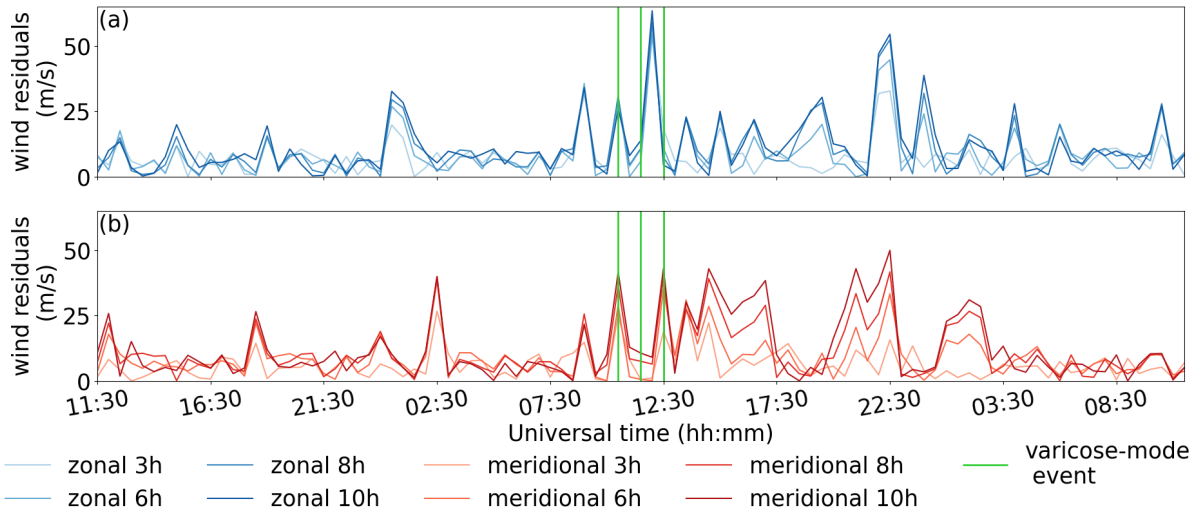


Figure 6.6: Absolute magnitudes of the zonal (a) and meridional (b) wind components at 85 km altitude, measured by MMARIA Norway over the course of 48 hours around the events (green vertical lines).

dow. These patterns are also visible in the time series of absolute residual magnitudes at 85 km (see Fig. 6.6). The meridional component generally shows higher values than the zonal component, particularly after 07:30 UT on the day before the events. For the meridional residuals, local maxima coincide with the first and third events, while in the zonal component, only the first event aligns with a distinct peak. The other two events occur close to broader increases in residual magnitude.
Considering a longer time period of 10 days (see Figs. A0.4 and A0.5 in section A0.2.1), enhanced magnitudes in the background wind components appear frequently, with even more pronounced peaks occurring outside the event timeframe.

6.1.2 Observed Saura Dynamics

To complement the insights gained from the residual wind and radial velocity measurements with MAARSY, additional diagnostics from the Saura PRR (see section 3.11) were analyzed. Specifically, radial velocity and spectral width (Fig. 6.7) were examined, along with signal strength (see section A0.9) to investigate whether these parameters contain signatures of varicose-mode events, reflect conducive background conditions, or indicate turbulence or shear-induced broadening associated with the events.
The analysis focuses first on spectral width, as this parameter serves as a crucial filter to identify dynamically active regions. Radial velocity on its own is not sufficient for detecting event signatures, as it naturally varies across time and space. In contrast, localized enhancements in spectral width can indicate turbulence, shear layers, or instability regions, making them useful for identifying where meaningful changes in radial velocity may correspond to physical processes rather than background variability. Only when both spectral width and radial velocity show coincident features is a link to varicose-mode events considered plausible. Only the NE, SE, and SW beams are shown here, as they exhibit the clearest visual signatures. The remaining beams and

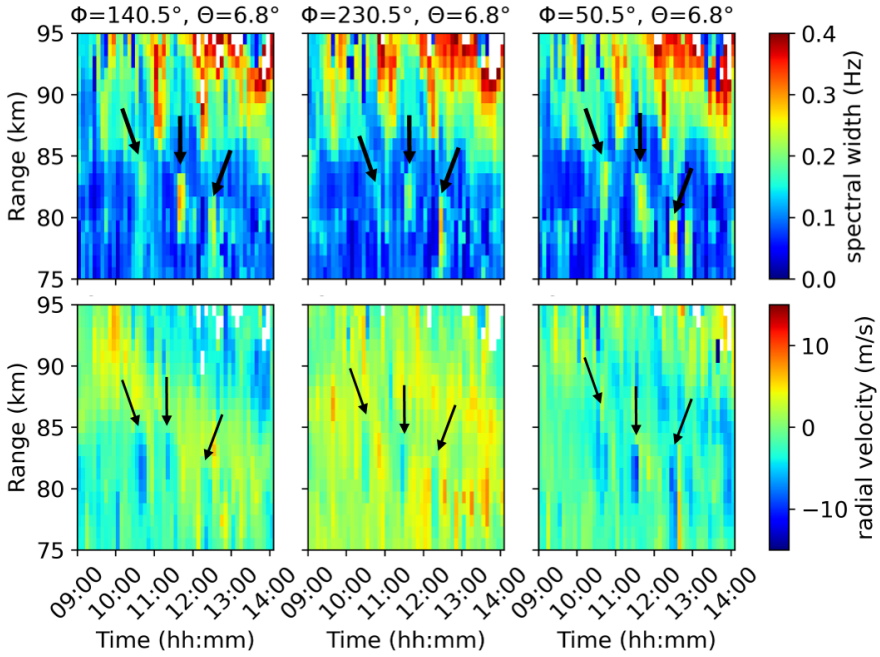


Figure 6.7: Spectral width (top) and radial velocity (bottom) around the time of the event observation with MAARSY. Shown are the NE, SE, and SW beam measurements (left to right). Black arrows point at patterns that coincide with the timing of the three events of Case I.

corresponding signal strength plots are included in the Appendix section A0.2.1. This selection strategy was applied consistently across all case studies involving Saura PRR data. In all three beams, the spectral width displays narrow, localized enhancements between 80 and 85 km in range, marked by black arrows. These bands align with the time frames of the events observed by MAARSY. In addition, the radial velocity plots show abrupt variations – up to and including a change in sign (i.e., to negative values) – within the same altitude range. Since negative radial velocity denotes motion toward the radar, this suggests that Saura PRR captured the downward phase of the varicose-mode structures. This interpretation is consistent with the altitude range of the observed downdrafts in the MAARSY data.
While there is a small difference between range and true altitude, it is negligible here: given the beam inclination angle $\Theta < 7°$, the altitude error remains below 5 km. Interestingly, the range of the spectral width anomalies remains fairly constant across the three events, whereas the altitude of the radial velocity disturbances appears to decrease slightly from the first to the third event. This descent pattern is not evident in the Range-Time-Velocity diagram shown in Fig. 6.1.

6.1.3 MAARSY Imaging

While the range-time plots from MAARSY provide detailed insights into vertical velocities, spectral widths, and intensities, they are inherently constrained to two-dimensional representations of the events. To overcome this limitation, radar imaging is employed. As described in 3.2.2, this technique enables the capture of spatio-temporal information for

events within the radar's illuminated volume. By reconstructing the three-dimensional distribution of vertical velocities and signal strength, radar imaging allows structures to be viewed from multiple perspectives and cross-sectional cuts to be examined in detail, enabling a more comprehensive analysis of the events' spatial development over time. For interpretive clarity, note that the coordinate system is rotated 45° E of N, meaning that the y-axis represents the SE-NW (North-West) axis, while the x-axis represents the SW-NE (North-East) axis. Snapshots at various times for each event, viewed through a cut with a constant y-value (y = 0), are shown in Fig. 6.8. The corresponding snapshots with a constant x-value (x = 0) are shown in Fig. 6.9. Each row represents one of the three events, while columns depict different time steps within a 20-minute window, capturing each event's evolution. In these images, vertical velocities – similar to RTDI plots – are color-coded: blue for downward, red for upward, and green for near-zero velocities, with brightness indicating signal strength. Both figures clearly show the widening of the PMSE layer as the event progresses, contributing to the varicose mode structure. During all three of them, the PMSE layer appears to split into multiple layers, particularly in the first two events, eventually uniting into two layers. The cuts through y = 0 in Fig. 6.8 indicate that the event is spatially localized along the x-axis, spanning roughly 4 to 10 km, while the cuts along x in Fig. 6.9 show an elongation along the entire FOV in the y-direction. This can also be seen by looking at Fig. 6.10. At a given time, the drafts appear only in a few localized regions along the y-axis (a), whereas they cover the entire

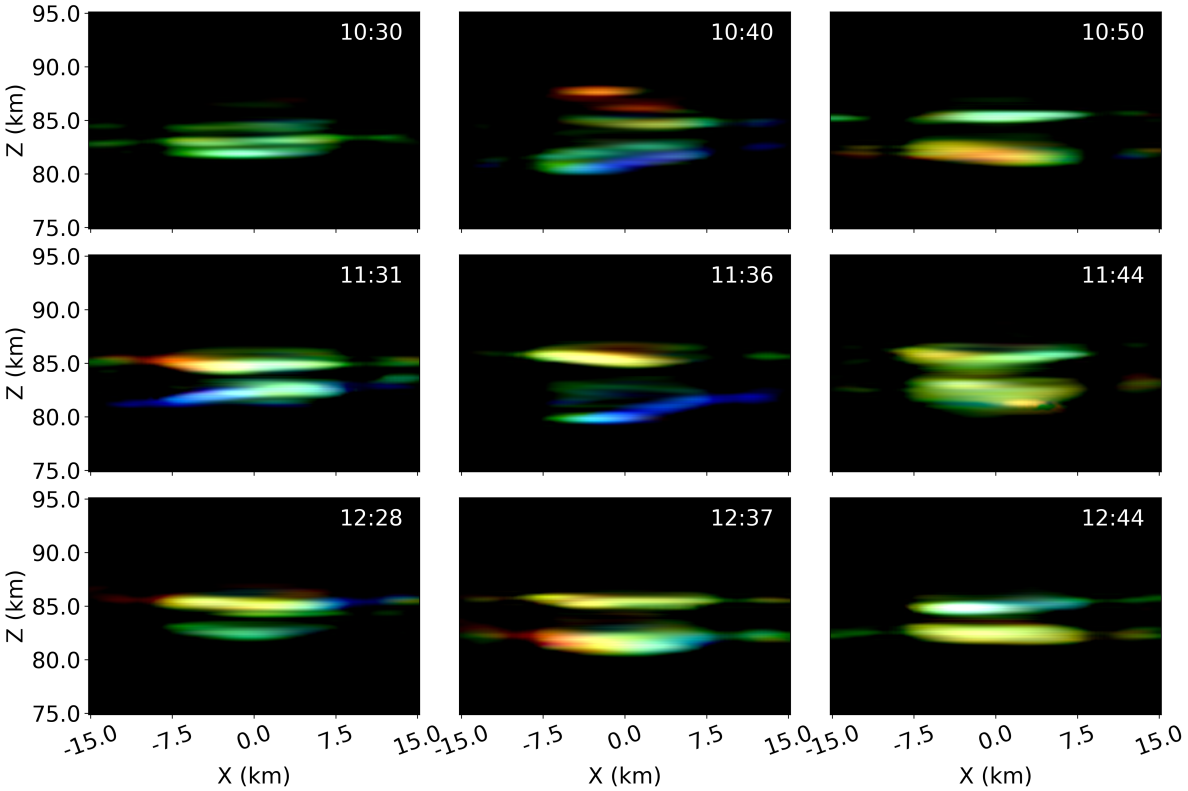


Figure 6.8: Temporal evolution of the three events of this case (first to third row, respectively) from along x-axis and altitude at a fixed point y = 0 from their initial to their final stage. The colors represent the vertical velocity (blue: downward, red: upward, green: no vertical movement), and the strength of the color represents the strength of the received signal.

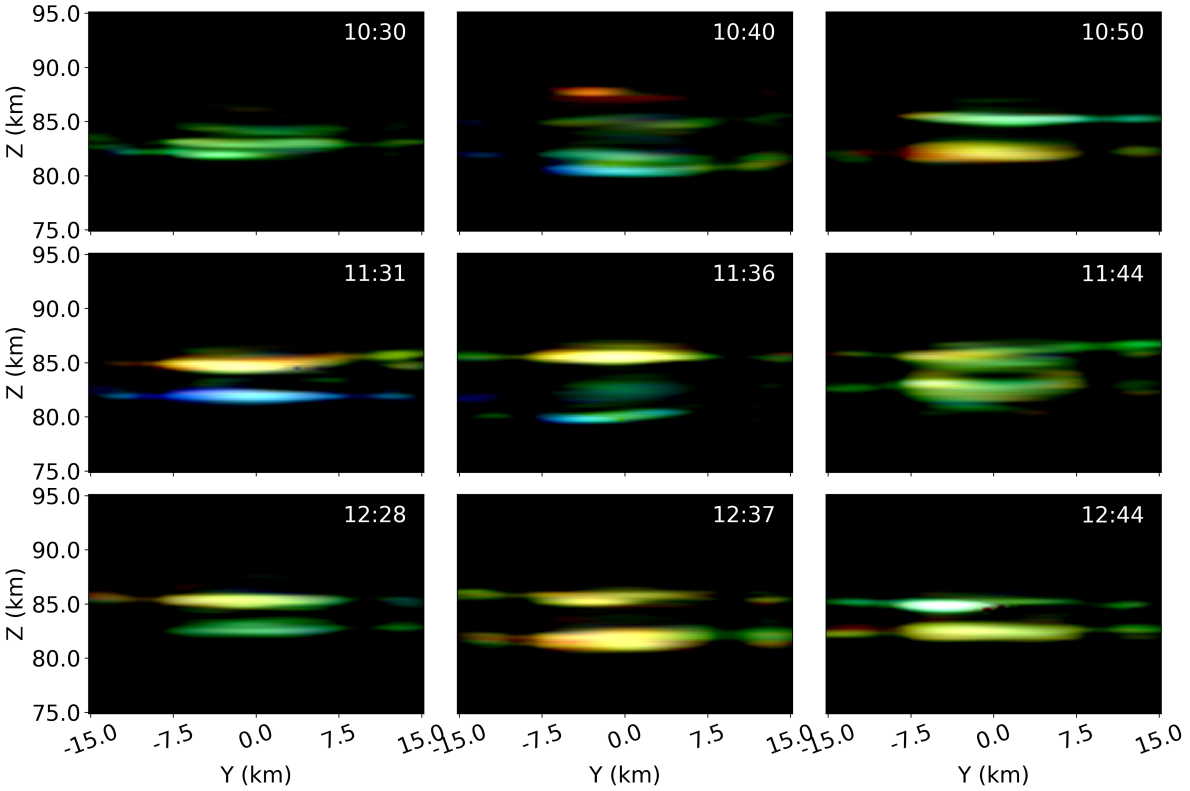


Figure 6.9: Same as Fig. 6.8 but along y-axis and altitude at a fixed point x = 0.

x-axis (b). The two plots contain information on whether the events are moving across the radar FOV.

The progression of the event along the y-axis with time at 81 km altitude, as depicted in Fig. 6.10a), clearly illustrates that the drafts (again shown in red and blue) are moving along the y-axis. As no movement along the x-axis can be seen from the imaging, the orientation of the event front seen clockwise from N is 45° (along y, which is 45° E of N). From this axis-over-time plot, the velocity with which the front is moving across the radar field of view can also be estimated simply by using the eye. It can be taken from the plot that the downdraft of the first event (blue) starts at approximately 10:36 at y = -8 km and ends at around 10:46 at y = 7.5 km. In around 10 minutes, the front left 15.5 km behind it, which means that the speed it moved was around 26 m/s. For the second event, the downdraft starts at around 11:31 at y = -8 km and ends at around 11:39 at y = 8 km, resulting in a speed of around 33 m/s. For the third event, the updraft is seen more intensely in the plot. It starts at around 12:36 and ends at around 12:42. The draft is only seen between y = -7.5 and y = 6. This makes a speed of approx. 38 m/s. A sketch of this can be found in Fig. A0.34 in section A0.3.3 in the Appendix. The temporal resolution of the radar measurements used for the imaging is 1.5 minutes and the altitude resolution is 250 m. Thus, the maximum error that can be made reading the time is 1.5 minutes and reading the position in y from the plots is 250 m. With these errors, the maximum error that can be made in determining the velocity is approximately 0.41 m/s, 0.70 m/s, and 1.01 m/s for the first, second, and third events, respectively. This indicates a movement from SE to NW. In contrast, Fig. 6.10b) does not display a similarly distinct movement pattern along the SW-NE axis. This can be

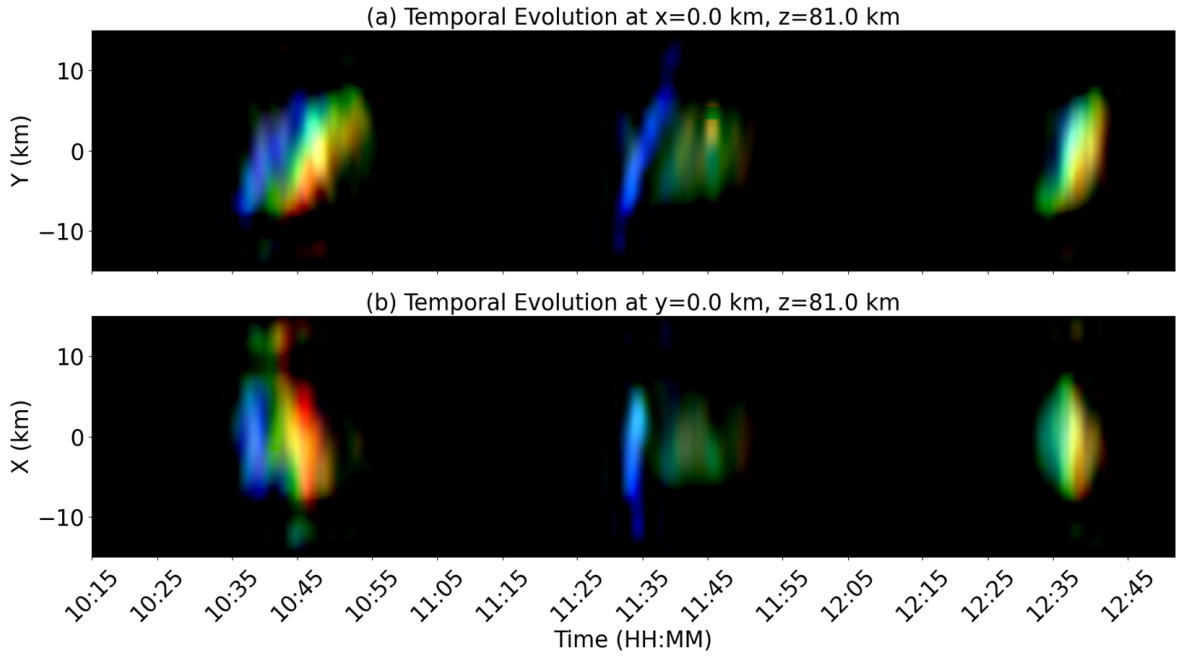


Figure 6.10: Temporal evolution of the three events of this case from along y-axis (a) and along the x-axis (b) at a fixed altitude z = 81 km over a time period of 2.5 h. The color representation is the same as in 6.8.

confirmed by looking at the events from yet another perspective. Figs. A0.6 to A0.8 in section A0.2.1 show how the events evolve in time in the xy-plane at one fixed altitude with the color-coding as usual. At the fixed altitude of approximately 81 km, the plots initially show the downdraft (blue) of each event, followed by a green transition zone as the downdraft shifts into the updraft, which is then represented by red. This progression is particularly distinct for the first and third events but appears less pronounced for the second event.

6.1.4 SABER Temperatures

The spatial structures observed in radar imaging suggest potential ducting mechanisms, which may be linked to mesospheric temperature inversions. Temperature measurements near MAARSY during the summer months, especially above the Arctic Circle at altitudes above 70 km, are scarce. While lidars could provide the necessary temporal and altitude resolution and are located closest to MAARSY, unfortunately, none of the measurements conducted by IAP's lidar in ALOMAR coincided in time or altitude with any varicose-mode events included in this study. Conversely, satellite-based temperature measurements offer only mean profiles averaged over extensive areas and several minutes. The Thermosphere Ionosphere Mesosphere Energetics and Dynamics (TIMED) satellite, equipped with the Sounding of the Atmosphere using Broadband Emission Radiometry (SABER) instrument, measures kinetic temperature profiles, among other parameters. Although SABER does not provide the precision required to resolve atmospheric conditions specific to the varicose-mode events, it offers insights into general temperature trends within a broad area around MAARSY. Within a 4° latitude and

longitude radius around MAARSY, covering an area of approximately 159 x 444 km, two temperature profiles were recorded on June 2, 2015, around 4:30 UT and 19:11 UT, respectively. Both profiles are presented in Fig. 6.11 together with a mean summer temperature profile (also see Fig. 1.1) for comparison in green. In the altitude range of interest, between 82 and 87 km, the measured temperatures diverge from the typical summer temperature profile. While a minimum is generally expected around 85 km, the temperatures in these profiles increase by approximately 25 K, alternating back and forth with altitude, until reaching a maximum just below 100 km in the dashed black profile. This oscillating gradient indicates wave activity. A similar pattern is observed in the solid profile, though without reaching a maximum at 100 km but above. Both profiles suggest the presence of a temperature inversion layer between 85 and 95 km (indicated by the red arrow) in comparison to the expected mean summer temperature profile in green in the same plot. To verify whether this inversion layer persisted until at least 13:00 UT (when the last event ended), it is useful to examine temperature profiles from days before and after the events. Fig. 6.11 presents these results. Here, the day of interest (June 2, 2015) is labeled as D, with profiles for up to five days before (D–x) and after (D+x) plotted if available. The specific temperature values are less relevant here; instead, this plot helps to identify whether a temperature inversion was present.

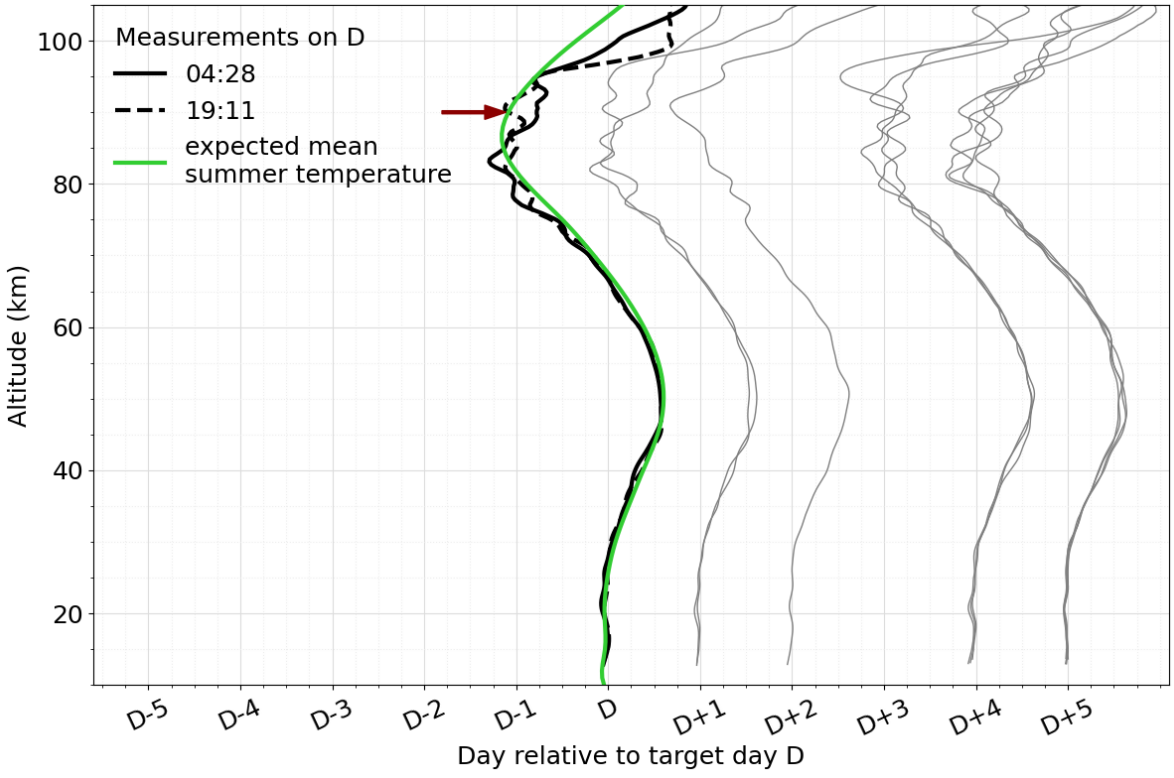


Figure 6.11: SABER temperature profiles near MAARSY (±250 km) for a period of ±5 days around the target date (D) 2 June 2015. Profiles obtained on D are shown in black, with individual profiles differentiated by line styles. Profiles from days after D are shown in grey, with profiles horizontally offset for better visibility. There were no available temperature measurements prior to D. As a comparison, the mean summer temperature profile is shown in green.

Before D, no temperature profiles were available in the study area. After D, several profiles were obtained; most deviated from the assumed profile, indicating wave activity of varying strength

6.2 Case II: 03.07.2018

The second case, observed on July 3, 2018, began at 15:25 UT and lasted for 20 minutes, displaying a particularly distinct varicose structure within an altitude range of approximately 80 to 87 km (see Fig. 6.12).

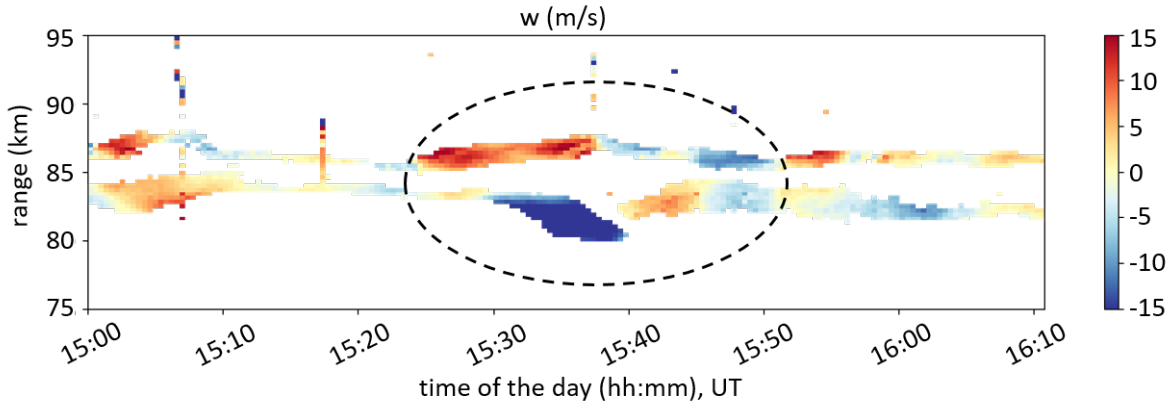


Figure 6.12: Range-time-radial velocity representation of Case II, observed on July 3, 2018, between 15:25 and 15:45 UT. The event is highlighted by the dashed ellipse.

During this event, the PMSE layer reached a maximum width of 9 km, indicating a widening factor of 4.5. In contrast to the first case, the PMSE layer splits into two distinct layers, with the separation growing larger due to the simultaneous up- and downdrafts. The most intense vertical velocities were measured as 15 m/s in the updraft and 22 m/s in the downdraft, with the highest values concentrated in the initial phase of the structure. Interestingly, near the end of this first phase, just before the downdraft subsides, there is a short gap in the PMSE layer, which then resumes as the updraft emerges. Post-event, small increases in spectral width occur, particularly after the initial updraft and in the lower region of the PMSE layer, yet they do not suggest substantially enhanced turbulence (see A0.10).
For this case, background horizontal wind conditions, MAARSY multibeam data, and complementary measurements from the Saura PRR are presented. The multibeam data are used as a substitute for unavailable radar imaging, and the analysis method is explained here in detail. For the following cases, only the results will be referenced in the main text, while the corresponding plots are provided in section A0.2.2 the Appendix.

6.2.1 MMARIA Norway Mean Winds

For this event, the mean wind magnitude ranged from nearly 0 m/s to about 100 m/s, with a pronounced maximum at the lower boundary of the PMSE layer around 80 km, and a minimum near 90 km, just above the upper boundary (see Fig. 6.13). The wind

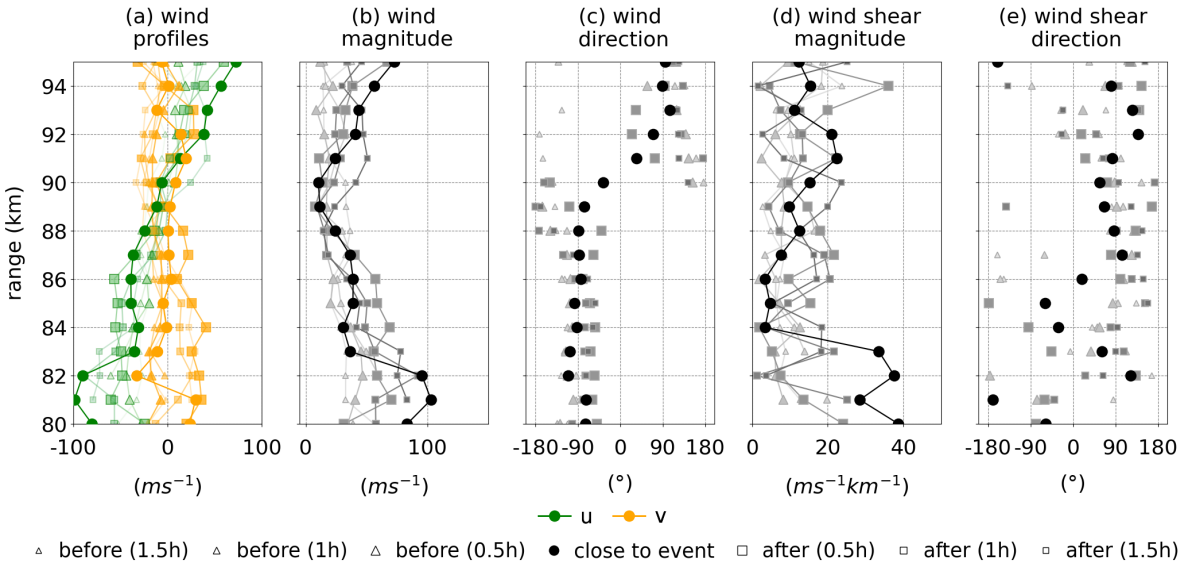


Figure 6.13: Mean wind parameters around the first event on July 3, 2018, at 15:30 UT, from horizontal wind components u (green) and v (orange) in panel a. Panels b–e show wind magnitude, direction (0° = North), shear, and shear direction. Strongest colors in panel a and black in panels b–e indicate measurements closest to the event; different symbols and lighter shades of colors indicate ±1.5 hours.

direction remained relatively constant toward the SW, with slight shifts toward the W with increasing altitude. Wind shear reached a maximum of 40 m/s/km near the lower boundary of the PMSE layer, decreased between 84 and 87 km, and showed a smaller secondary peak of about 25 m/s/km close to the upper boundary. The shear direction varied strongly with altitude, transitioning from NW through N to the SE.
Residual wind analysis over a two-day period around the event (Fig. A0.11) shows no striking deviations compared to the surrounding conditions. In fact, the residual magnitudes were lower during and for several hours around the event than at the beginning or end of the examined interval. A closer look at the absolute residual magnitudes (Fig. A0.13), confirms this picture: the meridional component shows only a slight increase during the event, while the zonal component remains at the median. Stronger enhancements of the zonal residuals occurred on several days before and after the event, but not during it. The meridional increase is most evident in the 10-hour residual and least pronounced in the 3-hour residual. Extending the view to the full 10-day period (Figs. A0.12 and A0.14) further supports these findings: residual magnitudes were relatively low around the day of the event, whereas clear increases in both zonal and meridional components occurred several days before and after.

6.2.2 MAARSY Multibeam

MAARSY's multibeam capability enables tracking of the event as it moves across the radar's FOV, provided the event is indeed in motion. As described in Section 3.2.1, MAARSY's beam can rapidly switch between five directions, allowing near-simultaneous vertical velocity measurements across five FOVs. Fig. 6.14 presents the results for this case, where the event appears in each beam at slightly different times.

It is important to note that the assumptions of a rigid wave crest and a non-evolving structure within the FOV are not fully met here. In each beam, the event manifests as an alternating up-and-down movement within the PMSE layer, though the duration of these drafts, and hence the event duration, appears variable.
To interpret the radial velocities, recall that in a Doppler radar system with beam-swinging, the measured radial velocity ν_{rad} depends on the projections of both horizontal and vertical wind components along the radar beam direction. For an off-zenith angle Θ, the horizontal wind component contributes based on the beam's angle from vertical:

$$V_{r,h} = V_h \sin(\Theta) \tag{6.1}$$

where $V_{r,h}$ is the horizontal wind component projected along the radar beam, and V_h is the total horizontal wind speed. This relationship shows that as Θ increases, the contribution of the horizontal wind to V_r also increases. For a vertical beam ($\Theta = 0°$), no horizontal wind is measured, while at an off-zenith angle approaching 90°, the radial velocity fully reflects horizontal wind speed. To assess if the event is moving across MAARSY's FOV, the focus is on structural changes in the PMSE layer rather than specific velocities. Visually, the event structure first appears in the W beam, followed shortly by detections in the N, V, and S beams, and finally in the E beam. This sequence suggests a W-to-E movement with a slight N-S tilt. To quantify this movement, two approaches were applied: (1) visual identification of prominent structural features in each beam, with timings recorded to determine time lags between beams, and (2) cross-correlation analysis, as described in Section 4.2. The altitudes compared for the different beam pairs are listed in Tab. A0.3 in Section A0.3.4 in the Appendix. For the analysis of propagation, the time differences from Method 1 (visual identification) were used. The identification was always based on a combination of velocity and SNR plots. For presentation, only the velocity plots are shown, as they provide the clearest view of varicose-mode structures, especially for readers less familiar with the events. The corresponding SNR plots (A0.15 for this case) are available in Section A0.2.2 of the Appendix. Depending on which representation provided the most reliable signature in the analysis, either the end or the widest part of the event was selected in each case to determine the lag times. The discrepancies between Method 1 and Method 2 (cross-correlation) served as uncertainty estimates, with a minimum threshold of 1.5 min, corresponding to the radar's resolution. For consistency, cross-correlation results were rounded to whole minutes. Both methods confirmed the visual impression that the event moved from NW to SE across the FOV. Using the Method-1 time differences and the derived uncertainties, the velocity and orientation of the event front were calculated for four triplets of beams, corresponding to the quadrants of the antenna field. The results are summarized in Tab. 6.2, which also lists beam positions at 85 km altitude, referenced to the vertical beam as origin.
The orientation and phase speed were determined by calculating the front angle relative to N and the corresponding velocity vector, including the maximum time lag uncertainties. This yielded eight slopes (with associated uncertainty ranges) and eight velocity vectors, as shown in Fig. 6.15. For each quadrant, two slopes – denoted m_1 and m_2 – were derived, resulting in one slope pair per quadrant. The slope m_1 is calculated using the first triplet of beams assigned to that quadrant (e.g., in the first quadrant, formed

by points V, W, and N, m_1 is computed from the configuration where W appears twice in the equation – as the beam referred to as b_1 in Eq. A0.41 in the appendix), while m_2 is based on the second triplet (with N appearing twice, referred to as b_1 in that configuration). To distinguish the results, solid lines and filled arrows represent m_1 and the corresponding velocity vector (thick lines for average values, thin lines for uncertainty bounds), whereas dashed lines and open arrows indicate m_2 and its associated velocity. Note that the labels m_1 and m_2 refer exclusively to the beam configurations within each quadrant and are not related to the methodological distinction introduced earlier in this section. Arrow lengths are normalized to highlight differences in phase speed between quadrants. Row colors in Tab. 6.2 correspond to the same quadrant color scheme. The

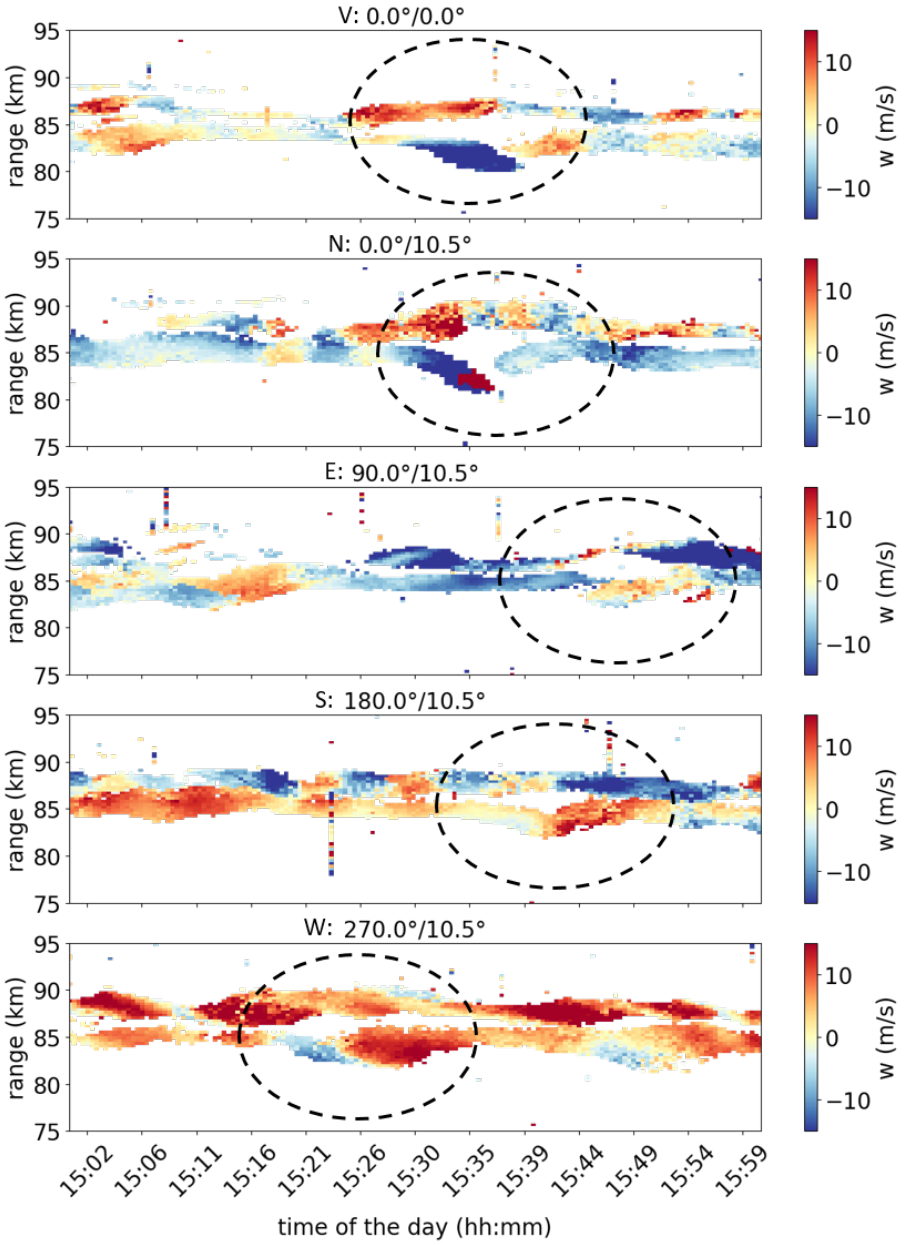


Figure 6.14: Vertical velocity measurements for Case II for 5 beam pointing directions (top to bottom: Vertical, North, East, South and West) using MAARSY.

same procedure was applied to the following cases and will not be repeated in detail. As illustrated in Fig. 6.15, the slope of the event front varies across MAARSY's FOV, suggesting a rotating or shifting pattern. Higher phase speeds were found in the W-V-N and E-V-N quadrants compared to the others. Results from the two triplets in each quadrant were largely consistent, with only minor differences in the E-V-N and W-V-S quadrants, all within the calculated uncertainties. This supports the assumption of an approximately constant velocity within each quadrant. An average propagation velocity of about 21 m/s was found as the event front entered MAARSY's FOV. Slightly lower velocities in the southern compared to the northern part of the structure caused a gradual slope change: the entry angle relative to N was 28°, flattening to 70° as the event moved further across the FOV, and returning to 22° upon exit. Overall, the velocity remained relatively stable, with only minor deviations in the W-V-S quadrant, well within error bounds. Dashed lines and open arrows represent results from the second point triplets.

Table 6.2: Summary of geographic directions, beam positions at 85 km altitude, time differences determined by eye and by using cross-correlation, and mean velocities and angles of the event front for Case II determined by using the time differences observed by eye. Row colors correspond to the quadrant colors used in the Fig. 6.15.

Case II: 03.07.2018			
Geographic Direction	**Beam Position**		**Time of the Event**
	x	**y**	
V	0	0	15:37
N	0	15	15:35
E	15	0	15:48
S	0	-15	15:42
W	-15	0	15:25
Time Differences (min)			
Beam Combination	**method 1**	**method 2**	**Difference**
V → N	-2	3	1.5
V → E	11	-8	3
V → S	5	-5	1.5
V → W	-12	14	2
W → N	10	11	1.5
W → S	17	-14	4
E → N	-13	12	1.5
E → S	-6	6	1.5
Mean Velocity of the Front (m/s)		**Mean Angle of the Front (°)**	
from m_1	**from m_2**	**from m_1**	**from m_2**
50 ($44 < V < 57$)	32 ($23 < V < 45$)	168 ($151 < \theta < 180$)	13 ($4 < \theta < 22$)
35 ($32 < V < 39$)	35 ($31 < V < 39$)	45 ($32 < \theta < 56$)	45 ($26 < \theta < 68$)
45 ($41 < V < 52$)	42 ($31 < V < 52$)	34 ($17 < \theta < 50$)	21 ($4 < \theta < 47$)
52 ($43 < V < 63$)	26 ($20 < V < 35$)	14 ($2 < \theta < 26$)	30 ($24 < \theta < 35$)

Arrow lengths normalized for clarity, highlight phase speed variations between quadrants. The results are also summarized in the lower section of Tab. 6.2, with row colors corresponding to the quadrant colors in the figure. The same procedure to investigate event propagation and orientation is used for the following cases similarly and won't be explained again in the next sections. Visualized in Fig. 6.15, the slope of the event front varies across MAARSY's FOV, suggesting a rotating or shifting pattern as it advances. This interpretation aligns with higher phase speeds observed in the W-V-N and E-V-N quadrants compared to the other two. While the results from the two triplets of beam positions in each quadrant are largely similar, minor variations are noted, particularly in the E-V-N and W-V-S quadrants. However, these differences lie within the calculated uncertainty range, supporting the assumption of a roughly constant velocity within each quadrant. An average propagation velocity of around 21 m/s was found as the event front entered MAARSY's FOV. As the event progressed, a slightly lower propagation velocity was observed in the southern part of the structure compared to the northern part, contributing to a gradual change in slope. The entry angle relative to N was approximately 28°, flattening to 70° as the event moved further across the FOV due to lower velocities in the W-V-S. Upon exiting the FOV, the front angle was similar to the entry angle (22°). Overall, the velocity remained relatively stable across the FOV, with slight deviations in the W-V-S quadrant, though these remained within the error bounds.

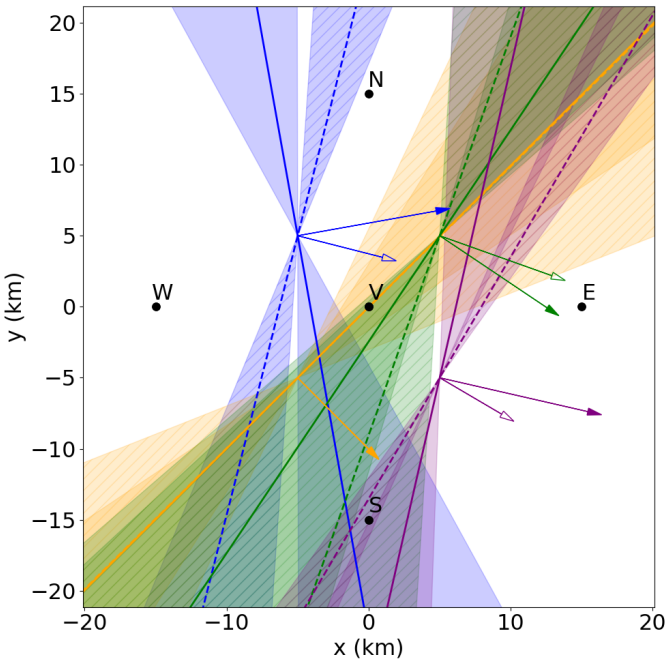


Figure 6.15: Event front slopes and velocities derived from beam positions and time differences in the Multibeam data obtained for Case II. Different colors represent each quadrant, with solid and dashed lines indicating results from two distinct beam triplet combinations per quadrant. Filled and empty arrows depict velocities, with thick lines and arrows representing mean values, while thin lines indicate results within the uncertainty range of lag times. To improve clarity, only the mean velocity arrows are shown for the thin-line solutions.

6.2.3 Observed Saura Dynamics

Complementary observations from Saura PRR provide additional insight into spectral width and radial velocity for three representative beam directions (see Fig. 6.16).
A pronounced enhancement in spectral width was detected between 80 and just below 90 km, clearly standing out from the background variability. In contrast, the corresponding radial velocity variations at these altitudes are less distinct, as they blend with the naturally high variability typically present below and around 80 km. This highlights the importance of spectral width as the more reliable indicator for identifying small-scale dynamic structures, whereas radial velocity alone proves more difficult to interpret.
The observed spectral width enhancement strongly suggests the passage of a small-scale, wave-like structure through the Saura PRR field of view. Interestingly, this feature does not coincide with the timing of the varicose-mode event observed by MAARSY, but occurs roughly 30 minutes earlier.

In addition, the radial velocity data reveal a clear updraft–downdraft pattern, with a red (positive) region above a blue (negative) region. This feature coincides with the vertical location of the varicose-mode event observed by MAARSY and is consistent with its expected vertical structure. The spectral width enhancements extend across the same altitude range, from about 80 to just below 90 km. As in the previous case, only those beams with the clearest signatures are described here, while results from additional beam directions and the corresponding signal strength plots are provided in Fig. A0.16.

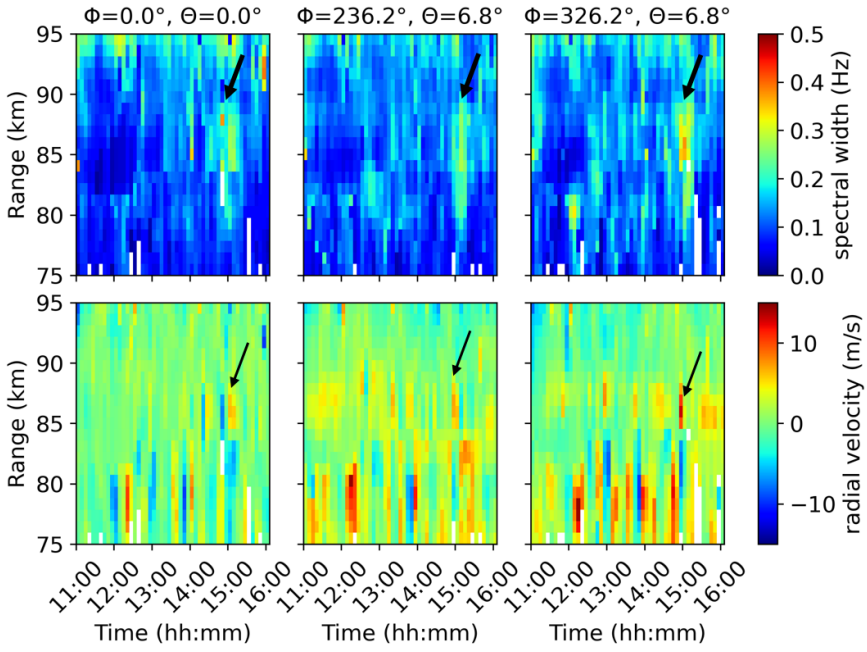


Figure 6.16: Spectral width (top) and radial velocity (bottom) around the time of the event observation with MAARSY. Shown are the vertical, SW, and NW beam measurements (left to right). Black arrows point at patterns that coincide with the timing of the event of Case II.

6.3 Case III: 01.08.2018

Observed on August 1, 2018, the third case is an example of one of the most extreme varicose-mode events in this study. Beginning at 19:57 UT, it persisted for approximately 23 minutes, exhibiting peak velocities of 45 and 26 m/s in the updraft and downdraft, respectively, that stand out among all documented cases. It spans altitudes from 82 to 92 km and its varicose structure widens the PMSE layer by a factor of approximately 1.4, reaching a maximum width of 10 km. The simultaneous updrafts and downdrafts are prominent throughout both phases of the event. Similar to Case II, the PMSE layer initially splits into two, with the separation growing during the first phase. However,

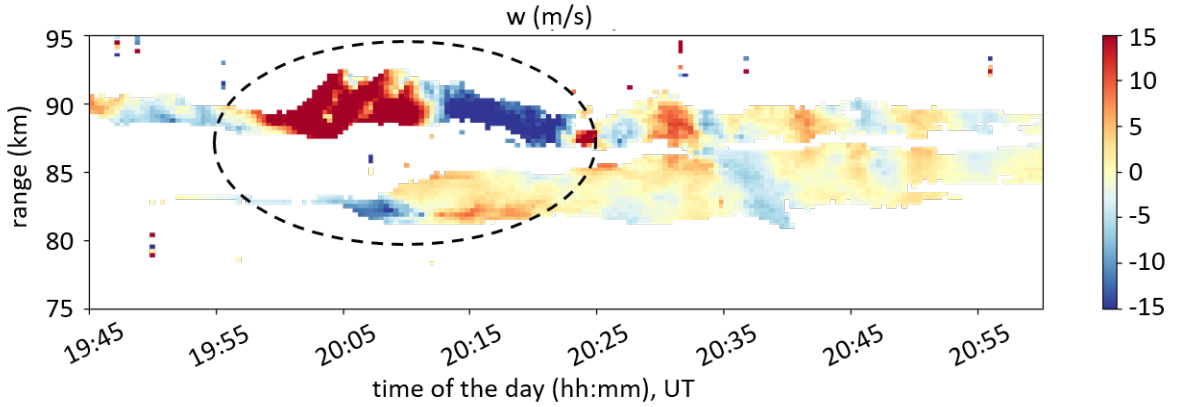


Figure 6.17: Range-time-radial velocity representation of Case III, observed on August 1, 2018, between 19:45 and 21:00 UT. The event is highlighted by the dashed ellipse.

unlike Case II, the layer reconnects in the second half. In contrast to the previous two cases, the spectral width in this instance exhibits notably high values in the upper portion of the varicose structure, consistently present before, during, and after the event. While some range gates in the lower part of the PMSE layer also show spectral width enhancements during the event, values remain low to moderate before and after. Overall, the lower part of the PMSE and event region demonstrates lower spectral width values compared to the upper portion. For this case, the following section will present measurements of background horizontal wind conditions, and analyses of MAARSY multibeam data.

6.3.1 MMARIA Norway Mean Winds

For this event, the mean wind magnitude varied from slightly above 0 m/s to just over 100 m/s within the altitude range of the PMSE layer (see Fig. 6.18). A distinct maximum occurred between 82 and 92 km, while wind speeds at the boundaries themselves remained comparatively low. Wind direction showed no significant shifts, remaining between 135° and 175° counterclockwise from N, indicating a predominantly SW-ward flow with a slight W-ward tendency near the boundaries. Wind shear displayed strong altitude-dependent variability, with two pronounced peaks of about 33 and 37 m/s/km near 82.5 and 87.5 km, separated by a region of minimal shear. The shear direction changed rapidly with altitude, rotating from S clockwise through N to SE.
Residual winds during the event showed a clear enhancement in the 6- and 10-hour com-

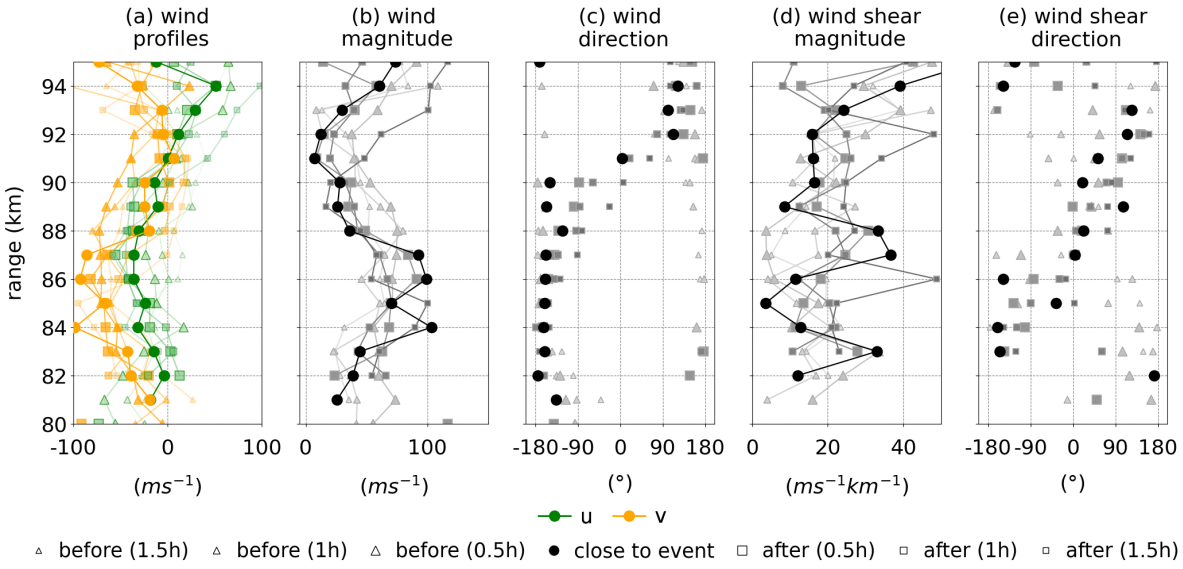


Figure 6.18: Mean wind parameters around the first event on August 1, 2018, at 20:00 UT, from horizontal wind components u (green) and v (orange) in panel a. Panels b–e show wind magnitude, direction (0° = North), shear, and shear direction. Strongest colors in panel a and black in panels b–e indicate measurements closest to the event; different symbols and lighter shades of colors indicate ±1.5 hours.

ponents, while the 3- and 8-hour residuals remained comparatively low (Fig. A0.18). For the meridional component, increases were visible in the 3-, 6-, and 8-hour residuals, whereas the 10-hour residuals were generally higher across the full period, making event-related changes less distinct.

At a fixed altitude of 85 km, the zonal residuals showed no enhancement at the time of the event; instead, an increase appeared later, consistent with the vertical tilt of the residual structures that causes their timing to vary with altitude (see Fig. A0.20). In contrast, the meridional residuals at this altitude exhibited clear event-time enhancements in the 8- and 10-hour components, while shorter residuals showed no notable variations.

An extended 10-day view (Figs. A0.19 and A0.21 in Section A0.2.3) reveals that enhanced residual magnitudes occurred in both zonal and meridional components even during periods without observed events. Elevated residuals were particularly apparent about one and five days before the event, as well as on the following day. These findings indicate that such enhancements are not uniquely associated with the event itself but also reflect other transient dynamical features in the background wind field.

6.3.2 MAARSY Multibeam

Similar to the approach taken for Case II, the event's progression across MAARSY's FOV was analyzed using Multibeam data to determine lag times between different beams. The vertical velocity and SNR measurements obtained by MAARSY for this case are shown in Figs. A0.24 and A0.25 in the Appendix.

The varicose structure is clearly visible in the vertical, N, and E beams, primarily due to the distinct structure of the updraft in the first half of the event. However, this structure

is less apparent in the S and W beams. By visually identifying the characteristic thin PMSE layer at approximately 83 km just before the event – clearly visible in the first three beams – the event could be discerned in the S and W beams as well, allowing time differences between beams to be estimated by eye (method 1). For method 2 (cross-correlation), however, the lower similarity between the S and W beams and the other beams resulted in less reliable lag time determination for certain beam combinations. Tab. A0.1 summarizes the beam positions, timing data, and lag time results obtained from both methods, along with the calculated uncertainties based on the differences between the methods. A preliminary assessment of Fig. A0.24 suggests that the event

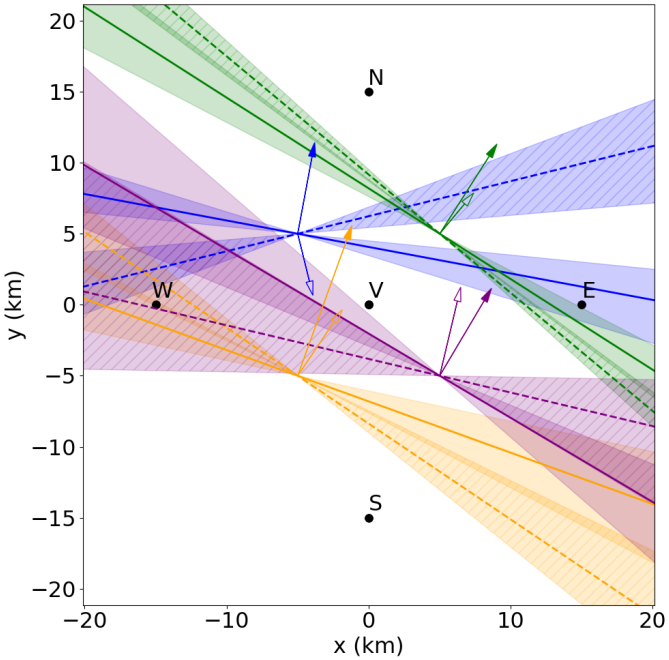


Figure 6.19: Event front slopes and velocities derived from beam positions and time differences in the multibeam data obtained for Case III. Color coding and arrow conventions follow Fig. 6.15.

is moving from the SW to the NE. This observation is confirmed by the timings of the event's appearance in each beam.

The calculated slopes and velocities for each quadrant of the radar field are shown in Fig. 6.19. The angle of the event front relative to the positive y-axis (North) changes as the event moves across MAARSY's FOV. It enters with a velocity of about 30 m/s at an angle of 111°, slows to approximately 18 m/s while keeping the same angle, and then further decreases to around 16 m/s as the slope becomes flatter, with the angle increasing to 144° relative to N.

The results from both beam triplet combinations per quadrant show a high degree of consistency, even when accounting for the uncertainty range. This consistency supports the assumption of a constant velocity and a stable, rigid wavefront for this event.

6.4 Case IV: 01.07.2023

The fourth and final case, recorded on July 1, 2023, lasted from 11:10 UT to 11:32 UT, with a maximum vertical extent of 11 km between 80 and 91 km. During this event, the PMSE layer is widened by a factor of 1.6. With updraft and downdraft velocities

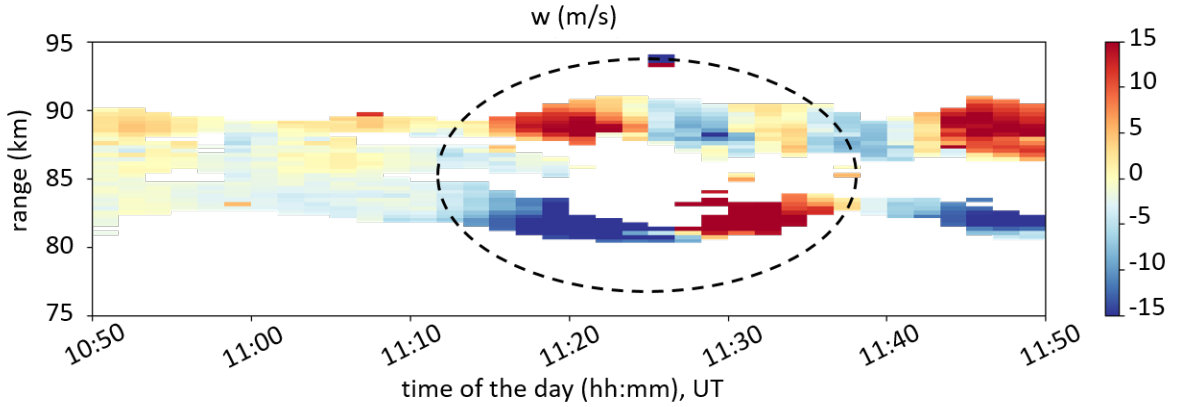


Figure 6.20: Range-time-radial velocity representation of Case IV, observed on July 1, 2023, between 10:50 and 11:50 UT. The event is highlighted by the dashed ellipse.

of 24 and 25 m/s, this case stands out as a higher-velocity event in this study. Unlike the previous cases, where the PMSE layer was already separated prior to the event, it appears that here the varicose-mode structure actively leads to the layer's separation. The spectral width is notably enhanced in the upper region of the PMSE layer and in the lowest parts of the lower layer, coinciding with the locations where the event reaches its maximum extent. As this event ends, another movement appears to emerge, showing a brief downward motion followed by an upward motion in the lower part of the layer. However, since this does not match the characteristics of a varicose-mode event, it is not included in this category.
For this case, background horizontal wind conditions, MAARSY multibeam data, and complementary measurements from the Saura PRR are presented, including both raw data observations and imaging analyses.

6.4.1 MMARIA Norway Mean Winds

The background wind conditions during the event, as measured with MMARIA Norway, along with the derived wind parameters, are summarized in Fig. 6.21.
The wind magnitude profile (panel b) shows velocities ranging from approximately 10 to nearly 100 m/s, with two distinct maxima at 81 and 87 km, both occurring within the PMSE layer. The wind direction (panel c) remains consistently toward the W but shifts to the SW above 85 km. The wind shear magnitude (panel d) exhibits strong altitude-dependent variability, with three maxima at 80, 85, and 90 km, where moderate values of up to 25 m/s/km are observed. Between these maxima, the shear magnitude approaches zero. The shear direction (panel e) changes from S to W over N to SE with altitude. Additional insights into the background conditions are provided by the residuals of the zonal and meridional wind components shown in Fig. A0.27.
Over the entire time period shown in Fig. A0.29, the residual magnitudes are generally

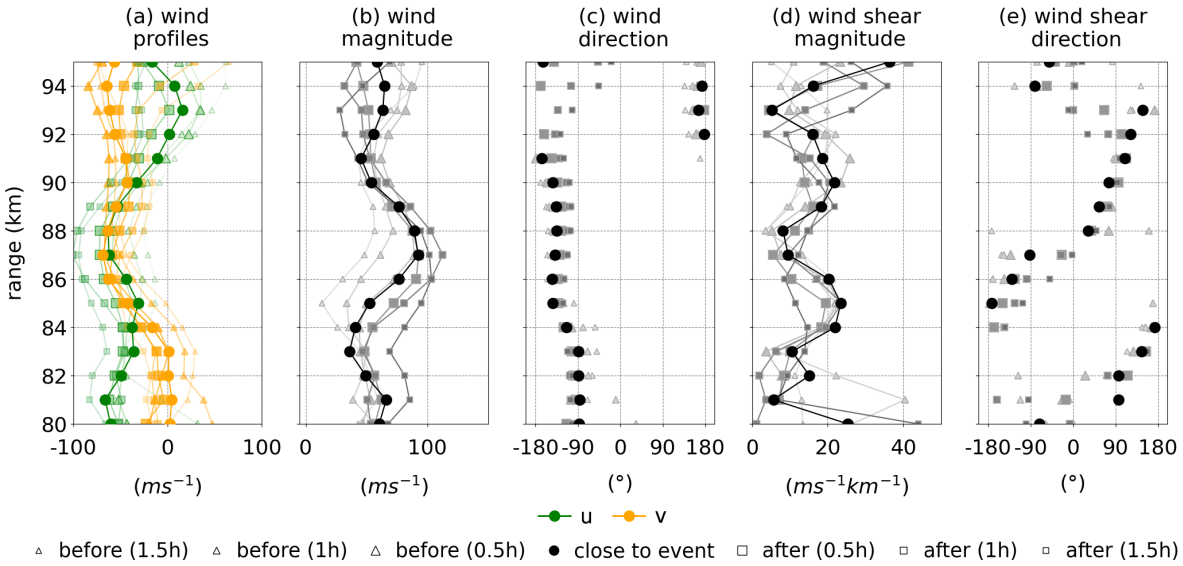


Figure 6.21: Mean wind parameters around the first event on July 1, 2023, at 11:00 UT, from horizontal wind components u (green) and v (orange) in panel a. Panels b–e show wind magnitude, direction (0° = North), shear, and shear direction. Strongest colors in panel a and black in panels b – e indicate measurements closest to the event; different symbols and lighter shades of colors indicate ±1.5 hours.

higher than in the other cases. This applies to all meridional residuals and to the 6- and 10-hour residuals of the zonal component. In contrast, the 3- and 8-hour zonal residuals remain within a similar range as in previous cases without notable variation.
A clear increase in residual magnitude directly linked to the timing of the varicose-mode event is not apparent by eye. To better evaluate whether the event coincides with a rise in residuals, Fig. A0.20, which shows the time series at 85 km altitude, provides more detail. Here, no distinct change is seen in the zonal component around the event time. The residual structures show a tilted vertical pattern, with maxima occurring at different times depending on altitude. In the meridional component, the residuals show a rise that coincides with the event, especially in the 8- and 10-hour components. An additional look at the extended 10-day time series (see Figs. A0.28 and A0.30 in the Appendix in section A0.2.4) reveals that elevated residuals also occur in both the zonal and meridional components during periods without any observed event.
Elevated magnitudes are seen around one and five days before the event, as well as on the following day. It can also be observed that, where present, the enhancements are not uniform across all residuals but are most pronounced in the 8- and 10-hour components.

6.4.2 MAARSY Multibeam

To determine whether this event propagated across MAARSY's FOV, the multibeam vertical velocity data were analyzed (Fig. A0.24). The widening of the PMSE layer was apparent in most beams, with the exception of the W beam, where the structure alone did not allow a clear identification. In this case, the event was identified by combining the overall PMSE layer structure with velocity patterns. This revealed that the first

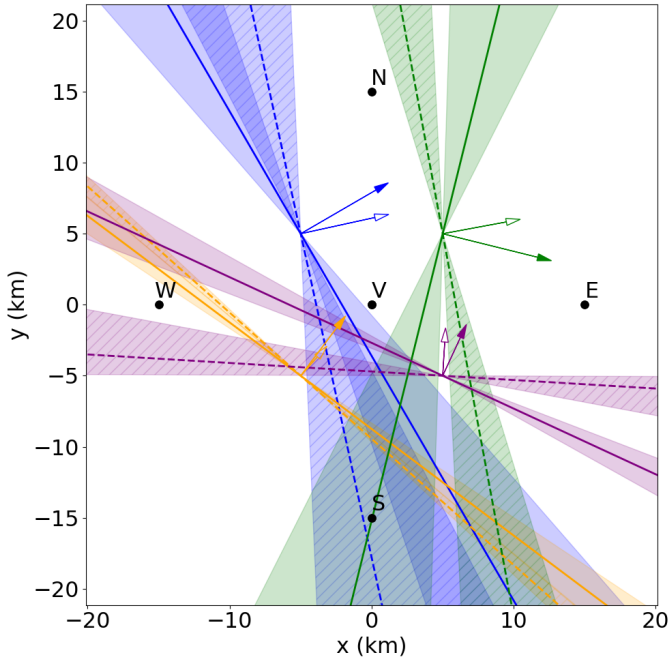


Figure 6.22: Event front slopes and velocities derived from beam positions and time differences in the multibeam data obtained for Case III. Color coding and arrow conventions follow Fig. 6.15.

pair of updrafts corresponded to the varicose-mode event, whereas a later pair of strong updrafts represented a separate, non-varicose structure.
A characteristic feature of this event is the presence of varicose-mode-typical velocity patterns—simultaneous upward and downward motions—in all beams, underlining its coherent nature. The sequence of detections across the individual beams confirms that the event propagated through MAARSY's FOV: it appeared first in the S, then in the W, V, and N beams, and finally in the E, consistent with a movement from SW to NE. The results (Tab. A0.2, Fig. 6.22) show that the front became progressively steeper with respect to N as it crossed the radar's field. On entry, the front propagated at an average velocity of 9 m/s with an angle of 129° clockwise from N. The orientation and velocity remained similar in the E-V-S quadrant.
In contrast, the slope steepened in the W-V-N quadrant, where a slightly higher average velocity of 15 m/s was found. By the time the event exited the field, the slope had further steepened, with the angle increasing to 157°.

6.4.3 Observed Saura Dynamics

In Case IV, the Saura PRR data show a broad enhancement in spectral width between about 09:00 and 12:00 UT, with the strongest increase around 11:00 UT. This feature is visible in all three selected beam directions and coincides well with the timing of the Case IV event detected by MAARSY (see Fig. 6.23).
The radial velocity data, however, are less clear. A strong updraft-downdraft pair appeared around 11:40 UT, resembling the second half of a varicose-mode oscillation. Yet

its timing does not match the MAARSY observation and it is inconsistent with the known propagation direction of the event.

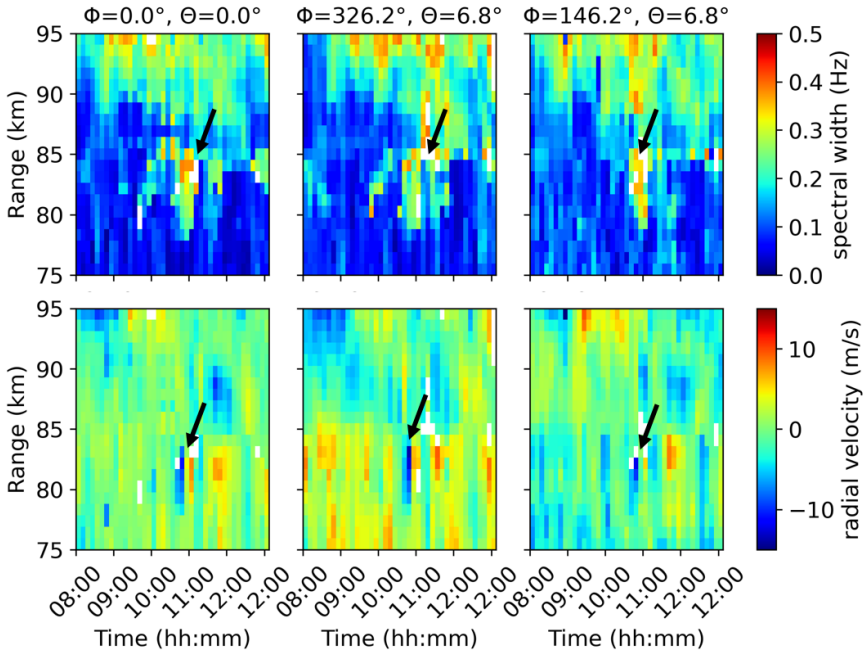


Figure 6.23: Spectral width (top) and radial velocity (bottom) around the time of the event observation with MAARSY. Shown are the vertical, NW, and SE beam measurements (left to right). Black arrows point at patterns that coincide with the timing of the event of Case IV.

A smaller feature, consisting of a weak negative patch followed by a transition to positive velocities, occurred slightly earlier. Although visually less pronounced, this structure aligns both with the spectral width enhancement and the timing of the MAARSY detection, making it the more likely radial velocity counterpart of the varicose-mode event.

MUSIC (Imaging)

Owing to the multibeam capabilities of the Saura PRR, the direction of propagation of strong reflection signals can be determined using the MUSIC algorithm (see Section 3.4.1). This method was applied to data from around the time of the Case IV event, and the resulting output is shown in Fig. 6.24. The plot displays signal strength from weak (blue) to strong (red) reflections. The two rows represent the two polarization modes in which the observations were made: the top row corresponds to cross polarization and the bottom row to parallel polarization. All data were collected within a range interval between 78 and 81 km. Between 11:04 UT and 11:31 UT, the MUSIC results reveal an elongated region of enhanced signal moving from the SW to the NE across the full field of view of the Saura antenna array. This directional motion is consistently observed in both polarization modes and along with the findings using MAARSY multi-beam.

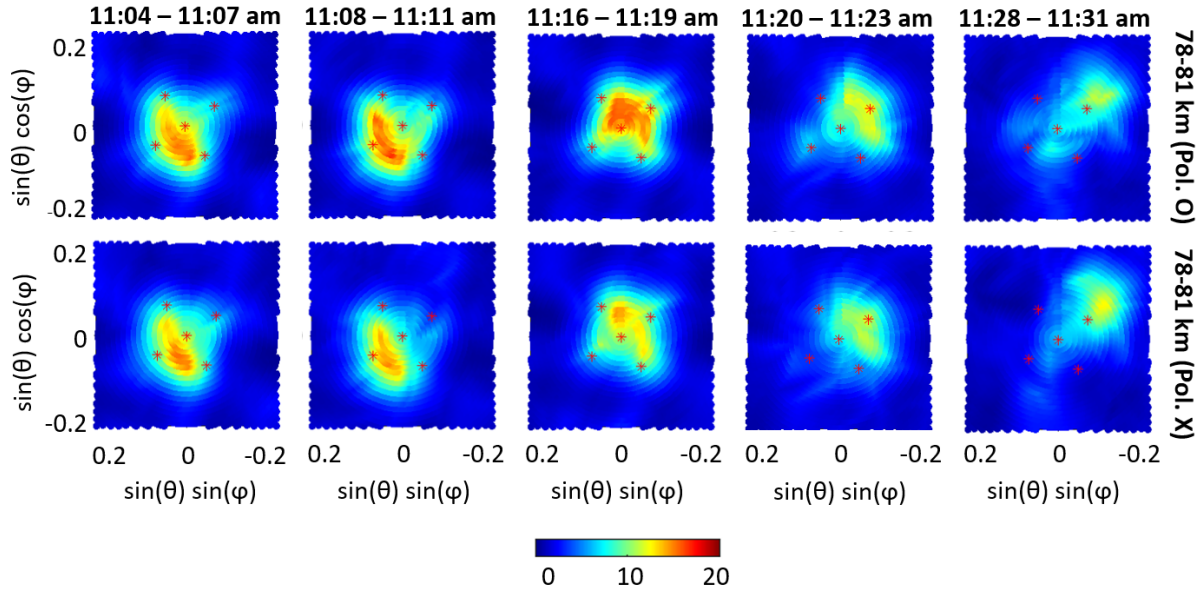


Figure 6.24: Directional analysis of strong reflections during the Case IV event using the MUSIC algorithm. Signal intensity is shown from weak (blue) to strong (red) across azimuth and elevation. Data were collected between 78–81 km. Top: parallel polarization; bottom: cross-polarization.

6.5 Summary and Discussion: Multi-Instrument Case Studies

6.5.1 Event Characteristics and Classification

The case studies included the detailed investigation of four events, all exhibiting the defining varicose-mode signature: (quasi-)simultaneous updrafts and downdrafts that significantly widen the PMSE layer by factors ranging from 1.4 to 4.5. These signatures are illustrated in Fig. 6.25, which shows the Range-Time-Intensity, Range-Time-Velocity, and Range-Time-Spectral Width plots for all four cases. The plots highlight characteristic features such as alternating vertical motions, layer broadening, and, in some cases, enhancements in spectral width.

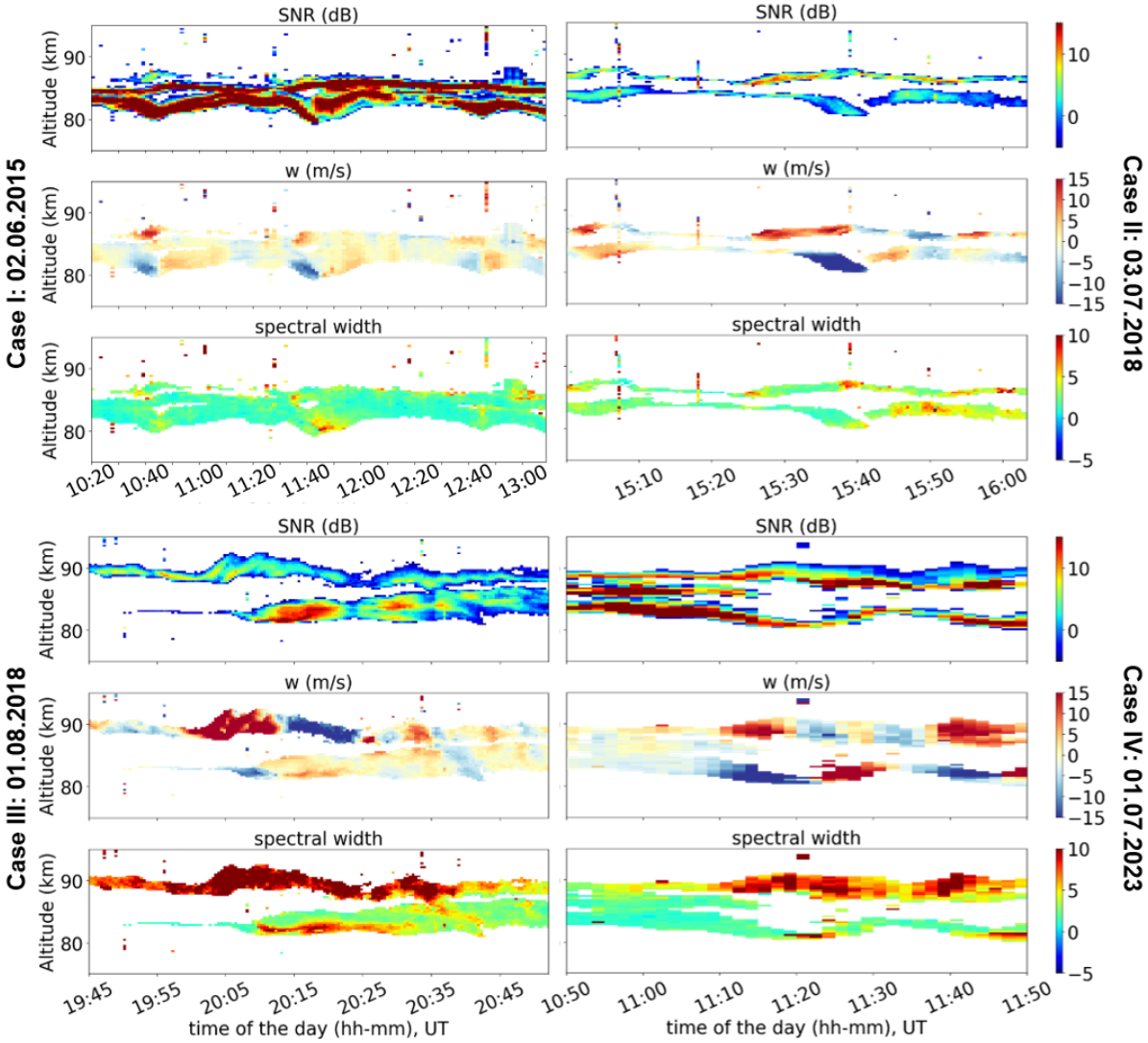


Figure 6.25: Summary of the selected varicose-mode events for case studies. Shown are the Range-Time-Intensity, Range-Time-Velocity, and Range-Time-Spectral Width plots for each case. The plots illustrate the temporal evolution and vertical structure of the observed events, enabling direct comparison across cases.

This characteristic behavior closely resembles mesospheric bores, which are known for their alternating vertical motion and horizontal layer expansion (e.g. Dewan and Picard, 1998; Fritts et al., 2020). These events were observed within the PMSE layer at altitudes between 80 and 90 km, and their dynamics prompt comparisons with both undular and turbulent bores observed in past studies (e.g. Seyler, 2005a; Mondal et al., 2021). Despite this resemblance, notable differences emerge, particularly the absence of trailing waves and unusually high vertical velocities in the observed events. The former raises an important question: Can these events still be classified as mesospheric bores? The lack of trailing waves does not necessarily disqualify these events from being mesospheric bores. Simulations by Ramachandran et al. (2023) suggest that high atmospheric viscosity can suppress trailing wave formation, limiting the energy dissipation typically associated with such features, resulting in solitary wave-like bores without trailing structures.
Alternatively, it is plausible that trailing waves are present but remain undetectable by MAARSY due to low vertical velocities or interference from other phenomena, masking finer structures. This interpretation aligns with observations from other studies suggesting that trailing features can be subtle or absent under specific conditions. Hozumi et al. (2018) add that duct depth variations can create undulating or rotating phase fronts, potentially masking or altering the appearance of trailing waves. Similarly, Mondal et al. (2021) highlight the role of local atmospheric variability in obscuring such features. Observations by Fritts et al. (2020) further support this variability, with some mesospheric bores exhibiting minimal trailing waves under specific conditions, such as reduced duct depth, increased viscosity, and interactions with wind shear structures. Thus, the observed varicose-mode events may reflect either inherent environmental constraints or observational limitations. These insights collectively suggest that the absence of visible trailing waves does not preclude the classification of these events as mesospheric bores.
Comparing the observed events to mesospheric bores reveals both similarities and differences. While all cases share common features such as vertical divergence and horizontal layer expansion, their turbulence levels vary. Cases I and II exhibit characteristics similar to undular bores, while Cases III and IV, with enhanced spectral width, align more closely with turbulent bores (e.g. Seyler, 2005a; Mondal et al., 2021). The spectral width variability across the cases indicates that turbulence is not a necessary condition for varicose-mode events to form but may instead result from their interaction with the environment.

6.5.2 Propagation and Horizontal Dynamics

One of the critical questions was whether these events genuinely move across MAARSY's FOV. Observations indicate that all events propagate across MAARSY's FOV, with velocities ranging from 15 to 75 m/s. These phase speeds align with mesospheric bores observed in previous studies, including the 15 to 100 m/s range reported by Taylor et al. (1995), the 31 $\pm$ 5 m/s average recorded by Mondal et al. (2021), and the 44 to 55 m/s speeds documented by Fritts et al. (2020). Importantly, the case study events consistently propagate at angles or even against the prevailing background wind, as visualized in Fig. 6.26. This behavior suggests the influence of ducting mechanisms, such as temperature inversions or wind shear layers, which allow propagation independent of the mean wind direction and is commonly observed in mesospheric bore events (e.g. Dewan and Picard, 1998; Smith, 2003; Mondal et al., 2021). Fig. 6.26 illustrates the variability

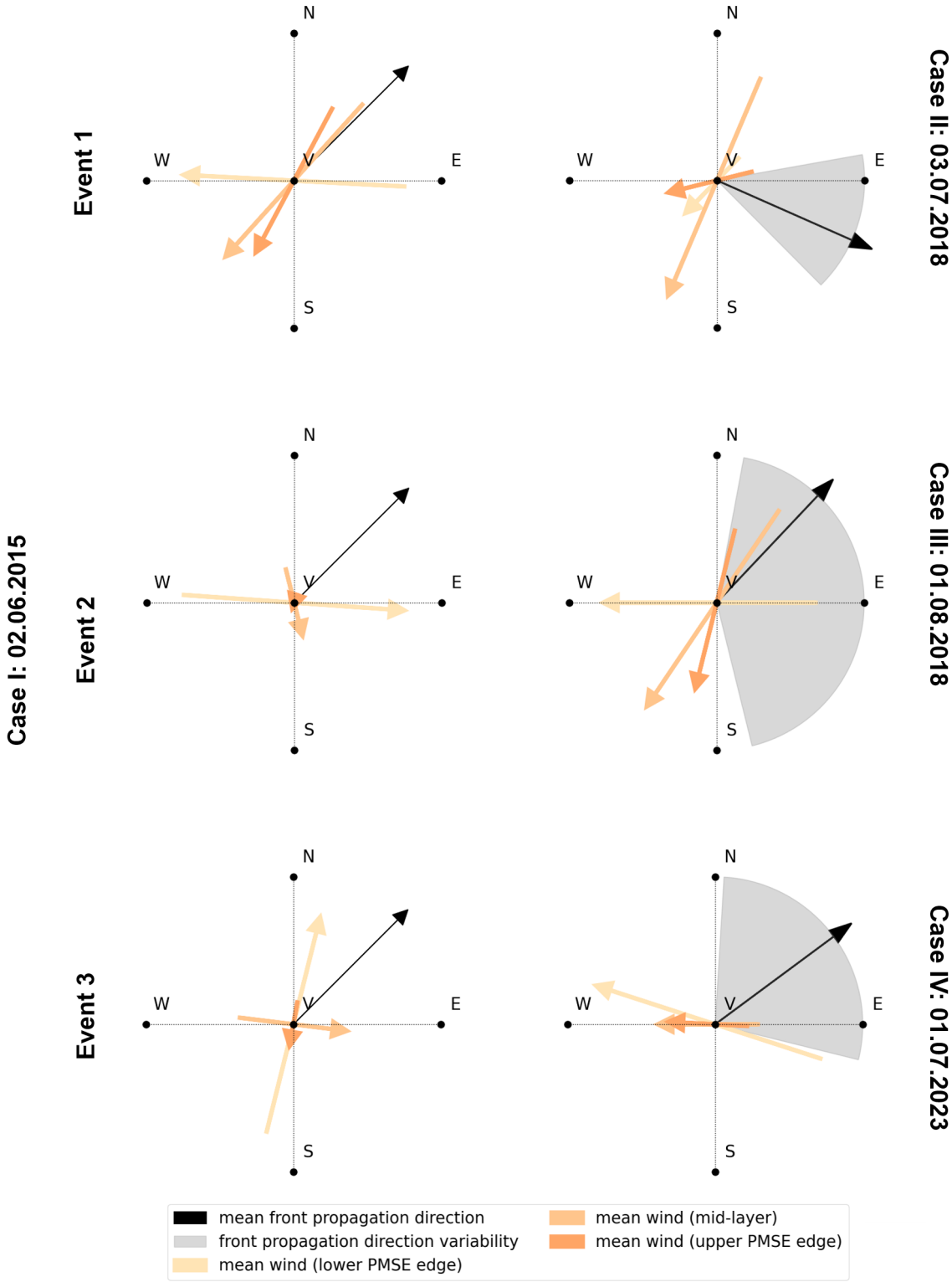


Figure 6.26: Summary of wind and event propagation directions for all four cases. The first column shows the three events of Case I; the second column shows Cases II–IV. Black arrows indicate mean front propagation: from radar imaging for Case I and time-delay estimates for Cases II–IV. Gray sectors represent angular uncertainty. Orange arrows show mean wind direction and relative strength at three PMSE altitudes (lower, middle, upper).

in event-to-mean-wind directions across cases and altitudes. The first column depicts the three events in Case I, while the second column presents Cases II to IV from top to bottom. Black arrows and gray areas indicate the range of propagation directions, and orange arrows represent the mean wind direction and its normalized magnitude, with shading distinguishing different altitudes. Interestingly, the angles of the fronts and their propagation velocities vary significantly across different quadrants spanned by the five different beams of MAARSY's DBS mode. This inconsistency hints at a rotating front, with clockwise rotation evident in all four cases. Hozumi et al. (2018) attribute such rotation to variations in duct depth, which can alter the propagation speed and direction of individual sections of the bore front. Differential interactions with horizontal wind dynamics further amplify these distortions, leading to a coherent rotational motion. Similar behavior has been observed in mesospheric bores, where localized atmospheric variability, such as changes in wind shear and duct properties, drives rotational or undulating features (e.g. Smith, 2003; Mondal et al., 2021). Additionally, studies suggest that undulating bore fronts could mimic rotational structures, as uneven phase speeds along the front can arise from variations in duct depth (e.g. Hozumi et al., 2018; Mondal et al., 2021).

The guiding mechanisms for these events warrant closer examination. Case I, for example, hints at a potential temperature inversion layer acting as a duct, based on temperature measurements averaged over an area of approximately 250 by 250 km. Such ducts can trap and guide wave energy, enabling propagation that defies ambient wind conditions (e.g. Dewan and Picard, 1998; Hozumi et al., 2018; Mondal et al., 2021; Ramachandran et al., 2023). Additionally, enhanced wind residuals, particularly in the meridional component, often coincide with these events, potentially amplifying local wind shear and creating favorable conditions for bore formation. However, the findings reveal that residuals are neither consistently correlated with nor a prerequisite for the occurrence of varicose-mode events.

Finally, the extreme vertical velocities observed in these events, such as the 40 m/s recorded in Case III, surpass typical predictions for mesospheric bores. Theoretical studies, such as those by Fritts et al. (2020), suggest that such velocities can develop under conditions of strong ducting and localized wave amplification. These high velocities might also reflect interactions between gravity waves and mesospheric turbulence, further underscoring the complexity of these events.

6.5.3 Complementary Observations from MAARSY and Saura PRR

To investigate the spatial extent and propagation characteristics of varicose-mode events, we combine observations from two mesospheric radar systems: MAARSY, a VHF radar operating near 53 MHz, and Saura PRR, an HF radar at approximately 3 MHz. Despite a horizontal separation of about 17 km, both systems probe the atmosphere around 80 km altitude, but through distinct measurement principles. MAARSY detects small-scale refractive index fluctuations via coherent backscatter, yielding high-resolution vertical profiles, while Saura PRR observes Doppler shifts and spectral width across multiple beam directions, providing horizontal context and flow orientation.

In two out of three analyzed events, Saura PRR recorded signatures that coincided in

time and altitude with varicose-mode structures identified in MAARSY data. These included enhancements in radial velocity – regardless of sign – and notable increases in spectral width and signal power. The temporal and altitudinal alignment across both systems makes a coincidental detection unlikely and points toward a physically coherent, horizontally extended structure. Notably, each of these cases showed signatures in at least three Saura PRR beams, supporting the interpretation of a spatially broad disturbance intersecting multiple viewing geometries. The physical interpretation of these radar signatures is essential: Enhancements in radial velocity, whether positive or negative, reflect intensified vertical motions – typically linked to wave-like disturbances such as varicose-mode events, gravity waves, or mesospheric bores. Abrupt sign changes in radial velocity further indicate vertically oscillating flows with steep vertical gradients. In contrast, increases in spectral width signify elevated variability along the line of sight, commonly associated with turbulence, wave breaking, or shear instabilities. However, broadening can also result from non-turbulent processes such as confined wave propa-

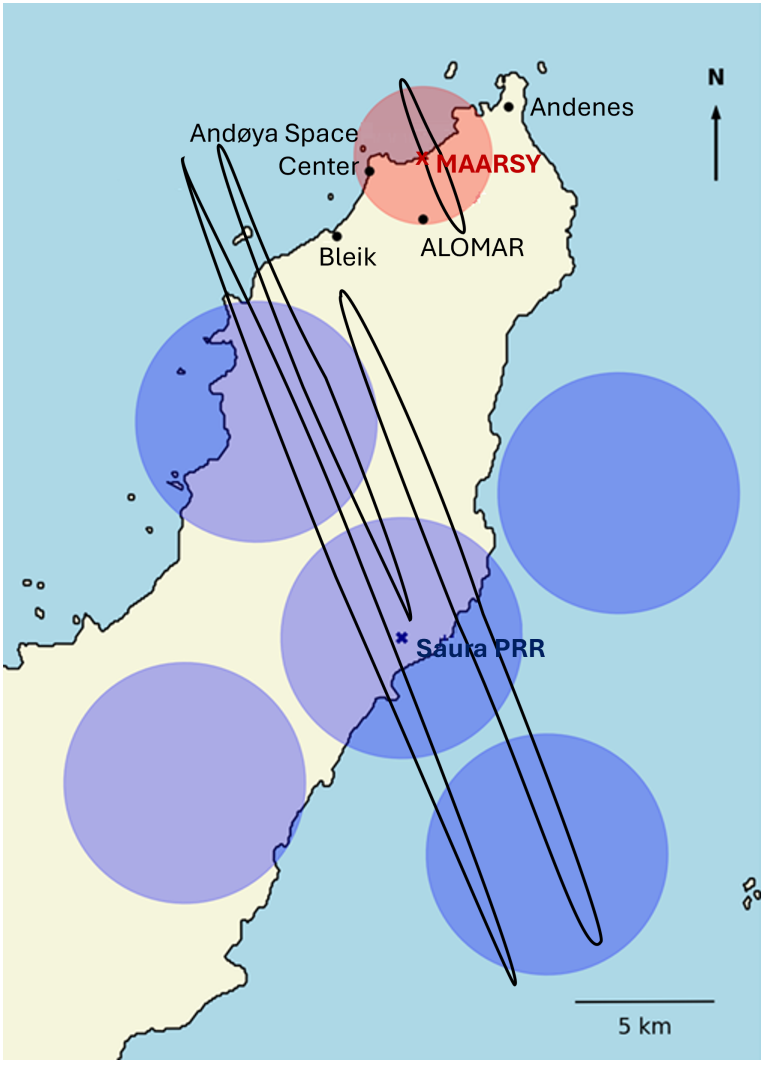


Figure 6.27: Schematic of selected scenarios illustrating how a varicose-mode event (black contours) may pass over the FOVs of MAARSY (red) and Saura PRR (blue). The event is assumed to propagate from southwest to northeast with a slight inclination, representative of typical observations.

gation within narrow ducts (e.g., Hocking, 1986; Hocking, 1996; Lübken, 2014). When such spectral width enhancements coincide with structured radial velocity features, the combined evidence strongly favors the presence of real, organized vertical motion rather than background variability.
These radar signatures did not appear uniformly across all beam directions. This beam-specific visibility suggests that the events were horizontally anisotropic – tilted, narrow, or localized – such that only certain beam paths intersected the active region. Importantly, this applies to both systems. In some instances, events were clearly visible in MAARSY but left no discernible trace in Saura PRR data. In others, Saura measurements exhibited a pronounced response, while MAARSY showed only weak backscatter and lower radial velocities. To illustrate this beam-dependent visibility, Fig. 6.27 presents four schematic scenarios of elongated, slightly inclined structures propagating from SW to NE. These examples show how the same event can register strongly in one system while remaining weak or absent in the other. This variability underscores the importance of radar geometry and beam orientation in the detection of spatially confined structures.

6.5.4 Residual Wind Variability

The background wind fields provide essential information on the broader atmospheric state but do not resolve shorter-period fluctuations that may be relevant for the initiation

Table 6.3: Residual-wind summary for four cases: event presence, components, timescales, off-event enhancements, vertical structure

Residual Wind Signature Summary				
Aspect	**Case I**	**Case II**	**Case III**	**Case IV**
Enhancement at event time?	Yes, clear peaks at 3 events	No, lower residuals	Partial: only meridional	Unclear, residuals generally high
Component(s) affected?	Zonal + Meridional	Slightly meridional	Mainly meridional	Meridional + zonal (6–10 h)
Dominant time scales	3 h, 8 h	10 h (meridional)	3–8 h (meridional), 6–10 h (zonal)	8 h, 10 h
Enhancements at other times?	Yes, less pronounced	Yes, before and after	Yes, 1 and 5 days before	Yes, on nearby days
Altitude dependence?	Peaks at 82 and 97 km	Minor	Shifted timing with height	Vertical tilt across layers

or modulation of varicose-mode events. To isolate such variability, the horizontal wind components were filtered using running means of 3, 6, 8, and 10 hours. This residual analysis suppresses longer-period oscillations such as tides and gravity waves, thereby highlighting transient deviations from the mean flow that could indicate mesoscale disturbances or localized wind variability.

Table 6.4: Summary of key findings for each case study.

Key Findings Summary				
Aspect	**Case I**	**Case II**	**Case III**	**Case IV**
Shear at the bottom of the PMSE layer?	moderate, 15 m/s/km	strong, 40 m/s/km	strong, 30 m/s/km	moderate, 25 m/s/km
Shear at the center of the PMSE layer?	minimal	minimal	minimal	minimal
Shear at the top of the PMSE layer?	moderate, 15 m/s/km	moderate, 30 m/s/km	strong, 30 m/s/km	moderate, 25 m/s/km
Horizontal wind magnitude maxima and position?	80 - 85 m/s, center	100 m/s, lower boundary	100 m/s, center	90 m/s, upper boundary
Movement relative to mean wind?	at an angle to opposite	at an angle	at an angle	at an angle to opposite
Duration of event?	18–24 min	20 min	23 min	22 min
Maximum vertical velocity (m/s)?	up to 14 m/s	up to 22 m/s	up to 45 m/s	up to 25 m/s
Layer expansion factor?	1.4 - 1.6	4.5	1.4	1.6
Vertical extent of the PMSE layer?	8 - 9 km	9 km	10 km	11 km
Spectral width observations?	low to minimal	slight increases post-event	high in upper PMSE layer	enhanced at upper PMSE layer
Temperature inversion layer detected?	likely	–	–	–
Movement direction?	SE to NW	NW to SE	SW to NE	SW to NE
Wind residual enhancements?	yes (zonal + meridional)	yes (meridional), no (zonal)	minimal (meridional), no (zonal)	yes (meridional + zonal)
Signatures in Saura PRR?	yes	yes	–	yes

The results, summarized in Tab. 6.3, show enhanced residuals in three out of four case studies, with deviations appearing close in time and altitude to the observed events. In two cases, both zonal and meridional residuals were elevated; in one case, the enhancement was limited to the meridional component. Only one case exhibited weak or absent residual signatures. These findings suggest that short-term fluctuations in the horizontal wind field, particularly in the meridional direction, may contribute to the formation or amplification of varicose-mode structures by increasing local shear or supporting ducted wave propagation.

However, similar enhancements also occur at other times in the 10-day residual time series without coinciding with any varicose-mode events. This indicates that while residual wind variability may influence the likelihood or characteristics of an event, it is not a sufficient condition on its own. Other factors – such as vertical wind structure, background stratification, and the presence of ducts – likely play an equally or more critical role. Nonetheless, the residual wind analysis offers valuable insight into the dynamic background environment and helps identify conditions that may favor the occurrence of small-scale disturbances, even if the connection is not universally predictive.

The findings discussed above are summarized in Tab. 6.4, which outlines key observational metrics for each case, including vertical velocities, spectral widths, propagation characteristics, wind residuals, and radar signatures.

7 Conclusions and Outlook

This thesis presents the first dedicated study of varicose-mode events in the polar mesosphere, combining a comprehensive statistical analysis with multi-instrument case studies. The findings confirm that these events are not isolated anomalies but recurrent features of the upper atmosphere. Notably, the extreme event reported by Chau et al. (2021) is not an outlier, but one example of a broader population of dynamic structures that occur regularly under suitable conditions. They appear as coherent wave-like disturbances with sharp vertical gradients and relatively small vertical extent compared to their horizontal scale (e.g. 8 km vertical vs. $\geq$ 17 km horizontal), adding a new piece to the puzzle of how the upper atmosphere behaves. While some events maintain a clear structure over time and space, others evolve more irregularly – pointing to diverse formation mechanisms and local atmospheric influences.

A total of 707 varicose-mode events were identified in MAARSY radar data from 2015 to 2021, of which 187 exhibited vertical velocities exceeding 15 m/s, more than twice the expected maximum for this region. This demonstrates that high-velocity, structured wave activity is a recurring mesospheric phenomenon. Events were detected in every PMSE season, with the highest occurrence rates observed in June and July. Diurnal variation revealed a maximum between 12:00 and 16:00 UT and a minimum between 18:00 and 20:00 UT. This suggests that their occurrence is linked not only to the seasonal presence of PMSE but also to specific wave and instability conditions in the mesosphere. The events consistently featured quasi-simultaneous up- and downdrafts lasting on average 20 minutes, causing a vertical expansion of the PMSE layer by a factor of up to 1.7 to approximately 8 km. The 187 high-velocity events had slightly longer durations and smaller average vertical extents, but exhibited more pronounced vertical expansions relative to the background PMSE layer.
Interestingly, no direct correlation was found between vertical velocity, event duration, and expansion factor. This suggests that the dynamics are governed by a combination of local atmospheric conditions, rather than a single controlling parameter.

Four case studies further showed that these structures propagate horizontally across the radar field of view, with all four analyzed events exhibiting motion at angles to or even against the background wind. Horizontal extents exceeded 17 km, with anisotropic fronts varying in height, strength, and internal structure. Observations from MAARSY and Saura PRR confirmed that these events can be captured across different radar systems, underlining their mesoscale coherence and the value of complementary measurements.
These results collectively establish varicose-mode events as important and underexplored components of mesospheric dynamics. Their ability to transport momentum vertically, modulate turbulence, and evolve independently of mean wind flow highlights their potential role in atmospheric coupling processes.

To build on these insights, future research should aim to extend the observational foundation and improve diagnostic capability. This includes incorporating additional years of MAARSY data and revisiting older datasets such as those from the ALomar WINd radar (ALWIN). Owing to its long coherent integration times, ALWIN has a comparatively

low Nyquist velocity, which limits its ability to quantitatively resolve the strongest, high-velocity events discussed in this study. Nevertheless, its records may still be exploited to identify varicose-mode events in general, to examine their occurrence, morphology, and vertical extent, and to place the MAARSY-based results into a longer-term climatological context, while acknowledging that vertical velocities approaching or exceeding the Nyquist limit will be affected by aliasing.

Expanding the analysis to other high-latitude radar stations, such as the European Incoherent SCATter Scientific Association (EISCAT) UHF radar in Tromsø, the EISCAT facility in Kiruna, or the EISCAT Svalbard Radar (ESR) in Ny-Ålesund, would allow for comparative studies and assess whether such events are a broader polar phenomenon. In addition, the Kilpisjärvi Atmospheric Imaging Receiver Array (KAIRA) offers opportunities for multistatic observations in conjunction with MAARSY. This setup could improve spatial coverage and temporal resolution of wind fields and wave structures, enabling refined insights into the morphology and evolution of varicose-mode events.
Improved spatial resolution is needed to better understand the morphology and structure of these events. Applying radar imaging techniques, particularly coherent MIMO systems, would help resolve horizontal features at kilometer-scale resolution and clarify whether the observed anisotropy reflects true event geometry or observational artifacts.
To better understand the environmental conditions that enable varicose-mode events, co-located measurements of temperature and wind should be conducted using instruments like SIMONe or iron lidars. These data could confirm the presence of thermal ducts or inversion layers and clarify their role in trapping and guiding these structures.
Airglow imaging represents a useful complementary technique for identifying trailing wave activity and detecting subtle vertical motions in the mesopause region. However, such observations are not possible during the polar summer, when continuous daylight prevents the detection of airglow emissions. Since the MAARSY observations in this study were conducted under polar-summer conditions and rely on PMSE as tracers, airglow imaging cannot be applied here. Nevertheless, outside the PMSE season—when no suitable tracer is available—airglow imagers offer a promising alternative for detecting varicose-mode events and assessing their vertical and horizontal extent.
A deeper theoretical understanding is needed to contextualize the observations. Future work should include DNS with realistic atmospheric profiles and wind shear. Such simulations would help test hypotheses about the onset and evolution of these events and evaluate whether current model physics can reproduce the extreme velocities and structural variability observed.
A coordinated multi-instrument campaign during June and July – when event likelihood is highest – would be an ideal strategy for capturing the full lifecycle of varicose-mode events. Integrating vertical profiling (e.g. MAARSY), horizontal context (e.g. Saura PRR and MAARSY multibeam mode), background condition monitoring (e.g. lidar), and wide-field imaging (e.g. airglow) would provide a comprehensive dataset for both empirical analysis and model validation.

The use of physics-informed machine learning tools such as HYPER (HYbrid Pattern Extraction and Recognition), developed at IAP, may offer new opportunities to detect weak or morphologically complex events in large radar datasets. By combining physical constraints with advanced pattern recognition, such methods could help uncover finer-scale dynamics and support more robust event classification. These tools may also

provide improved initial conditions for simulations and facilitate the identification of structures otherwise hidden in noisy or ambiguous observations (Urco et al., 2024).

While the dynamics of varicose-mode events are increasingly understood, they remain absent from current general circulation and climate models. Their scale and rapid evolution pose challenges for representation in global simulations, yet their contribution to vertical momentum transport and mesospheric turbulence could influence broader atmospheric processes. A better observational and theoretical understanding will be essential to develop meaningful parameterizations that could be integrated into large-scale models.

Moreover, small-scale instabilities in the MLT region – such as those investigated here – may act as precursors to larger-scale responses in the thermosphere. These vertical couplings remain underrepresented in most operational models. For instance, the unexpected loss of Starlink satellites in February 2022 has demonstrated the vulnerability of space operations to poorly resolved or predicted upper atmospheric dynamics. While the primary driver in that case was enhanced thermospheric drag during a geomagnetic storm (Baruah et al., 2024), unresolved mesoscale structures in the lower thermosphere and mesosphere may contribute to localized density enhancements or turbulence that further complicate forecasts.
As commercial spaceflight and satellite operations continue to expand, particularly in low-Earth and suborbital orbits, accurate knowledge of upper-atmospheric variability becomes increasingly important. Varicose-mode events represent one manifestation of small-scale dynamical disturbances that can modify winds, temperatures, and—through adiabatic and hydrostatic effects—local density structures in the mesopause region. Although the present study does not directly observe density changes, such responses are a well-established consequence of small-scale wave dynamics. Improved understanding of these processes contributes to refining upper-atmospheric models used for satellite drag estimation, trajectory planning, and space-weather applications. Continued investigation of varicose-mode events, therefore, advances both fundamental understanding and the reliability of operational models of the near-space environment.

This study lays a robust foundation for future investigations and redefines varicose-mode events as integral elements of the polar mesosphere. Their recurrence, variability, and scale make them deserving of continued and expanded scientific attention, both to better understand their dynamics and to explore their broader role in upper atmospheric processes. As such, this work should also serve as a motivation to recognize and systematically investigate small-scale atmospheric dynamics, which continue to be underrepresented in both theory and practice despite their disproportionate influence on larger-scale processes.

Appendix

A0.1 Additional Plots

A0.1.1 Examples of Varicose-Mode Events and Schematics

Figure A0.1 shows two examples of varicose-mode events, with vertical velocity data (top) and schematic representations (bottom).

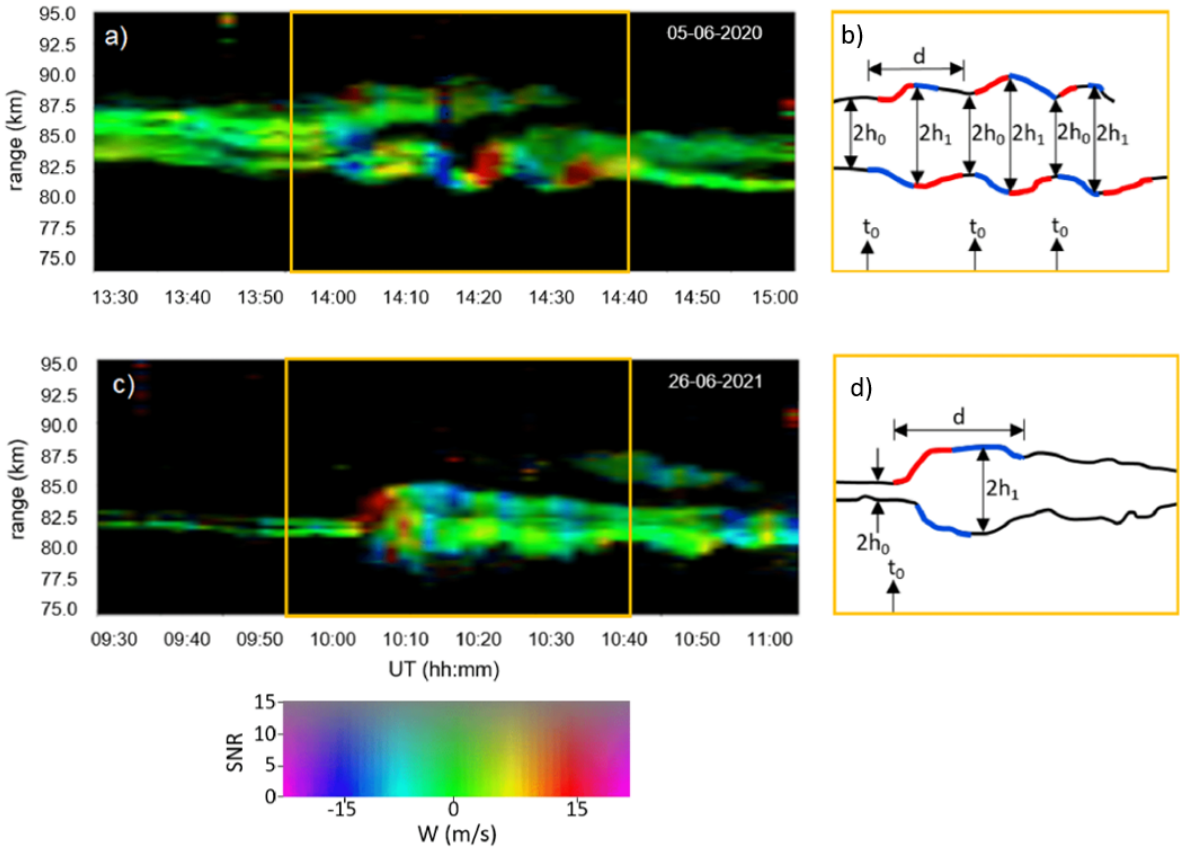


Figure A0.1: Two Examples of varicose-mode events found on 5 June 2020 and 26 June 2021. a) and c) Shown is the vertical velocity evolution in time (color-coded) in an altitude range between 75 and 95 km, exhibiting the simultaneous up and downwards motions (varicose modes). b) and d) depict the schematics of the events with h_0 and h_1 as the thickness of the PMSE layer in its undisturbed and disturbed state, respectively. t_0 represents the starting time and d their duration. The red and blue colors emphasize the vertical wind direction, similar to a) and c). (adapted from Hartisch et al. (2024))

A0.1.2 Intermediate Data Cleaning Step

Illustration of the vertical velocity field before and after applying a data mask to enhance event visibility.

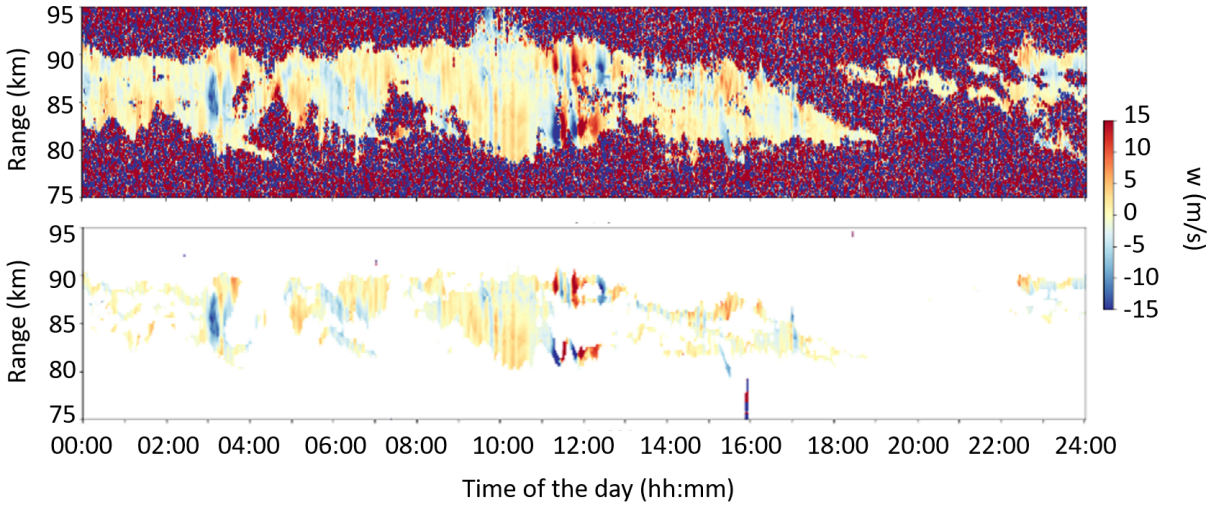


Figure A0.2: Range-Time-radial velocity plots. Top: before applying data cleaning via applying masks. Bottom: cleaned dataset for varicose-mode event identification.

A0.2 Multi-Instrument Case Studies

A0.2.1 Case I

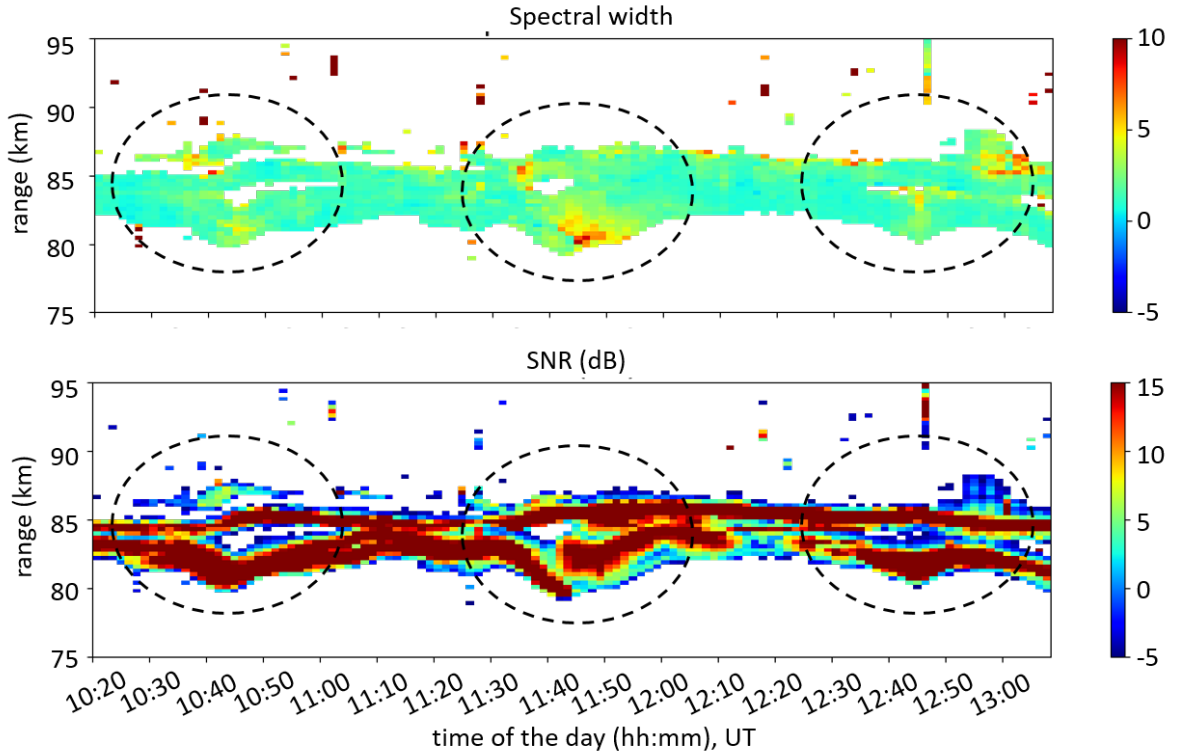


Figure A0.3: Range-time-spectral width (top) and -signal-to-noise-ratio (bottom) representation of case I, observed on June 2, 2015, between 10:30 UT and 12:30 UT. The events are highlighted by the dashed ellipses.

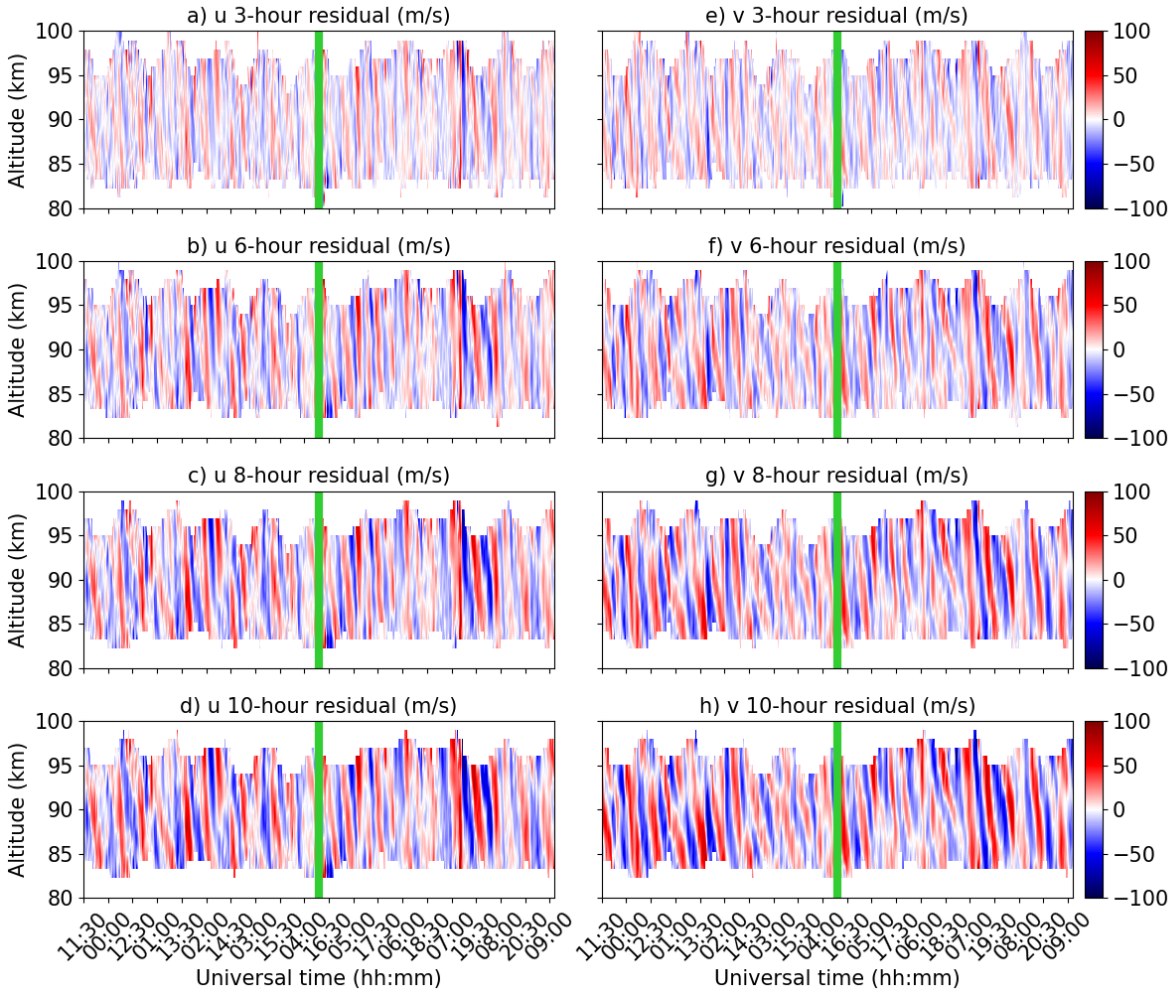


Figure A0.4: Residuals of zonal (left) and meridional (right) wind components from MMARIA Norway, after removing a running mean over 3, 6, 8, and 10 hours (rows 1–4), for 5 days before and after the event (green vertical lines).

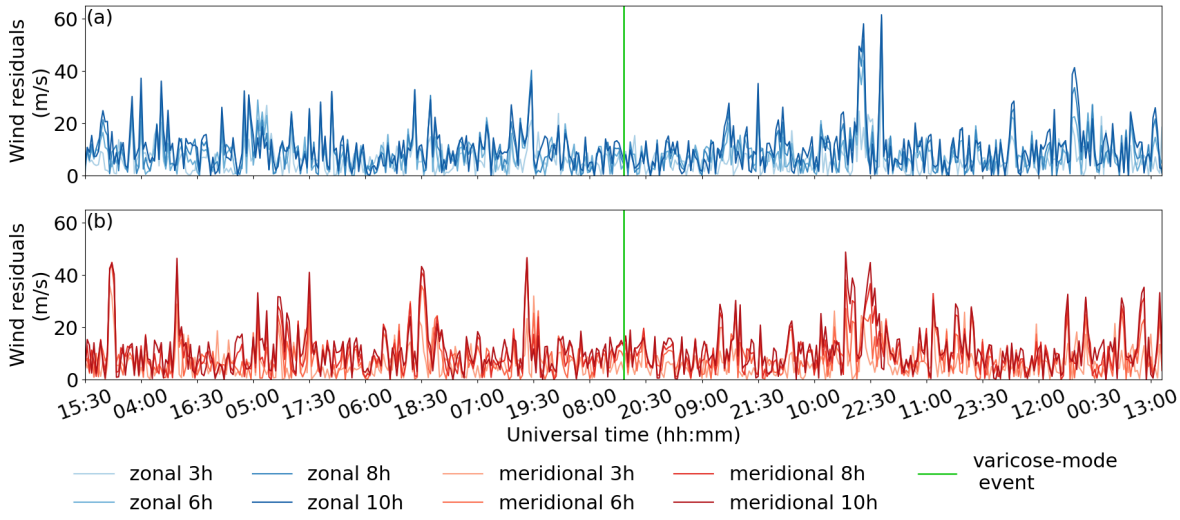


Figure A0.5: Absolute magnitudes of the zonal (a) and meridional (b) wind components at 85 km altitude, measured by MMARIA Norway over the course of 48 hours around the events (green vertical lines).

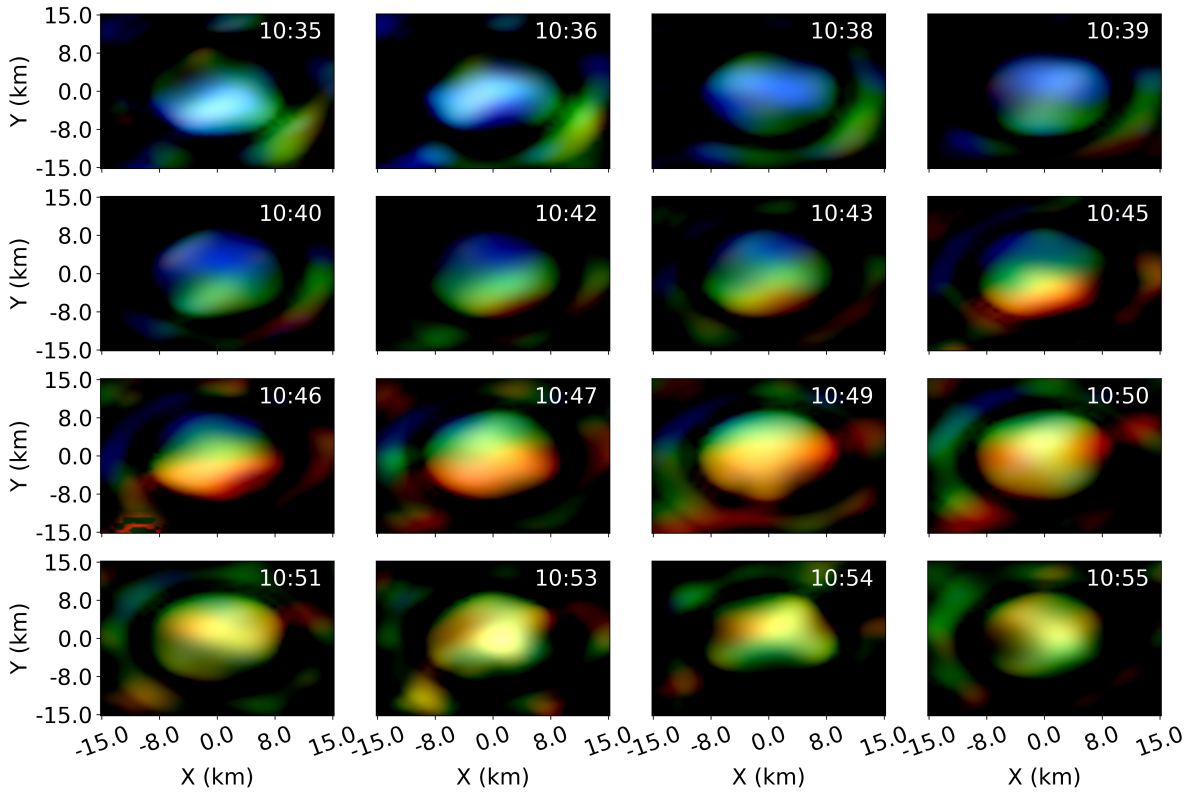


Figure A0.6: Temporal evolution of the first event of this case along xy-plane at a fixed altitude of z = 81 km from their initial to their final stage. The color representation is the same as in Fig. 6.8.

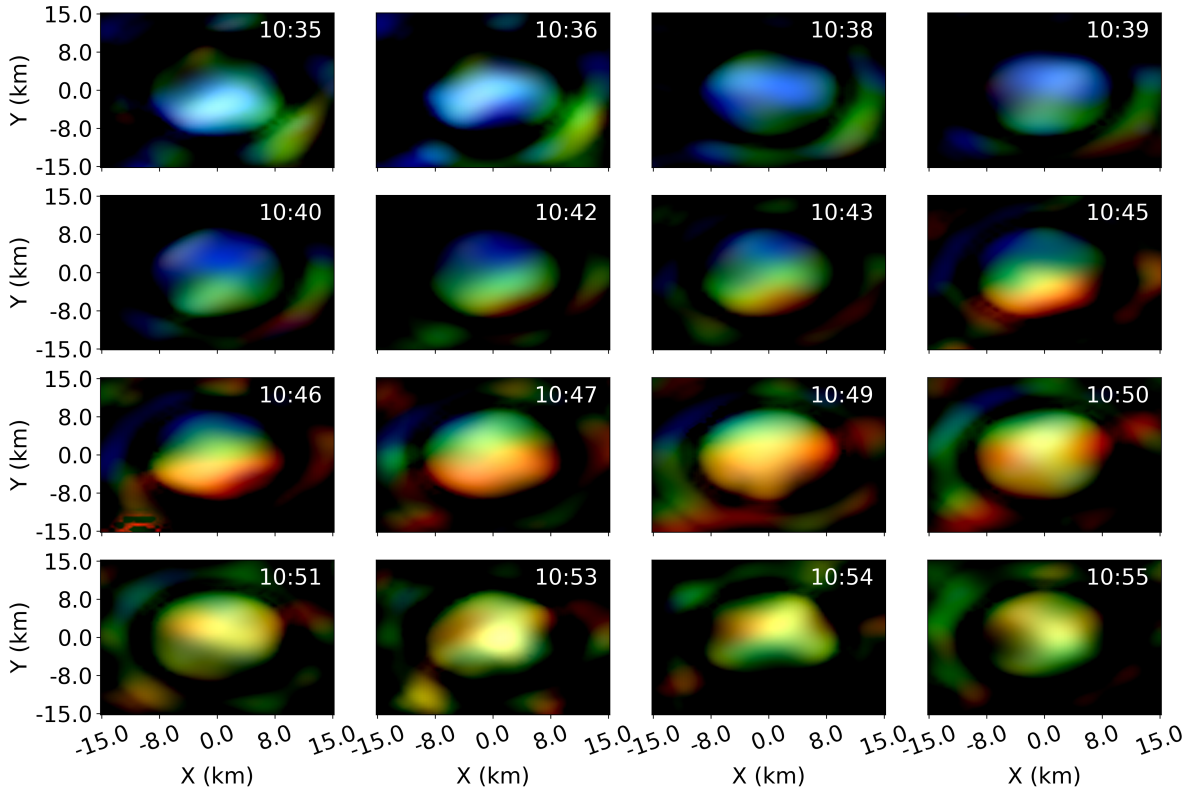


Figure A0.7: Same as Fig. A0.6 but for the second event.

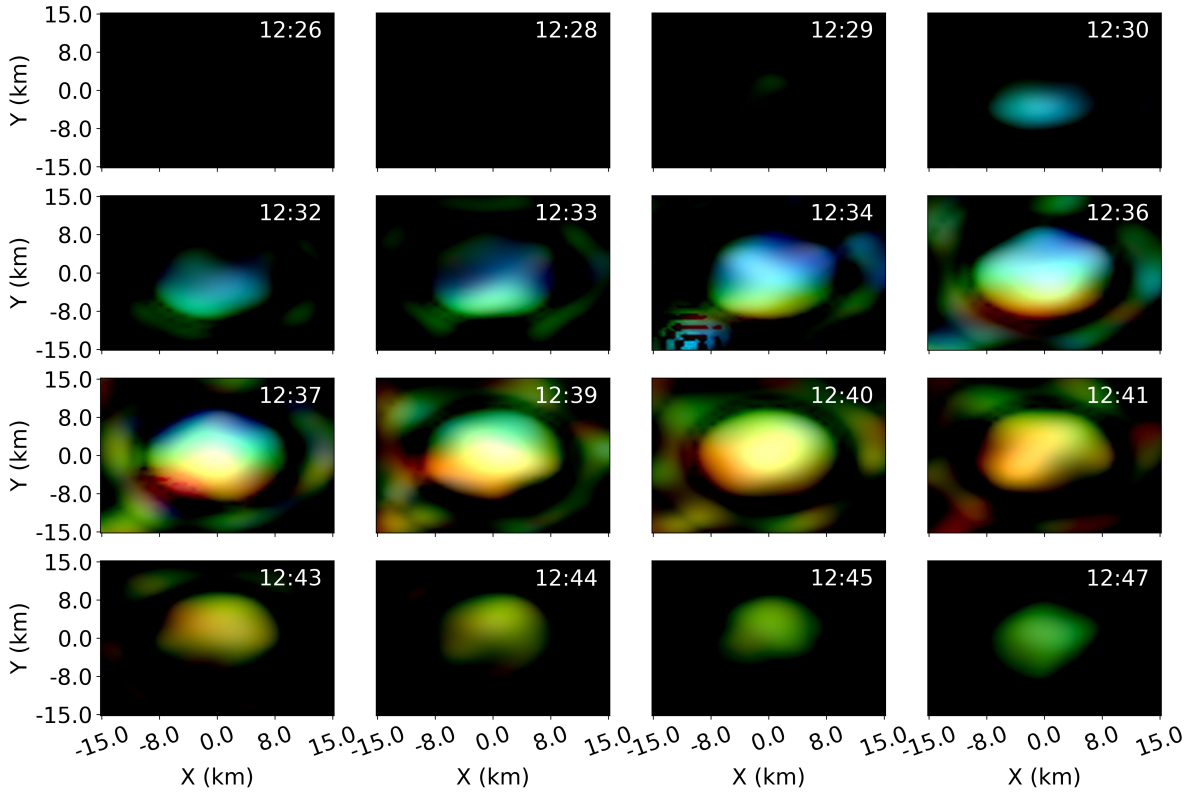


Figure A0.8: Same as Fig. A0.6 but for the third event.

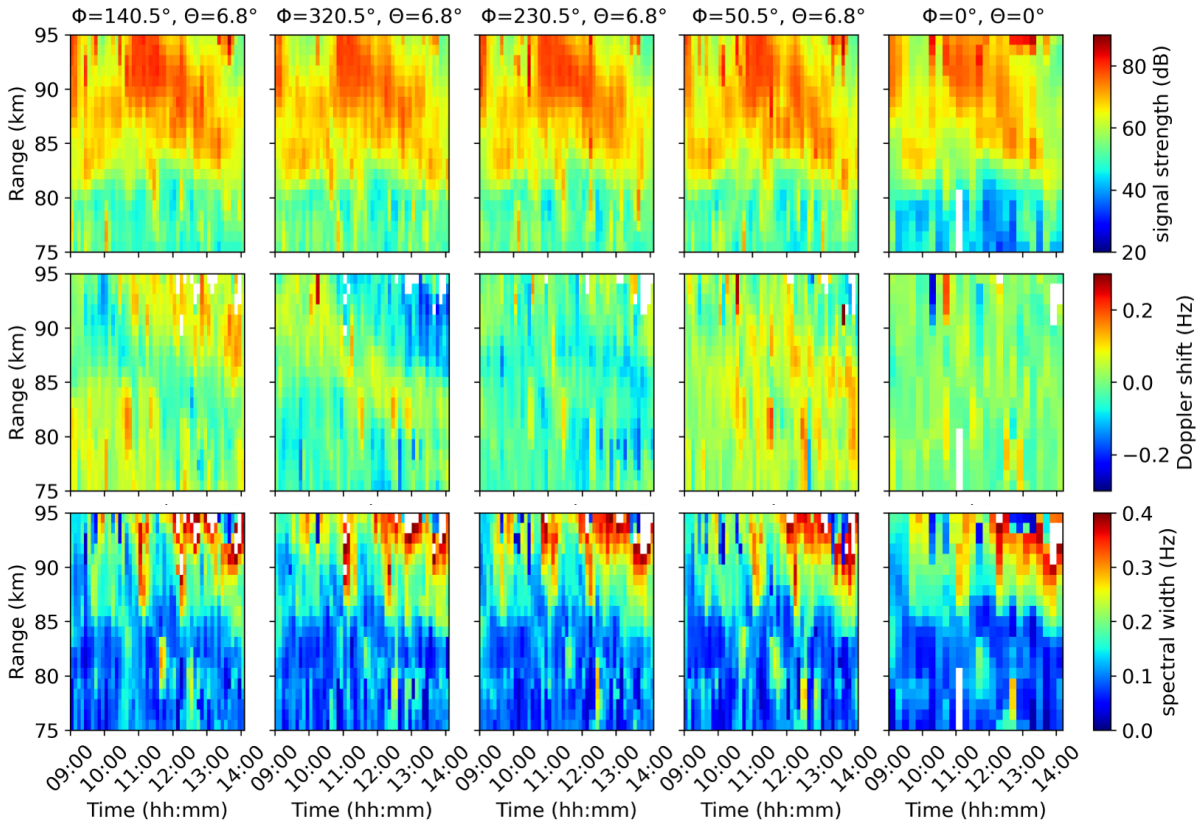


Figure A0.9: Signal strength (top), Doppler shift (middle), and spectral width (bottom) around the time of the Case I event observation with MAARSY. Shown are all five beam pointing directions: vertical, NE, SW, NW, and SE (left to right).

A0.2.2 case II

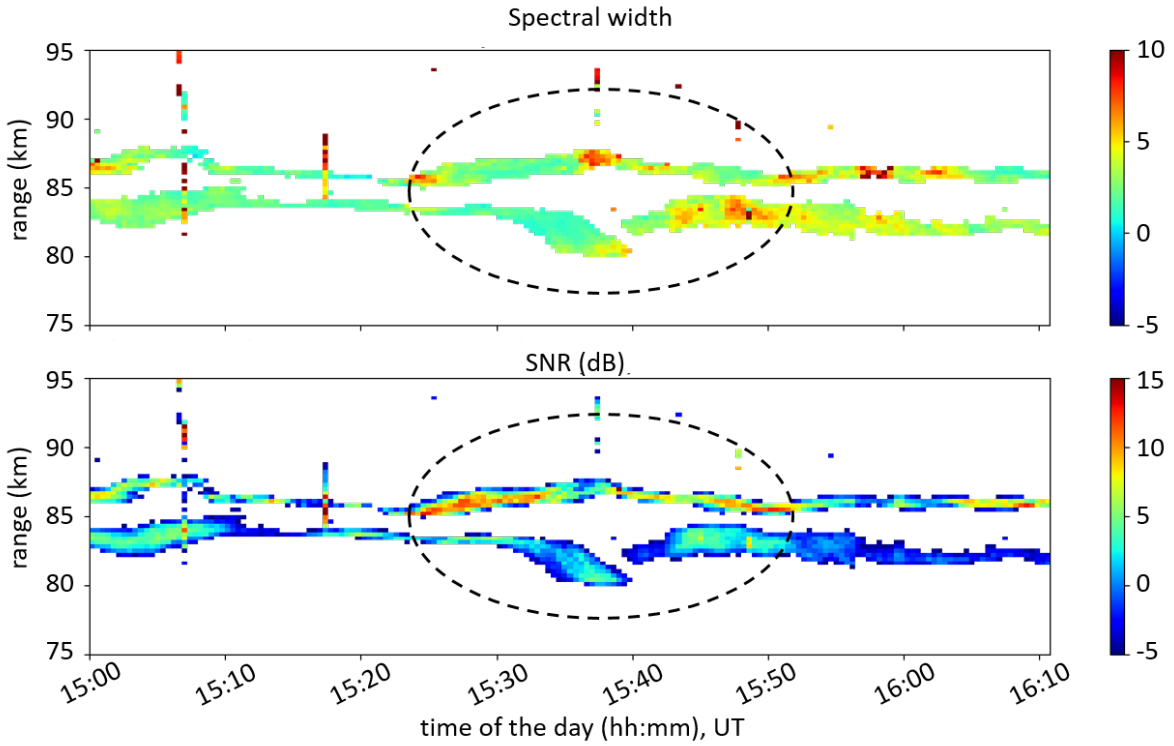


Figure A0.10: Same as Fig. A0.3 but for Case II.

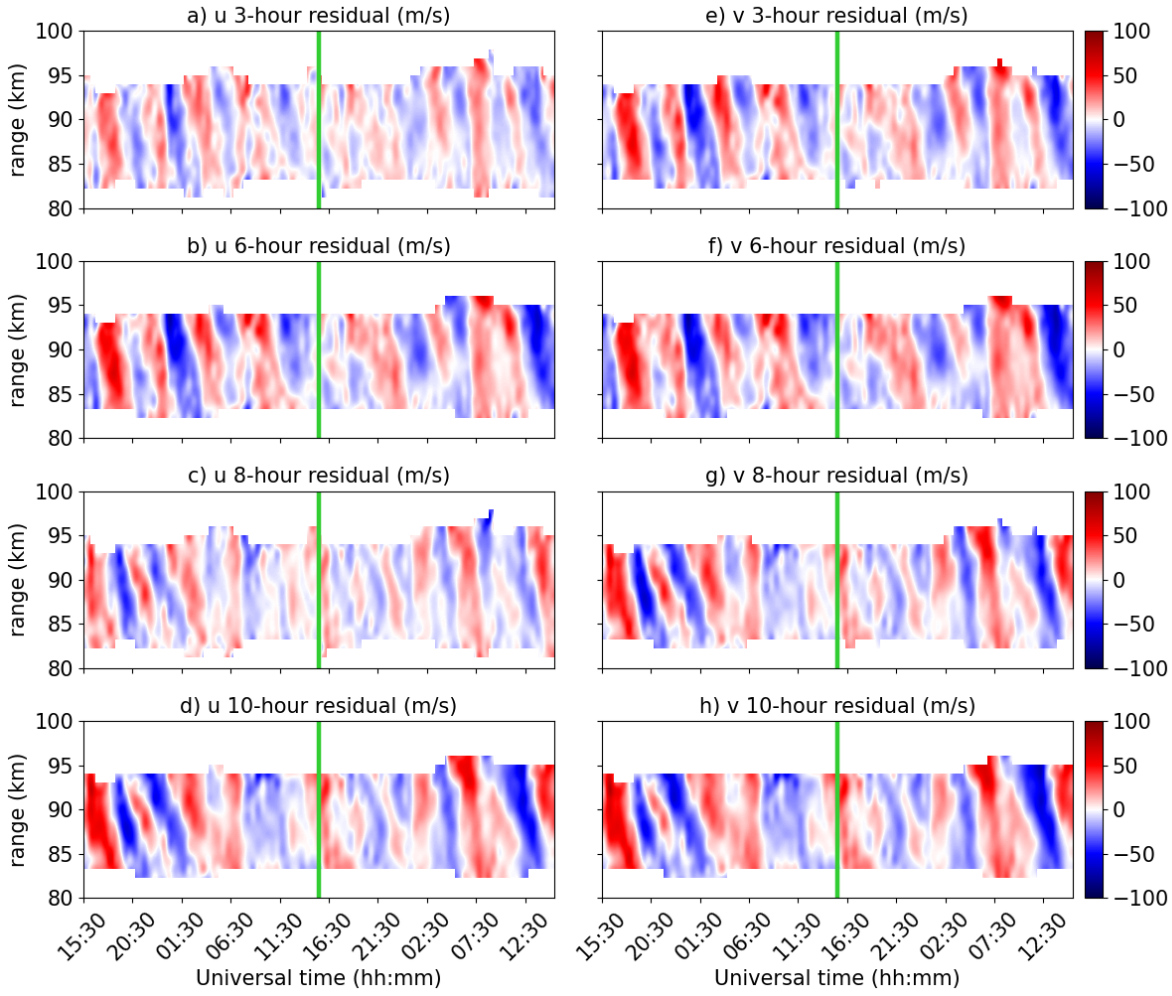


Figure A0.11: Residuals of zonal (left) and meridional (right) wind components from MMARIA Norway, after removing a running mean over 3, 6, 8, and 10 hours, for 48 hours around the event (green vertical lines).

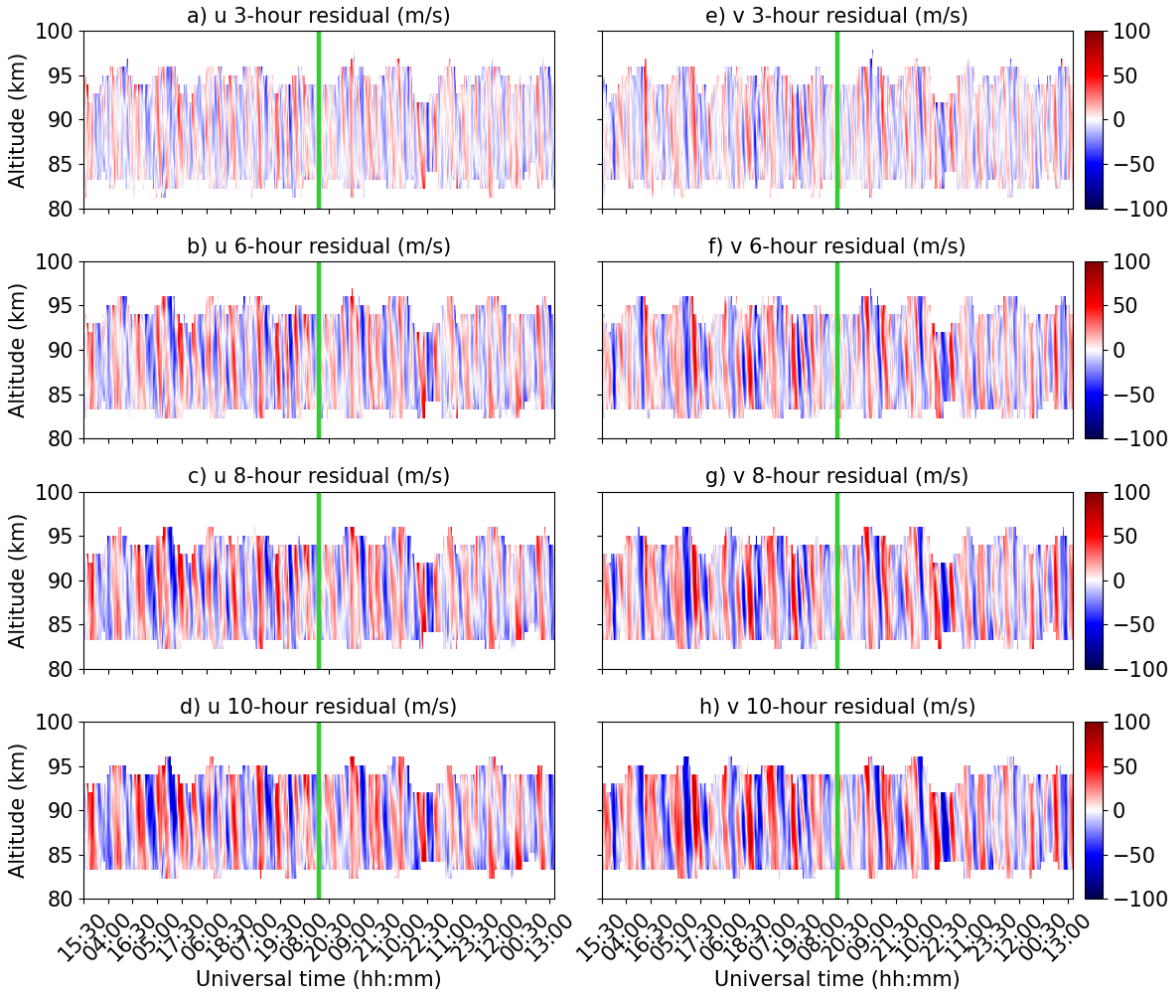


Figure A0.12: Same as Fig. A0.4 but for Case II.

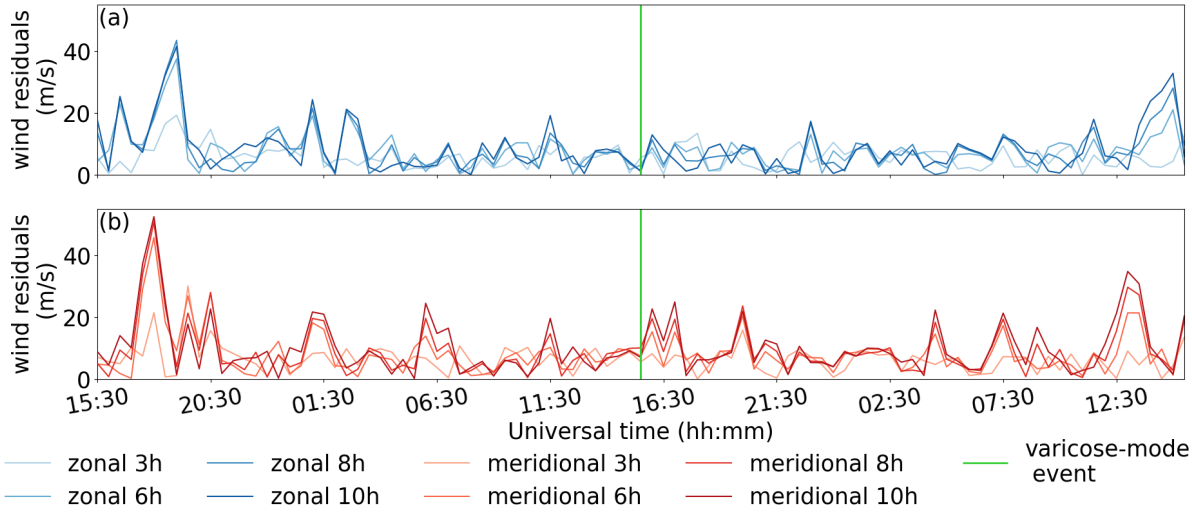


Figure A0.13: Absolute magnitudes of the zonal (a) and meridional (b) wind components at 85 km altitude, measured by MMARIA Norway over the course of 48 hours around the events (green vertical lines).

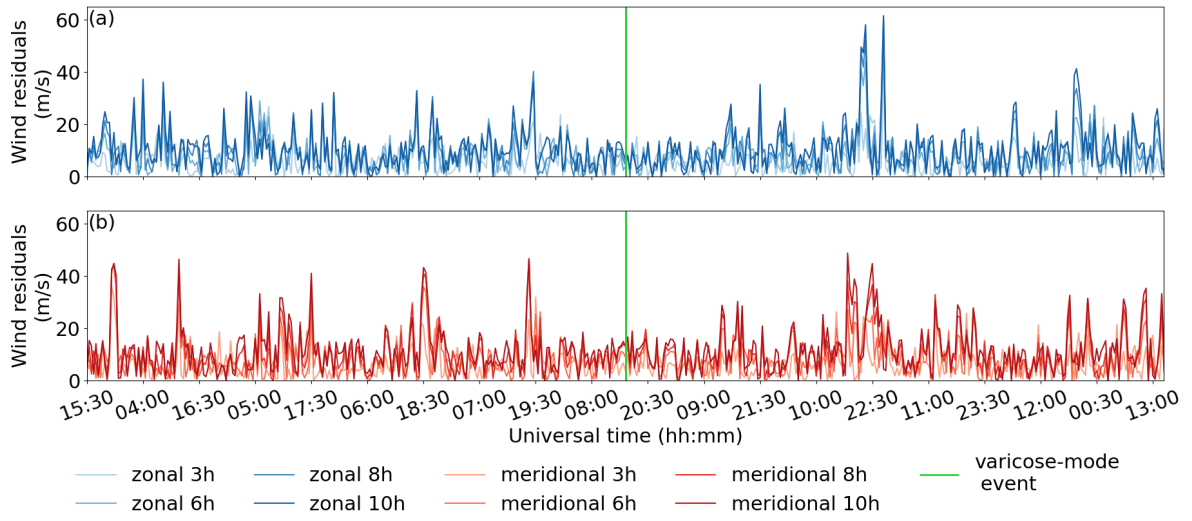


Figure A0.14: Same as Fig. A0.5 but for Case II.

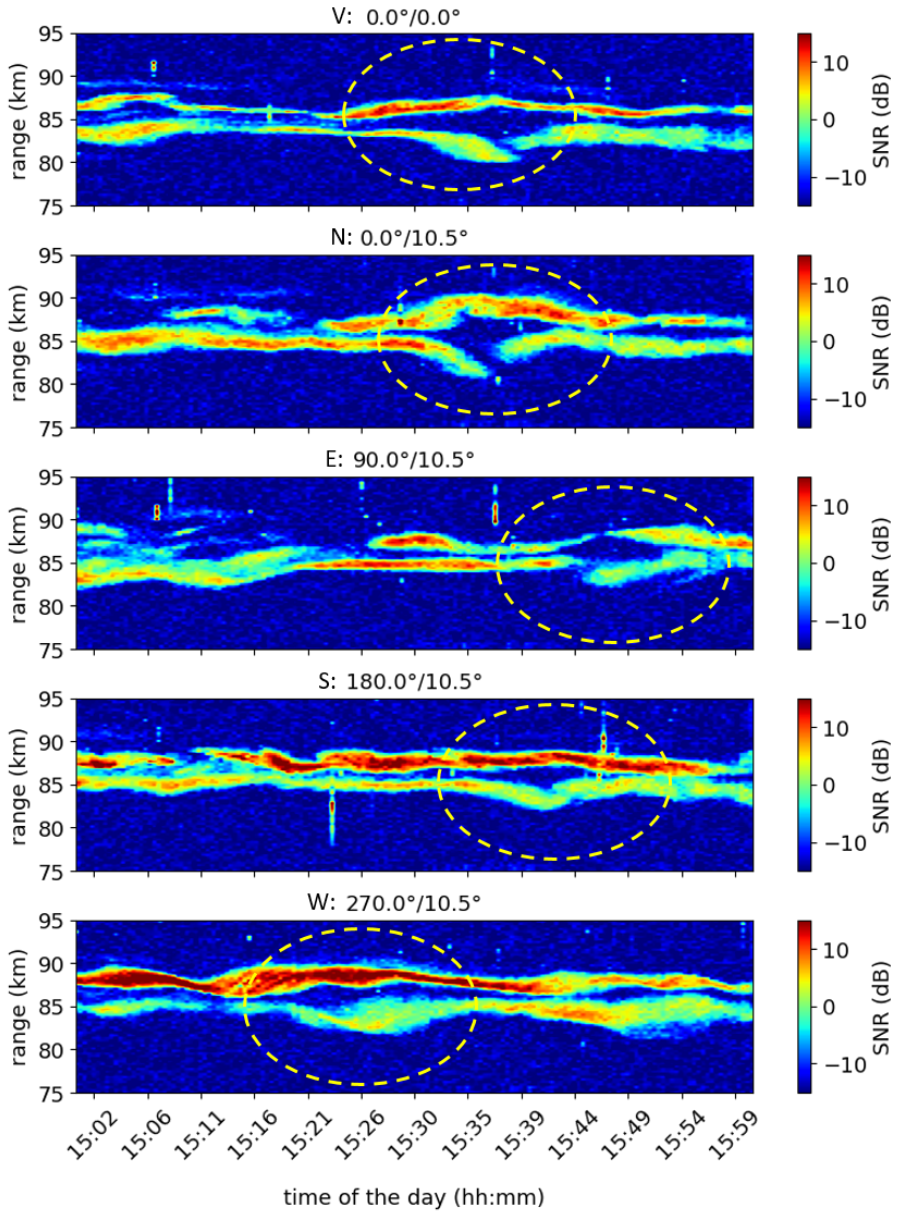


Figure A0.15: Signal-to-Noise ratio for Case II for 5 beam pointing directions (top to bottom: Vertical, North, East, South and West) using MAARSY. The event is highlighted with yellow ellipses.

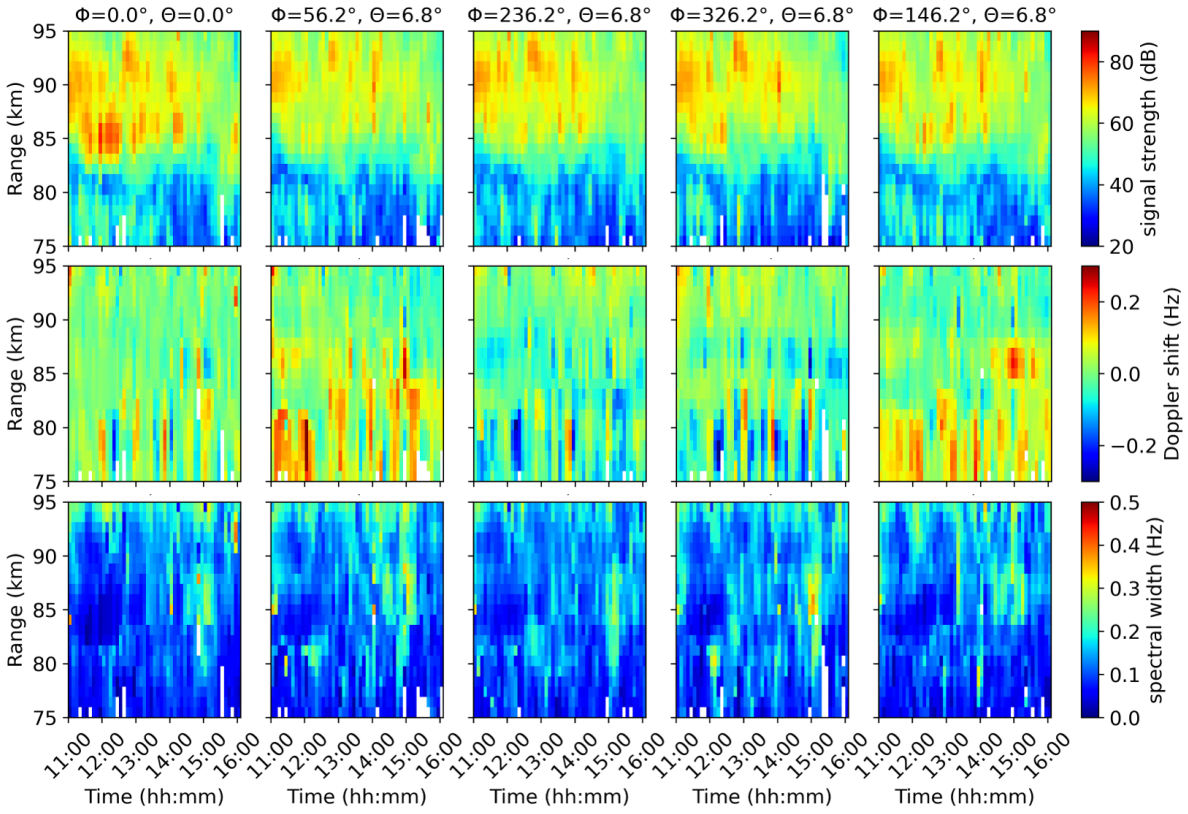


Figure A0.16: Same as Fig. A0.9 but for Case II.

A0.2.3 case III

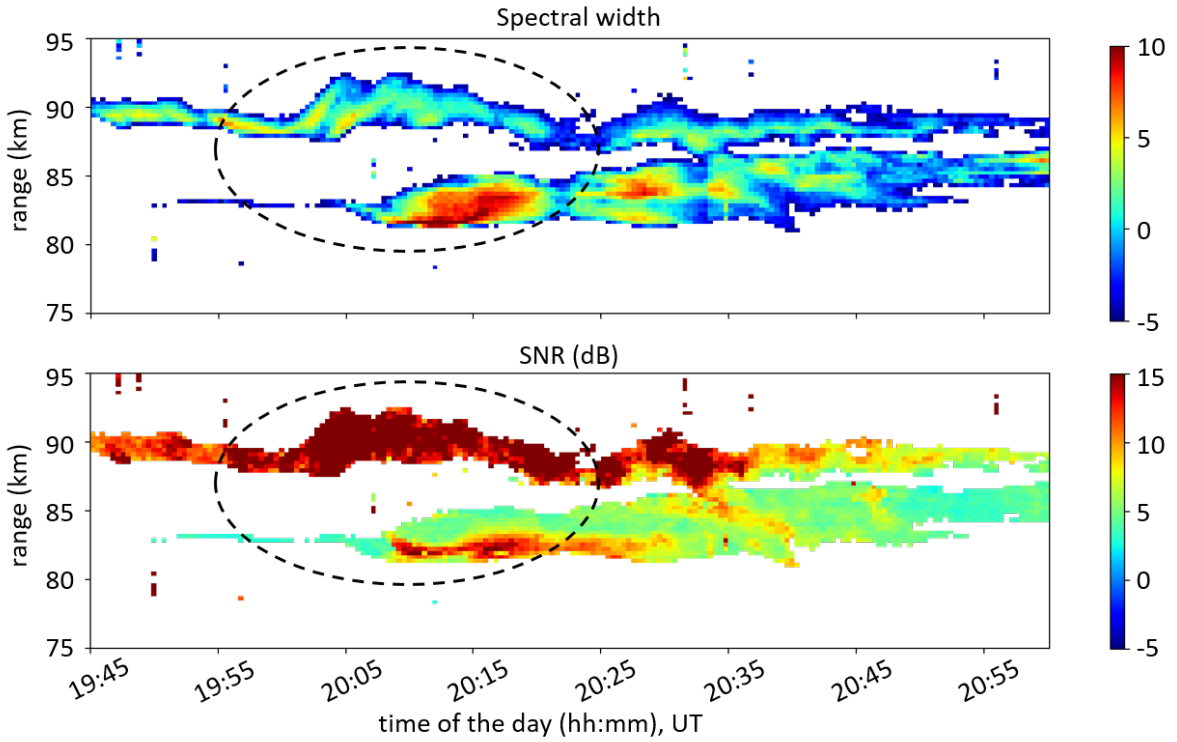


Figure A0.17: Same as Fig. A0.3 but for Case III.

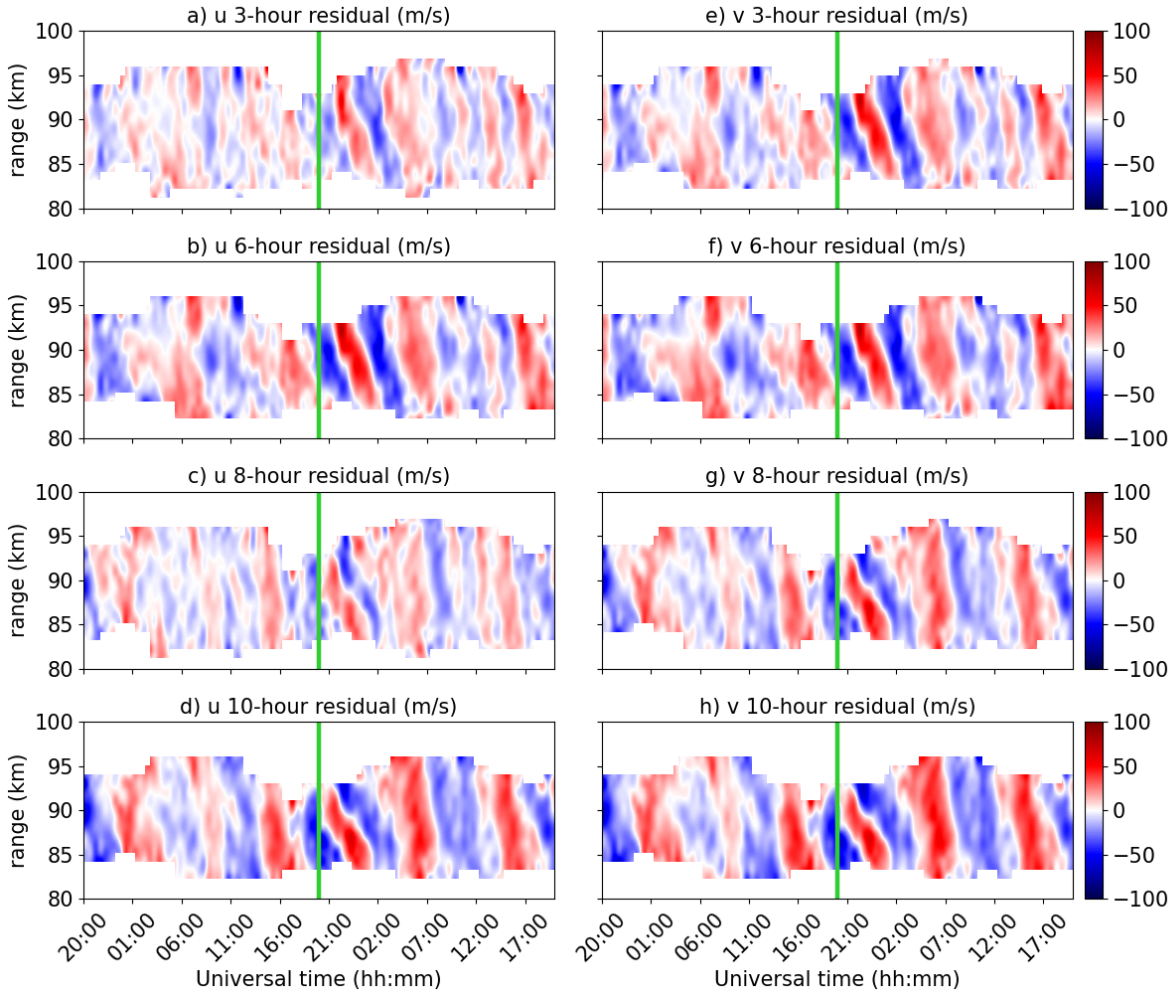


Figure A0.18: Same as Fig. A0.11 but for Case III.

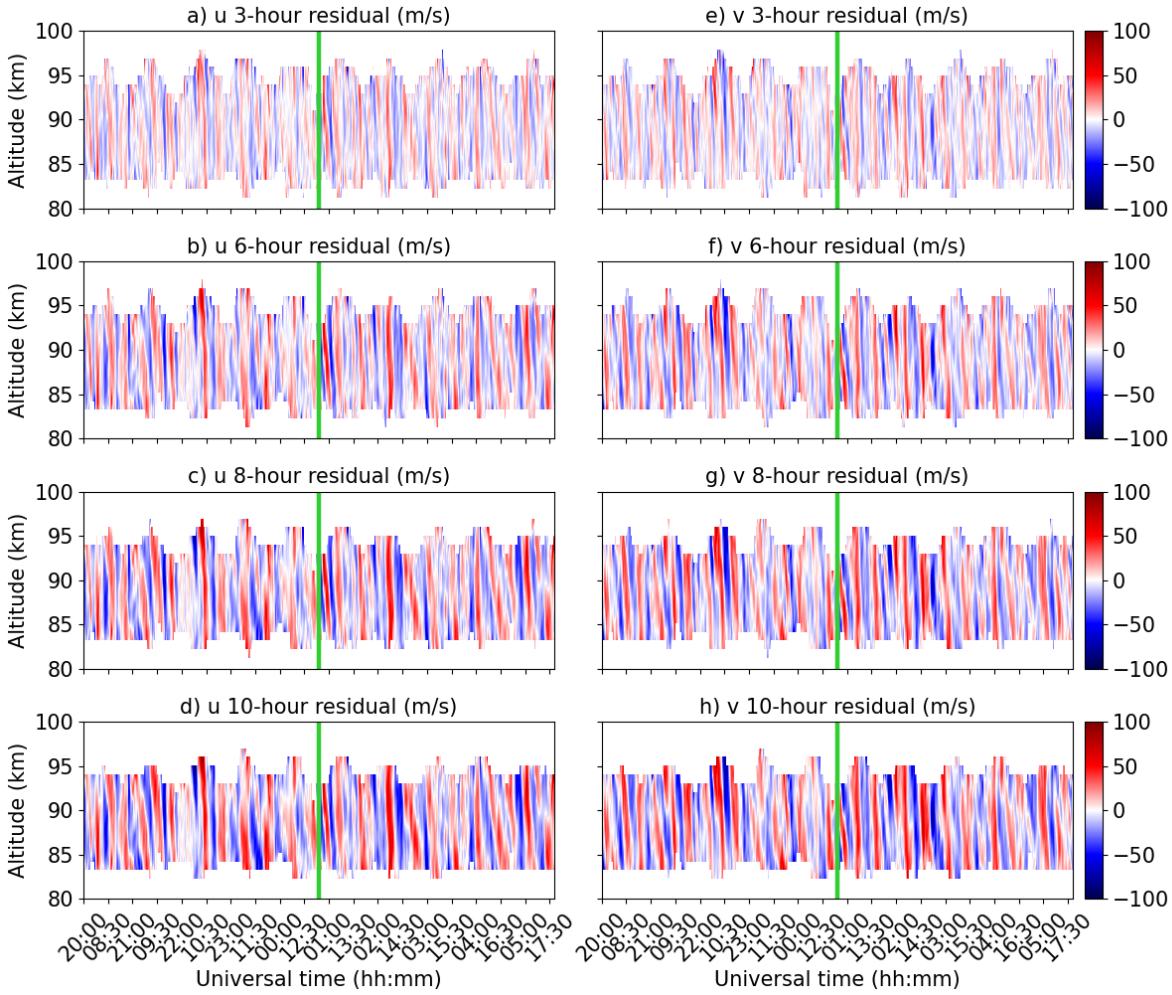


Figure A0.19: Same as Fig. A0.4 but for Case III.

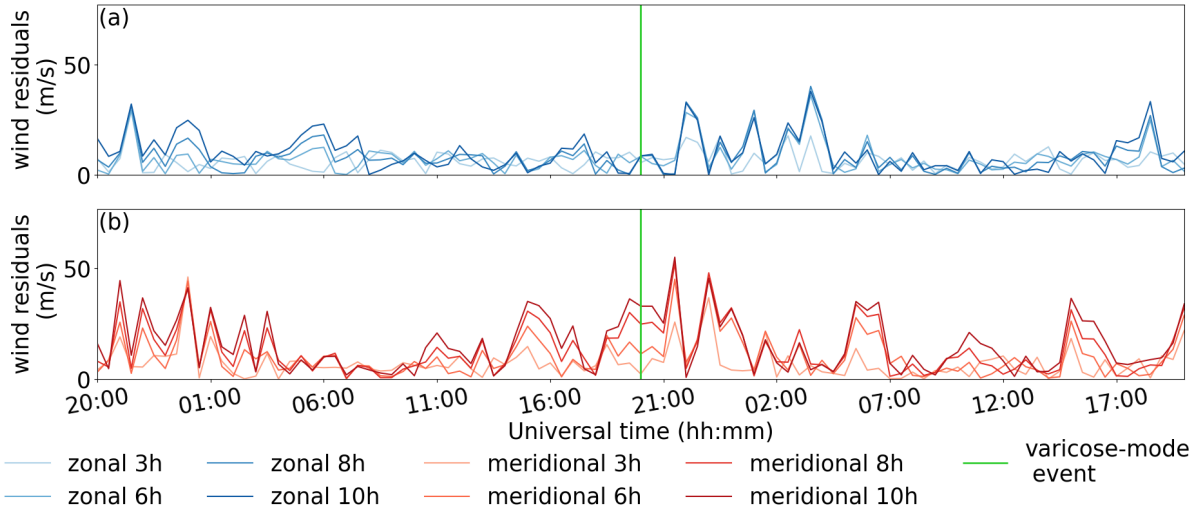


Figure A0.20: Absolute magnitudes of the zonal (a) and meridional (b) wind components at 85 km altitude, measured by MMARIA Norway over the course of 48 hours around the events (green vertical lines).

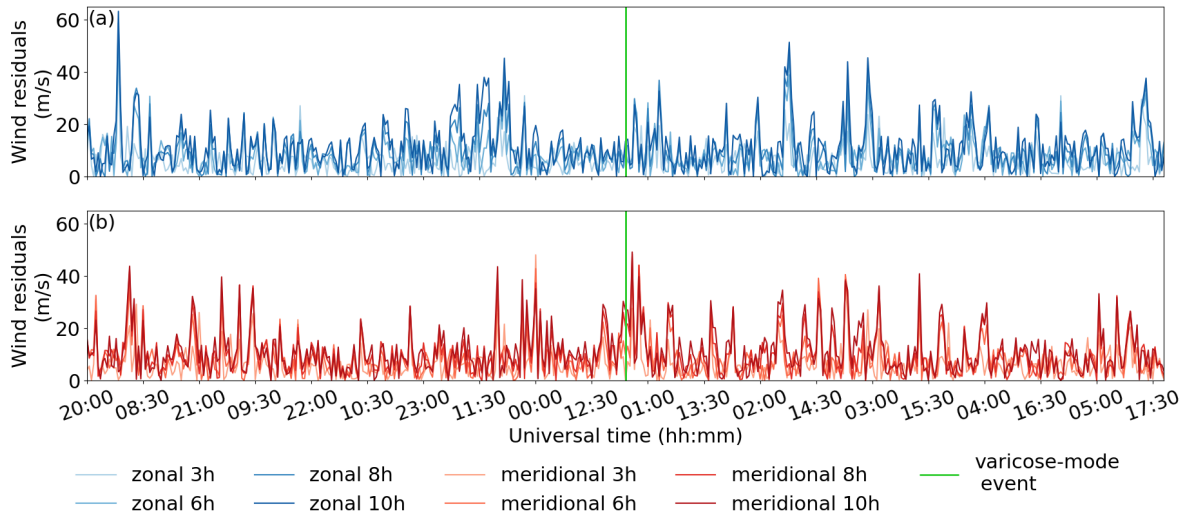


Figure A0.21: Same as Fig. A0.5 but for Case III.

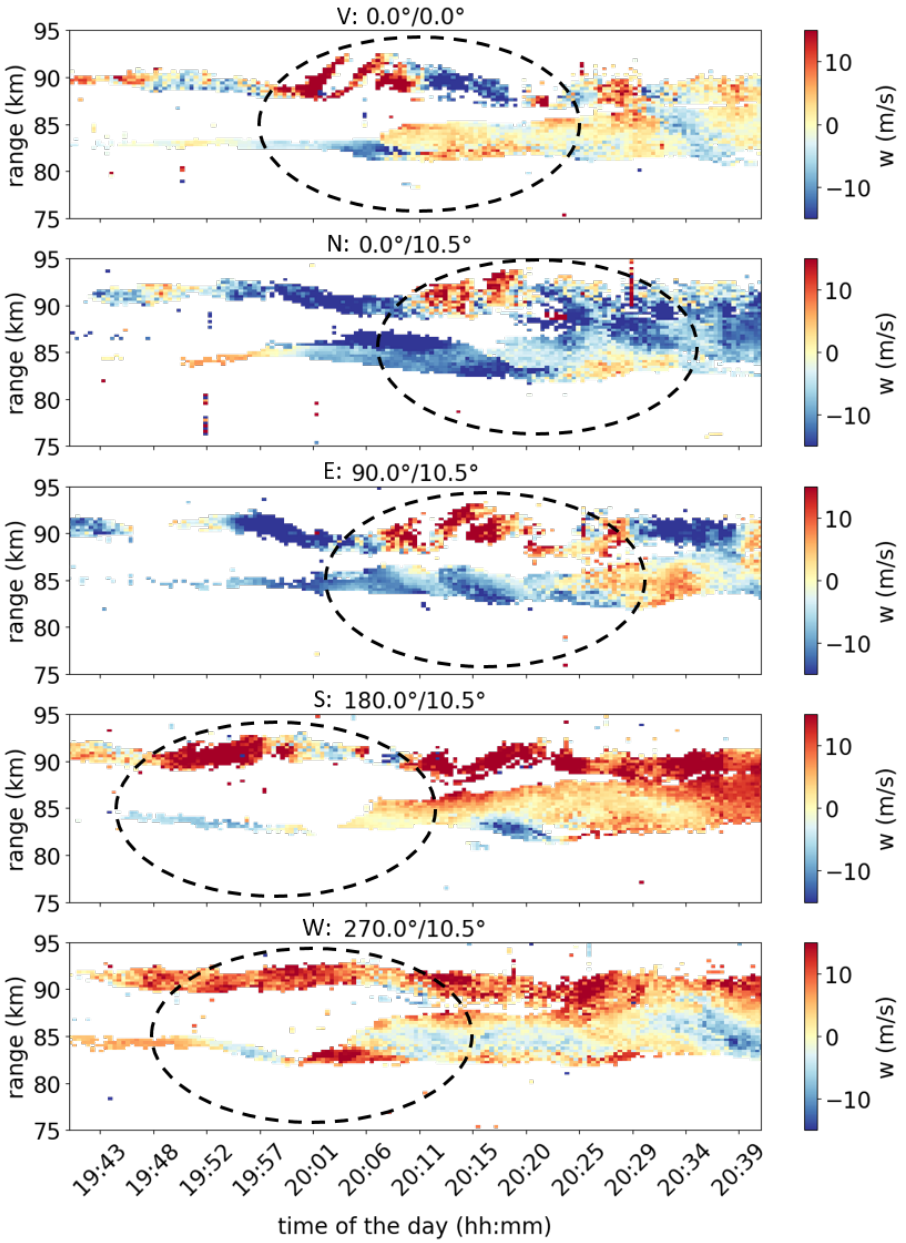


Figure A0.22: Vertical velocity measurements for Case III for 5 beam pointing directions (top to bottom: Vertical, North, East, South and West) using MAARSY.

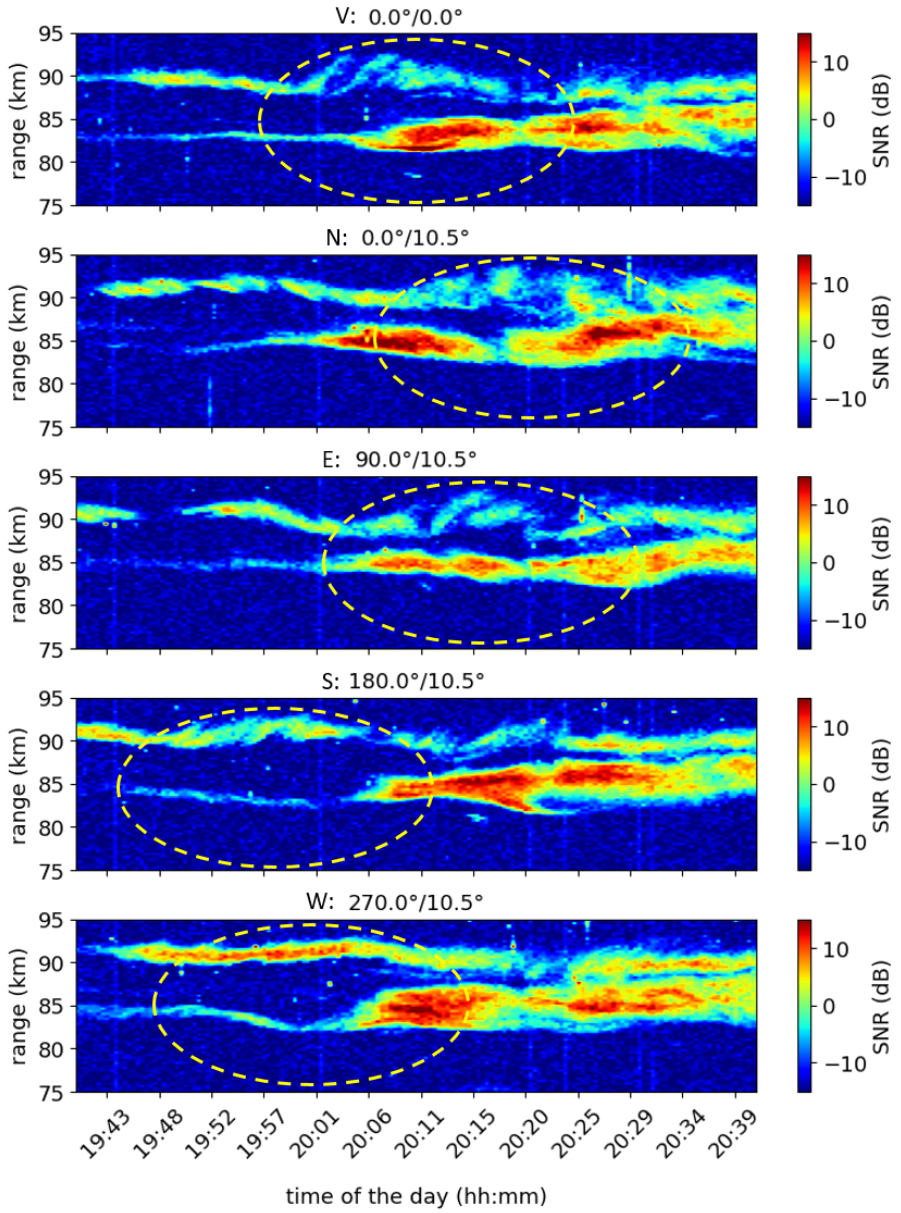


Figure A0.23: Signal-to-Noise ratio for Case III for 5 beam pointing directions (top to bottom: Vertical, North, East, South and West) using MAARSY.

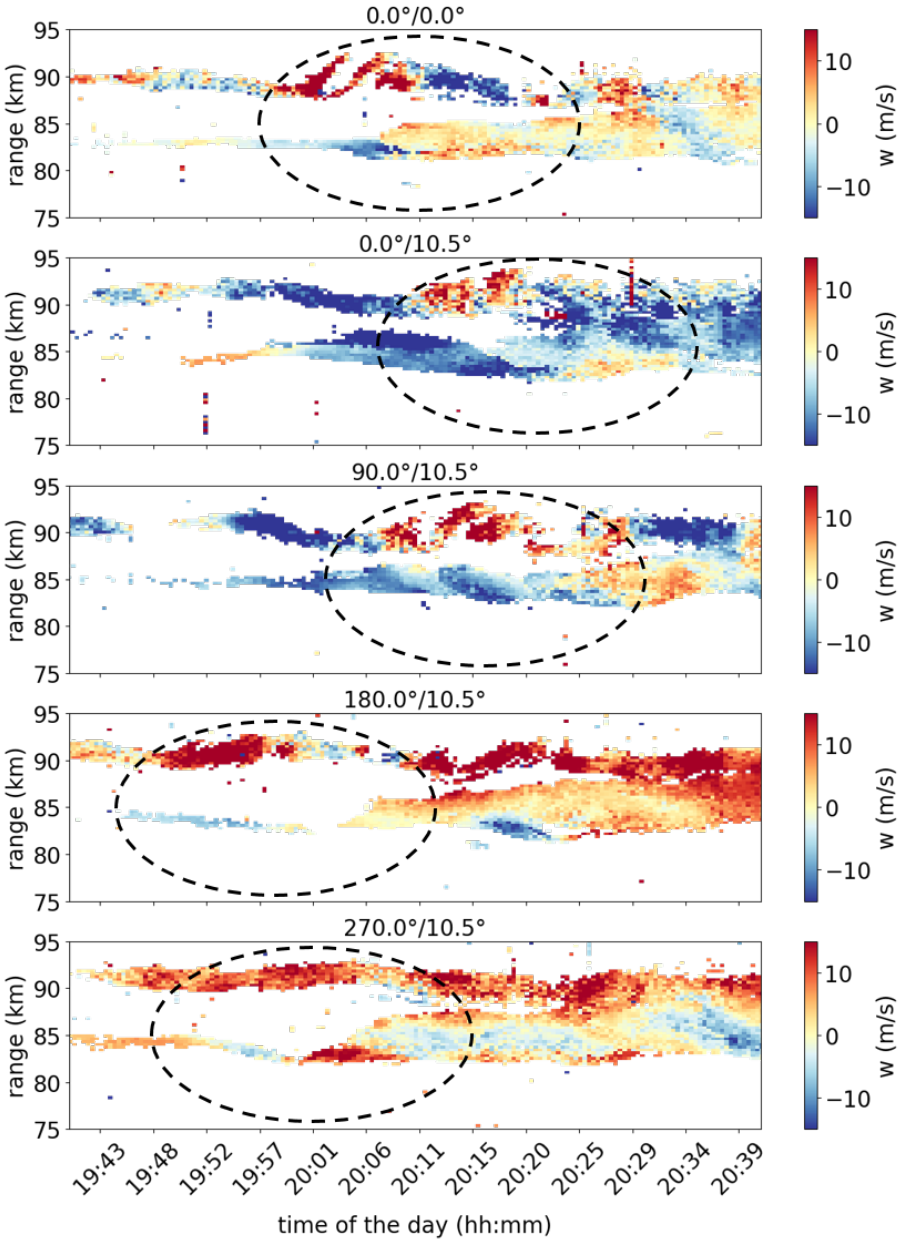


Figure A0.24: Vertical velocity measurements for Case III for 5 beam pointing directions (top to bottom: Vertical, North, East, South and West) using MAARSY. The event is highlighted with black ellipses.

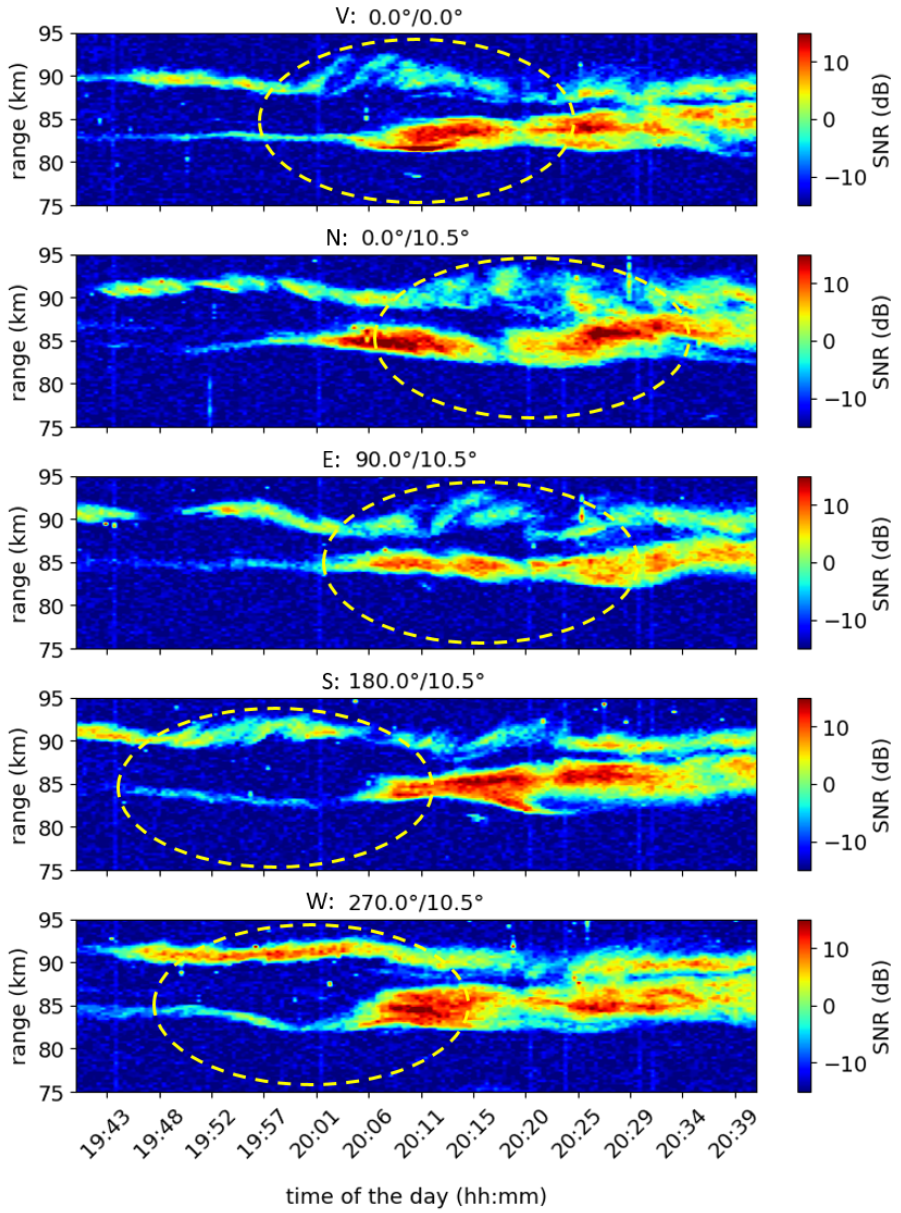


Figure A0.25: Same as Fig. A0.15 but for Case III.

Table A0.1: Summary of geographic directions, beam positions at 85 km altitude, time differences determined by eye and by using cross-correlation, and mean velocities and angles of the event front for Case III determined by using the time differences observed by eye. Row colors correspond to the quadrant colors used in the Fig. 6.19.

Case III: 01.08.2018			
Geographic Direction	**Beam Position**		**Time of the Event**
	x	**y**	
V	0	0	19:57
N	0	15	20:11
E	15	0	20:07
S	0	-15	19:48
W	-15	0	19:53
Time Differences (min)			
Beam Combination	**method 1**	**method 2**	**Difference**
V → N	14	-11	4
V → E	10	-10	1.5
V → S	-9	10	1.5
V → W	-4	11	6
W → N	18	-22	3
W → S	-5	5	1.5
E → N	4	-2	2
E → S	-19	–	1.5
Mean Velocity of the Front (m/s)		**Mean Angle of the Front (°)**	
from m_1	**from m_2**	**from m_1**	**from m_2**
28 ($24 < V < 32$)	17 ($15 < V < 20$)	101 ($96 < \theta < 107$)	76 ($69 < \theta < 85$)
53 ($38 < V < 77$)	23 ($19 < V < 30$)	110 ($102 < \theta < 118$)	76 ($69 < \theta < 85$)
33 ($27 < V < 41$)	14 ($12 < V < 16$)	123 ($118 < \theta < 127$)	130 ($127 < \theta < 132$)
31 ($27 < V < 34$)	27 ($24 < V < 31$)	121 ($113 < \theta < 131$)	105 ($91 < \theta < 121$)

A0.2.4 case IV

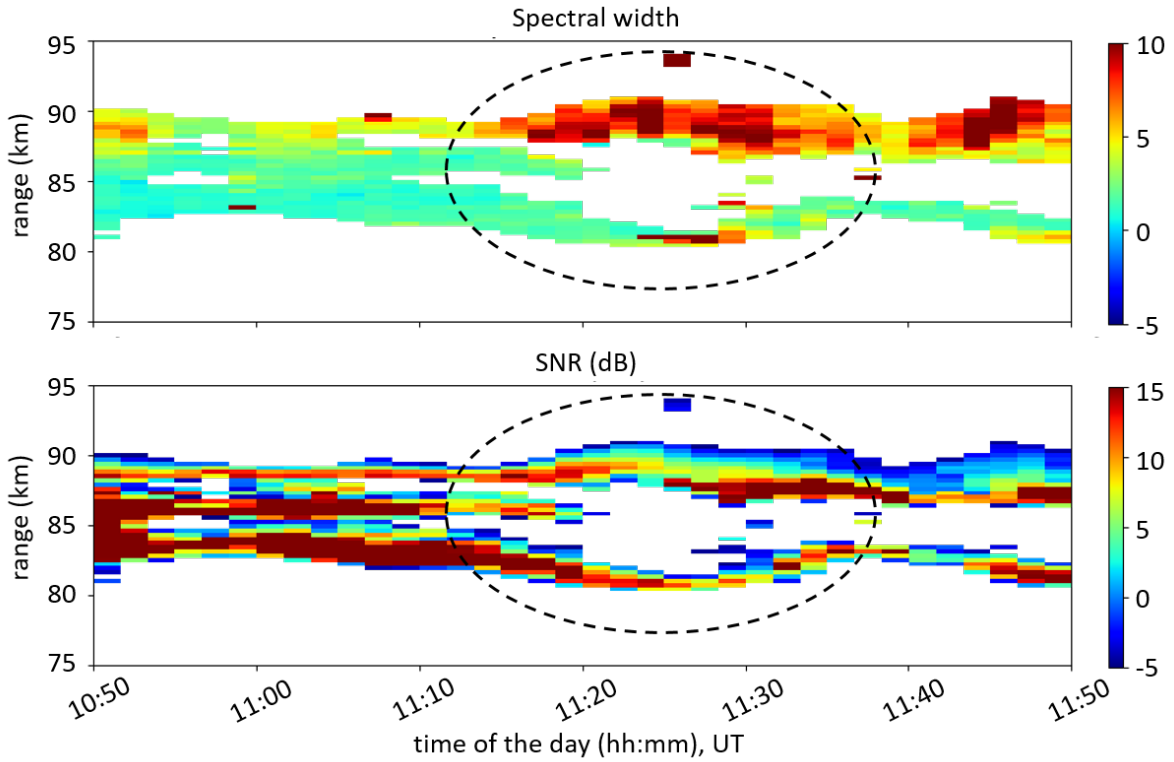


Figure A0.26: Same as Fig. A0.3 but for Case IV.

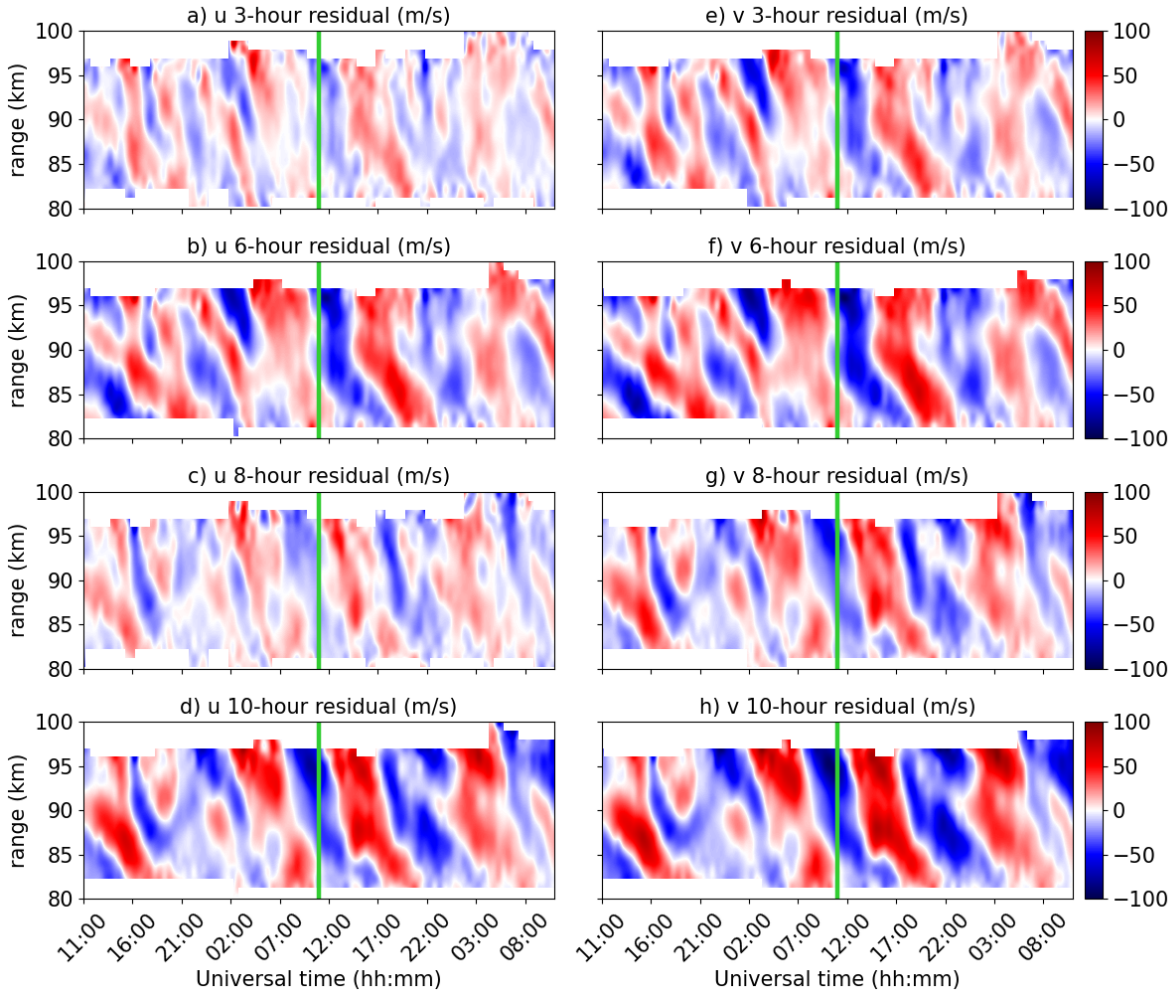


Figure A0.27: Same as Fig. A0.18 but for Case IV.

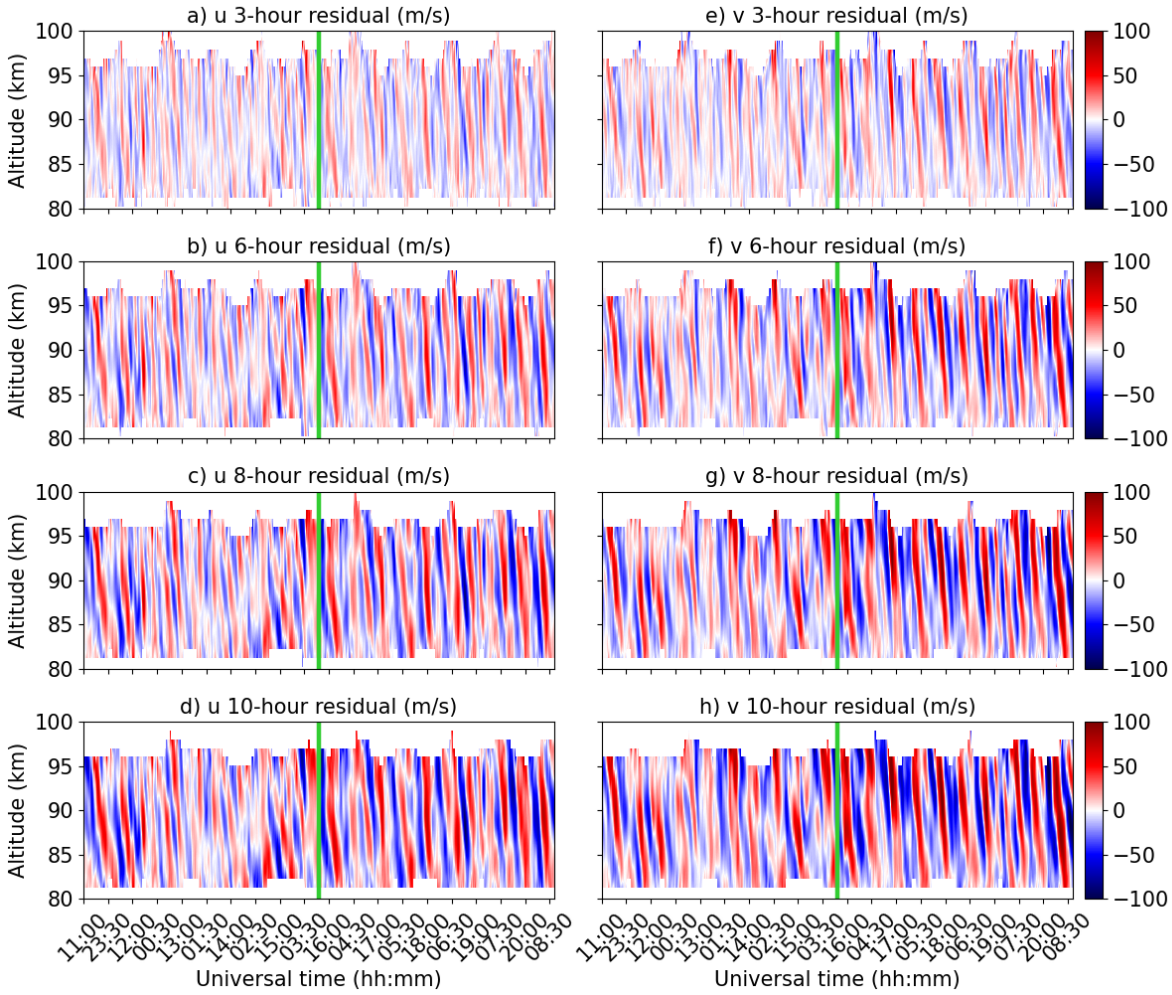


Figure A0.28: Same as Fig. A0.4 but for Case IV.

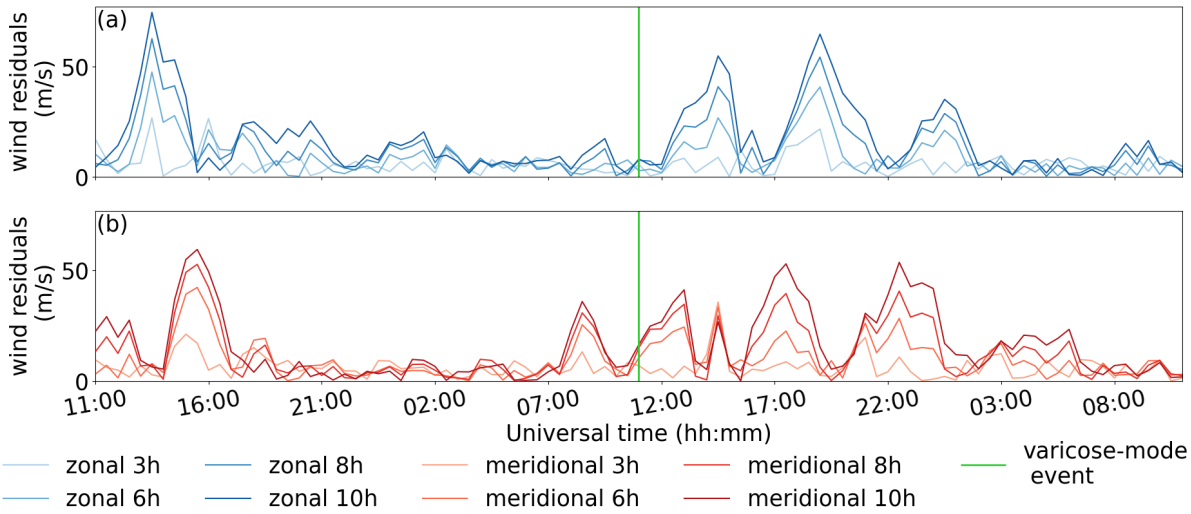


Figure A0.29: Same as Fig. A0.20 but for Case IV.

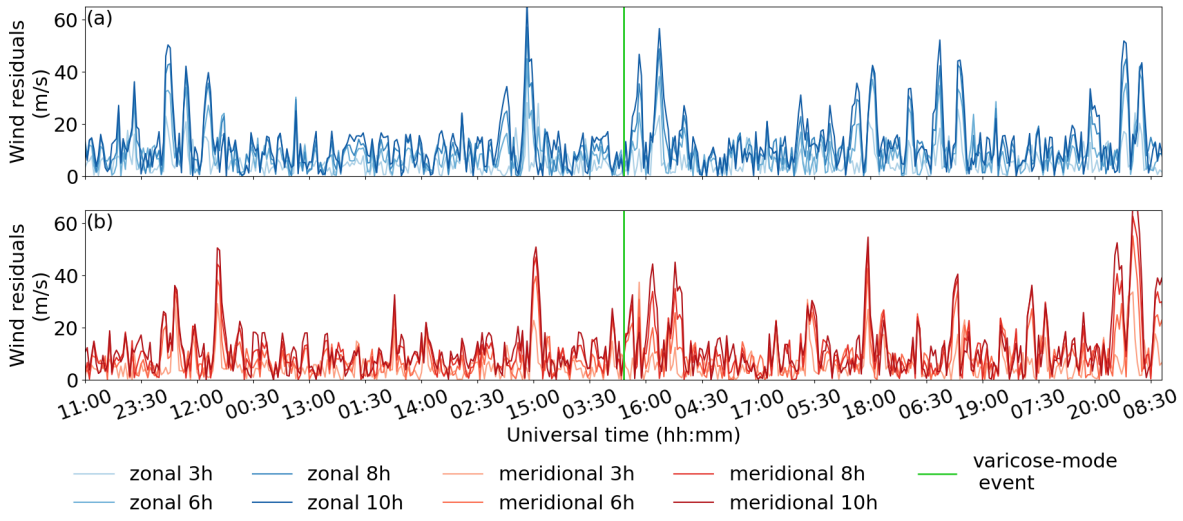


Figure A0.30: Same as Fig. A0.5 but for Case IV.

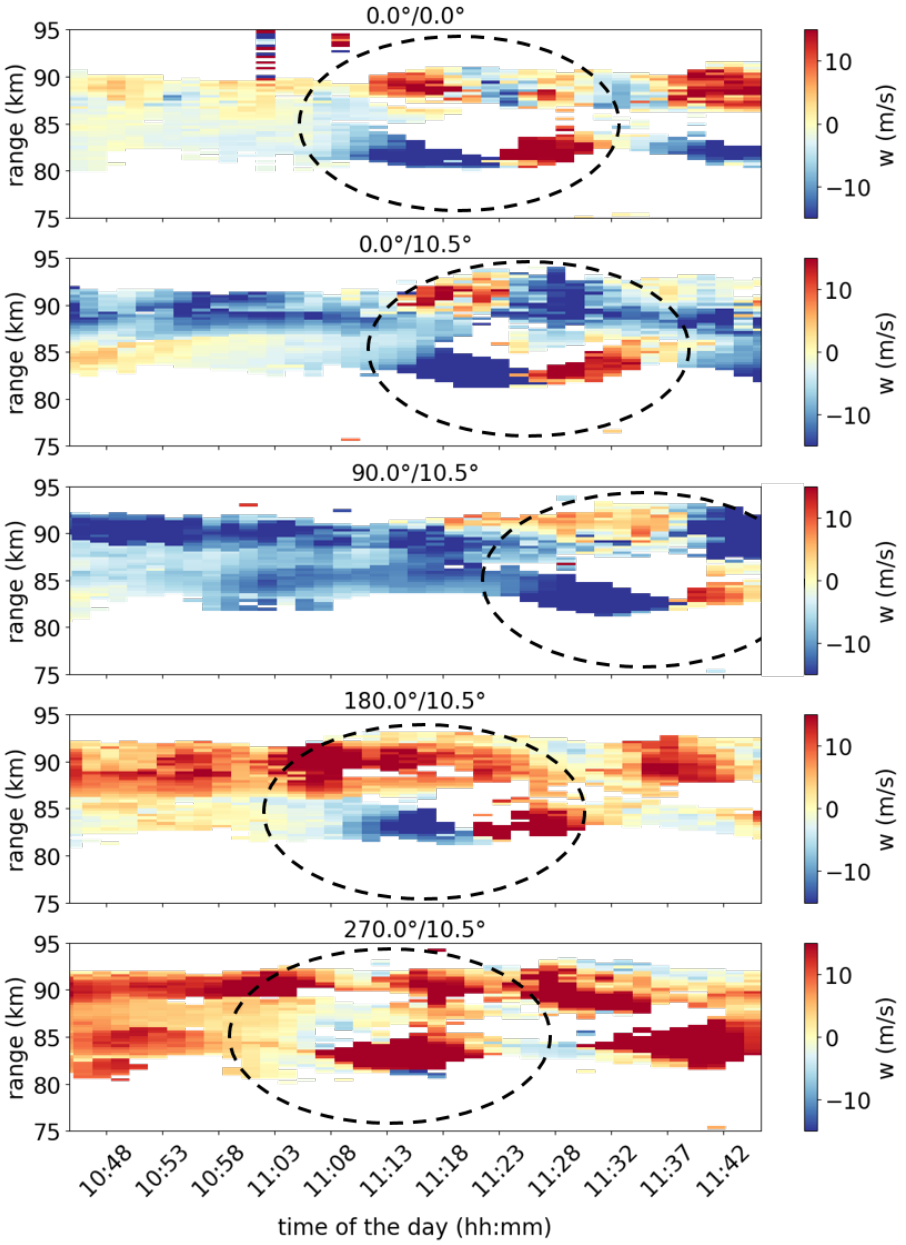


Figure A0.31: Same as Fig. A0.24 but for Case IV.

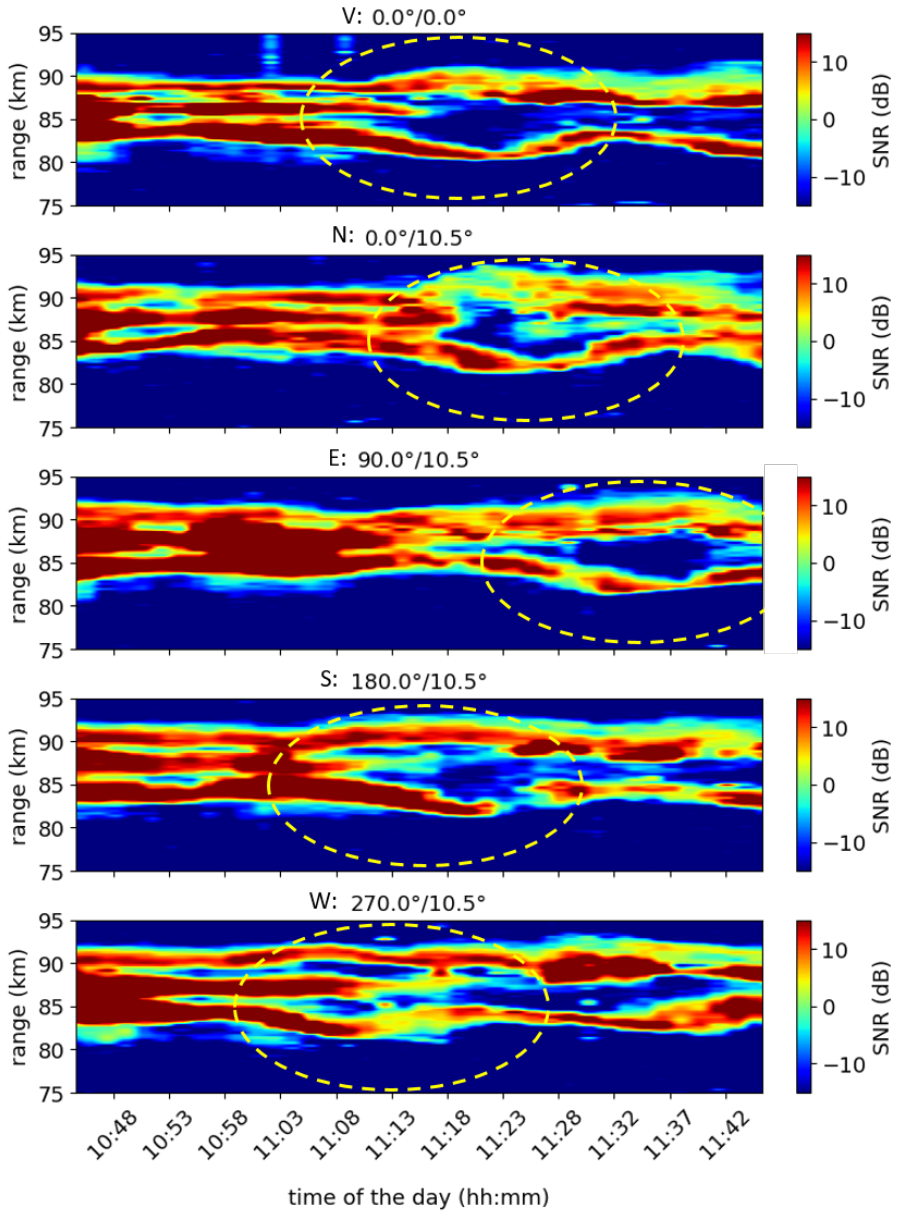


Figure A0.32: Same as Fig. A0.15 but for Case IV.

Table A0.2: Same as Tab. A0.1 but for Case IV.

Case IV: 01.07.2023			
Geographic Direction	**Beam Position**		**Time of the Event**
	x	**y**	
V	0	0	11:23
N	0	15	11:25
E	15	0	11:40
S	0	-15	11:02
W	-15	0	11:06
Time Differences (min)			
Beam Combination	**method 1**	**method 2**	**Difference**
V $\rightarrow$ N	2	-3	1.5
V $\rightarrow$ E	17	-15	2
V $\rightarrow$ S	-2	5	3
V $\rightarrow$ W	-17	15	2
W $\rightarrow$ N	19	-20	1.5
W $\rightarrow$ S	15	11	4
E $\rightarrow$ N	-15	13	2
E $\rightarrow$ S	-19	20	1.5
Mean Velocity of the Front (m/s)		**Mean Angle of the Front (°)**	
from m_1	**from m_2**	**from m_1**	**from m_2**
31 ($28 < V < 33$)	27 ($21 < V < 33$)	150 ($139 < \theta < 161$)	167 ($153 < \theta < 178$)
21 ($19 < V < 25$)	9 ($8 < V < 10$)	127 ($124 < \theta < 130$)	132 ($130 < \theta < 133$)
34 ($32 < V < 38$)	23 ($18 < V < 30$)	14 ($1 < \theta < 27$)	170 ($163 < \theta < 177$)
15 ($14 < V < 16$)	12 ($11 < V < 13$)	115 ($111 < \theta < 119$)	95 ($90 < \theta < 101$)

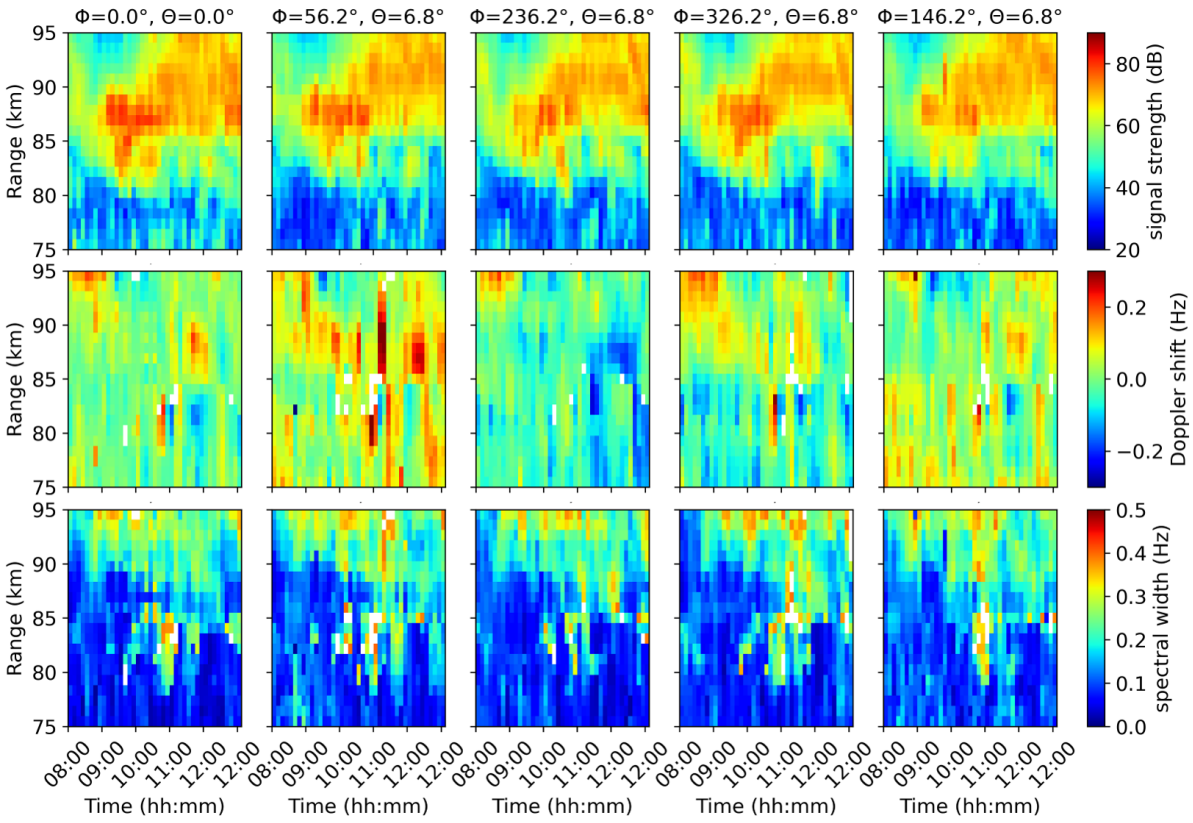


Figure A0.33: Same as Fig. A0.9 but for Case IV.

A0.3 Additional Equation Derivations

A0.3.1 Wind and Shear Parameter Definitions

The **wind magnitude** and the **shear magnitude** were determined calculating:

$M = \sqrt{u^2 + v^2}$
and
$M_{shear} = \sqrt{\frac{du}{dz}^2 + \frac{dv}{dz}^2}$,
respectively.

The **wind direction angle**, θ, is calculated from the zonal (u) and meridional (v) components using the following formula:

$$\theta = \begin{cases} \arctan\left(\frac{u}{v}\right) & \text{if } v > 0 \\ \arctan\left(\frac{u}{v}\right) + 180° & \text{if } u \geq 0 \text{ and } v < 0 \\ \arctan\left(\frac{u}{v}\right) - 180° & \text{if } u < 0 \text{ and } v < 0 \\ 90° & \text{if } u > 0 \text{ and } v = 0 \\ 270° & \text{if } u < 0 \text{ and } v = 0 \end{cases}$$

In this equation $\arctan\left(\frac{u}{v}\right)$ computes the angle relative to the North-South axis. The function adjusts based on the signs of u and v to correctly account for the quadrant: for $v > 0$, the angle lies in the fourth quadrant, so no adjustments are necessary. When $v < 0$, adjustments by $\pm 180°$ ensure the angle is calculated in the correct third quadrant. When $v = 0$, the direction is due East (90°) or due West (270°), based solely on u. This ensures θ is within the range $0° \leq \theta < 360°$, representing the full circle and taking into account the directional nature of wind data. The same kind of approach was made for the wind shear direction, using $\frac{du}{dz}$ and $\frac{dv}{dz}$ instead of u and v.

A0.3.2 Geometric Derivation: Front Speed and Angle

To determine the phase speed and angle of the event front, we calculate the intersection point between lines with known slope.

To determine this distance d12 one first needs to find P12. In this point the slope m of L2 and Lv (see Eq. A0.2 and A0.4) are equal:

$$L_1: \quad y_1 = (x - x_1)m + b_1 \tag{A0.1}$$

$$L_2: \quad y_2 = (x - x_2)m + b_2 \tag{A0.2}$$

$$L_3: \quad y_3 = (x - x_3)m + b_3 \tag{A0.3}$$

$$L_v: \quad y_v = (x - x_1)\left(-\frac{1}{m}\right) + b_1 \tag{A0.4}$$

$$(x - x_2)m + b_2 = (x - x_1)\left(-\frac{1}{m}\right) + b_1 \tag{A0.5}$$

To find the intersection point P_{12} between lines L_2 and L_v, we start with their equations and set the equations equal to each other at the intersection:

$$(x - x_2)m + b_2 = (x - x_1) - (\frac{1}{m}) + b_1 \tag{A0.6}$$

$$xm - x_2m + b_2 = -\frac{x}{m} + \left(\frac{x_1}{m}\right) + b_1 \tag{A0.7}$$

$$xm + \frac{x}{m} = x_1\frac{1}{m} + b_1 - b_2 + x_2m \tag{A0.8}$$

$$x\left(m + \frac{1}{m}\right) = x_1\frac{1}{m} + b_1 - b_2 + x_2m \tag{A0.9}$$

$$x = \frac{\frac{x_1}{m} + b_1 - b_2 + x_2m}{m + \frac{1}{m}} \tag{A0.10}$$

$$x = \frac{(\frac{x_1}{m} + b_1 - b_2 + x_2m)m}{m^2 + 1} \tag{A0.11}$$

$$x = \frac{x_1 + m(b_1 - b_2) + m^2 x_2}{m^2 + 1} \tag{A0.12}$$

$$x = x_{12} = \frac{m^2 x_2 + x_1 - m(b_2 - b_1)}{m^2 + 1} \tag{A0.13}$$

x_{12} is the x-coordinate for point P_{12}. To get the y coordinate (b_v) for this point, one now inserts x_{12} into y_v

$$b_{12} = b_v = (x_{12} - x_1)(-\frac{1}{m}) + b_1 \tag{A0.14}$$

insert x_{12} Eq. A0.13:

$$b_v = \left(\frac{m^2 x_2 + x_1 - m(b_2 - b_1)}{m^2 + 1} - x_1\right)\left(-\frac{1}{m}\right) + b_1 \tag{A0.15}$$

Now one can determinde d_{12} as:

$$\begin{aligned} d_{12} &= \|\vec{P_{12}} - \vec{P_1}\| \\ &= \sqrt{(x_{12} - x_1)^2 + (b_{12} - b_1)^2} \end{aligned} \tag{A0.16}$$

$$\begin{aligned} x_{21} - x_1 &= \frac{m^2 x_2 + x_1 - m(b_2 - b_1)}{m^2 + 1} - x_1 \\ &= \frac{m^2 x_2 + x_1 - m(b_2 - b_1) - x_1(m^2 + 1)}{m^2 + 1} \\ &= \frac{m^2 x_2 + x_1 - m(b_2 - b_1) - x_1 m^2 - x_1}{m^2 + 1} \\ &= \frac{m^2 x_2 - m^2 x_1 - m(b_2 - b_1)}{m^2 + 1} \\ &= \frac{m^2(x_2 - x_1) - m(b_2 - b_1)}{m^2 + 1} \end{aligned} \tag{A0.17}$$

$$
\begin{aligned}
b_{12} - b_1 &= \left(\frac{m^2 x_2 + x_1 - m(b_2 - b_1)}{m^2 + 1} - x_1 \right) \left(-\frac{1}{m} \right) + b_1 - b_1 \\
&= \left(\frac{m^2 x_2 + x_1 - m(b_2 - b_1)}{m^2 + 1} - x_1 \right) \left(-\frac{1}{m} \right) \\
&= -\frac{m^2 x_2 + x_1 - m(b_2 - b_1) - x_1(m^2 + 1)}{(m^2 + 1)m} \\
&= -\frac{m^2 x_2 + x_1 - m(b_2 - b_1) - x_1 m^2 - x_1}{(m^2 + 1)m} \\
&= -\frac{m^2 x_2 - m(b_2 - b_1) - x_1 m^2}{(m^2 + 1)m} \\
&= -\frac{m^2 (x_2 - x_1) - m(b_2 - b_1)}{(m^2 + 1)m}
\end{aligned} \tag{A0.18}
$$

$$
d_{12} = \sqrt{(x_{12} - x_1)^2 + (b_{12} - b_1)^2} \tag{A0.19}
$$

Since the slope of the line connecting these points is given by:

$$
m = \frac{b_{12} - b_1}{x_{12} - x_1} \tag{A0.20}
$$

we can express the vertical difference $b_{12} - b_1$ as:

$$
b_{12} - b_1 = m(x_{12} - x_1) \tag{A0.21}
$$

Substituting this into the distance formula, we get:

$$
d_{12} = \sqrt{(x_{12} - x_1)^2 + \left[m(x_{12} - x_1) \right]^2} \tag{A0.22}
$$

Simplifying the terms inside the square root:

$$
d_{12} = \sqrt{(x_{12} - x_1)^2 \left(1 + m^2\right)} \tag{A0.23}
$$

Factoring out $(x_{12} - x_1)^2$, we get:

$$d_{12} = |x_{12} - x_1| \cdot \sqrt{1 + m^2} \tag{A0.24}$$

Now we proceed to express d_{12} and d_{31}, the distance between P_3 and P_1, similarly:

$$d_{31} = |x_{13} - x_1| \cdot \sqrt{1 + m^2} \tag{A0.25}$$

The front propagates at a constant velocity V, and the distances are related to the time intervals $t_{21} = t_2 - t_1$ and $t_{31} = t_3 - t_1$:

$$d_{12} = V \cdot t_{21} \tag{A0.26}$$

$$d_{31} = V \cdot t_{31} \tag{A0.27}$$

Substituting the expressions for d_{12} and d_{31} into these equations:

$$|x_{12} - x_1| \cdot \sqrt{1 + m^2} = V \cdot t_{21} \tag{A0.28}$$

$$|x_{13} - x_1| \cdot \sqrt{1 + m^2} = V \cdot t_{31} \tag{A0.29}$$

To eliminate V, we divide the first equation by the second:

$$\frac{|x_{12} - x_1|}{|x_{13} - x_1|} = \frac{t_{21}}{t_{31}} \tag{A0.30}$$

This gives a relationship between the x-coordinates and the time intervals:

$$|x_{12} - x_1| \cdot t_{31} = |x_{13} - x_1| \cdot t_{21} \tag{A0.31}$$

Now, express $x_{12} - x_1$ and $x_{13} - x_1$ using the known coordinates and the slope m. From the earlier derivations:

$$x_{12} = \frac{m^2 x_2 + x_1 - m(b_2 - b_1)}{m^2 + 1} \tag{A0.32}$$

$$x_{13} = \frac{m^2 x_3 + x_1 - m(b_3 - b_1)}{m^2 + 1} \tag{A0.33}$$

Substitute these into the previous equation:

$$\frac{m^2(x_2 - x_1) - m(b_2 - b_1)}{m^2 + 1} \cdot t_{31} = \frac{m^2(x_3 - x_1) - m(b_3 - b_1)}{m^2 + 1} \cdot t_{21} \tag{A0.34}$$

Canceling $(m^2 + 1)$ from both sides:

$$(m^2(x_2 - x_1) - m(b_2 - b_1)) \cdot t_{31} = (m^2(x_3 - x_1) - m(b_3 - b_1)) \cdot t_{21} \tag{A0.35}$$

Now rearrange this into a quadratic form:

$$m^2 \left[(x_2 - x_1) \cdot t_{31} - (x_3 - x_1) \cdot t_{21}\right] = m \left[(b_3 - b_1) \cdot t_{21} - (b_2 - b_1) \cdot t_{31}\right] \tag{A0.36}$$

Finally, solve for m:

$$m^2 A + mB = 0 \tag{A0.37}$$

where:

$$A = (x_2 - x_1) \cdot t_{31} - (x_3 - x_1) \cdot t_{21} \tag{A0.38}$$

$$B = (b_3 - b_1) \cdot t_{21} - (b_2 - b_1) \cdot t_{31} \tag{A0.39}$$

Factoring out m, we get:

$$m(mA + B) = 0 \tag{A0.40}$$

This leads to two solutions:

1. $m = 0$, which corresponds to a horizontal front (unlikely in this context).
2. $m = \frac{-B}{A}$, where:

$$m = \frac{(b_2 - b_1) \cdot t_{31} - (b_3 - b_1) \cdot t_{21}}{(x_2 - x_1) \cdot t_{31} - (x_3 - x_1) \cdot t_{21}} \tag{A0.41}$$

A0.3.3 Velocity and Error from Imaging Slope

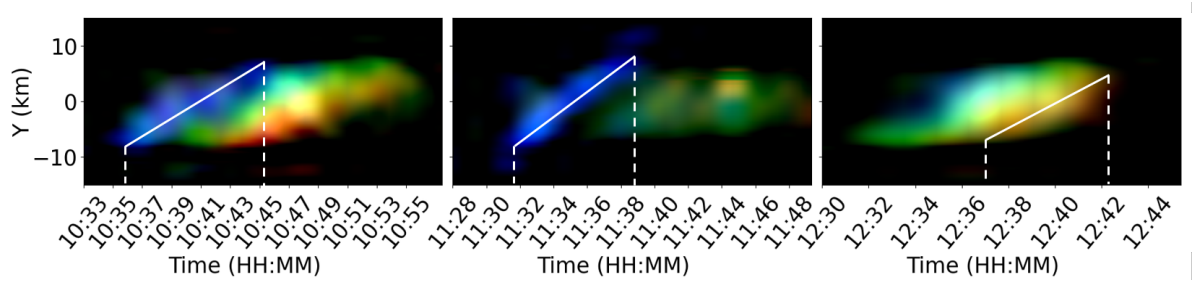


Figure A0.34: Temporal evolution of the three events of Case I along y-axis and altitude at a fixed point x = 0 from their initial to their final stage. The color representation is the same as in Fig. 6.8.

The velocity is calculated using the formula:

$$v = \frac{\Delta y}{\Delta t} \tag{A0.42}$$

where:

- Δy is the difference in distance between the two points: $\Delta y = y_2 - y_1$
- Δt is the difference in time between the two points: $\Delta t = t_2 - t_1$

Substituting the given values:

$$\Delta y = 15.5\,\text{km} = 15500\,\text{m}, \quad \Delta t = 10\,\text{minutes} = 600\,\text{s} \tag{A0.43}$$

we find:

$$v = \frac{15500\,\text{m}}{600\,\text{s}} = 25.83\,\text{m/s}. \tag{A0.44}$$

The uncertainty in the velocity, σ_v, is calculated using the error propagation formula:

$$\sigma_v = \sqrt{\left(\frac{\sigma_{\Delta y}}{\Delta t}\right)^2 + \left(\frac{\Delta y \cdot \sigma_{\Delta t}}{\Delta t^2}\right)^2} \tag{A0.45}$$

where:

$$\sigma_{\Delta y} = \sqrt{\sigma_{y_1}^2 + \sigma_{y_2}^2}, \tag{A0.46}$$

and:

$$\sigma_{\Delta t} = \sqrt{\sigma_{t_1}^2 + \sigma_{t_2}^2}. \tag{A0.47}$$

Substituting the uncertainties for the y-coordinates:

$$\sigma_{\Delta y} = \sqrt{250^2 + 250^2} = 354\,\text{m}, \tag{A0.48}$$

and the uncertainties for the t-coordinates:

$$\sigma_{\Delta t} = \sqrt{90^2 + 90^2} = 127\,\text{s}. \tag{A0.49}$$

Substituting into the error propagation formula:

$$\sigma_v = \sqrt{\left(\frac{354}{600}\right)^2 + \left(\frac{15500 \cdot 127}{600^2}\right)^2}, \tag{A0.50}$$

we find:

$$\sigma_v = 5.51\,\text{m/s}. \tag{A0.51}$$

Thus, the velocity with its uncertainty is:

$$v = 25.83 \pm 5.51\,\text{m/s}. \tag{A0.52}$$

A0.3.4 Beam-Pair Altitudes for Cross-Correlation

The following table lists the altitude combinations used for cross-correlation analysis between beam pairs in each case study. These altitudes were selected based on the regions of signal overlap and coherence.

Table A0.3: Crossing altitudes for beam pairs in each case study.

Beam pair	Case I		Case II		Case III	
	alt. A (km)	alt. B (km)	alt. A (km)	alt. B (km)	alt. A (km)	alt. B (km)
V - N	81.5	83.3	84.2	83.2	81.8	82.7
V - E	83.0	83.9	91.4	92.3	82.4	83.9
V - S	82.7	85.4	89.3	91.7	81.8	83.3
V - W	81.5	84.2	83.3	82.7	82.7	83.0
W - N	83.3	83.3	83.0	83.6	82.7	83.0
W - S	83.6	83.3	91.4	92.0	82.7	82.7
E - N	88.1	87.8	89.9	89.9	–	–
E - S	88.1	87.5	–	–	83.3	82.7

Bibliography

Achatz, Ulrich et al. (2010). "Gravity waves, scale asymptotics and the pseudo-incom-equations". In: *Journal of Fluid Mechanics* 663, pp. 120–147. DOI: 10.1017/S00221 12010003411.

Ahrens, Donald C. (2012). *Meteorology Today: An Introduction to Weather, Climate, and the Environment*. Cengage Learning.

Andrews, David G. et al. (1987). "Middle Atmosphere Dynamics". In: vol. 40. International Geophysics. Academic Press. Chap. 4 - Linear Wave Theory, pp. 150–219. DOI: https://doi.org/10.1016/B978-0-12-058575-5.50009-8. URL: https://www.sciencedirect.com/science/article/pii/B9780120585755500098.

Avsarkisov, Victor et al. (2022). "Turbulent Parameters in the Middle Atmosphere: Theoretical Estimates Deduced from a Gravity Wave–Resolving General Circulation Model". In: *Journal of the Atmospheric Sciences* 79.4, pp. 933–952. DOI: 10.1175/JAS-D-21-0005.1. URL: https://journals.ametsoc.org/view/journals/atsc/79/4/JAS-D-21-0005.1.xml.

Baruah, Yoshita et al. (2024). "The Loss of Starlink Satellites in February 2022: How Moderate Geomagnetic Storms Can Adversely Affect Assets in Low-Earth Orbit". In: *Space Weather* 22.4. e2023SW003716 2023SW003716, e2023SW003716. DOI: https://doi.org/10.1029/2023SW003716. eprint: https://agupubs.onlinelibrary.wiley.com/doi/pdf/10.1029/2023SW003716. URL: https://agupubs.onlinelibrary.wiley.com/doi/abs/10.1029/2023SW003716.

Baumgarten, G. et al. (2002). "First observation of one noctilucent cloud by a twin lidar in two different directions". In: *Annales Geophysicae* 20.11, pp. 1863–1868. DOI: 10.5194/angeo-20-1863-2002. URL: https://angeo.copernicus.org/articles/20/1863/2002/.

Baumgarten, Gerd and Fritts, David C. (2014). "Quantifying Kelvin-Helmholtz instability dynamics observed in noctilucent clouds: 1. Methods and observations". In: *Journal of Geophysical Research: Atmospheres* 119.15, pp. 9324–9337. DOI: https://doi.org/10.1002/2014JD021832. eprint: https://agupubs.onlinelibrary.wiley.com/doi/pdf/10.1002/2014JD021832. URL: https://agupubs.onlinelibrary.wiley.com/doi/abs/10.1002/2014JD021832.

Beard, A.G. et al. (1999). "Non-linear interactions between tides and planetary waves resulting in periodic tidal variability". In: *Journal of Atmospheric and Solar-Terrestrial Physics* 61.5, pp. 363–376. ISSN: 1364-6826. DOI: https://doi.org/10.1016/S1364

-6826(99)00003-6. URL: https://www.sciencedirect.com/science/article/pii/S1364682699000036.

Chanson, Hubert (2010). "TIDAL BORES, AEGIR AND POROROCA: THE GEOPHYSICAL WONDERS". In: URL: https://api.semanticscholar.org/CorpusID:129573374.

Chau, J. L. et al. (Aug. 2021). "Radar Observation of Extreme Vertical Drafts in the Polar Summer Mesosphere". In: *Geophysical Research Letters* 48.16. ISSN: 0094-8276. DOI: 10.1029/2021GL094918. URL: https://onlinelibrary.wiley.com/doi/10.1029/2021GL094918.

Dewan, E. M. and Picard, R. H. (1998). "Mesospheric bores". In: *Journal of Geophysical Research Atmospheres* 103.D6, pp. 6295–6305. ISSN: 01480227. DOI: 10.1029/97JD02498.

Dewan, E. M. and Picard, R. H. (2001). "On the origin of mesospheric bores". In: *Journal of Geophysical Research: Atmospheres* 106.D3, pp. 2921–2927. DOI: https://doi.org/10.1029/2000JD900697. eprint: https://agupubs.onlinelibrary.wiley.com/doi/pdf/10.1029/2000JD900697. URL: https://agupubs.onlinelibrary.wiley.com/doi/abs/10.1029/2000JD900697.

Dong, Wenjun et al. (July 2021). "Modeling Responses of Polar Mesospheric Clouds to Gravity Wave and Instability Dynamics and Induced Large-Scale Motions". In: *Journal of Geophysical Research: Atmospheres* 126.13, e2021JD034643. ISSN: 2169-8996. DOI: 10.1029/2021JD034643. URL: https://onlinelibrary.wiley.com/doi/full/10.1029/2021JD034643%20https://onlinelibrary.wiley.com/doi/abs/10.1029/2021JD034643%20https://agupubs.onlinelibrary.wiley.com/doi/10.1029/2021JD034643.

Drazin, P.G. (2015). "DYNAMICAL METEOROLOGY | Kelvin–Helmholtz Instability". In: *Encyclopedia of Atmospheric Sciences (Second Edition)*. Ed. by North, Gerald R. et al. Second Edition. Oxford: Academic Press, pp. 343–346. ISBN: 978-0-12-382225-3. DOI: https://doi.org/10.1016/B978-0-12-382225-3.00190-0. URL: https://www.sciencedirect.com/science/article/pii/B9780123822253001900.

Ehard, B. et al. (Nov. 2014). "Long-term lidar observations of wintertime gravity wave activity over northern Sweden". In: *Annales Geophysicae* 32, pp. 1395–1405. DOI: 10.5194/angeo-32-1395-2014.

Farley, D. T. (1985). "On-line data processing techniques for MST radars". In: *Radio Science* 20.6, pp. 1177–1184. DOI: 10.1029/RS020i006p01177.

Feraco, F. et al. (June 2018). "Vertical drafts and mixing in stratified turbulence: sharp transition with Froude number". In: arXiv: 1806.00342v1. URL: https://ww

w.researchgate.net/publication/325543895_Vertical_drafts_and_mixing_in_stratified_turbulence_sharp_transition_with_Froude_number.

FIEDLER, Franz and PANOFSKY, Hans A. (1970). "atmospheric scales and spectral gaps". In: *Bulletin of the American Meteorological Society* 51.12, pp. 1114–1120. DOI: 10.1175/1520-0477(1970)051<1114:ASASG>2.0.CO;2. URL: https://journals.ametsoc.org/view/journals/bams/51/12/1520-0477_1970_051_1114_asasg_2_0_co_2.xml.

FRITTS, David C. (1984). "Gravity wave saturation in the middle atmosphere: A review of theory and observations". In: *Reviews of Geophysics* 22.3, pp. 275–308. DOI: https://doi.org/10.1029/RG022i003p00275. eprint: https://agupubs.onlinelibrary.wiley.com/doi/pdf/10.1029/RG022i003p00275. URL: https://agupubs.onlinelibrary.wiley.com/doi/abs/10.1029/RG022i003p00275.

FRITTS, David C. and ALEXANDER, M. Joan (Mar. 2003). "Gravity wave dynamics and effects in the middle atmosphere". In: *Reviews of Geophysics* 41.1, p. 1003. ISSN: 1944-9208. DOI: 10.1029/2001RG000106. URL: https://onlinelibrary.wiley.com/doi/full/10.1029/2001RG000106%20https://onlinelibrary.wiley.com/doi/abs/10.1029/2001RG000106%20https://agupubs.onlinelibrary.wiley.com/doi/10.1029/2001RG000106.

FRITTS, David C. and RASTOGI, Prabhat K. (1985). "Convective and dynamical instabilities due to gravity wave motions in the lower and middle atmosphere: Theory and observations". In: *Radio Science* 20.6, pp. 1247–1277. DOI: https://doi.org/10.1029/RS020i006p01247. eprint: https://agupubs.onlinelibrary.wiley.com/doi/pdf/10.1029/RS020i006p01247. URL: https://agupubs.onlinelibrary.wiley.com/doi/abs/10.1029/RS020i006p01247.

FRITTS, David C. and VINCENT, Robert A. (1987). "Mesospheric Momentum Flux Studies at Adelaide, Australia: Observations and a Gravity Wave–Tidal Interaction Model". In: *Journal of Atmospheric Sciences* 44.3, pp. 605–619. DOI: 10.1175/1520-0469(1987)044<0605:MMFSAA>2.0.CO;2. URL: https://journals.ametsoc.org/view/journals/atsc/44/3/1520-0469_1987_044_0605_mmfsaa_2_0_co_2.xml.

FRITTS, David C. et al. (2020). "Mesospheric Bore Evolution and Instability Dynamics Observed in PMC Turbo Imaging and Rayleigh Lidar Profiling Over Northeastern Canada on 13 July 2018". In: *Journal of Geophysical Research: Atmospheres* 125.14. ISSN: 21698996. DOI: 10.1029/2019JD032037.

FUKAO, Shoichiro and HAMAZU, Kyosuke (July 2014). "Radar for meteorological and atmospheric observations". In: *Radar for Meteorological and Atmospheric Observations* 9784431543343, pp. 1–537. DOI: 10.1007/978-4-431-54334-3/COVER.

GARCIA, Rolando R. (1989). "Dynamics, radiation, and photochemistry in the mesosphere: Implications for the formation of noctilucent clouds". In: *Journal of Geo-*

physical Research: Atmospheres 94.D12, pp. 14605–14615. DOI: https://doi.org/10.1029/JD094iD12p14605. eprint: https://agupubs.onlinelibrary.wiley.com/doi/pdf/10.1029/JD094iD12p14605. URL: https://agupubs.onlinelibrary.wiley.com/doi/abs/10.1029/JD094iD12p14605.

GUDADZE, Nikoloz et al. (Apr. 2019). "Can VHF radars at polar latitudes measure mean vertical winds in the presence of PMSE?" In: *Atmospheric Chemistry and Physics* 19.7, pp. 4485–4497. ISSN: 16807324. DOI: 10.5194/ACP-19-4485-2019.

HAGAN, M. E. and FORBES, J. M. (Feb. 2003). "Migrating and nonmigrating semidiurnal tides in the upper atmosphere excited by tropospheric latent heat release". In: *Journal of Geophysical Research: Space Physics* 108.A2, p. 1062. ISSN: 2156-2202. DOI: 10.1029/2002JA009466. URL: https://onlinelibrary.wiley.com/doi/full/10.1029/2002JA009466%20https://onlinelibrary.wiley.com/doi/abs/10.1029/2002JA009466%20https://agupubs.onlinelibrary.wiley.com/doi/10.1029/2002JA009466.

HÄGGSTRÖM, I. (2017). "3.8. Incoherent and coherent scatter radars". In: *Access to data from near-Earth space*. Les Ulis: EDP Sciences, pp. 117–126. ISBN: 9782759819492. DOI: doi:10.1051/978-2-7598-1949-2.c012. URL: https://doi.org/10.1051/978-2-7598-1949-2.c012.

HARTISCH, J. et al. (2024). "Observations of polar mesospheric summer echoes resembling kilometer-scale varicose-mode flows". In: *Annales Geophysicae* 42.1, pp. 29–43. DOI: 10.5194/angeo-42-29-2024. URL: https://angeo.copernicus.org/articles/42/29/2024/.

HE, Maosheng et al. (2024). "Nonlinear Interactions of Planetary-Scale Waves in Mesospheric Winds Observed at 52°N Latitude and Two Longitudes". In: *Geophysical Research Letters* 51.24. e2024GL110629 2024GL110629, e2024GL110629. DOI: https://doi.org/10.1029/2024GL110629. eprint: https://agupubs.onlinelibrary.wiley.com/doi/pdf/10.1029/2024GL110629. URL: https://agupubs.onlinelibrary.wiley.com/doi/abs/10.1029/2024GL110629.

HOCKING, W.K (1996). "An assessment of the capabilities and limitations of radars in measurements of upper atmosphere turbulence". In: *Advances in Space Research* 17.11, pp. 37–47. ISSN: 0273-1177. DOI: https://doi.org/10.1016/0273-1177(95)00728-W. URL: https://www.sciencedirect.com/science/article/pii/0273117795007 28W.

HOCKING, W.K. (1986). "Observation and measurement of turbulence m the middle atmosphere with a VHF radar". In: *Journal of Atmospheric and Terrestrial Physics* 48.7, pp. 655–670. ISSN: 0021-9169. DOI: https://doi.org/10.1016/0021-9169(86)90015-2. URL: https://www.sciencedirect.com/science/article/pii/0021916986900152.

Hocking, Wayne K. et al. (2016). *Atmospheric Radar: Application and Science of MST Radars in the Earth's Mesosphere, Stratosphere, Troposphere, and Weakly Ionized Regions*. Cambridge University Press.

Hoffmann, Peter et al. (June 1999). "Mean seasonal and diurnal variations of PMSE and winds from 4 years of radar observations at ALOMAR". In: *Geophysical Research Letters* 26.11, pp. 1525–1528. ISSN: 1944-8007. DOI: 10.1029/1999GL900279. URL: https://onlinelibrary.wiley.com/doi/full/10.1029/1999GL900279%20https://onlinelibrary.wiley.com/doi/abs/10.1029/1999GL900279%20https://agupubs.onlinelibrary.wiley.com/doi/10.1029/1999GL900279.

Holton, James R. (2004). *An Introduction to Dynamic Meteorology*. Elsevier.

Hoppe, U.-P. and Fritts, D. C. (Mar. 1995). "On the downward bias in vertical velocity measurements by VHF radars". In: *Geophysical Research Letters* 22.5, pp. 619–622. ISSN: 1944-8007. DOI: 10.1029/95GL00165. URL: https://onlinelibrary.wiley.com/doi/full/10.1029/95GL00165%20https://onlinelibrary.wiley.com/doi/abs/10.1029/95GL00165%20https://agupubs.onlinelibrary.wiley.com/doi/10.1029/95GL00165.

Hozumi, Y. et al. (2018). "Mesospheric bores at southern midlatitudes observed by ISS-IMAP/VISI: a first report of an undulating wave front". In: *Atmospheric Chemistry and Physics* 18.22, pp. 16399–16407. DOI: 10.5194/acp-18-16399-2018. URL: https://acp.copernicus.org/articles/18/16399/2018/.

Hozumi, Yuta et al. (May 2019). "Geographical and Seasonal Variability of Mesospheric Bores Observed from the International Space Station". In: *Journal of Geophysical Research: Space Physics* 124.5, pp. 3775–3785. ISSN: 2169-9402. DOI: 10.1029/2019JA026635. URL: https://onlinelibrary.wiley.com/doi/full/10.1029/2019JA026635%20https://onlinelibrary.wiley.com/doi/abs/10.1029/2019JA026635%20https://agupubs.onlinelibrary.wiley.com/doi/10.1029/2019JA026635.

Jean, J. (2024). "Long-term studies and variability of the mesosphere and lower thermosphere summer wind dynamics at middle and high latitudes". PhD thesis. Universität Rostock.

Kalashnikova, Olga et al. (Oct. 2000). "Meteoric smoke production in the atmosphere". In: *Geophysical Research Letters - GEOPHYS RES LETT* 27. DOI: 10.1029/1999GL011338.

Kjellstrand, C. Bjorn et al. (2022). "Multi-Scale Kelvin-Helmholtz Instability Dynamics Observed by PMC Turbo on 12 July 2018: 1. Secondary Instabilities and Billow Interactions". In: *Journal of Geophysical Research: Atmospheres* 127.18. e2021JD036232 2021JD036232. DOI: https://doi.org/10.1029/2021JD036232. eprint: https://agupubs.onlinelibrary.wiley.com/doi/pdf/10.1029/2021JD0

36232. URL: https://agupubs.onlinelibrary.wiley.com/doi/abs/10.1029/2021JD036232.

Koch, Steven E. et al. (Aug. 2008). "An Atmospheric Soliton Observed with Doppler Radar, Differential Absorption Lidar, and a Molecular Doppler Lidar". In: *Journal of Atmospheric and Oceanic Technology* 25.8, pp. 1267–1287. ISSN: 0739-0572. DOI: 10.1175/2007JTECHA951.1. URL: https://journals.ametsoc.org/view/journals/atot/25/8/2007jtecha951_1.xml.

Kolmogorov, A. (1941). "The Local Structure of Turbulence in Incompressible Viscous Fluid for Very Large Reynolds' Numbers". In: *Akademiia Nauk SSSR Doklady* 30, pp. 301–305.

Lamb, Horace (1916). *Hydrodynamics*. 6th. Cambridge: Cambridge University Press.

Latteck, R. and Bremer, J. (Oct. 2017). "Long-term variations of polar mesospheric summer echoes observed at Andøya (69°N)". In: *Journal of Atmospheric and Solar-Terrestrial Physics* 163, pp. 31–37. ISSN: 1364-6826. DOI: 10.1016/J.JASTP.2017.07.005.

Latteck, R. et al. (Oct. 2010). "MAARSY – the new MST radar on Andøya/Norway". In: *Advances in Radio Science* 8.GHJ.1-1/1-, pp. 219–224. ISSN: 1684-9965. DOI: 10.5194/ARS-8-219-2010. URL: www.adv-radio-sci.net/8/219/2010/.

Latteck, R. et al. (2012). "MAARSY: The new MST radar on AndyaSystem description and first results". In: *Radio Science* 47.1. ISSN: 00486604. DOI: 10.1029/2011RS004775.

Latteck, Ralph et al. (May 2021). "Two decades of long-term observations of polar mesospheric echoes at 69°N". In: *Journal of Atmospheric and Solar-Terrestrial Physics* 216. ISSN: 13646826. DOI: 10.1016/J.JASTP.2021.105576.

Lehmann, Rüdiger (2013). "3σ-Rule for Outlier Detection from the Viewpoint of Geodetic Adjustment". In: *Journal of Surveying Engineering* 139.4, pp. 157–165. DOI: 10.1061/(ASCE)SU.1943-5428.0000112. eprint: https://ascelibrary.org/doi/pdf/10.1061/%28ASCE%29SU.1943-5428.0000112. URL: https://ascelibrary.org/doi/abs/10.1061/%28ASCE%29SU.1943-5428.0000112.

Lighthill, J. (1979). "Waves in Fluids". In: *Journal of Fluid Mechanics* 90.3, pp. 605–607. DOI: 10.1017/S0022112079212421.

Lindzen, Richard S. and Chapman, Sydney (Oct. 1969). "Atmospheric tides". In: *Space Science Reviews* 10.1, pp. 3–188. ISSN: 00386308. DOI: 10.1007/BF00171584/METRICS. URL: https://link.springer.com/article/10.1007/BF00171584.

Liu, X. et al. (2020). "Gravity-wave-perturbed wind shears derived from SABER temperature observations". In: *Atmospheric Chemistry and Physics* 20.22, pp. 14437–14456. DOI: 10.5194/acp-20-14437-2020. URL: https://acp.copernicus.org/articles/20/14437/2020/.

Lübken, F.-J. et al. (1996). "Noctilucent clouds and the thermal structure near the Arctic mesopause in summer". In: *Journal of Geophysical Research: Atmospheres* 101.D5, pp. 9489–9508. DOI: https://doi.org/10.1029/96JD00444. eprint: https://agupubs.onlinelibrary.wiley.com/doi/pdf/10.1029/96JD00444. URL: https://agupubs.onlinelibrary.wiley.com/doi/abs/10.1029/96JD00444.

Lübken, Franz Josef et al. (Dec. 1999a). "First in situ temperature measurements at the Antarctic summer mesopause". In: *Geophysical Research Letters* 26.24, pp. 3581–3584. ISSN: 1944-8007. DOI: 10.1029/1999GL010719. URL: https://onlinelibrary.wiley.com/doi/full/10.1029/1999GL010719%20https://onlinelibrary.wiley.com/doi/abs/10.1029/1999GL010719%20https://agupubs.onlinelibrary.wiley.com/doi/10.1029/1999GL010719.

Lübken, Franz-Josef (2014). "Turbulent scattering for radars: A summary". In: *Journal of Atmospheric and Solar-Terrestrial Physics* 107, pp. 1–7. ISSN: 1364-6826. DOI: https://doi.org/10.1016/j.jastp.2013.10.015. URL: https://www.sciencedirect.com/science/article/pii/S1364682613002861.

Lübken, Franz-Josef et al. (1999b). "First in situ temperature measurements at the Antarctic summer mesopause". In: *Geophysical Research Letters* 26.24, pp. 3581–3584. DOI: https://doi.org/10.1029/1999GL010719. eprint: https://agupubs.onlinelibrary.wiley.com/doi/pdf/10.1029/1999GL010719. URL: https://agupubs.onlinelibrary.wiley.com/doi/abs/10.1029/1999GL010719.

MMARIA/SIMONe (2024). [MMARIA/SIMONe Germany Real-time Monitor Webpage; accessed August 7, 2024]. URL: http://maarsy.rocketrange.no/SIMONe/SIMONe_NOR/index.html.

Mondal, Subarna et al. (Mar. 2021). "A case study of a thermally ducted undular mesospheric bore accompanied by ripples over the western Himalayan region". In: *Advances in Space Research* 68. DOI: 10.1016/j.asr.2021.03.026.

Nappo, Carmen J. (2002). "An Introduction to Atmospheric Gravity Waves". In: vol. 85. International Geophysics. Academic Press, pp. 1–24. DOI: https://doi.org/10.1016/S0074-6142(02)80269-8. URL: https://www.sciencedirect.com/science/article/pii/S0074614202802698.

Nielsen, K. et al. (2006). "An unusual mesospheric bore event observed at high latitudes over Antarctica". In: *Geophysical Research Letters* 33.7. DOI: https://doi.org/10.1029/2005GL025649. eprint: https://agupubs.onlinelibrary.wiley.com/doi/pdf/10.1029/2005GL025649. URL: https://agupubs.onlinelibrary.wiley.com/doi/abs/10.1029/2005GL025649.

Philippi, Paulo et al. (Nov. 2015). "KINETIC PROJECTION AND STABILITY IN LATTICE- BOLTZMANN SCHEMES". In: DOI: 10.20906/CPS/CILAMCE2015-0398.

Poblet, Facundo L. et al. (2023). "Horizontal Correlation Functions of Wind Fluctuations in the Mesosphere and Lower Thermosphere". In: *Journal of Geophysical Research: Atmospheres* 128.6. e2022JD038092 2022JD038092, e2022JD038092. doi: https://doi.org/10.1029/2022JD038092. eprint: https://agupubs.onlinelibrary.wiley.com/doi/pdf/10.1029/2022JD038092. url: https://agupubs.onlinelibrary.wiley.com/doi/abs/10.1029/2022JD038092.

Ramachandran, Kesava et al. (Apr. 2023). "Investigation of a Dissipating Mesospheric Bore Using Airglow Imager and Direct Numerical Simulation". In: *Journal of Geophysical Research: Space Physics* 128.4, e2022JA031114. issn: 2169-9402. doi: 10.1029/2022JA031114. url: https://onlinelibrary.wiley.com/doi/full/10.1029/2022JA031114%20https://onlinelibrary.wiley.com/doi/abs/10.1029/2022JA031114%20https://agupubs.onlinelibrary.wiley.com/doi/10.1029/2022JA031114.

Rapp, M. and Lübken, F.-J. (2004). "Polar mesosphere summer echoes (PMSE): Review of observations and current understanding". In: *Atmospheric Chemistry and Physics* 4.11/12, pp. 2601–2633. doi: 10.5194/acp-4-2601-2004. url: https://acp.copernicus.org/articles/4/2601/2004/.

Reid, Iain M. (2024). "Meteor Radar for Investigation of the MLT Region: A Review". In: *Atmosphere* 15.4. issn: 2073-4433. doi: 10.3390/atmos15040505. url: https://www.mdpi.com/2073-4433/15/4/505.

Reid, Iain Murray (2015). "MF and HF radar techniques for investigating the dynamics and structure of the 50 to 110 km height region: a review". In: *Progress in Earth and Planetary Science* 2.33. doi: 10.1186/s40645-015-0060-7.

Renkwitz, T. et al. (2017). "VHF antenna pattern characterization by the observation of meteor head echoes". In: *Atmospheric Measurement Techniques* 10.2, pp. 527–535. doi: 10.5194/amt-10-527-2017. url: https://amt.copernicus.org/articles/10/527/2017/.

Renkwitz, Toralf and Latteck, Ralph (2019). "On improving radar echo spectral width analysis for atmospheric turbulence estimates". In: *2019 International Interdisciplinary PhD Workshop (IIPhDW)*, pp. 19–23. doi: 10.1109/IIPHDW.2019.8755421.

Renkwitz, Toralf et al. (2018). "On the role of anisotropic MF/HF scattering in mesospheric wind estimation". In: *Earth, Planets and Space* 70, p. 158. doi: 10.1186/s40623-018-0927-0. url: https://doi.org/10.1186/s40623-018-0927-0.

Russell, J. Scott (1845). *Report on Waves*. PDF available. London: John Murray, 311–390, Plates XLVII–LVII.

Salby, Murry L. (2012). *Physics of the Atmosphere and Climate*. Cambridge University Press.

Saunders, R. W. et al. (2012). "Interactions of meteoric smoke particles with sulphuric acid in the Earth's stratosphere". In: *Atmospheric Chemistry and Physics* 12.10, pp. 4387–4398. DOI: 10.5194/acp-12-4387-2012. URL: https://acp.copernicus.org/articles/12/4387/2012/.

Savigny, Christian (Oct. 2017). "Airglow in the Earth atmosphere: basic characteristics and excitation mechanisms". In: *ChemTexts* 3. DOI: 10.1007/s40828-017-0051-y.

Savigny, Christian v. et al. (Jan. 2020). "Noctilucent Clouds: General Properties and Remote Sensing". In: pp. 469–503. ISBN: 978-3-030-33565-6. DOI: 10.1007/978-3-030-33566-3_8.

Schmidt, R. (1986). "Multiple emitter location and signal parameter estimation". In: *IEEE Transactions on Antennas and Propagation* 34.3, pp. 276–280. DOI: 10.1109/TAP.1986.1143830.

Seyler, C. E. (2005a). "Internal waves and undular bores in mesospheric inversion layers". In: *Journal of Geophysical Research: Atmospheres* 110.D9. DOI: https://doi.org/10.1029/2004JD004685. eprint: https://agupubs.onlinelibrary.wiley.com/doi/pdf/10.1029/2004JD004685. URL: https://agupubs.onlinelibrary.wiley.com/doi/abs/10.1029/2004JD004685.

Seyler, C. E. (2005b). "Internal waves and undular bores in mesospheric inversion layers". In: *Journal of Geophysical Research: Atmospheres* 110.D9. DOI: https://doi.org/10.1029/2004JD004685. eprint: https://agupubs.onlinelibrary.wiley.com/doi/pdf/10.1029/2004JD004685. URL: https://agupubs.onlinelibrary.wiley.com/doi/abs/10.1029/2004JD004685.

She, C. Y. et al. (Nov. 2004). "Concurrent OH imager and sodium temperature/wind lidar observation of a mesopause region undular bore event over Fort Collins/Platteville, Colorado". In: *Journal of Geophysical Research: Atmospheres* 109.D22, pp. 1–8. ISSN: 2156-2202. DOI: 10.1029/2004JD004742. URL: https://onlinelibrary.wiley.com/doi/full/10.1029/2004JD004742%20https://onlinelibrary.wiley.com/doi/abs/10.1029/2004JD004742%20https://agupubs.onlinelibrary.wiley.com/doi/10.1029/2004JD004742.

Shepherd, Theodore G (2000). "The middle atmosphere". In: *Journal of Atmospheric and Solar-Terrestrial Physics* 62.17, pp. 1587–1601. ISSN: 1364-6826. DOI: https://doi.org/10.1016/S1364-6826(00)00114-0. URL: https://www.sciencedirect.com/science/article/pii/S1364682600001140.

Smith, Anne K. (2003). "The Origin of Stationary Planetary Waves in the Upper Mesosphere". In: *Journal of the Atmospheric Sciences* 60.24, pp. 3033–3041. DOI: 10.1175/1520-0469(2003)060<3033:TOOSPW>2.0.CO;2. URL: https://journals.ametsoc.org/view/journals/atsc/60/24/1520-0469_2003_060_3033_toospw_2.0.co_2.xml.

Smith, Anne K. (2012). "Global Dynamics of the MLT". In: *Surveys in Geophysics* 33.6, pp. 1177–1230. ISSN: 01693298. DOI: 10.1007/s10712-012-9196-9.

Smith, Steven M. et al. (Sept. 2017). "Characterization of a Double Mesospheric Bore Over Europe". In: *Journal of Geophysical Research: Space Physics* 122.9, pp. 9738–9750. DOI: 10.1002/2017JA024225.

Strelnikov, B. et al. (2006). "In situ observations of small scale neutral and plasma dynamics in the mesosphere/lower thermosphere at 79°N". In: *Advances in Space Research* 38.11. Middle and Upper Atmospheres, Active Experiments, and Dusty Plasmas, pp. 2388–2393. ISSN: 0273-1177. DOI: https://doi.org/10.1016/j.asr.2005.03.097. URL: https://www.sciencedirect.com/science/article/pii/S0273117705003479.

Strelnikova, I. (2009). "Mesospheric aerosol particles: Evidence from rocket and radar techniques". PhD thesis. Universität Rostock.

Taylor, M. J. et al. (Oct. 1995). "Spectrometric and imaging measurements of a spectacular gravity wave event observed during the ALOHA-93 Campaign". In: *Geophysical Research Letters* 22.20, pp. 2849–2852. ISSN: 1944-8007. DOI: 10.1029/95GL02948. URL: https://onlinelibrary.wiley.com/doi/full/10.1029/95GL02948%20https://onlinelibrary.wiley.com/doi/abs/10.1029/95GL02948%20https://agupubs.onlinelibrary.wiley.com/doi/10.1029/95GL02948.

Urco, Juan M. et al. (2024). "Augmented Four-Dimensional Mesosphere and Lower Thermosphere Wind Field Reconstruction via the Physics-Informed Machine Learning Approach HYPER". In: *Journal of Geophysical Research: Machine Learning and Computation* 1.3, e2024JH000162. DOI: https://doi.org/10.1029/2024JH000162. URL: https://agupubs.onlinelibrary.wiley.com/doi/abs/10.1029/2024JH000162.

Urco Cordero, Juan Miguel Edgar (2020). *Beyond the spatio-temporal limits of atmospheric radars: inverse problem techniques and MIMO systems*. English. Dissertation Universität Rostock 2021. Universität Rostock. URL: https://doi.org/10.18453/rosdok_id00003356.

Vadas, Sharon L. and Fritts, David C. (2005). "Thermospheric responses to gravity waves: Influences of increasing viscosity and thermal diffusivity". In: *Journal of Geophysical Research: Atmospheres* 110.D15. DOI: https://doi.org/10.1029/2004JD005574. eprint: https://agupubs.onlinelibrary.wiley.com/doi/pdf/10.1029/2004JD005574. URL: https://agupubs.onlinelibrary.wiley.com/doi/abs/10.1029/2004JD005574.

Vaste, O.A. (1993). "Noctilucent clouds". In: *Journal of Atmospheric and Terrestrial Physics* 55.2, pp. 133–143. ISSN: 0021-9169. DOI: https://doi.org/10.1016/0021-

9169(93)90118-I. URL: https://www.sciencedirect.com/science/article/pii/002191699390118I.

VIERINEN, J. et al. (2019). "Observing Mesospheric Turbulence With Specular Meteor Radars: A Novel Method for Estimating Second-Order Statistics of Wind Velocity". In: *Earth and Space Science* 6.7, pp. 1171–1195. DOI: https://doi.org/10.1029/2019EA000570. eprint: https://agupubs.onlinelibrary.wiley.com/doi/pdf/10.1029/2019EA000570. URL: https://agupubs.onlinelibrary.wiley.com/doi/abs/10.1029/2019EA000570.

VINCENT, Robert A. (Dec. 2015). "The dynamics of the mesosphere and lower thermosphere: a brief review". In: *Progress in Earth and Planetary Science* 2.1, pp. 1–13. ISSN: 21974284. DOI: 10.1186/S40645-015-0035-8/FIGURES/10. URL: https://progearthplanetsci.springeropen.com/articles/10.1186/s40645-015-0035-8.

WALLACE, John M. and HOBBS, Peter V. (2006). *Atmospheric Science: An Introductory Survey*. Academic Press.

WHITE, F.M. (1999). *Fluid Mechanics*. McGraw-Hill International Editions. ISBN: 9780070697164. URL: https://books.google.de/books?id=fa_pAAAAMAAJ.

YUE, Jia et al. (2010). "Mesospheric bore formation from large-scale gravity wave perturbations observed by collocated all-sky OH imager and sodium lidar". In: *Journal of Atmospheric and Solar-Terrestrial Physics* 72.1, pp. 7–18. ISSN: 1364-6826. DOI: https://doi.org/10.1016/j.jastp.2009.10.002. URL: https://www.sciencedirect.com/science/article/pii/S1364682609002582.

ZECHA, M. (1999). "Untersuchung der polaren sommerlichen Mesosphäre mit unterschiedlichen Radarverfahren im VHF-Bereich". PhD thesis. Universität Rostock.